Wijeratne, I. (2013). Second harmonic generation in novel optical waveguides. (Unpublished Doctoral thesis, City University London)

**CITY UNIVERSITY LONDON**
EST 1894

**Original citation**: Wijeratne, I. (2013). Second harmonic generation in novel optical waveguides. (Unpublished Doctoral thesis, City University London)

**Permanent City Research Online URL**: http://openaccess.city.ac.uk/3015/

# Second Harmonic Generation in Novel Optical Waveguides

by

*Isuru Nagitha Mahalie Wijeratne*

A thesis submitted in fulfilment of the requirements for the

Degree of Doctor of Philosophy

**CITY UNIVERSITY LONDON**

Photonics Modelling Group,
School of Engineering and Mathematical Sciences
City University London
Northampton Square, London EC1V 0HB
United Kingdom

April 2013

# To My Mother & My Wife

"Sometimes in life you have to risk the dark in order to see the light"

# Table of Contents

# List of Figures and Tables

# Acknowledgements

# Declaration

The author grants powers of discretion to the University Librarian to allow this thesis to be copied in whole or in part without further reference to the author. This permission covers only single copies made for study purposes, subject to normal conditions of acknowledgement.

# Abstract

Second Harmonic Generation has traditionally been restricted to crystals; however, due to the development of highly sophisticated fabrication technology, poling and phase matching techniques, it has now become feasible in glass fibres and waveguides which are widely used in nonlinear optics. For instance, silica glass based Photonic Crystal Fibres (PCF) exhibit long coherence lengths and controllable optical properties such as chromatic dispersion despite low second order nonlinearity. Given such benefits, the numerical modelling and analysis of optical waveguides accurately and efficiently has become vital for the advancement of nonlinear optics. Hence, this thesis focuses on enhancing the Second Harmonic Generation in optical waveguides through the use of different structures and different materials, and demonstrating the same by numerical simulations.

In this thesis, the accurate and numerically efficient Finite Element based Beam Propagation Method has been employed to investigate the evolution of Second Harmonic Generation in highly nonlinear $SF57$ soft glass Equiangular Spiral PCFs. Further, the $H$-field based Finite Element Method has been employed for the stationary analysis of Photonic Crystal Fibres. It is shown here that the second harmonic output power in highly nonlinear $SF57$ soft glass PCF exploiting the complex Equiangular Spiral design is significantly higher in comparison with silica PCF with hexagonal air-hole arrangements. The effects of fabrication tolerances on the coherence length and the modal properties of Equiangular Spiral PCF are also illustrated by using the Finite Element Method. Moreover, phase matching between the fundamental and second harmonic modes is achieved through the use of the Quasi Phase Matching technique: this includes demonstrating the effects of higher order Quasi Phase Matching.

In parallel to the aforementioned investigations, a rigorous, full vectorial Finite Element based Beam Propagation Method has been developed to study the Second Harmonic Generation in planar Zinc Oxide ($ZnO$) waveguides where the supported modes are hybrid in nature. The investigations on planar $ZnO$ waveguides have been carried out in order to investigate possibilities of enhancing Second Harmonic Generation by optimisation of the planar waveguide. It is shown here that the second harmonic output power is significantly improved when the planar waveguide structure is optimised. Moreover, Quasi Phase Matching has been implemented in order to eliminate the phase mismatch. It has also been established that the normalised conversion efficiency $ZnO$ optical waveguide devices is significantly higher than the reported value of periodically poled Lithium Niobate ($LiNbO_3$) ones.

# List of Abbreviations and Symbols

BEM ................................................................................ Boundary Element Method
BPM ................................................................................ Beam Propagation Method
CATV .............................................................................................................. Cable TV
CMOS .................................................... Complementary Metal Oxide Semiconductor
CN ............................................................................................... Crank Nicolson
CW ................................................................................................. Continuous Wave
DC .................................................................................................... Direct Current
DLC .............................................................................................. Diamond Like Carbon
EIM ........................................................................................... Effective Index Method
ENM ........................................................................................ Equivalent Network Method
ES .............................................................................................. Equiangular Spiral
FDM ........................................................................................ Finite Difference Method
FEM ........................................................................................... Finite Element Method
FFT .............................................................................................. Fast Fourier Transform
FTTC ........................................................................................... Fibre To The Cabinet
FTTP ........................................................................................... Fibre To The Premises
FV ................................................................................................. Full Vectorial
FWM ........................................................................................... Four Wave Mixing
GVD ........................................................................................ Group Velocity Dispersion
IC ..................................................................................................... Integrated Circuit
IO ......................................................................................................... Input Output
LED ............................................................................................ Light Emitting Diode
MM .............................................................................................. Marcatili's Method
MMM ........................................................................................ Mode Matching Method
NLO ................................................................................................. Nonlinear Optics
PCF .............................................................................................. Photonic Crystal Fibre
PIC ............................................................................................ Photonic Integrated Circuit
PML .............................................................................................. Perfectly Matched Layer
PMM .............................................................................................. Point Matching Method
QPM ............................................................................................ Quasi Phase Matching
RAM ............................................................................................ Ray Approximation Method
SHG ............................................................................................ Second Harmonic Generation
SIM .............................................................................................. Spectral Index Method
SVEA ........................................................................ Slowly Varying Envelope Approximation
TE ................................................................................................ Transverse Electric
TIR .............................................................................................. Total Internal Reflection
TM .............................................................................................. Transverse Magnetic
WKB ............................................................................................ Wentzel Kramer and Brillouin

# Introduction

This chapter sets the scene for the work described in the thesis and first presents a short overview of the evolution of optical waveguides, followed by a description of a number of fundamental issues relevant to the work such as integrated optics (Section 1.2), optical nonlinearity (Section 1.4), phase matching (Section 1.5) and analytical and numerical approximations to optical waveguide problems (Section 1.6), all of which are very important in defining the aims and objectives of the work which are set out next. This chapter then concludes with an overview of the structure of the thesis.

## 1.1 LIGHTWAVE TECHNOLOGY

The development of optical communication systems is perhaps best discussed by considering the nature of light itself. Historically speaking, communication using light started when human beings started exchanging messages through hand signals early on in the history of civilisation. Limited in transmission distance and leaving room for misinterpretation of information, this was a primitive but effective if slow form of optic communication. The rest of this section explores the path from these

primitive means of communication to the sophistication of today's fibre optic technologies.

### *1.1.1   Historical Development*

One form of early communication using light was with smoke signals where different messages could be conveyed by varying the pattern of smoke. This system required a coding system [1] which was to be understood by the sender and receiver of messages and in that sense was similar to modern digital systems that use pulse codes. Reflecting mirrors and signalling lamps are two other forms of early optical communication. Further, ancient Greeks and Romans who pioneered in glass manufacturing technology discovered that light can be guided through a glass rod [2]. Similarly, the British experimented by transmitting light through a narrow jet of water in the early 19th century [3]. Prior to this, Galileo's invention of the telescope in 1609 [4] and the understanding of what is now known as Snell's Law in 1626 greatly contributed towards the development of optical communication systems [5]. Other early contributions to this sector include the creation of the reflection telescope by Newton in 1668 [6], Maxwell's prediction of electromagnetic waves in 1873 [7], Hertz's confirmation of the existence of electromagnetic waves and their oneness with light [8], analysis of a waveguide by Rayleigh in 1897 [9] and Marconi's invention of the radio detector in 1902 [10].

Perhaps the most significant invention in the field of optical communications was the invention of a light communication system called the photophone by Alexander Graham Bell in 1880 [11]. This invention enabled communication via sunlight and a thin voice-modulated mirror. When light was received at the receiving end of a message, the modulating sunlight fell on a photo-conducting selenium cell, which converted the message to an electrical current.

The origination of indicator lamps such as blinker lights used in naval communications (and indeed automobile turn signals and traffic lights too) are deep rooted in optical communication systems. The invention of the LASER (Light Amplification by Stimulated Emission of Radiation) in 1960 was a major breakthrough in the history of optical communication systems. It provided a narrow-band source of optical radiation suitable for use as a carrier of information [1].

Intensive research in the United States resulted in the first successful operation of the solid-state ruby laser (1960), the helium / neon gas laser (1961) and the gallium arsenide semiconductor laser (1962) [12].

The 1960s also saw a huge number of experiments in the communications field carried out in the United States of America using the xenon lamp as a light source. Attempts were also made in Japan at communication through glass fibres at the start of this decade. However the breakthrough was in 1966 when Kao and Hockham first suggested the concept of using glass fibres as a transmission medium [13]. This was followed by the invention of unguided optic communication systems by way of non-fibre optics and led to the development of low-loss fibre in 1970.

The 1970s brought about two results of great importance to optical communication which are the continuous operation of semiconductor lasers at room temperature in America and Japan and further reduction of the transmission loss (i.e. the $150dB/km$ achieved in England was reduced to $20dB/km$ in America and Japan [12] which was being seen as a threshold for an effective fibre-based communication system).

Other significant discoveries and inventions impacting the sphere of optical communication systems include the invention of liquid-core fibres by Ogilvie and Esdaile in 1972 [14], the invention of Gigahertz bandwidth over 1km by Gambling *et al.* the same year [15] and the prediction of zero material dispersion by Payne and Gambling in 1975 [16].

Pinnow *et al.* (1978), Van Uitert and Wemple (1978) and Goodman (1978) first discussed the possibility of ultra-low loss in infrared materials and these discussions motivated the research efforts on non-silica-based infrared optical fibres [17].

Development of fibre technology, e.g. encompassing other fibre types such as polarisation-maintaining fibres as well as glass materials suitable for even longer wavelengths in the mid and far infrared regions, has been rapid over recent years. This has facilitated the development of reliable optical fibre communication systems with high performance in today's telecommunication networks. A number of relevant developments in this area are discussed in Section 1.1.2.

### *1.1.2   Evolution of Optical Fibre*

The interest in optical fibre has grown dramatically over the past two decades as it has become a vital part in modern day communication systems. It is also used in a variety of other fields such as optical fibre sensor technology. In comparison to other methods of telecommunication such as microwave and satellite transmission, the introduction of fibre optics in the early seventies caused a complete revolution. This new form of communication offered an exciting alternative to the traditional mechanisms where, instead of electrons moving through copper wires carrying signals, photons were guided by glass fibres. Fibre optics have many advantages over conventional copper wires in the context of telecommunication. The fibre optic bandwidth (i.e. information carrying capacity) is thousand times greater than the bandwidth of conventional coaxial cables and the data loss over long distances is minimal. Therefore, it can transfer more information across greater distances, which is vital for today's communications systems.

In a broader sense, using light for communication purposes has progressed rapidly since the invention of the first low-loss fibres and as a result, most countries have already established their own optical communication links. Further, nowadays the field of fibre optics is receiving great interest from areas as diverse as spectroscopy, metrology, biomedicine, imaging, industrial machinery, and military applications. For example, according to the latest research developments in bio-medical engineering, it has been discovered that the delivery of Neodymium: Yttrium-Aluminum-Garnet ($Nd{:}YAG$), Argon ($Ar$) and Carbon Dioxide ($CO_2$) laser light would be of potential use when treating patients suffering from various types of cancer [18].

Given the numerous advantages of fibre optics, researchers and engineers are actively involved in the research and development of fibre optic components and systems. In fact, this revolution has the potential to affect our lives as much as computers and IC (Integrated Circuit) equipment once did.

## 1.2   INTEGRATED OPTICS AND APPLICATIONS

Integrated optics, also known as planar-optic technology, allows the possibility of integrating the three functions transmission, switching and routing of guided optical

beams on a plane, on a single substrate in a compact device. A number of optical functions such as waveguiding, mirroring, filtering, routing and polarisation-splitting etc. have been demonstrated in planar optical waveguides made out of semiconductor materials, silica ($SiO_2$) and polymer. Further, these optical waveguides act as the photonic equivalent of copper circuits in ICs serving as interconnects among various discrete components on a chip: this type of circuit is known as a Photonic Integrated Circuit (PIC). The refractive index of an active or core layer, which is sandwiched between two cladding layers with a lower index of refraction, causes total internal reflection which helps continue and route a particular wavelength of light. However, for slot waveguides and Hollow-core PCFs, the guidance is not via total internal reflection.

PICs are currently being manufactured by a variety of vendors worldwide as part of commercial systems and are the key to advanced transmitters in many fibre-optic based devices and applications. The basic devices are based on planar optical waveguides, in which light is confined to channels on the substrate surface and routed across the chip. These channels are typically less than $10 \, \mu m$ and are patterned using micro lithography techniques [19]. Furthermore, the invention of Photonic crystal structures [20] open the way for such integration and interconnection of several optical functions on a single PIC chip.

Applications of integrated optics have historically been in the analogue, digital, and sensor fibre-optic markets; at present, however, major new markets are emerging. The largest new market is telecommunications, where IO (Input Output) devices are used for multi-gigabit data transmission, signal splitting and loop distribution, and in bi-directional communication modules. In a third market, i.e. instrumentation, a major application is fibre-optic gyroscopes. High-speed telecommunication and fibre gyro applications are common to markets across the world today, and there have been high interest in Cable TV (CATV) and other analogue fibre-optic link applications of IO technologies [21].

Integrated Optics is mainly applied in the following areas:

- Optical communication systems
- Optical storage technology
- Photonic devices and materials
- Optical sensor technology

These are briefly discussed below.

*Optical communication systems*:

The ability of optical fibre to transmit data at high rates over long distances has been greatly exploited in telecommunications systems including cable TV. One of the most notable developments in UK is BT Infinity which expects to deliver broadband speeds 8 times higher than the typical average (e.g. $80Mbps$ downstream), initially with Fibre-To-The-Cabinet (FTTC) and more recently with Fibre-To-The-Premises (FTTP) [22]. Moreover, all-optical routers are becoming popular in providing a "cut-through-connection", i.e. eliminating the need to convert between electrical and optical signals thereby saving energy and further improving the speed [23]. Additional advantages of using optical fibre as the communication medium are increased reliability due to immunity to electromagnetic interference and data security: it is almost impossible to intercept data transmitted via optical fibre as there are no magnetic fields around optical fibres.

*Optical storage technology:*

As in all data storage systems, optical disk systems are characterised by their capacity, data transfer rate, access time, and cost. The storage capacity of an optical disk is a direct function of the spot-size (i.e. minimum dimension of a stored bit) and geometrical dimensions of the media. Therefore, developments in optical storage devices typically target reducing the spot-size by using lower wavelength light sources (see Figure 1.1). Attempts have also been made at increasing rotation speeds using higher optical power lasers and improving the efficiency of error correction codes. In addition to providing a high storage capacity (e.g. 50 GB with Blu-ray disks: see Figure 1.2), optical disks provide a more durable means of storage compared to magnetic storage mainly due to its immunity to electromagnetic interference.
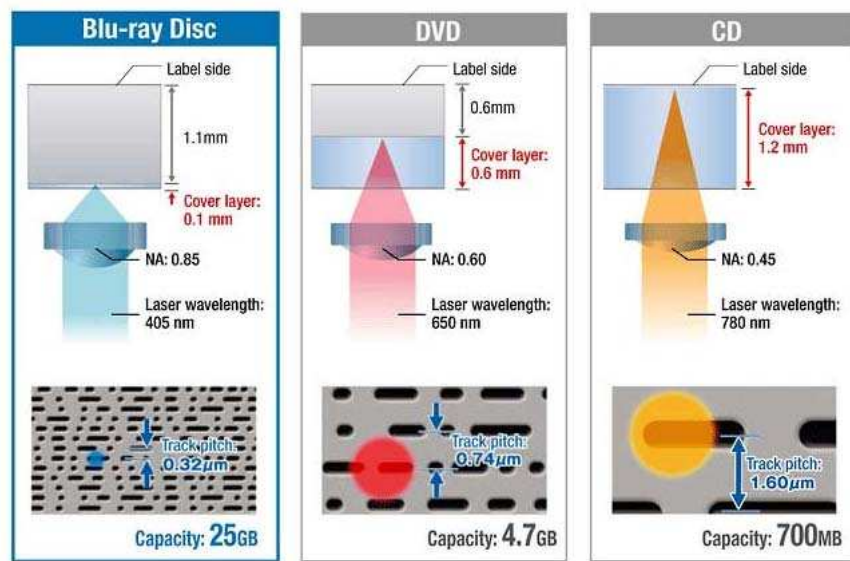
Figure 1.1 Light sources with different wavelengths [24].
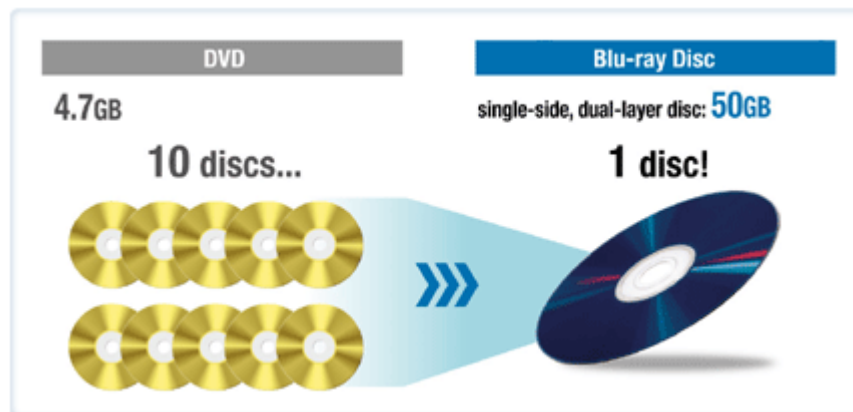


Figure 1.2 Comparison of different storage devices [25].

*Photonic devices and materials*:

Photonic devices can be categorised as Light Emitting Diodes (LEDs), lasers, semiconductor optical amplifiers, modulators, switches and integrated receivers. Further discussions on LEDs and different types of lasers are presented in this section as these are important in optical communication systems.

An LED is an optoelectronic device which generates light via electroluminescence and forms the light sources used for many semiconductor-based devices. The *AlGaInP* material system is widely used in generating highly efficient red lights for

the automobile industry, traffic light systems and low data rate ($< 50 Mbps$) optical links [26].

LEDs do not exhibit laser action although the fundamental process of light generation is the same as in laser diodes except that LEDs do not exploit stimulated emission, unlike laser devices.

There are many types of lasers available such as gas lasers (e.g.: $CO_2$ lasers, with typical wavelength of $9.4\,\mu m$ or $10.6\,\mu m$[27]), solid state lasers (e.g.: $Nd{:}YAG$ lasers (neodymium-doped yttrium aluminum garnet; $Nd{:}Y_3Al_5O_{12}$) with typical wavelength of $1064\,nm$ [28] and $Er{:}YAG$ lasers (Erbium-doped Yttrium Aluminium Garnet; $Er{:}Y_3Al_5O_{12}$) with typical wavelength of $2940\,nm$ [29]) and semiconductor lasers which are commercially available as laser diodes with typical wavelengths ranging from $375\,nm$ to $3500\,nm$ (e.g.: $GaAs$, $InGaP$, $InP$ and $InGaAs$). Lasers have been widely used in a number of areas such as dentistry, ophthalmology, oncology, fluid dynamics, military and defence, laser pumping and the automotive industry. $Nd{:}YAG$ lasers are used for soft tissue surgeries in dentistry, $Er{:}YAG$ lasers are used for laser resurfacing of human skin (i.e. reduce facial wrinkles and skin irregularities such as blemishes or acne scars) and $CO_2$ lasers are used for industrial applications such as cutting and welding.

$Nd{:}YAG$ lasers which emit light at $1064\,nm$ is the most common type of lasers. It also has transitions near $940\,nm$, $1120\,nm$, $1320\,nm$ and $1440\,nm$. For the $1064\,nm$ fundamental of $Nd{:}YAG$ laser, the second harmonic wavelength is $532\,nm$ [1]: these wavelength values are used in this thesis. Another feature is that the $Nd{:}YAG$ lasers operate in both pulsed and continuous mode. However optical communications systems have been revolutionised by the development of the semiconductor laser as a pump source.

*Optical sensor technology*:

Optical fibre sensors are now commonly employed in monitoring chemical, biological or physical changes in a variety of applications. For example, optical sensors can provide a wide range of data about environmental conditions, oil reserve

---

[1] Frequency doubling or second harmonic generation (SHG) is a technique used to produce a wavelength that is one-half of the fundamental wavelength. See Chapter 3.

levels and quality control or detect changes in the electromagnetic waves as they interact with a chemical. Optical sensors also enable the integration of chemical sensing to 'lab-on-a-chip' devices which bring together multiple chemical processes on to a single chip, saving on costs and reducing chemical waste [30]. Other advantages of optical sensors are increased sensitivity, geometric versatility in that fibre sensors can be configured in arbitrary shapes, low power consumption and immunity to electromagnetic interference.

### 1.3   OPTICAL WAVEGUIDES

An optical waveguide is a structure that guides a light wave by confining it to travel along a certain direction. In optical waveguides, light is trapped to the core region which is made from a material with index of refraction $n_{core}$ by the surrounding cladding region which is made from a material with index of refraction $n_{cladding}$. For the propagation of light the condition $n_{core} > n_{cladding}$ must be satisfied.

The relationship between angles of incidence and refraction for a wave imposing on an interface between two media with different refractive indices is defined by Snell's law (i.e. law of refraction). This general relationship is expressed by equation (1.1) ;

$$n_1 sin\theta_1 = n_2 sin\theta_2 \qquad (1.1)$$

where $n_1$ is the low refractive index, $n_2$ is the high refractive index, $\theta_1$ is the incident angle and $\theta_2$ is the refractive angle. Figure 1.3 shows the light ray refracted from a low to high refractive index interface.
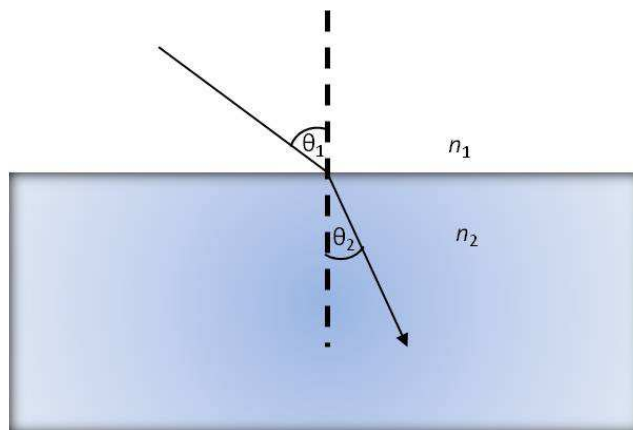


Figure 1.3 Light ray refracted from a low to high refractive index interface.

The concept of light propagation along an optical fibre is the process of Total Internal Reflection (TIR) in which light is reflected between the core/cladding interfaces. The TIR is an important principle in optical fibres. For the propagation of light within an optical fibre, it is necessary to consider the refractive index of the dielectric medium. The refractive index of a medium is defined as the ratio of the velocity of light in a vacuum to the velocity of light in the medium. There are two requirements for the TIR which are;

- Light ray must travel from a high optically dense medium to low optically dense medium.
- The angle of incidence must be greater than the critical angle.

The behaviour of the incident light ray on the interface between two dielectrics is shown in Figure 1.4.



|        (a)        |        (b)        |        (c)        |
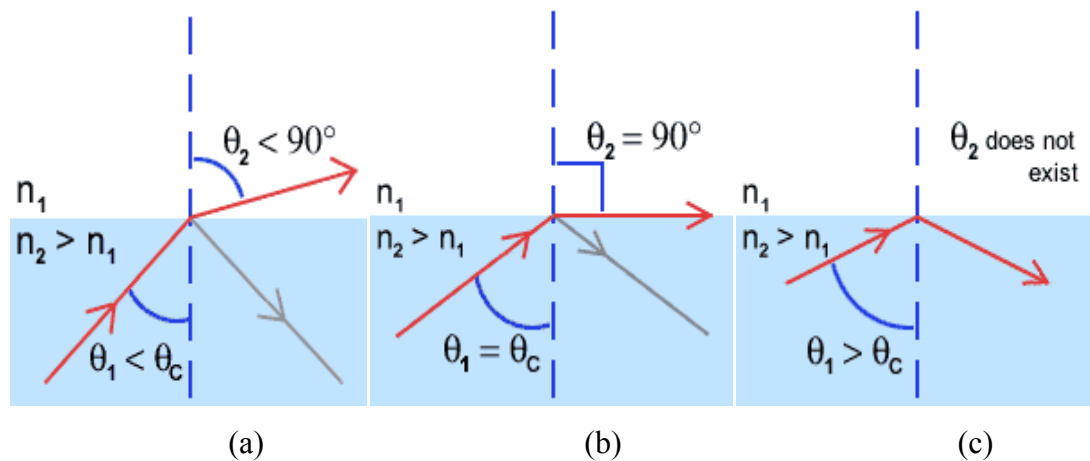
Figure 1.4 Light ray incident from a high to low refractive index interface [31].

In Figure 1.4 (a), the light ray is refracted away from the normal as it travels from a higher refractive index medium ($n_2$) to a lower refractive index medium ($n_1$); in this case the incident angle ($\theta_1$) is less than the critical angle ($\theta_c$). Figure 1.4 (b) shows that further increasing the angle of the incident light ray produces an angle of refraction ($\theta_2$) of $90^0$, which is known as the critical angle and the bent light ray lies between the two media. When the $\theta_1$ is further increased the refraction is not possible and the light ray is reflected back into the higher refractive index medium ($n_2$); this is shown in Figure 1.4 (c) which satisfies the condition $\theta_1 > \theta_c$. This phenomenon is known as the Total Internal Reflection (TIR). Figure 1.5 shows TIR in an optical

fibre. It can be observed that the light, once it is inside, is trapped and confined in the guide and propagates in a zig-zag path along the fibre axis.
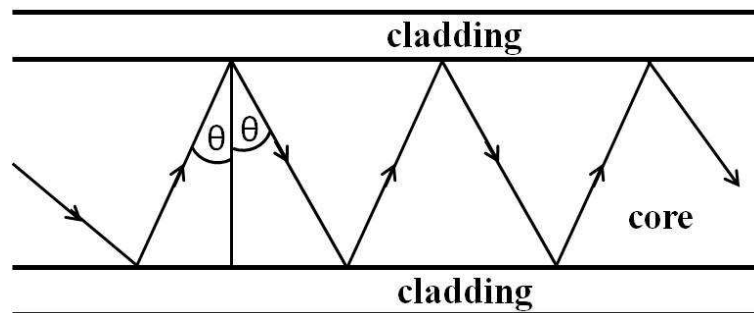


Figure 1.5 Total internal reflection in an optical fibre.

Waveguides can be categorised as one-dimensional (1-D) or two-dimensional (2-D), depending on their geometry. An example of a 1-D waveguide is an asymmetric slab waveguide, consisting of a thin film deposited on a dielectric slab. The opposite side of the film is usually air. Examples of 2-D waveguides are rectangular channel waveguides (a rectangular channel embedded in a dielectric slab) and an optical fibre. Further, to achieve the desired features in optical integrated circuits and optical communication systems, there are many types of optical waveguides which have been used, such as Photonic Crystal Fibres, optical fibres, rib waveguides and channel waveguides which follow the same wave guiding principles as mentioned above.

## 1.4   OPTICAL NONLINEARITY

The basic concept of nonlinearity is that the output result of a system is not directly proportional to its input and thus in other words, in a real physical system the response is not directly proportional to its stimulus. Nonlinear effects in electromagnetism have been known for a long time. Nonlinear optics can be used with lasers due to their highly directional nature. The nonlinear optical wave can be characterised by defining either one of its electric field or magnetic field (and it is possible to relate the electric field to the magnetic field with the use of Maxwell's equations which are discussed in Chapter 3).

The relationship between the linear polarisation *P* and the applied electric field $\boldsymbol{E}$ can be represented as [32];

$$P = \varepsilon_0 \chi^{(1)} \boldsymbol{E} \qquad (1.2)$$

where $\chi^{(1)}$ is the linear susceptibility and $\varepsilon_0$ is the permittivity of free-space.

Nonlinear optical effects were introduced by Rev. John Kerr in the 1870s when he demonstrated that the refractive index of a number of solids and fluids varies proportionally to the square of the DC field: this phenomenon is known as the Kerr effect and is observable in liquids and amorphous solids [33]. In the 1890s, Friedrich Pockels discovered that the refractive index change in non-centrosymmetric crystal material is directly proportional to the applied DC field.

Since the first invention of the inherently nonlinear lasers in 1960, nonlinear optics became a wider field exploiting the high power of the laser. In 1961, Peter Franken *et al*. discovered the Second Harmonic Generation (SHG). The equation (1.3) shows the general relationship between the nonlinear polarisation, $P_{NL}$, and the electric field, $\boldsymbol{E}$ [32];

$$P_{NL} = \varepsilon_0 \left( \chi^{(1)} \boldsymbol{E} + \underbrace{\chi^{(2)} \boldsymbol{EE}} + \underbrace{\chi^{(3)} \boldsymbol{EEE}} + \cdots \right) \qquad (1.3)$$

Second order nonlinearity        Third order nonlinearity

where $\chi^{(n)}$ is the nonlinear susceptibility ($n = 1, 2, 3, ...$).

The optical nonlinearities with an instantaneous response based on the $\chi^{(2)}$ and $\chi^{(3)}$ nonlinearity of a medium is known as parametric nonlinearity. Parametric nonlinearities give rise to effects such as optical parametric amplification, sum frequency generation and SHG which are described in the rest of this section. Materials with a lack of inversion symmetry exhibit higher $\chi^{(2)}$ nonlinearity.

*Parametric amplification*:

In parametric amplification the signal wave (or beam) propagates through the nonlinear crystal together with a pump wave (or beam) of shorter wavelength. Photons of the pump wave are then converted into low level energy signal photons and the same number of so-called idler photons; the photon energies of the idler wave are the differences between the photon energies of pump and signal

waves. Eventually the pump energy is fully converted (i.e. there is no residual pump energy) into the energy of signal and idler beams. This phenomenon is shown in Figure 1.6.
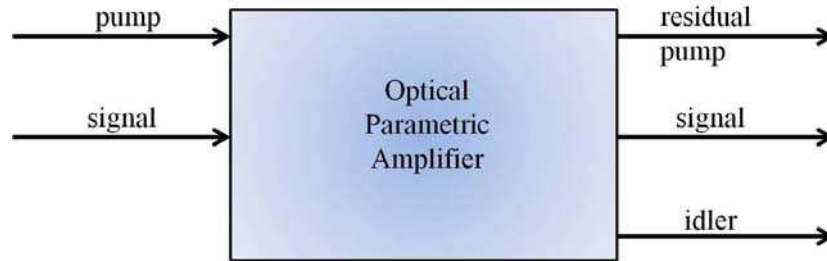


Figure 1.6 Optical parametric amplification.

In the case without pump depletion, the signal and idler waves establish themselves physically as separate beams. However, there are parametric amplifiers with depletion where the signal and idler waves are identical, with the same frequency and same polarisation. The output signal frequency then becomes exactly half the pump frequency (i.e. second harmonic frequency), and the phase relationship between signal and pump determines the direction of energy flow (i.e. whether there is amplification or de-amplification of the signal) [34, 35].

*Sum frequency generation*:

A sum frequency can occur where two pump beams generate another beam where the frequency is the sum of the optical frequencies of the pump beams. i.e., the two input photons at angular frequencies $\omega_1$ and $\omega_2$ are converted completely to energy approximately equivalent to the sum of their energies in another photon with the angular frequency of $\omega_3$ (i.e. $\omega_3 = \omega_1 + \omega_2$). Figure 1.7 shows the principle of sum frequency generation [36].
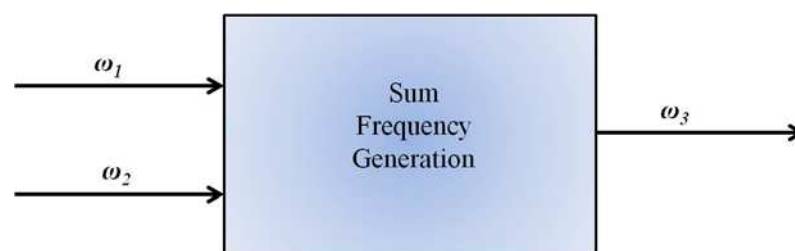


Figure 1.7 Sum frequency generation.

*Second Harmonic Generation (SHG)*:

Figure 1.8 illustrates the principle of SHG, which is also known as frequency doubling. In this process, two photons with an angular frequency of $\omega$ are effectively combined with each other in a nonlinear material (i.e. material which lacks inversion symmetry) producing another photon with twice the energy and angular frequency (i.e. $2\omega$) and thus half the wavelength of the initial photons [37].



Figure 1.8 Second Harmonic Generation.

According to equation (1.3) there can also exist parametric nonlinearities related to $\chi^{(3)}$ known as third order nonlinearity. It can generate effects such as self-phase modulation, Four-Wave Mixing and cross-phase modulation etc. which are described below.

*Self-phase modulation*:

This is a nonlinear effect where light particles interact with each other. In self-phase modulation, an intense optical pulse (i.e. ultra-short pulse) propagates through a nonlinear medium while it gains an additional phase as a result of the nonlinear change in the refractive index due to the Kerr effect [38].

*Four-wave mixing*:

This mechanism refers to the interaction of four waves in a nonlinear medium via $\chi^{(3)}$. Waves having at least two different frequency components $\omega_1$ and $\omega_2$ ($\omega_1 < \omega_2$) propagating together in a nonlinear medium, leads to a refractive index modulation at the difference frequency [39]. Therefore, it will create two additional frequency components $\omega_3$ and $\omega_4$ where $\omega_3$ and $\omega_4$ can be identified as follows;

$$\omega_3 = \omega_1 - (\omega_2 - \omega_1) = 2\omega_1 - \omega_2 \tag{1.4}$$

$$\omega_4 = \omega_2 + (\omega_2 - \omega_1) = 2\omega_2 - \omega_1 \tag{1.5}$$

*Cross-phase modulation*:

Cross-phase modulation occurs when two or more waves interact in a third order medium while the phase of one wave can be modulated by the intensity of the other wave(s). Further, in cross-phase modulation the change in the optical phase of a light beam occurs due to the interaction with another beam in a nonlinear medium which is known as a Kerr medium [40].

Overall, the study of nonlinear optics of the second order (e.g. SHG) is particularly beneficial for several reasons such as the continuous improvement in materials and the feasibility of implementation with nonlinear response devices, e.g. micro and nano scale optical waveguides for quasi phase matching. SHG and quasi phase matching are discussed further in Chapter 3.

## 1.5 PHASE MATCHING

Phase matching is an important feature in nonlinear optics, especially in parametric processes such as sum frequency generation, parametric amplification, Four-Wave Mixing (FWM) and Second Harmonic Generation (SHG), in achieving higher efficiency. Phase matching means matching the phase velocities of the required wave and its driving nonlinear polarisation wave. The key principle behind phase matching is that the direction of energy flow between interacting waves (i.e. fundamental and harmonic waves) along the propagation direction is determined by the relative phase between the nonlinear polarisation and the harmonic field. To achieve such a condition, amplitude contributions from different parts of the nonlinear crystal to the harmonic wave needs to be in phase at the end of the nonlinear crystal [41]. Furthermore, if the fundamental mode and second harmonic refractive indices of the crystal are the same, the energy will keep flowing along the propagation direction over a long distance. When there is zero phase mismatch, it is possible to achieve an effective nonlinear interaction. However, if there is a phase mismatch, then the energy will cycle forwards and backwards between the fundamental and the harmonics (i.e. frequently reversing the direction) [42]. As an example, the phase mismatch in SHG can be represented by equation (1.6) ;

$$\Delta k = k_2 - 2k_1 \qquad\qquad (1.6)$$

where $k_1$ and $k_2$ are the wavenumbers of the fundamental and second harmonic waves respectively. In equation (1.6) for the ideal case the phase mismatch should be zero (i.e. $k_2 = 2k_1$). However, perfect phase matching cannot be realised in practice due to chromatic dispersion and Figure 1.9 shows the general case of SHG phase mismatch.
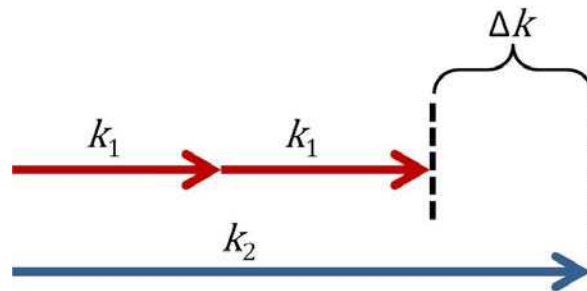


Figure 1.9 Phase mismatch of SHG.

There are several different methods that have been used to eliminate phase mismatching (i.e. phase matching techniques) and increase the efficiency of frequency conversion in practice: some of the widely used techniques are;

- Angle phase matching.
- Temperature phase matching.
- Čerenkov phase matching.
- Quasi phase matching.

These are discussed briefly below.

*Angle phase matching*:

The phenomenon of angle phase matching can be divided into two types which are known as scalar and vector angle phase matching. Scalar angle phase matching is a very common technique used when the interacting waves propagate collinearly. In this case the two pump waves have the same polarisation. On the other hand, vector angle phase matching is applied when the waves do not propagate collinearly due to the orthogonal polarisation of the pump waves. For example, in the case of SHG, in scalar phase matching the pump wave is either ordinary or extraordinary, whereas in

vector angle phase matching the pump is polarised and one of its orthogonal components is ordinary and the other is extraordinary [43].

*Temperature phase matching*:

Temperature phase matching is also known as non-critical phase matching. In temperature phase matching, the phase mismatch can be minimised by adjusting the operating temperature (as the refractive index is a function of temperature) of the crystal so that the phase velocities of the interacting beams become equal. Further, the interacting beams are aligned in order to propagate along the propagation axis of the nonlinear crystal [44].

*Čerenkov radiation phase matching*:

The basic concept Čerenkov radiation phase matching is as follows. Consider a charged particle is travelling in a medium with a velocity exceeding the phase velocity of light. However, because of particular conditions, it is possible to achieve the emission of radiation, if a charged particle is moving with a constant velocity lower than the phase velocity of light. For example, the SHG can be observed in the form of Čerenkov radiation due to the phase matching between the guided mode of fundamental wave and the radiation mode of the harmonic wave [45]. Moreover, in this technique the generated second harmonic wave in the nonlinear crystal guides with a phase velocity faster than in the substrate of an optical waveguide.

*Quasi phase matching*:

Quasi phase matching is an attractive technique which works by inverting the nonlinear susceptibility at every coherence length in crystals with lack of inversion symmetry [46]. This technique allows for a phase mismatch over some propagation distance in the optical waveguide and then reverses the nonlinear interaction at regular intervals (i.e. coherence length) to avoid the interaction with the wrong direction of conversion. Further, it is possible to achieve higher power conversion efficiency in SHG by using the quasi phase matching technique. Further details are given in Chapter 3.

## 1.6 SOLUTIONS FOR OPTICAL WAVEGUIDE PROBLEMS

Careful analysis of optical waveguides is essential in order to determine the electric or magnetic field distribution of the optical fields or the intensity distribution associated with the light propagation constants and field profiles of all the modes that the waveguide supports within the waveguide structure. This can be achieved by solving the well-known Maxwell's equations on the electromagnetic fields in a given structure and satisfying the boundary condition which defines the waveguide cross-section. However, analysing optical waveguides to implement Maxwell's equations is challenging due to complex structures, arbitrary refractive index distribution (graded optical waveguides), anisotropic and non-linear optical materials as well as materials with complex refractive index such as semiconductors and metals. Numerous analysis methods have been proposed, which fall into the following two broad categories:

- Analytical Approximations
- Numerical Approximations

These are briefly discussed below.

### 1.6.1 Analytical Approximations

Exact analytical solutions are not always feasible, e.g. if the waveguide has an arbitrary refractive index distribution; hence, analytical approximations are widely used. Typical applications are in the modelling of optoelectronic waveguides such as buried waveguides, rib waveguides, tapers and directional couplers. This group of methods has always been very popular with the optoelectronic circuit designers, especially before the advent of modern computers.

Well-known approximation methods used with 2-D waveguides are the Ray Approximation Method (RAM) [47] and the Wentzel, Kramers and Brillouin (WKB) method [48]. These methods however, do not handle boundary conditions and are therefore not suited for the analysis of 3-D waveguides.

3-D optical waveguides which are commonly used in PICs, require hybrid mode analysis as their fields are of hybrid nature. Marcatili's Method (MM) and the Effective Index Method (EIM) are examples of such methods, which are discussed in the rest of this section. These techniques however, do not treat these modes as hybrid

but often as purely *TE* or *TM* modes. Hence, their accuracy deteriorates near the cut-off frequency.

### 1.6.1.1  Marcatili's Method

Marcatili's Method can be used to calculate the propagation constants and modal fields supported by a rectangular dielectric waveguide (i.e. a dielectric rod with a rectangular cross-section, surrounded by four different dielectrics of lower refractive indices) by approximating to the fields in two slab waveguides, obtained by extending the width and the height of the rectangular core to infinity. The waveguide is assumed to support a well-confined mode which means only the regions on either side of the dielectric rod contain a considerable field and the problem is reduced to two slab waveguides, one vertical and the other horizontal. The field is assumed to vary sinusoidally in the core region and exponentially in the four cladding regions. The axial propagation constant is determined by simultaneously solving two transcendental or eigenvalue equations for each slab waveguide. MM works well in the regions far from cut-off, but performs poorly near the cut-off region [49].

### 1.6.1.2  The Effective Index Method

The Effective Index Method (EIM), proposed by Knox and Toulios in 1970 [50] is an improvement on MM [51] for the analysis of a rectangular waveguide. In this approach, the core of the rectangular dielectric waveguide is replaced by two slabs where one depends on the other (unlike in MM where the two slabs are mutually independent [52]); i.e. the first step solves the transcendental equation for a vertical slab waveguide by applying the appropriate boundary conditions. The effective index which is calculated is used as the refractive index of the horizontal slab waveguide, and by solving the eigenvalue equation a good approximation of the effective index of the original waveguide structure can be obtained. As only the solutions for slab waveguides are required, this method is significantly more efficient than those methods that solve the rectangular structure directly.

The EIM can be applied to a wide variety of structures, including ridge waveguides, diffused waveguides [53], channel waveguides, strip waveguides and arrays of such waveguides [54], also for various types of optical fibres and fibre devices [55, 56].

The drawback is that, as with MM, it does not work very well near the cut-off region. Various improvements of the EIM have been proposed over the years such as the EIM based on linear combinations of solutions [57, 58] and the EIM with perturbation correction [54].

### 1.6.2   Numerical Approximations

Advances in integrated optics mean that it is often necessary to analyse arbitrarily shaped dielectric waveguides, which in many cases are also arbitrarily inhomogeneous and/or arbitrarily anisotropic. In most cases, such arbitrariness makes it difficult to use analytical solutions: numerical solutions should be employed instead.

Numerical techniques can generally be more computationally complex compared to analytical methods; however, they are very powerful. Numerical techniques can analyse the entire input geometry without having to make assumptions about which field interactions are most important.

Various factors need to be taken into consideration in the selection of an appropriate numerical method for a particular waveguide analysis problem. The key factors are summarised below [59-61]:

- the shape of the cross-section of the structure, whether it is curved or polygonal or whether it is convex or non-convex.
- whether a computer program requiring human intervention or some exploratory work is needed.
- whether the method should be programmable to facilitate a wide range of structures or it has to be written especially for each region of the structure separately.
- whether the dominant mode only, or a number of the higher order modes are required.
- whether the field distribution and/or the cut-off frequency is/are needed.
- the level of accuracy needed for eigenvalues and perhaps eigen functions.
- the accuracy of the method in modelling the dielectric boundaries and regions.

- the accuracy of the method in specific frequency ranges, e.g. near the cut-off frequency.

- whether the method has a mechanism of generating spurious numerical solutions and if so whether the method can identify and/or eliminate them.

- the computational efficiency of the method, including its computer storage requirements (both volatile and non-volatile).

- the assumptions and limitations of the method.

In practice, each method represents some sort of compromise between the above aspects and no specific method is superior to the other in all aspects. A selection must be made depending on what would be optimal for the scenario at hand.

Numerical solutions fall into two main categories, i.e. domain solutions and boundary solutions. Domain solutions, also called differential solutions, include the whole domain of the optical waveguide structure as the operational area, whereas boundary solutions, also called integral solutions, include only the boundaries as the operational area. Some examples of boundary solutions are the Boundary Element Method (BEM), Point-Matching Method (PMM) and Mode-Matching Method (MMM). Examples of domain solutions are the Spectral Index Method (SIM), Finite Difference Method (FDM), Beam Propagation Method (BPM) and Finite Element Method (FEM). Selected important methods are discussed in the rest of this section.

### 1.6.2.1   The Boundary Element method

The Boundary Element Method (BEM) is a combination of the conventional boundary integral equation method and a discretisation technique [62]. The BEM can be applied as a general technique to solve boundary integral equations. The derivation of the integral equations with respect to the unknown fields at boundaries is obtained by using the method of weighted residuals or Green's formula. These integral equations are then discretised into a set of linear equations to be solved by the numerical methods. The main advantage of BEM is that, discretisations are restricted only to the boundaries, therefore, data generation becomes much easier and it can be used to analyse problems with infinite domains. Further, it is not necessary to truncate the domain at a finite distance and impose artificial boundary conditions: this is due to the discretisation of elements being confined to the internal boundaries.

The BEM can be used for the analysis of arbitrarily shaped discontinuities similar to the FEM, with the BEM using far fewer nodes than FEM does. In 1986 Koshiba and Suzuki presented a numerical approach based on the BEM for the analysis of discontinuity problems in a dielectric slab waveguide for *TE* and *TM* modes [63]. However, the disadvantage is that the BEM can only be applied to homogeneous structures [64] due to the matrices involved being dense matrices unlike those in FEM which are sparse and highly numerically efficient.

### 1.6.2.2   The Point Matching Method

The Point Matching Method (PMM) is a boundary solution technique used for the analysis of isotropic homogeneous dielectric waveguides. In 1969, J.E. Goell described a computer-based analysis of the propagating modes of a rectangular dielectric waveguide [65]. An expansion of the electromagnetic field in terms of a series of circular harmonics has been derived based on Goell's analysis, i.e. Bessel and modified Bessel functions multiplied by trigonometric functions. Further, a system of linear equations can be obtained by matching the tangential fields at optimally selected points around the boundary which is known as 'matching points'. A characteristic equation including the propagation constant is obtained and solved for the appropriate eigenvalues by applying the condition of nontrivial solutions. Then the original matrix equation can be solved for each mode with the use of standard matrix techniques.

The PMM is used for many waveguide structures such as dielectric waveguides with arbitrary cross-sections, composite structures and for computing coupling coefficients between two rectangular rods. Rotating the grid of equiangularly spaced matching points in order to place a matching point at the corner of a rectangular dielectric waveguide yields improved results for the PMM [66]. A drawback is that the PMM is not suitable in the case of 3-D waveguide structures with inhomogeneous index distribution, such as graded index fibres.

### 1.6.2.3   The Mode Matching Method

The Mode Matching Method (MMM) is a powerful electromagnetic numerical modal analysing technique and is broadly used for simulating different dielectric

waveguide problems and the numerical complexity is significantly lower than in other methods [67]. It is also known as the Equivalent Network Method (ENM). In MMM, the continuous spectra artificially bound the structure with conducting planes. The waveguide structures can be viewed in terms of two basic building blocks. These building blocks are uniform regions of the dielectric waveguide interfaced by the dielectric step discontinuities. Then each block is analysed individually and combined together for the desired structure. Characterising the step discontinuities as transformers and the representation of the uniform dielectric regions as uniform transmission lines leads to a transverse equivalent network of the waveguide structure. Further, the dispersion relation can be derived in order to obtain the propagation characteristics of the waveguide.

Initially, the continuous spectrum [67] and *TE* to *TM* coupling at the sides of the waveguide were neglected in the MMM, due to the artificial bounding of the structure. In 1986, Dagli and Fonstad presented a modification where the continuous spectra are discretised by converting integrals into summations using suitable basis function expansions rather than artificially bounding the structure to discretise the continuous modal spectrum [68].

### 1.6.2.4   The Spectral Index Method

The Spectral Index Method (SIM) was initially used to analyse propagation constants and guided modes of semiconductor rib waveguides [69, 70] and semiconductor waveguides with multiple ribs [71, 72]. In SIM, the wave equation is expressed in terms of the Fourier transform and the Fourier series. This method replaces the original rib structure with an effective structure in order to simplify the analysis of the rib waveguide. Then in order to model the penetration of the optical field into the cladding, it is necessary to replace the actual physical dimensions by new ones where the optical field is zero. The SIM has the ability of expanding the field in terms of local modes and matching the fields along the base of the rib. Further, the field inside the rib of the waveguide can be represented in terms of trial functions. Moreover, the Fourier transform can be applied to reduce the problem to a 1-D structure, whereas in the rib region the wave equation of $H$ (magnetic) or $E$ (electric) fields are expanded in the form of a Fourier series. Then the transfer

relationship is used to link the two solutions; as a result the propagation constant of the original rib waveguide can be determined.

### 1.6.2.5   The Finite Difference Method

The Finite Difference Method (FDM) is another versatile numerical technique used for analysing dielectric waveguide problems. The FDM involves substituting the partial derivatives in the partial differential equation describing the physical process by an algebraic approximation based on simple relationships between the values of the function of the desired system. Due to the small finite distances between consecutive values of the function, this method is known as FDM. Further, the FDM is an ideal candidate for modelling inhomogeneous media and complicated boundaries by discretising a cross-section of the system. In order to apply the FDM to a dielectric waveguide, the following steps are needed [73];

- I.    Generate a grid (i.e. mesh) for the desired system.
- II.   Substitute the derivatives in an ordinary or partial differential system of equations with finite difference schemes. Then the ordinary or partial differential equation(s) become(s) a linear or nonlinear system of algebraic equations.
- III.  Solve the system of algebraic equations.
- IV.   Implement and test the computer code.

Moreover, the accuracy of the FDM depends on the size of the mesh, the order of the finite difference scheme used and the nature of the electromagnetic field (scalar or vector).

### 1.6.2.6   The Beam Propagation Method

The Beam Propagation Method (BPM) is the most powerful technique used for investigating linear and nonlinear lightwave propagation phenomena in longitudinally varying waveguides and has been first applied in optoelectronics in the early 1980s [74]. Initially, the BPM was based on the Fast Fourier Transform (FFT) where the wave propagation is analysed only for scalar solutions by considering paraxial approximation in weakly-guiding waveguides. In 1996, Tsuji and Koshiba presented the unified Finite Element Beam Propagation Method (FE-

BPM) for the both *TE* and *TM* modes in strongly-guiding longitudinally varying optical waveguides [75]. Then in 2000, Obayya *et al*. presented a full vectorial BPM for 3-D optical waveguides. Further discussions on the BPM and its importance for this work are presented in Chapter 2.

### 1.6.2.7   The Finite Element Method

The Finite Element Method (FEM) is a versatile and accurate method for the stationary analysis of optical waveguides. The FEM is capable of analysing the behaviour of the modes in optical waveguides with arbitrary and complicated cross-sectional geometries. In the FEM, the domain of the problem is discretised into small elements. Then the problem is approximated in each element then connected at the nodal points to solve the system domain. In 1984 Rahman and Davies introduced the FEM for integrated optical waveguides with infinite elements and the elimination of the spurious solutions by using a penalty term in the variational expression [76-78]. Further discussions, including the derivation of FEM, are presented in Chapter 2.

### 1.7   AIMS AND OBJECTIVES

The work undertaken was designed to address a number of the 'gaps' in current knowledge and was thus motivated by research into more practical implementation of SHG optical waveguides. Specifically the focus was on the need to maximise the power conversion efficiency and the distance along the waveguide before which the SH output power starts to drop (the coherence length). The research showed that these two aspects could be enhanced by optimising the optical waveguide structures (for example in terms of the nature of the structure and/or its dimensions and the materials from which it is made) in order to achieve a better coherence length (i.e. distance for which both the fundamental and SH are in phase). The work has shown that however, there is a trade off between these two aspects and hence this leads to an optimisation problem where the optimum solution can best be determined by the target practical application of the waveguide.

In light of the above, the specific objectives of the work carried out were as follows:

(i)   To produce a stationary analysis of different types of optical waveguides using different materials by implementing the Finite Element Method (FEM) based on the rigorous full vectorial **H**-field formulation.

(ii)  To develop the scalar and full vectorial Beam Propagation Method (BPM) in order to analyse guided wave propagation in hexagonal Photonic Crystal Fibres (PCFs), Equiangular Spiral Photonics Crystal Fibres (ES-PCFs) and waveguides.

(iii) To investigate Second Harmonic Generation (SHG) in nonlinear materials such as $SiO_2$, $SF57$ and $ZnO$ and their crystal orientations; also to optimise second harmonic output power with the use of the Quasi Phase Matching (QPM) technique and by adjusting the poling direction.

(iv)  To apply the methods developed in (i) and (ii) to study the behaviour of the second harmonic output power in optimised structures of hexagonal PCF and ES-PCF with $SiO_2$ and $SF57$ materials and $ZnO$ waveguides.

(v)   To investigate error tolerances of the coherence length and the fabrication errors in the QPM technique.

(vi)  To report the results of these investigations to the community through papers published in the international journals.

## 1.8   THESIS OVERVIEW

The author of this thesis carried out the research presented on the rigorous analysis of optical waveguides using **H**-field based full vectorial finite element methods (FEM) and finite element-beam propagation method (FE-BPM) techniques. The work reported in this thesis has been mainly devoted to the study of the nonlinear phenomenon of second harmonic generation (SHG) in different optical waveguides with dielectric materials.

The thesis has been structured as follows. In Chapter 1 a review of the research carried out in the optoelectronics field and reported in the literature is given and provides the context for the research carried out by the author. Further, the fundamental aspects of the physics of the optical waveguides are presented, followed by a brief discussion of the field of integrated optics and their applications. Particular emphasis has been given to specific topics such as "optical nonlinearity" and "phase matching" due to the importance of their contribution to second harmonic generation in optical waveguides. Further, the basics of several important numerical methods are discussed, considering both stationary and guided propagation of the optical waves.

In Chapter 2, a detailed derivation of the full vectorial FEM is presented. Further, its application to dielectric optical waveguides is given, this being followed by a brief background to the method. Further, the elimination of spurious modes by introducing the "penalty function" is described. The full vectorial BPM and its origins are presented later in this chapter. The derivation of guided-wave formulation and finite element approach are also considered.

Chapter 3 presents results on SHG together with the studies on second order nonlinear susceptibility in different materials and with different crystal orientations. Thorough discussions of the coherence length, quasi-phase matching and poling techniques are also discussed. Following that, a thorough discussion of the significance of the poling direction of optical waveguides is presented. Based on these, the choices of the poling method and type of material to be used for the development of the SHG in optical waveguides are then justified. The last section of this chapter derives the scalar BPM for SHG with and without pump depletion and also the full vectorial BPM.

Chapter 4 outlines the considerations that have led to the selection of the novel ES-PCF design concept which was originated at City University London (CUL) and shows how the relevant parameter values were optimised to obtain the maximum second harmonic power conversion efficiency. Detailed results obtained are compared to those from hexagonal PCF designs. Further, the results of numerical simulations using conventional optical fibre are considered and then validated. This

chapter also includes numerical studies for the determination of QPM in PCFs and ES-PCFs and the effect of fabrication errors is also presented.

In Chapter 5, SHG in *ZnO* planar optical waveguides is described. In particular the implementation of full vectorial BPM for the analysis of second harmonic output power is given in this chapter. Further, a comparison between the normalised power conversion efficiency of the optimised *ZnO* planar optical waveguide structure and that of Lithium Niobate (LN) optical waveguide is also presented.

Chapter 6 represents a summary of the achievements of the work of the author which are presented in this thesis. This chapter also draws conclusions from the research carried out and presents suggestions for potential future work, focusing mainly on the improvements to achieving better SHG in dielectric optical waveguides.

# Chapter 2

# Numerical Methods

Numerical algorithms are widely used to analyse complex engineering systems. The Finite Element Method (FEM) and the Beam Propagation Method (BPM) are the two major numerical paradigms used in this thesis, the former for the stationary analysis of the optical waveguides and the latter for the study of the electromagnetic wave propagations. This chapter will describe the FEM and BPM methods in Sections 2.1 and 2.2 respectively. This is followed by the power calculation of optical waveguides in Section 2.3.

## 2.1 THE FINITE ELEMENT METHOD

This section first introduces the Finite Element Method (FEM) in the context of this thesis, briefly discussing the evolution and applications of FEM. Following this, the relevant basic equations and variational formulations are presented in Sections 2.1.5 and 2.1.6 respectively. Then the formulation of FEM is discussed in Section 2.1.9.

### *2.1.1 Overview of Finite Element Method*

The FEM has been the dominant and arguably the most powerful numerical method in computational mechanics for many decades. It has been successfully applied to solve problems encountered in many engineering disciplines such as fluid dynamics, heat conduction, aeronautical, biomechanical and electromagnetics.

The FEM is a very powerful numerical technique for solving geometrically complicated systems. The basic concept in the FEM is to find a solution for a complicated system by replacing it with a finite number of well defined elements or sub-regions. The method consists of two distinct features over other numerical methods. First, a physical system is identified as a collection of non-intersecting simple sub domains or finite elements, and is applied to the main domain to approximate the solution which provides a systematic approach to the piecewise approximation of the unknown function. Second, the solution of the governing equations is approximated over each element by a linear combination of algebraic polynomials. The solution of the system is approximated for each element, and connected at the nodal points of each element to produce the solution for the system in the entire analysis domain. Therefore, FEM is applicable in the analysis of the electromagnetic field in complicated domain structures. The behaviour of the field variable within a finite element can be approximated by a simple function. These approximating functions (also known as interpolation functions) are defined in terms of the values of the field variables at each the nodal points of each element in the domain structure. Therefore, the unknown variables of the field equations will be the nodal values of the field variable. The nodal values will be known by solving the field equations in the form of matrix equations, and then all of the element contributions to the entire domain are assembled to form the functional. Furthermore, it is possible to minimise the possible error in the solution by employing more elements and thus reducing the element size in the system. The rest of this section presents the evolution, problem-solving steps, applications, equations and different methods of the FEM.

### *2.1.2    The Evolution of FEM*

The basic concept originating the FEM dates back to early 1940s. Mathematicians and engineers have applied different techniques to solve the governing equations of a complicated system through a discretisation process. The FEM was first initiated by the German mathematician Richard Courant in 1943  through the use of piecewise continuous functions defined over a triangulated domain to approximate numerical problems [79]. In 1956, M. J. Turner, R. W. Clough, H. C. Martin, and L. J. Topp from the Boeing Aircraft Company established a broader approach to the FEM. They utilised FEM to investigate the structural dynamics problems in aircraft models [80]. Further, in 1959 J. Greenstadt employed a discretisation technique to divide the domain into "cells" instead of points, and assigned a different function to each cell by applying the variational principle. The method then reduces a continuous problem to a discrete one [81].

In the 1960s, the FEM was applied to the world of engineering by R. W. Clough [82]. Since then the name FEM has become the most versatile analytical method among engineers and mathematicians. During this period, the use of FEM in the structural analysis method was first demonstrated in solving the stresses and displacements in continuous structures. Since the late 1960s the mathematical literature on the FEM has received widespread acceptance in engineering.

### *2.1.3    Problem solving steps in Finite Element Method*

Certain steps can be defined for the formulation of the FEM of a physical system common to structural, heat transfer, fluid flow or some other engineering systems: these steps are;

i.   *Discretisation of the domain structures:* the first step is to divide the structure or the system into subdivisions or elements. When analysing a complex system, it is necessary to consider various factors such as type, size, number and the pattern of arranging the elements.

ii.  *Selection of interpolation function:* the interpolation function analyses the variation of the field within each element. The field variable may be scalar or vector. The displacement solution of a complex system cannot be predicted exactly under any specific load conditions. Therefore, it can be assumed that

some suitable solution exists within an element to approximate the unknown solution. The assumed solution should satisfy certain convergence requirements. In general, polynomials are used as interpolation functions for the field variations in order to reduce the complexity of the integration and the differentiation.

iii. *Derivation of the matrix equations:* once the assumed displacement model has been established by employing the interpolation function and the elements, it is possible to derive the matrix equation by utilising the properties of the individual elements.

iv. *Assemblage of element equations to obtain the overall system equations:* The element equations for each element in the finite element network (commonly referred to as 'mesh') are assembled into a set of global equations that model the properties of the entire complex system. The behaviour of the matrix equations is similar to that of the individual element, except that they consist of an extra term to represent all the nodes.

v. *Application of boundary conditions:* the global equations have to be modified to account for the boundary conditions of the system before obtaining the solution. The solution cannot be obtained unless boundary conditions are applied. They reflect the known values for certain primary unknowns.

vi. *Computation of system equations:* The assembly process produces a set of simultaneous equations. Then the simultaneous equations are solved for the primary unknown nodal values of the system. Linear or nonlinear ordinary differential equations are used to solve the unsteady systems where the unknown nodal values are a function of time; whereas linear or nonlinear algebraic equations are used to solve steady systems.

The above steps can be followed in order to numerically analyse one-dimensional (i.e. planar) and two-dimensional optical waveguides.

### 2.1.4  Applications of FEM

Depending on the nature of the problem, applications of FEM can be categorised into three: they are;

- *Equilibrium (i.e. steady-state) or time-independent problems:* For the solution of equilibrium problems in the solid mechanics area, it is important to calculate the steady-state displacement or stress distribution, and temperature or heat flux distribution if it is a heat transfer problem; similarly, pressure or velocity distribution if it is a fluid mechanics problem.

- *Eigenvalue problems:* These are also time-independent and considered to be an extension of equilibrium problems. These are discussed in Section 2.1.6 for the purpose of numerical analysis and characterisation of optical waveguides with one dimensional and two dimensional cross-sections.

- *Propagation or transient problems:* These are time-dependent problems. Problems of this type are encountered when finding the response of a structure under a time-varying force or under sudden heating or cooling variations in the field of heat transfer. These problems can be solved by applying the time dimension to the first two categories.

### 2.1.5   Basic Equations for lightwaves

This section discusses the fundamentals of lightwaves based on Maxwell's equations and the boundary condition, both of which are important aspects when devising mathematical solutions to optical waveguide problems.

#### 2.1.5.1   Maxwell's Equations

Maxwell's equations explain the complete behaviour of the electromagnetic fields. Maxwell's equations can be expressed in the form of a differential equation and an equivalent integral equation. The FEM is mainly applied by solving the differential form of Maxwell's equations.

The differential version of Maxwell's equations in a time-varying electromagnetic field is stated in equation (2.1) to equation (2.4) ;

$$\nabla \times \boldsymbol{E} = -\frac{\partial \boldsymbol{B}}{\partial t} \qquad \text{(Faraday's law)} \qquad (2.1)$$

$$\nabla \times \boldsymbol{H} = -\frac{\partial \boldsymbol{D}}{\partial t} + \boldsymbol{J} \qquad \text{(Ampere's law)} \qquad (2.2)$$

$$\nabla . \boldsymbol{D} = \rho \qquad \text{(Gauss's law)} \qquad (2.3)$$

$$\nabla . \boldsymbol{B} = 0 \qquad \text{(Gauss's law for magnetics)} \qquad (2.4)$$

where,

$\boldsymbol{E}$ = electric field intensity (Volts / meter)

$\boldsymbol{H}$ = magnetic field intensity (Amperes / meter)

$\boldsymbol{D}$ = electric flux density (Coulombs / meter$^2$)

$\boldsymbol{B}$ = magnetic flux density (Webers / meter$^2$)

$\boldsymbol{J}$ = electric current density (Amperes / meter$^2$)

$\rho$ = electric charge density (Coulombs / meter$^3$)

By using Ampere's law (2.2) and Gauss's law (2.3) , the current continuity equation (2.5) can be derived, which explains the local conservation of electric charge;

$$\nabla . \boldsymbol{J} = \frac{-\partial \rho}{\partial t} \qquad (2.5)$$

The electric field $\boldsymbol{E}$ and the magnetic filed $\boldsymbol{H}$ vectors are related through the constitutive equations, which explain the behaviour of the electromagnetic field in materials. The constitutive relations are;

$$\boldsymbol{D} = \varepsilon \boldsymbol{E} \qquad (2.6)$$

$$\boldsymbol{B} = \mu \boldsymbol{H} \qquad (2.7)$$

where $\varepsilon$ is the permittivity (measured in Farad/meter) and $\mu$ is the permeability (measured in Henry/meter) of the medium and can be defined as;

$$\varepsilon = \varepsilon_0 \varepsilon_r \qquad (2.8)$$

$$\mu = \mu_0 \mu_r \qquad (2.9)$$

where $\varepsilon_0$, $\varepsilon_r$, $\mu_0$ and $\mu_r$ are the permittivity of the vacuum ($8.854 \times 10^{-12}$ Farad/meter), the relative permittivity of the medium, the permeability of the

vacuum ($4\pi \times 10^{-7}$ Henry/meter) and the relative permeability of the medium respectively.

The behaviour of the electric and magnetic fields given time-varying charges and current distributions is discussed as follows. Assume a complex time dependence through the factor $e^{(j\omega t)}$, where $j$ is the imaginary part, $\omega$ is the angular frequency and $t$ is the time. The differential form of Maxwell's equations can be written as;

$$\nabla \times \boldsymbol{E} = -j\omega \boldsymbol{B} \tag{2.10}$$

$$\nabla \times \boldsymbol{H} = j\omega \boldsymbol{D} + \boldsymbol{J} \tag{2.11}$$

$$\nabla \cdot \boldsymbol{D} = \rho \tag{2.12}$$

$$\nabla \times \boldsymbol{B} = 0 \tag{2.13}$$

Therefore, the current continuity equation can be written as;

$$\nabla \times \boldsymbol{J} = -j\omega \rho \tag{2.14}$$

### 2.1.5.2   Boundary conditions

Electromagnetic problems often involve media with different physical properties, therefore it is necessary to analyse the relationship of the electromagnetic field quantities at an interface between two media. Maxwell's equations are employed to study electromagnetic fields and it must satisfy the boundary conditions that are applicable at the interfaces between two media.  Figure 2.1 shows the boundary between two media, i.e. medium 1 and medium 2. As shown, the unit vector $\boldsymbol{n}$ is normal to the surface and pointing from medium 1 to medium 2.
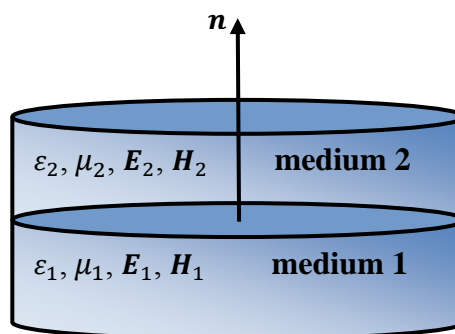


Figure 2.1 Boundary conditions at the interface between two media.

In the interface between medium 1 and medium 2 with no surface charges ($\rho = 0$) and no surface currents ($J = 0$), the fields must satisfy the following conditions (also known as field continuity conditions);

i. The tangential components of the electric field $E$ must be continuous.

$$n \times (E_{t1} - E_{t2}) = 0 \qquad (2.15)$$

Therefore the tangential component of the electric field in medium 1 ($E_{t1}$) and the tangential component of the electric field in medium 2 ($E_{t2}$) become equal.

ii. The tangential components of the magnetic field $H$ must be continuous.

$$n \times (H_{t1} - H_{t2}) = 0 \qquad (2.16)$$

Similarly, tangential magnetic fields for both medium 1 and medium 2 become equal ($H_{t1} = H_{t2}$).

iii. The normal components of the electric flux density $D$ must be continuous.

$$n \cdot (D_{n1} - D_{n2}) = 0 \qquad (2.17)$$

Hence, $D_{n1} = D_{n2}$ where $D_{n1}$ and $D_{n2}$ are the normal components of the electric flux densities in medium 1 and medium 2 respectively. From equation (2.6) , $\varepsilon_1 E_{n1} = \varepsilon_2 E_{n2}$. Hence, the $E_{n1} \neq E_{n2}$. Therefore, the normal components of the electric field vectors in medium 1 and medium 2 become unequal at the boundary.

iv. The normal components of the magnetic flux density $B$ must be continuous.

$$n \cdot (B_1 - B_2) = 0 \qquad (2.18)$$

Hence, $B_{n1} = B_{n2}$ where $B_{n1}$ and $B_{n2}$ are the normal components of the magnetic flux densities in medium 1 and medium 2 respectively. From equation (2.7) , $\mu_1 H_{n1} = \mu_2 H_{n2}$. In dielectric optical waveguides the relative permeabilities ($\mu_r$) are equal to one. Therefore the relative permeabilities in medium 1 and medium 2 satisfy the condition $\mu_{r1} = \mu_{r2} = 1$. Hence, the normal components of the magnetic field vectors in medium 1 and medium 2 become equal at the boundaries.

Further, the boundary condition can be categorised into two sections. Assume in Figure 2.1, either medium 1 or medium 2 becomes a perfect electric conductor then the boundary condition can be written as;

$$\boldsymbol{n} \times \boldsymbol{E} = 0 \quad \text{or} \quad \boldsymbol{n} \cdot \boldsymbol{H} = 0 \tag{2.19}$$

To satisfy equation (2.19), the magnetic field vector $\boldsymbol{H}$ has to be vanishing while the normal components of the electric field vector $\boldsymbol{E}$ become continuous at the boundary. This is known as the electric wall boundary condition.

Similarly, when either of the media becomes a perfect magnetic conductor then the boundary condition can be written as;

$$\boldsymbol{n} \times \boldsymbol{H} = 0 \quad \text{or} \quad \boldsymbol{n} \cdot \boldsymbol{E} = 0 \tag{2.20}$$

In the same way, to fulfil equation (2.20), the normal components of the magnetic field $\boldsymbol{H}$ must be continuous and the electric field vector $\boldsymbol{E}$ vanishes at the boundary. This is known as the magnetic wall boundary condition.

### *2.1.6   Variational formulations*

There are two ways to realise the FEM: they are known as Variational Formulation and Weighted Residual method. The Weighted Residual method directly utilises the differential equation and boundary conditions, whereas Variational Formulation utilises a functional related to the differential equation and boundary conditions. The Weighted Residual method solutions are intuitive and simple. Variational Formulation, while much less intuitive, is more advantageous as the underlying theory is more involved. Therefore, Variational Formulation is an ideal technique to solve a wide range of electromagnetic problems, if possible. The scalar field approximation [83] and the vector field formulation [76, 84, 85] are two types of Variational Formulations which are used in FEM in this thesis and are described in Section 2.1.6.1 and Section 2.1.6.2 respectively.

In general Variational Formulation is transformed into a standard eigenvalue problem when it is applied in the FEM. This can be written as a matrix eigenvalue equation as follows;

$$[A]\{x\} - \lambda[B]\{x\} = 0 \tag{2.21}$$

where $[A]$ and $[B]$ are complex, non Hermitian and non symmetric matrices. The eigenvalue $\lambda$ may be $k_0^2$ ($k_0$ free-space wavenumber) or $\beta^2$ (where $\beta$ is the propagation constant) depending on the Variational Formulation and $\{x\}$ is the eigenvector representing the unknown nodal field values. For a rigorous and efficient solution, the resulting matrix equation has to be of the canonical form shown in equation (2.21) . It can be solved in many ways to obtain the different modal eigenvalues and associated eigenvectors. Furthermore, the assembly of $[A]$ and $[B]$ matrices are presented in Appendix 2.

### 2.1.6.1 The scalar field approximation

Scalar field approximation can be applied in many optical waveguide problems in order to obtain a practically acceptable solution. In this approximation method, the field components are split into two subcomponents which are known as Transverse Electric ($TE$) and Transverse Magnetic ($TM$) modes. This method can be applied to analyse the modes mainly as $TE$ or $TM$ modes. Therefore, this method is the simplest form of the different Variational Formulations. In 1982, Koshiba *et al*. described an approximate scalar finite element analysis of anisotropic optical waveguides [83]. The main advantages of scalar field approximation are,

- Less computational time
- No spurious modes
- The capability of easily computing higher order modes
- Smaller matrix dimensions

In 1981, Mabaya *et al*. described the computation of finite element analysis of optical waveguides and the accuracy of the both $TE$ and $TM$ modes approximated by two different finite element programs [86]. The scalar field approximation for the $TM$ modes is based on the following functional;

$$J(\phi) = \iint_{\Omega} \frac{1}{n^2}\left[\left(\frac{\partial\phi}{\partial x}\right)^2 + \left(\frac{\partial\phi}{\partial y}\right)^2 + (\beta^2 - k_0^2 n^2)\phi^2\right] dxdy \tag{2.22}$$

where $\beta$, $n$, and $k_0$ are propagation constant, refractive index profile and free-space wavenumber respectively.

In equation (2.22) $\Omega$ denotes the cross-sectional domain and the integration is carried out over the domain $\Omega$. A finite element program based on this functional yield $\beta^2$ as the eigenvalue of the matrix equation for a given $k_0$. The eigenvector $\phi(x,y)$ is the transverse field distribution, i.e. $H_x$ field component for the quasi-$TM$ modes.

Similarly, the scalar field approximation for the $TE$ modes is based on the following;

$$J(\psi) = \iint_\Omega \left[ \left(\frac{\partial \psi}{\partial x}\right)^2 + \left(\frac{\partial \psi}{\partial y}\right)^2 + (\beta^2 - k_0^2 n^2)\psi^2 \right] dxdy \qquad (2.23)$$

In equation (2.23) , the eigenvector $\psi(x,y)$ is the transverse field distribution, i.e. $E_x$ field component for the quasi-$TE$ modes. Similar to equation (2.22) a finite element program based on equation (2.23) yields $\beta^2$ as the eigenvalue of the matrix equation for a given $k_0$.

### 2.1.6.2  The vector field formulation

Vector field formulation facilitates finding the mode spectrum of an optical waveguide in an efficient and robust manner. In the inherently hybrid mode of anisotropic or inhomogeneous waveguides, implementation of the scalar field approximation is insufficient. The vector field formulation is able to provide all six electromagnetic field components [87, 88] in wave propagation problems. The main advantage of the vector field formulation is that it generates an enhanced solution convergence for some modal types than with scalar field approximation. However, when computing some vector formulations, the correct modes can be mixed with spurious modes.

The vector field formulation is used for different types of FEMs, depending on the electromagnetic fields (**E** and **H**) which are used for formulation: these types are;

    i.     FEM using the six electromagnetic field components (**E** and **H**).
   ii.     FEM using the three magnetic field components (**H**).
  iii.     FEM using the three electric field components (**E**).
   iv.     FEM using longitudinal or axial electromagnetic field components ($E_z + H_z$).
    v.     FEM using transverse electromagnetic field components ($TE$ and $TM$).
   vi.     FEM using transverse electric field components ($TE$).
  vii.     FEM using transverse magnetic field components ($TM$).

Because of the flexibility of the vector field formulation, it has been prominent in many numerical analyses. The FEM using the longitudinal (axial) electromagnetic field components ($E_z$ and $H_z$) is one of the first formulations used [89-92]. The application of the $E_z+H_z$ formulation [86] in general anisotropic problems without altering its standard form of the eigenvalue equation (2.21) is not possible. Also, satisfying the boundary conditions using the $E_z+H_z$ formulation for a waveguide with an arbitrary dielectric distribution is not straightforward. However, this method is used for microwave guides where $TE$ or $TM$ modes can have either $E_z$ or $H_z$.

In 1987, Angkaew *et al*. introduced the Variational Formulation for FEM in terms of *TE* and *TM* field components [93]. The disadvantage of this method is that the computational cost of transverse formulation is very high due to its additional complexity in differentiation [94].

The vector field formulation has been presented in the form of Rayleigh quotients for loss free resonators and microwave waveguides in terms of the *H*-field, *E*-field or a combination by Berk in 1956 [95]. A similar vector variational formulation was derived by Morishita in 1977 [84].

A vector *E*-field formulation based on the three electric field components has been applied in the literature to analyse cylindrical waveguides [88] and optical fibres [96, 97]. This formulation is only valid for general anisotropic lossless waveguide problems. However, one must ensure the continuity of the tangential electric field components at the dielectric interface. Further, the natural boundary conditions correspond to a magnetic wall in the vector *E*-field formulation; therefore, it is essential to enforce the electric wall ($n \times E = 0$) as a boundary condition which is difficult to implement for irregular-shaped structures.

### 2.1.6.3  The vector *H*-field formulation

The vector *H*-field formulation appears to be the most accurate method for general anisotropic optical waveguide problems with hybrid modes and dominant transverse components. Further, the literature contains various ways of eliminating spurious solutions for this method [76].

The vector **H**-field formulation involves terms of all three magnetic field components, which gives an advantage over all other formulations. This formulation is valid for general anisotropic problems with a non-diagonal permittivity tensor [76, 77, 98]. The natural boundary conditions correspond to those of the electric wall ($\boldsymbol{n} \times \boldsymbol{E} = 0$, $\boldsymbol{n}.\boldsymbol{H} = 0$); therefore, boundary conditions do not require to be enforced at the boundaries. Further, in dielectric waveguides, the permeability is always assumed to be that of free space; hence, all the components of **H** are continuous across the dielectric interface which means the variation of the refractive index does not need to impose interface boundary conditions.

The vector **H**-field formulation can be written as [78, 95];

$$\omega^2 = \frac{\int (\nabla \times \boldsymbol{H})^* \cdot \frac{1}{\hat{\varepsilon}} \cdot (\nabla \times \boldsymbol{H}) d\Omega}{\int \boldsymbol{H}^* \cdot \hat{\mu} \cdot \boldsymbol{H} \, d\Omega} \qquad (2.24)$$

where $\hat{\varepsilon}$ and $\hat{\mu}$ are the permittivity and permeability tensors respectively and $\omega$ is the angular frequency. The integration is carried out over the waveguide cross-section $\Omega$. In order to solve equation (2.24) the Rayleigh-Ritz procedure can be applied, which leads to a similar eigenvalue problem as in equation (2.21) where [**A**] and [**B**] are complex, non Hermitian and non symmetric matrices. The Hermitian matrices [**A**] and [**B**] can be transformed to real symmetric matrices for a lossless problem. In general, the matrices [**A**] and [**B**] are quite sparse. The eigenvector $\{x\}$ represents the unknown field components at the nodal points for different modes with $\lambda$ (wavelength) as their corresponding eigenvalues and $\lambda$ is proportional to $\omega^2$. In order to obtain a solution for a given $\lambda$, the propagation constant ($\beta$) has to be changed iteratively until the output eigenvalue corresponds to the desired $\lambda$. However, the resulting solution normally tends to be a combination of correct modes and spurious ones: Section 2.1.8 discusses ways to address this problem.

### 2.1.6.4 Natural Boundary Condition

Natural boundary condition is the boundary condition which, as the name suggests, is 'naturally' or automatically satisfied by a particular Variational Formulation [99-101]. The natural boundary conditions of the scalar functional are $(1/\boldsymbol{n}^2)(\partial\phi/\partial\boldsymbol{n})$ (for *TM* modes) and $(\partial\psi/\partial\boldsymbol{n})$ (for *TE* modes) according to equation (2.22) and

equation (2.23) respectively, where $\boldsymbol{n}$ is the unit vector normal to the surface of the boundary.

The boundary condition in the vector $\boldsymbol{H}$-field formulation equation (2.24) has the natural boundary condition of an electric wall, i.e. $\boldsymbol{n} \cdot \boldsymbol{H} = 0$. Therefore, imposing a boundary condition is not necessary. However, if necessary, it is possible to enforce the natural boundary condition, e.g. to reduce the matrix order. In some cases, it may even be necessary to alter the natural boundary condition by introducing an additional surface integral around the desired boundary. Waveguide symmetry should be exploited where possible: it may be necessary to consider complementary symmetry conditions in order to obtain all the modes though this exploitation makes the process computationally efficient.

### 2.1.7   Analysis of Optical Waveguides

Electromagnetic waveguide analysis can be categorised as follows;

   i.    one dimensional (1D)

  ii.    two dimensional (2D)

Figure 2.2 (a) shows a 1D waveguide (i.e. planar or axially symmetrical) while (b) shows a 2D waveguide (i.e. arbitrary shaped) where $n_1$ and $n_2$ are the refractive index of material one and material two respectively.
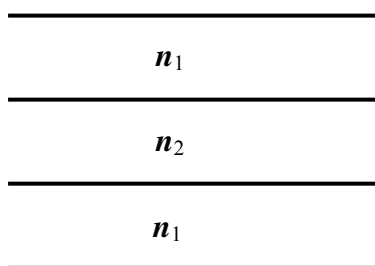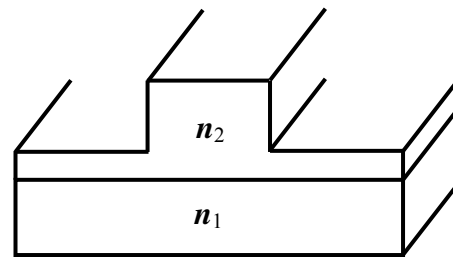


   (a) Planar Waveguide.            (b) Arbitrarily-shaped waveguide.

Figure 2.2 Optical waveguides.

The methods used to analyse an optical waveguide can be categorised as follows;

   i.    Scalar approximation

  ii.    Vector formulation

The choice depends on the eigenmode property of the waveguide. For 1D waveguides, the Scalar approximation is sufficient while for 2D waveguides, the Scalar approximation can be applied to analyse one field component at a time (i.e. *TE* mode or *TM* mode). The Vector formulation can be applied to analyse 2D waveguides more rigorously, e.g. the modes generated in the waveguide shown in Figure 2.2 (b) are hybrid modes; therefore, the Vector Formulation needs to be used for precise evaluation of their modal properties.
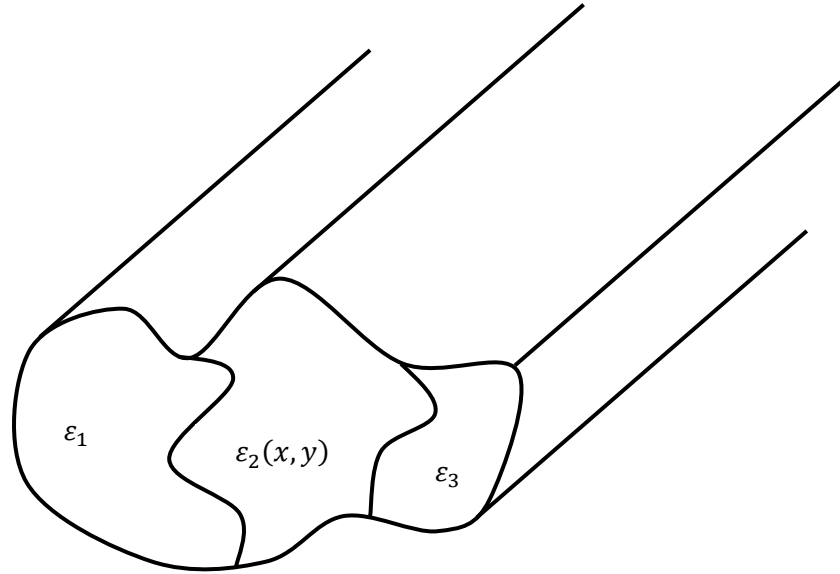


Figure 2.3 Optical waveguide with arbitrary cross-section with different materials.

Figure 2.3 shows an optical waveguide with arbitrary cross-sectional shape consisting of different materials. These materials can be described by the arbitrary permittivity $\varepsilon$ and $\mu$ tensors, which could be linear, nonlinear, isotropic, anisotropic lossy or lossless. Here $\varepsilon_1$ could be anisotropic or $\varepsilon_3$ may be nonlinear or complex and $\varepsilon_2(x, y)$ may have a diffused profile. The waveguide is assumed to be uniform along the direction of propagation (i.e. $z$ - axis). Assuming the time ($t$) and the $z$ variation to be given by $e^{(j\omega t)}$ and $e^{(-j\beta z)}$ functions respectively, the electric and magnetic ($E$ and $H$) fields can be written as;

$$H(x, y, z, t) = H(x, y)\, e^{j(\omega t - \beta z)} \qquad (2.25)$$

$$E(x, y, z, t) = E(x, y)\, e^{j(\omega t - \beta z)} \qquad (2.26)$$

where $\omega$ is the angular frequency and the $\beta$ is the propagation constant.

### *2.1.8 Spurious Solutions*

As mentioned earlier, Vector Field Formulation produces non-physical or spurious modes in addition to physical or true modes. Spurious modes do not exist in a Scalar approximation as the operator is positive definite, which is not the case with a Vector Field Formulation: spurious modes can spread all over the eigenvalue spectrum, with some of them appearing below any true modes and some in between [76, 78].

For electromagnetic waveguide problems, spurious modes do not arise if the trial field precisely satisfies $\nabla \cdot \boldsymbol{B} = 0$ [86, 102, 103]. In the Vector $\boldsymbol{H}$-field formulation, this divergence-free condition ($\nabla \cdot \boldsymbol{B} = 0$) is neither implied nor forced [76, 103] which may be the cause of these spurious modes.

The identification of spurious modes among the physical modes can be difficult. When a set of eigenmodes is computed, sometimes spurious modes can be spotted by their eigenvectors, where the field varies in a random way along the cross-section of the waveguide. The Penalty Function Method, introduced by Rahman and Davies [77], facilitates a way to formally distinguish between physical and spurious modes. The scheme works as follows. The value of $\nabla \cdot \boldsymbol{H}$ for each eigenvector of interest is calculated over the guide cross-section; only solutions with a low value of $\nabla \cdot \boldsymbol{H}$ will be considered as real modes as an eigenvector of a physical mode should satisfy ($\nabla \cdot \boldsymbol{B} = 0$). The values of $\nabla \cdot \boldsymbol{H}$ are calculated from the discrete nodal field values obtained after the solution of the eigenvalue equation (2.21).

In order to eliminate the spurious modes, an additional integral is added to the original functional (2.24) which satisfies $\nabla \cdot \boldsymbol{H} = 0$. The augmented functional can be written as;

$$\omega^2 = \frac{\int (\nabla \times \boldsymbol{H})^* \cdot {}^1/_{\hat{\varepsilon}} \cdot (\nabla \times \boldsymbol{H}) d\Omega + \left(\frac{\alpha}{\varepsilon_0}\right) \int (\nabla \cdot \boldsymbol{H})^* \cdot (\nabla \cdot \boldsymbol{H}) d\Omega}{\int \boldsymbol{H}^* \cdot \hat{\mu} \cdot \boldsymbol{H} \, d\Omega} \qquad (2.27)$$

where $\alpha$ is the dimensionless penalty coefficient. The value of $\nabla \cdot \boldsymbol{B} = 0$ can be estimated to be around $1/\varepsilon_g$, where $\varepsilon_g$ is the dielectric constant of the guide core. It is also found that this penalty function method considerably improves the quality of the field eigenvectors. Another advantage is that it does not increase the matrix order of the eigenvalue problem and the additional computational cost is negligible [77].

The literature also contains alternative ways of eliminating spurious modes, and one is the technique of working with scalars which can reduce the amount of computation and eliminate spurious modes, albeit at the expense of accuracy. Another approach which completely eliminates spurious modes is the use of the **H**-field formulation in terms of the transverse magnetic field components [104]. The $H_x$ and $H_y$ field components are represented in the order of the elemental shape functions; however, $H_z$ involves a stage of differentiation and is thus more approximately represented.

### 2.1.9    *Formulation of FEM*

As discussed in Section 2.1.3, the fundamental concept of the FEM is to find the solution to a complicated problem by dividing it into many small elements that can be solved in relation to each other. Therefore it is necessary to analyse the discretisation of the system domain, the behaviour of the field in each element by using the shape functions and the application of the element and global matrices.

### 2.1.9.1   **Finite Element Discretisation**

An appropriate basis of piecewise functions is used in the discretisation process. The term 'element' generally refers to a set basis functions used in FEM. There are many types of elements which can be used in various types of problems such as one, two and three dimensional elements. Figure 2.4 shows a one dimensional or linear element which can be used if the geometry, material properties and the field variable of the problem are described in terms of only one spatial coordinate.
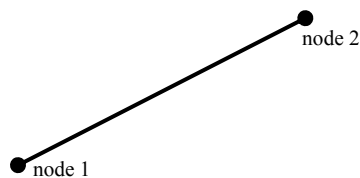


Figure 2.4 One dimensional element.

The two dimensional elements can be used when the configuration of the problem can be described in terms of two independent spatial coordinates.

Figure 2.5 shows some examples of two dimensional elements. The simplest type is the triangle linear plane element, which is employed in this thesis: here, each triangular element consists of three nodal points. Further, note that the accuracy of the approximate solution can be improved by increasing the number of elements during the process of discretisation.
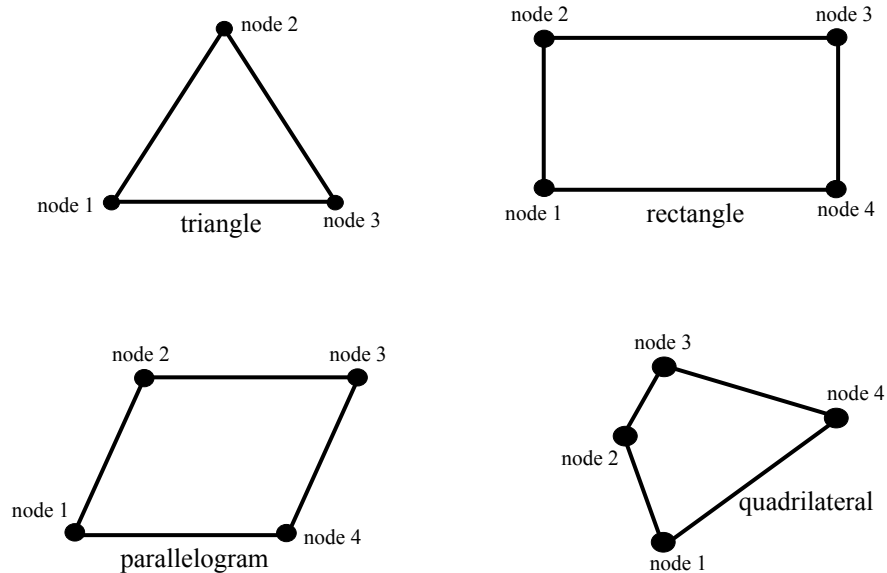
Figure 2.5 Two dimensional elements.

Figure 2.6 shows an example of the finite element discretisation of an optical waveguide with an arbitrary cross-section, using triangular elements. As explained throughout this thesis, it is very convenient and efficient to analyse the field behaviour and material properties in each element of the finite element mesh rather than analysing the cross-section as a whole. Therefore, the shape function has been utilise in order analyse the behaviour of the field in each triangle and the derivation of the shape function is presented in Appendix 2.
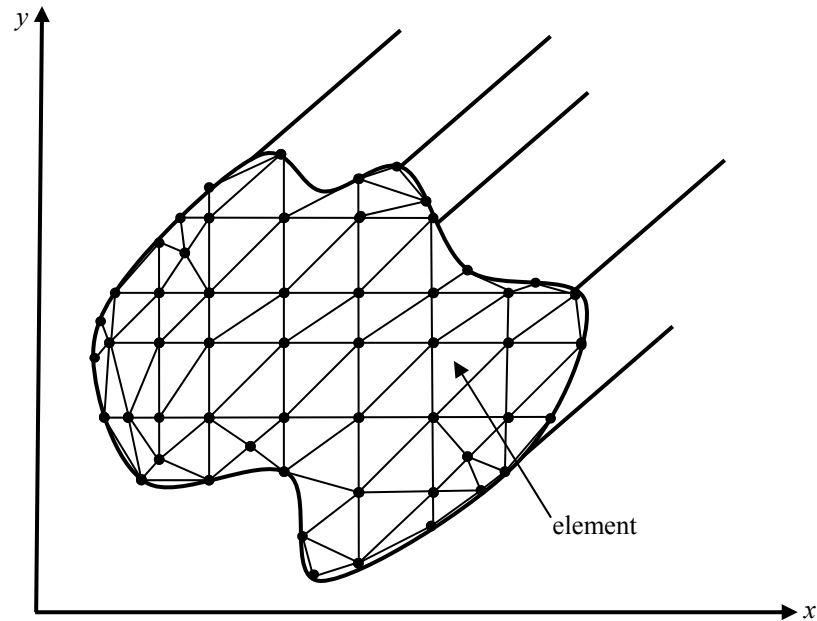
Figure 2.6 Finite element discretisation of an irregular waveguide cross-section.

### 2.1.9.2 The Infinite Elements

In general open-type waveguides the problem domain is represented by filling orthodox elements up to a chosen boundary. This simple method is susceptible to significant errors being generated if the boundary is too close, hence requires the consideration of excessively large domains. One solution is to recursively shift the virtual boundary wall until a criterion for maximum field strength is satisfied. Rahman and Davies [76] presents a rather elegant solution which adds infinite elements along the outer boundary of orthodox elements as shown in Figure 2.7: for a typical rectangular dielectric waveguide problem, a quarter of the structure is discretised into orthodox and infinite elements by assuming two fold symmetry. The advantage of this concept comes from the fact that the computational domain is extended to infinity without increasing the matrix order, thus causing almost no change in the computational complexity.
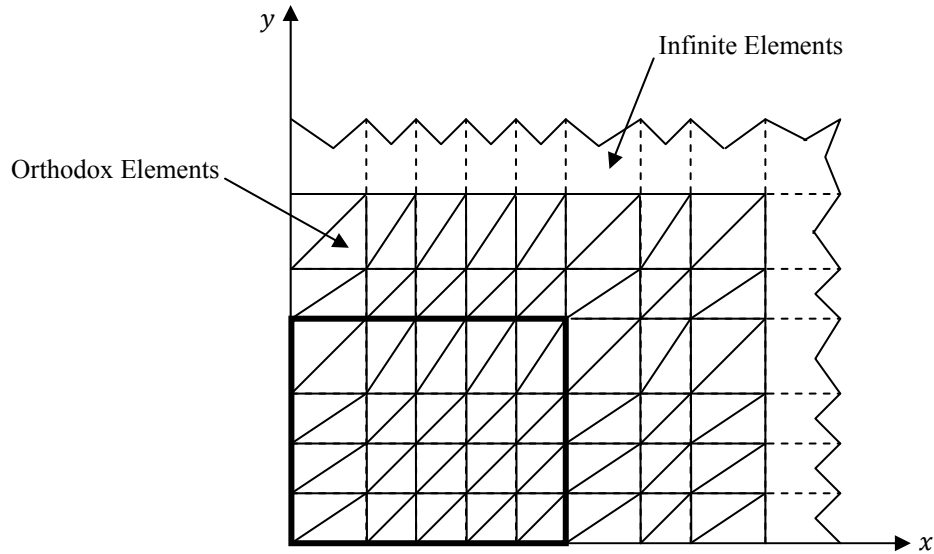
Figure 2.7 Discretisation of a dielectric waveguide with orthodox and infinite elements.

The shape functions of the infinite elements should decay exponentially in the direction where the field extends to infinity. If an element is extended to infinity in the positive $x$ -direction, the following shape function can be considered;

$$N(x,y) = N_y(y) \cdot N_x(x) = N_y(y) \cdot e^{[-x/L_x]} \tag{2.28}$$

where $L_x$ is the decay length in the $x$-direction. $L_x$ represents the decaying behaviour of the field outside the core region and depends on the structure under consideration. Further, elements can extend in the $y$-direction or both directions in a similar pattern to equation (2.28) [76].

## 2.2    THE BEAM PROPAGATION METHOD

This section first introduces beam propagation algorithms including their evolution in Section 2.2.1. This is followed by the derivation of the Finite Element Approach in Section 2.2.3.

### 2.2.1    *Overview of Beam Propagation Algorithms*

The Beam Propagation Method (BPM) is a numerical technique for analysing the guided wave propagation of an optical waveguide in the axial direction (i.e. direction

of propagation). Since the late 1970s, BPMs have been widely used to analyse integrated photonic circuits and fibre optics [74, 105].

Initially a number of assumptions have been made to BPM in order to reduce the complexity of its implementation without compromising the accuracy. For instance, it is possible to reduce the dimensionality of the partial differential equations to minimise the computational resources required. Various numerical techniques have been developed to implement BPM such as Fast Fourier Transform BPM (FFT-BPM), Finite Difference BPM (FD-BPM) and Finite Element BPM (FE-BPM). The FFT-BPM was widely used until the FD-BPM was developed [105]. However, in FFT-BPM it is assumed that the variation of refractive index in the transverse direction is very small. Therefore, the application of FFT-BPM is limited to waveguides with small refractive index discontinuities. Further, FFT-BPM can only be analysed for scalar wave propagation.

In 1986, Hendow and Shakir introduced the FD-BPM for the first time [106] in order to solve the paraxial scalar wave equation through cylindrically symmetric structures. The scalar FD-BPM is computationally efficient and has advantages over many numerical implementations [107, 108]. In 1990 Hayata *et al*. introduced a technique called split-step procedure which is a combination of FEM and Finite Difference method. In the split-step procedure the FEM is applied to the waveguide cross-section, while the Finite Difference method is applied to the propagation direction of the waveguide [109]. Hence, the split-step procedure significantly enhances the computational efficiency.

The Finite Difference Crank-Nicolson scheme which is the first approach to analyse the vector light wave propagation was introduced in 1991 by Clauberg and Allmen [110]. This method has the ability to analyse the vector characteristics that are inherent in light wave propagation through inhomogeneous anisotropic media. The semi vectorial BPM was introduced in 1993 by Liu *et al*.[111]. This method can distinguish between two orthogonal polarisation modes *TE* and *TM*. Numerically efficient full vectorial Finite Element BPM (FE-BPM) has been introduced by Polstyanko *et al*. in 1996 [112] with electric field formulation. Later in 2000 [113] Obayya *et al*. presented the full vectorial FE-BPM for three-dimensional (3-D) optical waveguides by using transverse magnetic field components. In addition,

Perfectly Matched Layer (PML) has also been incorporated in the algorithm in order to absorb the unwanted radiation out of the computational domain [113-115] which is described in Section 2.2.2.

In this thesis, the FE-BPM algorithms have been used to analyse the scalar and full vectorial light wave propagation in photonic crystal fibres, also nano-scale optical waveguides.

### 2.2.2 Perfectly Matched Layer

In numerical simulations the boundaries must be considered in order to form a practical solver. Therefore, the Perfectly Matched Layer (PML) is used as an artificial absorbing layer for escaping waves [116]. Generally in the FEM and BPM, boundary conditions assign the field to be zero just outside of the region under consideration. In the FDM and FEM, the PML is commonly used to truncate the computational regions to simulate problems with open boundaries. The PML is designed so that the waves incident upon it from a non-PML medium does not reflect at the interface, which helps distinguish it from an ordinary absorbing material. This also means the PML can strongly absorb outgoing waves from the interior of a computational region without reflecting them back into the interior. In 1994 Berenger formulated the PML by using Maxwell's equation for the first time. Figure 2.8 shows an optical waveguide cross-section with different PML regions.
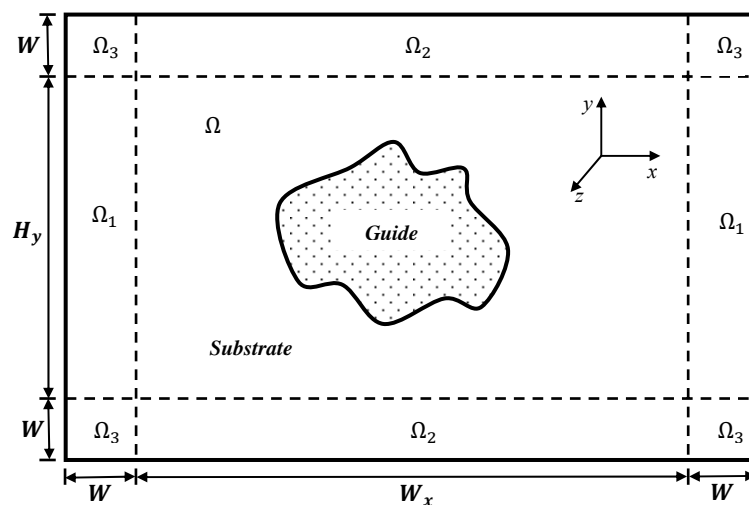


Figure 2.8 Optical waveguide cross-section with different PML regions.

In Figure 2.8, $x$ and $y$ are the transverse directions while $z$ is the propagation direction. $\Omega_2$ and $\Omega_1$ are the PML along the $x$ and $y$ directions respectively, $\Omega_3$ denotes the four corners of the PML region, $\Omega$ represents the computational domain, $\boldsymbol{W_x}$ and $\boldsymbol{H_y}$ are the width and height of the computational domain and $\boldsymbol{W}$ denotes both the width and height of the four corners of the PML.

From the Maxwell's equations (i.e. equations (2.10) and (2.11) ); the vector wave equation based on the magnetic field vector, $\boldsymbol{H}$ can be derived as follows;

$$\nabla \times (n^{-2}\nabla \times \boldsymbol{H}) - k_0^2 \boldsymbol{H} = 0 \tag{2.29}$$

where $k_0$ and $n$ are the free space wavenumber ($k_0 = \omega\sqrt{\mu_0 \varepsilon_0} = 2\pi/\lambda$) and the refractive index respectively and the del operator $\nabla$ can be defined as follows;

$$\nabla = \hat{\boldsymbol{x}}\alpha_x \frac{\partial}{\partial x} + \hat{\boldsymbol{y}}\alpha_y \frac{\partial}{\partial y} + \hat{\boldsymbol{z}}\alpha_z \frac{\partial}{\partial z} = \nabla_t + \hat{\boldsymbol{z}}\alpha_z \frac{\partial}{\partial z} \tag{2.30}$$

where $\hat{\boldsymbol{x}}$, $\hat{\boldsymbol{y}}$ and $\hat{\boldsymbol{z}}$ are the unit vectors in the $x$, $y$ and $z$ directions respectively and $\alpha_x$, $\alpha_y$ and $\alpha_z$ are parameters associated with the PML boundary condition which can be defined as;

i.  region $\Omega$ (computational domain)  $\quad : \alpha_x = 1$ and $\alpha_y = 1$
ii.  region $\Omega_1$(PML regions normal to $x$ direction)  $\quad : \alpha_x = \alpha_t$ and $\alpha_y = 1$
iii.  region $\Omega_2$(PML regions normal to $y$ direction)  $\quad : \alpha_x = 1$ and $\alpha_y = \alpha_t$
iv.  region $\Omega_3$  $\quad : \alpha_x = \alpha_t$ and $\alpha_y = \alpha_t$

where the parameter $\alpha_z$ is set to unity. Then the necessary condition for PML can be derived as [116, 117];

$$\alpha_t(t = x \text{ or } y) = 1 - j\frac{3\lambda\rho^2}{4\pi nd^3}ln\left(\frac{1}{R}\right) \tag{2.31}$$

where $n$ is the refractive index, $\rho$ is the distance from the inner PML interface, $\lambda$ is the wavelength, $d$ is the thickness of the PML which is constant in all directions and $R$ is the reflection coefficient. Due to these PML arrangements in different regions, the radiation waves from the computational domain are absorbed irrespective of the angle they hit the PML.

### 2.2.3   *Finite Element Approach*

The first step when numerically analysing an optical waveguide is that the cross-section of the waveguide is discretised into first order triangular elements. The Galerkin's procedure (Derivation of Guided wave formulation and Galerkin's procedure presented in Appendix 2) has been used to convert the differential equation problem into a discrete problem.

Subsequently, the whole cross-section of the computational window be divided into a number of triangular elements. Then the transverse magnetic field envelopes can be represented over each element (*e*) in terms of the shape functions ($N_i$), which can be written as follows;

$$\phi_x^e(x, y, z) = \sum_{i=1}^{3} h_{xi}(z) \, N_i(x, y) \tag{2.32}$$

$$\phi_y^e(x, y, z) = \sum_{i=1}^{3} h_{yi}(z) \, N_i(x, y) \tag{2.33}$$

where $N_{i(x,y)}$ are shape functions (local for each element) and $h_{xi}(z)$ and $h_{yi}(z)$ denote the element nodal values of the $x$ and $y$ components of the magnetic field, respectively. By substituting equation (2.32) and (2.33) into equations (A2.63) and (A2.64) the following equation can be derived;

$$[M] \frac{d^2\{h_t\}}{dz^2} - 2jn_0 k_0 [M] \frac{d\{h_t\}}{dz} + ([K] - n_0^2 k_0^2 [M])\{h_t\} = \{0\} \tag{2.34}$$

where {0} is a column vector with all zero entries, and

$$\{h_t\} = \begin{Bmatrix} h_x(z) \\ h_y(z) \end{Bmatrix} = \sum_e \begin{Bmatrix} h_{x1} \\ h_{x2} \\ h_{x3} \\ h_{y1} \\ h_{y2} \\ h_{y3} \end{Bmatrix} \tag{2.35}$$

where $h_x(z)$ and $h_y(z)$ are the nodal values of the $x$ and $y$ components of the magnetic field over the whole domain. The global matrix $[M]$ can be represented as a summation of the corresponding matrices;

$$[\boldsymbol{M}] = \sum_e [\boldsymbol{M}]_e = \sum_e \begin{bmatrix} [\boldsymbol{M}_{xx}]_{3\times 3} & [0]_{3\times 3} \\ [0]_{3\times 3} & [\boldsymbol{M}_{yy}]_{3\times 3} \end{bmatrix} \qquad (2.36)$$

similarly, the global matrix [$\boldsymbol{K}$] can be represented as follows;

$$[\boldsymbol{K}] = \sum_e [\boldsymbol{K}]_e = \sum_e \begin{bmatrix} [\boldsymbol{K}_{xx}]_{3\times 3} & [\boldsymbol{K}_{xy}]_{3\times 3} \\ [\boldsymbol{K}_{yx}]_{3\times 3} & [\boldsymbol{K}_{yy}]_{3\times 3} \end{bmatrix} \qquad (2.37)$$

In equations (2.36) and (2.37) , $\sum_e[\boldsymbol{M}]_e$ and $\sum_e[\boldsymbol{K}]_e$ represent the contribution of all element matrices into the global matrix. The derivation of the matrices $[\boldsymbol{M}_{xx}]$, $[\boldsymbol{M}_{yy}]$, $[\boldsymbol{K}_{xx}]$, $[\boldsymbol{K}_{yy}]$, $[\boldsymbol{K}_{xy}]$ and $[\boldsymbol{K}_{yx}]$ are presented in Appendix 2.

Further, a computationally efficient matrix solver based on LU-decomposition is used to store the sparse global matrices [$\boldsymbol{M}$] and [$\boldsymbol{K}$]. Equation (2.34) can also be used as a semi-vectorial magnetic field formulation where the hybrid nature of the field and the polarisation coupling is not very strong. Therefore, the global matrix [$\boldsymbol{K}$] can be reduced to two wave equations for $H_x$ and $H_y$ by neglecting $[\boldsymbol{K}_{xy}]$ and $[\boldsymbol{K}_{yx}]$ matrices. However, in the cases of weakly guiding waveguides the polarisation dependence can be neglected, thus, $[\boldsymbol{K}_{xx}]$ and $[\boldsymbol{K}_{yy}]$ can also be reduced to one matrix $[\boldsymbol{K}_{tt}]$ (see Appendix 2). Hence, the equation (2.34) can be reduced to a scalar magnetic field formulation for $H_x$ and $H_y$.

The Padé approximation has been applied to the equation (2.34) by neglecting the second order $z$ derivative ($\partial^2/\partial z^2 \approx 0$) [118]. The Padé approximation can be reduced to a paraxial approximation which is only valid for the cases where the propagation of light is very near to the $z$-axis (propagation axis), which is called zero order Padé approximation. In paraxial approximation, it is also necessary to assume that the envelope of the electric field changes slowly in the $z$-direction (propagation direction) for accurate approximation. However in the case of optical waveguides which guide the light at a large angle in the $z$-direction (wave propagating off the propagation direction), leading to wide-angle approximation (higher order Padé approximation). Therefore, $\partial^2/\partial z^2$ is required for wide-angle approximation. Hence, the computational requirements for wide-angle approximation increase significantly. In this thesis, paraxial approximation has been used for simulation experiments. Equation (2.34) can be re-arranged in the following form;

$$-2jn_0k_0[M]\frac{d\{h_t\}}{dz_{i+1}} = -\frac{([K]-n_0^2k_0^2[M])\{h_t\}}{1-\frac{1}{2jn_0k_0}\frac{d}{dz_i}} \tag{2.38}$$

By assigning $i=0$ in equation (2.38) , $d/dz=0$, then the recurrence Padé approximation can be written as;

$$-2jn_0k_0[\widetilde{M}]\frac{d\{h_t\}}{dz} + ([K]-n_0^2k_0^2[M])\{h_t\} = \{0\} \tag{2.39}$$

where,

$$[\widetilde{M}] = [M] + \frac{1}{4n_0^2k_0^2}([K]-n_0^2k_0^2[M]) \tag{2.40}$$

The paraxial equation can be expressed by substituting $[M]$ into $[\widetilde{M}]$.

Applying Finite Difference Method (FDM) to equation (2.39) results in;

$$[A]_k\{h_t\}_{k+1} = [B]_k\{h_t\}_k \tag{2.41}$$

with,

$$[A]_k = -2jn_0k_0[\widetilde{M}]_k + \theta\Delta z([K]_k - n_0^2k_0^2[M]_k) \tag{2.42}$$

$$[B]_k = -2jn_0k_0[\widetilde{M}]_k + (\theta-1)\Delta z([K]_k - n_0^2k_0^2[M]_k) \tag{2.43}$$

where $\Delta z$ is the propagation step size in the $z$- direction, and the subscripts $k$ and $k+1$ denote the quantities related to the $k^{th}$ and $(k+1)^{th}$ propagation steps respectively. $\theta$ is an artificial parameter ($0 \le \theta \le 1$); $\theta = 0, 0.5$ and $1$ for Forward Difference, Crank-Nicolson (CN) and Backward Difference schemes, respectively [99]. Further, the Forward Difference scheme is conditionally stable whereas the CN and Backward Difference schemes are unconditionally stable. For both CN and Backward Difference schemes, the exact choice of the parameter value is not crucial provided the values are within the range $0.5 \le \theta \le 1$. In this thesis the CN scheme

($\theta = 0.5$) has been adopted for numerical simulations of unconditionally stable systems.

## 2.3 POWER CALCULATION

Electromagnetic waves carry energy as they propagate through an optical waveguide. Therefore, the electromagnetic waves play a vital role in the transport of energy and analysing their power is essential. For instance, when studying the Second Harmonic Generation (which will be discussed in Chapter 3), it is crucial to analyse the amount of power at the fundamental wavelength that has been transferred to the second harmonic wavelength. The rate of energy propagation per unit area (i.e. power flow density) is described by the vector $\boldsymbol{S}$ which is known as Poynting vector [53].

$$\boldsymbol{S} = (\boldsymbol{E}^* \times \boldsymbol{H}) \quad W/m^2 \tag{2.44}$$

From Maxwell's equations, the transverse electric field components can be derived in terms of the magnetic field components as;

$$E_x^* = -\frac{1}{j\omega\varepsilon}\frac{\partial H_z^*}{\partial y} + \frac{\beta}{\omega\varepsilon}H_y^* \tag{2.45}$$

$$E_y^* = \frac{1}{j\omega\varepsilon}\frac{\partial H_z^*}{\partial x} - \frac{\beta}{\omega\varepsilon}H_x^* \tag{2.46}$$

Then equation (2.45) and equation (2.46) are applied to the *z-* component of the Poynting vector equation (2.44) in order to calculate the power along the propagation direction. Further, the shape function has been used to numerically analyse the power inside each triangle of the optical waveguide. The derivation of the power calculation is further discussed in Appendix 3.

## 2.4 SUMMARY

In this chapter, a Finite Element Method (FEM) based approach using the Variational Formulation has been presented to create the modal solutions of various optical waveguides. In addition, the derivation of electromagnetic wave equations from Maxwell's equations has been presented. Various aspects of the implementation of the FEM including domain discretisation, the use of different scalar and vector formulations, the use of boundary conditions, shape functions and the assembly of matrices have been discussed. The elimination of spurious fields by using the penalty term in the vector *H*-field formulation has also been discussed. Further, an elegant solution for infinite elements for an open boundary optical waveguide has been presented.

In addition, the BPM has been discussed as a tool for the numerical analysis of the electromagnetic wave propagation. The implementation of PML as an artificial absorbing layer and incorporated within the guided wave equations has been presented. Finally, a calculation of the power of the electromagnetic waves considered by using Poynting's theorem has been discussed. Thus in summary, this chapter provides a fundamental basis for the numerical methods that have been developed and applied in this research and which are presented in Chapter 3. Here, the application of the FEM in conjunction with the BPM is utilised for the analysis of the Second Harmonic Generation of optical waveguides in different dielectric materials.

# Chapter 3

# Second Harmonic Generation

Guided wave Second Harmonic Generation (SHG) devices implementing compact short wavelength coherent light sources are useful across a range of optoelectronic applications. SHG is a nonlinear effect that comes into play with the use of sufficiently intense electromagnetic fields. This chapter will discuss different materials demonstrating SHG and their crystal orientations that would optimise the SHG, in Section 3.2 and Section 3.6 respectively. Numerical analysis of SHG with Scalar and Full-Vectorial Beam Propagation Methods are explained in Section 3.7 and Section 3.8 respectively.

## 3.1 INTRODUCTION

Second Harmonic Generation (SHG) which is also known as 'frequency doubling' was first demonstrated in the early 1960s by Franken *et al*. [119, 120]. SHG is a nonlinear process, in which two photons with equal frequencies propagating through a nonlinear material which has non-inversion symmetry (i.e. non-centrosymmetric) effectively interact with each other and produce a new photon with twice the energy. Therefore, the frequency of the new photon is twice that of the original photons (i.e. the wavelength is half). In other words, the fundamental pump wave generates

nonlinear polarisation in the nonlinear material and radiates an electromagnetic field with doubled frequency. Then the pump wave transfers the energy to the second harmonic wave and the pump wave becomes depleted. During this process the intensity of the second harmonic wave gradually builds up by transferring energy from the pump wave: this is called 'power conversion'. There has been a growing interest in this phenomenon in many practical applications. Figure 3.1 shows the concept of SHG.
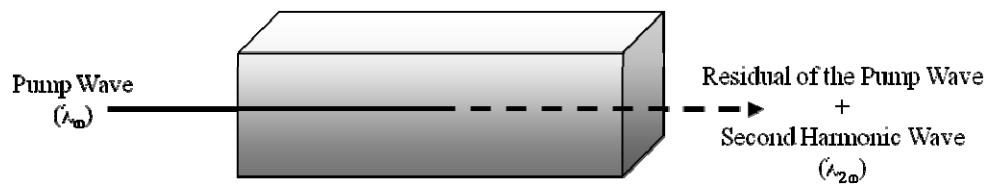


Figure 3.1 Second Harmonic Generation in a nonlinear material.

SHG in non-inversion symmetric (non-centrosymmetric) materials such as silica ($SiO_2$) and Zinc Oxide ($ZnO$) have been used in many optoelectronic devices. Generally, SHG is non-existent in silica due to its inversion symmetry. However, early 1980s experiments on $SiO_2$-based optical fibres have shown that SHG exists when the neodymium-doped yttrium aluminum garnet ($Nd{:}YAG$) laser with $1064nm$ intense pump pulses is applied [121-123]. In 1986, Osterberg and Margulis discovered that the second harmonic power grows considerably by exposing the single mode optical glass fibres to pump radiation for several hours (reaching saturation in about 10 hours); and the SHG power conversion efficiency is found to exponentially grow over more than 4 orders of magnitude. A maximum power conversion efficiency of 3% was observed during this process [124]. Since then, research on SHG in optical glass fibres such as Photonic Crystal Fibres (PCF) has been extensive. SHG in PCF with silica and silica-based materials is presented in Chapter 4.

Zinc Oxide is a highly nonlinear non-centrosymmetric material which is used in many optical waveguide SHG applications such as thin films [125], nanorods [126] and nanowires [127]. Numerical analysis of SHG in Zinc Oxide optical devices is presented in Chapter 5.

## 3.2 SECOND ORDER NONLINEAR SUSCEPTIBILITY

Through SHG, an optical wave of fundamental frequency $\omega$ propagating through a dielectric material is converted to a wave of second harmonic frequency $2\omega$. This is a result of the induced non-linear polarisation caused by the non-inversion symmetry of the material [128]. The induced non-linear polarisation ($P_{NL}$) in a crystal can be mathematically represented as follows [32, 129];

$$P_{NL} = \varepsilon_0\big(\chi^{(1)}\boldsymbol{E} + \chi^{(2)}\boldsymbol{EE} + \chi^{(3)}\boldsymbol{EEE} + \cdots\big) \qquad (3.1)$$

where $\varepsilon_0$ is the permittivity of free space. The second term in equation (3.1) represents second order nonlinearity. Therefore, second harmonic $P_{NL}$ is proportional to the second order nonlinear susceptibility $\chi^{(2)}$ and the square of the applied electric field ($\boldsymbol{E}$) as follows;

$$P_{NL} = \varepsilon_0\big(\chi^{(2)}\boldsymbol{EE}\big) \qquad (3.2)$$

In this nonlinear process, electromagnetic fields exchange energy between the fundamental and second harmonic frequencies: this represents the phenomenon known as SHG. However, only materials possessing non-inversion symmetry have a non-vanishing second order susceptibility tensor term. In general, the induced nonlinear polarisation can be written in the following matrix form [130];

$$P_{NL} = \begin{bmatrix} P_x \\ P_y \\ P_z \end{bmatrix} = \varepsilon_0 \begin{bmatrix} d_{11} & d_{12} & d_{13} & d_{14} & d_{15} & d_{16} \\ d_{21} & d_{22} & d_{23} & d_{24} & d_{25} & d_{26} \\ d_{31} & d_{32} & d_{33} & d_{34} & d_{35} & d_{36} \end{bmatrix} \begin{bmatrix} e_x^2 \\ e_y^2 \\ e_z^2 \\ 2e_y e_z \\ 2e_z e_x \\ 2e_x e_y \end{bmatrix} \qquad (3.3)$$

where $P_x$, $P_y$ and $P_z$ are the components of the nonlinear polarisation, $d_{ij}(i = 1\dots3, j = 1\dots6)$ are nonlinear susceptibility tensors and $e_x$, $e_y$ and $e_z$ are amplitudes of the $x$, $y$ and $z$ components of the electric fields, respectively. Nonlinear susceptibility tensors in equation (3.3) are unique for each material with specific symmetry groups.

### 3.2.1 Second order nonlinear susceptibility in Silicon Dioxide

Silicon Dioxide ($SiO_2$ or silica) has been used in many photonics applications (e.g. Photonic Crystal Fibres) and optical telecommunications because of its superior optical properties such as low loss and low fabrication cost. In general silica is a centrosymmetric material [32]. However, SH can be induced in silica by applying the thermal poling technique which is described in Section 3.5 [131]. Poled silica can be considered as belonging to the group symmetry $C_{\infty mm}$. From equation (3.3) the second order nonlinear susceptibility matrix for silica can be written as follows;

$$P_{NL} = \begin{bmatrix} P_x \\ P_y \\ P_z \end{bmatrix} = \varepsilon_0 \begin{bmatrix} 0 & 0 & 0 & 0 & d_{15} & 0 \\ 0 & 0 & 0 & d_{24} & 0 & 0 \\ d_{31} & d_{32} & d_{33} & 0 & 0 & 0 \end{bmatrix} \begin{bmatrix} e_x^2 \\ e_y^2 \\ e_z^2 \\ 2e_y e_z \\ 2e_z e_x \\ 2e_x e_y \end{bmatrix} \tag{3.4}$$

According to the Kleinman symmetry condition the number of independent elements of the second order nonlinear susceptibility can be reduced [129]. Therefore, the second order nonlinear susceptibilities for $x$, $y$ and $z$ directions in silica are given by;

$$P_{NL} = \begin{bmatrix} P_x \\ P_y \\ P_z \end{bmatrix} = \varepsilon_0 \begin{bmatrix} 0 & 0 & 0 & 0 & d_{31} & 0 \\ 0 & 0 & 0 & d_{31} & 0 & 0 \\ d_{31} & d_{31} & d_{33} & 0 & 0 & 0 \end{bmatrix} \begin{bmatrix} e_x^2 \\ e_y^2 \\ e_z^2 \\ 2e_y e_z \\ 2e_z e_x \\ 2e_x e_y \end{bmatrix} \tag{3.5}$$

Hence, the nonlinear polarisation for $x$, $y$ and $z$ can be written as,

$$P_{NL} = \begin{bmatrix} P_x \\ P_y \\ P_z \end{bmatrix} = \varepsilon_0 \begin{bmatrix} 2d_{31}E_x E_z \\ 2d_{31}E_y E_z \\ d_{31}E_x^2 + d_{31}E_y^2 + d_{33}E_z^2 \end{bmatrix} \tag{3.6}$$

In equation (3.6) the $d_{31}$ value is $\sim 0.07\, pm/V$ and the $d_{33}$ value is $\sim 0.22\, pm/V$ [132].

### 3.2.2 Second order nonlinear susceptibility in Lead Silicate glass

Commercially available Lead silicate glass also known as $SF57$ (manufactured by Schott) exhibits the highest nonlinearity among the other available lead silicate

glasses. $SF57$ has many advantages such as the possibility of fabricating complex optical waveguides like Photonic Crystal Fibres (PCFs) with the extrusion technique [133]. $SF57$ glass is essentially formed by $SiO_2$ and lead oxide ($PbO$) with a $40\% -$ $50\%$ lead ($Pb$) cationic content [134]. Further, large permanent second order nonlinear susceptibility values such as $d_{33} \sim 0.35 \ pm/V$ and $d_{31} \sim 0.12 \ pm/V$ can be achieved by electron-beam irradiation [135]. As with $SiO_2$, Silica based $SF57$ also belongs to the group symmetry of $C_{\infty mm}$. Therefore, the nonlinear polarisations for $x$, $y$ and $z$ directions are similar to those of $SiO_2$ (i.e. equation (3.6) ).

### 3.2.3   *Second order nonlinear susceptibility in Zinc Oxide*

In general $ZnO$ has a higher refractive index than those of $SiO_2$ and $SF57$, allowing for a tighter mode confinement. $ZnO$ is also a highly nonlinear material with a non-centrosymmetric structure and has group symmetry of $C_{6v}$. Furthermore, $ZnO$ is an easy to handle, non-toxic material and SHG in $ZnO$ has been widely used in many areas such as optical waveguide devices and cell imaging. The second order nonlinear susceptibilities of $ZnO$ are $d_{33} \sim 18.0 \ pm/V$ and $d_{15} = d_{31} = 2.88 \ pm/V$ [126]. These values are significantly higher than those of $SiO_2$ and $SF57$. Therefore, $ZnO$ exhibits high SHG compared to other centrosymmetric materials (i.e. $SiO_2$ and $SF57$). After applying Kleinman symmetry conditions, i.e. $d_{31} = d_{15}$, the nonlinear polarisations for $x, y$ and $z$ directions are similar to those of $SiO_2$ (i.e. equation (3.6) ) where the non-vanishing components are $d_{15}$, $d_{24} = d_{15}$, $d_{32} = d_{31}$ and $d_{33}$.

### 3.3   COHERENCE LENGTH

In this section the coherence length of the optical waveguides is discussed, which is an important parameter when it comes to the practical implementation of the SHG in optical waveguides. The fundamental and second harmonic waves accumulate a phase shift of $\pi$ over a distance known as the coherence length ($L_c$) after which the power exchange process reverses and the power reaches zero after another $L_c$. Here $L_c = \pi/\Delta\beta$ and $\Delta\beta = \beta_{2\omega} - 2\beta_\omega$, where $\beta_\omega$ and $\beta_{2\omega}$ are the propagation constants of the fundamental and second harmonic frequencies respectively. Quasi Phase Matching (QPM) is a technique used to prevent this phase mismatch which is explained in Section 3.4.

## 3.4 QUASI PHASE MATCHING

Phase matching is generally defined as a means for maintaining the phase relationship between the waves involved in nonlinear interactions which is a key contributor to the efficiency of the frequency conversion process. In 1962 Armstrong *et al.* proposed that in a Quasi Phase Matching (QPM) interaction, an accumulated phase mismatch (which occurs when waves with different phase velocities propagate through a nonlinear material) can be prevented by applying appropriate periodic modulation of the nonlinear material properties of an optical waveguide [46]. This technique has become one of the dominant techniques proposed in order to compensate for the effect of dispersion in nonlinear interactions and is applicable in a variety of optical waveguides with different nonlinear materials. Figure 3.2 shows the Quasi Phase Matched (QPM) and Non-QPM SH output power variation against propagation length. In Figure 3.2, $L_c$ is the distance for which both the fundamental and second harmonic waves are in phase and the SH power will decrease thereafter, reversing all the SHG gained and reaching zero after another $L_c$ (i.e. at $2L_c$) unless QPM is applied in which case the power will continue to increase.
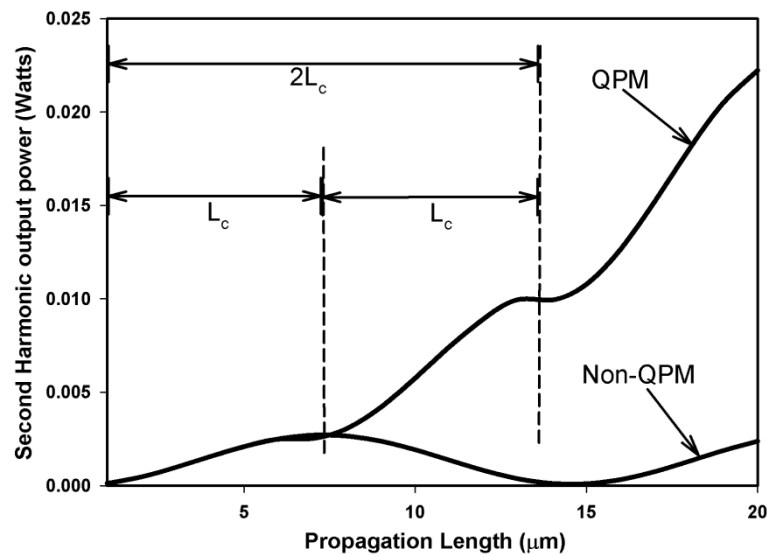


Figure 3.2 Quasi Phase matched and Non-QPM Second Harmonic output power variation with Propagation length.

The main concept behind SHG is that the phase matched power flow along the optical waveguide is constantly transferred from the fundamental to the second harmonic wave. Therefore, the second harmonic output power grows quadratically

over the distance of the optical waveguide. However, when phase mismatch occurs during this process of power transfer, the direction of power flow reverses periodically as the relative phase of the fundamental and second harmonic changes. This physical mechanism can be explained as follows. The direction of power flow between the fundamental and second harmonic waves depends on their relative phase of the fundamental and second harmonic waves and hence this changes sign for a distance equal to the coherence length ($L_c$). To overcome this problem, QPM technique works by changing the sign of the nonlinear susceptibility ($\chi^{(2)}$) at every $L_c$, cause the phase of the polarisation wave to be shifted by $\pi$, effectively re-phasing the interaction and leading to a monotonic power flow into the second harmonic wave [136]. Changing the sign of $\chi^2$ can be achieved by using poling techniques which are discussed in Section 3.5.

Further, the ideal condition shown in Figure 3.3 occurs when $n_{eff}^{\omega} = n_{eff}^{2\omega}$ (i.e. $\Delta\beta \approx 0$), (where $n_{eff}^{\omega}$ and $n_{eff}^{2\omega}$ are the fundamental and second harmonic effective indices (i.e. this is a waveguide)) which cannot be realised in practice due to the chromatic dispersion of the material.
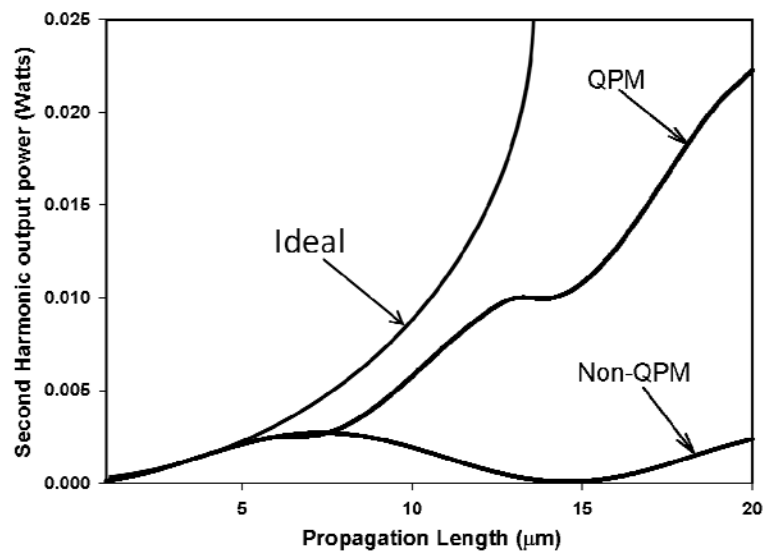


Figure 3.3 Quasi Phase Matched, Non-QPM and ideal Second Harmonic output power variation with Propagation length.

The most rapid growth of the SH output power can be achieved by changing the sign of $\chi^{(2)}$ at every $L_c$ (which is known as first order QPM) as shown in Figure 3.4. However, for some cases changing the sign of $\chi^{(2)}$ at every $L_c$ along the optical waveguide can be challenging in practice. Hence, higher order QPMs can be considered instead, i.e. $n^{th}$ order phase matching can be achieved by poling with a period of $nL_c$. The SHG output power with QPM for the first, third and fifth order modulations are compared in Figure 3.4. Note that higher order QPMs need a longer propagation distance to reach a given level of SH output power within the optical waveguide when compared to lower order ones. However, this difference in the micro-metre range is negligible given the length of an optical waveguide in practice and in fact, higher order QPMs make the fabrication process easier especially in the case of short coherence lengths.
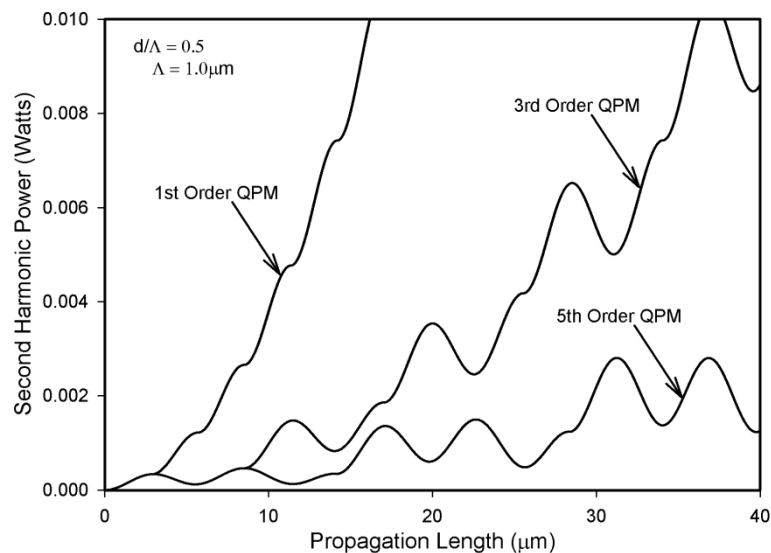


Figure 3.4 Second Harmonic Output power with first, third and fifth order quasi phase matching.

### 3.5 POLING TECHNIQUES

Due to the lack of inversion symmetry and the phase mismatch between the fundamental and second harmonic frequencies, the SH conversion efficiency becomes limited. Therefore, it is necessary to overcome this problem by using different poling techniques. Poling techniques have been introduced as early as 1964

by Miller, where it was concluded that multi-domain ferroelectrics could enhance the efficiency of nonlinear interactions by changing the sign of second order nonlinear susceptibility together with domain reversal [137]. Further research has been done in order to achieve QPM interactions in periodically poled media, although this method was found to be impractical in long range applications due to the lack of precise control [138, 139]. Then, the first lithographic technique which was based on the in-diffusion of a patterned dopant film [140], or ion exchange through a mask [141] was applied to obtain periodic poling on waveguide structures. In the early 1990s Matsumoto *et al*. introduced electric poling, where the electric field is applied to a periodic electrode pattern fabricated on the surface of the waveguide, which enables the domain penetration through millimetre-thick substrates [142]. Unlike the lithographic poling technique, the electric field poling can be applied to both bulk crystals and waveguides. Figure 3.5 shows the physical mechanism of electric field poling with the sign reversal of the second order nonlinear susceptibility in the periodic patterning domain. In general electric field poling, using a periodic pattern electrode on one surface of the optical waveguide and applying a voltage results in domain reversal in the electrode regions.
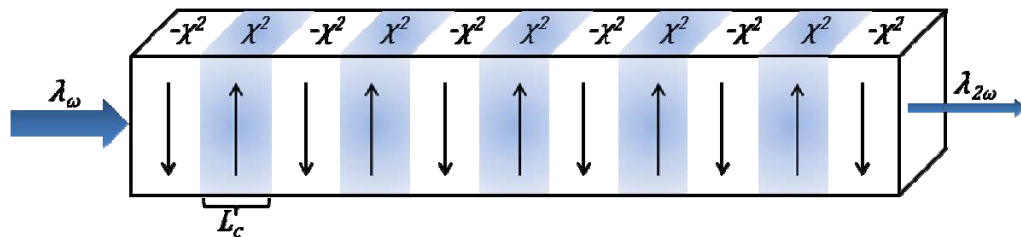


Figure 3.5 Patterning of a periodic second order nonlinear susceptibility in an optical waveguide.

Thermal poling is another technique used to achieve QPM especially in glass fibres. In thermal poling a high DC (Direct Current) electric field is applied across the core of the glass fibre at a very high temperature, i.e. between $250^0 C$ to $300^0 C$, for a duration of about 10 minutes to several hours. Following this process, the heat source is removed in order to cool down the fibre to the room temperature while the DC electric field is still applied. If the DC electric field is removed before removing the heat source the induced second order nonlinear susceptibility vanishes. Further, in order to achieve a constant $\chi^{(2)}$ across the entire fibre length the electrodes can be

inserted through two holes within the cladding of a fibre (i.e. one hole close to the core of the fibre while the other hole placed away from the fibre core). Then the anode is inserted to the hole close to the fibre core and the cathode is connected to the other. The hole with the anode is responsible for the charge migration and ionization process which is a key factor for inducing $\chi^{(2)}$ [143].

### 3.6  ORIENTATION OF THE WAVEGUIDE WITH RESPECT TO THE POLAR AXIS

This section discusses the induced polar axes of poled $SiO_2$ and $SF$57. The orientation of the polar axis with respect to the waveguide geometry determines the efficiency of SHG. For instance, if the polarisation of the electric field of the light is perpendicular to the polar axis one can expect a minimum SHG. Furthermore, in the case of silica the poling direction determines the polar axis. After poling, silica undertakes a $C_{\infty mm}$ symmetry. Hence, required waveguide geometry with respect to the poling direction parallel to $x$, $y$ and $z$ are presented in Sections 3.6.1, 3.6.2 and 3.6.3, respectively, where two frames of reference have been used to aid the explanation.

### 3.6.1  *Poling direction parallel to x*

In Fig 3.6, $X$, $Y$ and $Z$ denote the frame of reference (i.e. Cartesian coordinates) for the poling directions, while $x$, $y$ and $z$ denote the frame of reference of the optical waveguide. Figure 3.6 (a) shows the optical waveguide with poling direction $Z$ parallel to the $x$ axis. Figure 3.6 (b) represents the Cartesian co-ordinates of the optical waveguide directions (i.e. shown by $x$, $y$, $z$ inside the circle) and of the poling direction (i.e. shown by $X$, $Y$, $Z$ outside the circle). A rectangular waveguide structure is considered in the following analysis; however, it is possible to apply this analysis to any arbitrary waveguide structure.

(a) (b)

Figure 3.6 (a) Poling direction $Z$ parallel to the $x$ direction of the optical waveguide, (b) $x, y, z$ for optical waveguide coordinate axes and $X, Y, Z$ for poling directions.

By using the above coordinate systems, it is possible to analyse the second harmonic nonlinear polarisation in $x$, $y$ and $z$ directions. Furthermore, it simplifies the analysis of the nonlinear polarisation in $x$, $y$ and $z$ directions for both $TE$ and $TM$ modes in order to find the maximum SHG in the optical waveguide.

Equation (3.7) shows the non-zero second order nonlinear susceptibilities for $SiO_2$ and $SF57$ for $TE$ mode. For the quasi-$TE$ mode, the dominant electric field is in the $x$ direction (of the waveguide coordinate system), which is equivalent to the $Z$ direction for the poling axis. Further, $ZnO$ can also be represented in a similar manner due to the $C_{\infty mm}$ group symmetry.

$$P_{NL} = \begin{bmatrix} P_x \\ P_y \\ P_z \end{bmatrix} = \varepsilon_0 \begin{bmatrix} 0 & 0 & 0 & 0 & d_{31} & 0 \\ 0 & 0 & 0 & d_{31} & 0 & 0 \\ d_{31} & d_{31} & d_{33} & 0 & 0 & 0 \end{bmatrix} \begin{bmatrix} 0 \\ 0 \\ E_Z^2 \\ 0 \\ 0 \\ 0 \end{bmatrix} \tag{3.7}$$

$$= \varepsilon_0 \begin{bmatrix} 0 \\ 0 \\ d_{33}E_Z^2 \end{bmatrix} = \varepsilon_0 \begin{bmatrix} 0 \\ 0 \\ d_{33}e_x^2 \end{bmatrix}_{\rightarrow \parallel x} \tag{3.8}$$

where $E_Z$ denotes the electric field along the poling direction $Z$ which is identical to the $e_x$ component of the electric field along the $x$ direction of the optical waveguide. Equation (3.8) implies that in the present configuration only $P_z$ is induced due to the $TE$ mode; this is due to the $e_x$ component of the light generating nonlinear polarisation in the $Z$ direction, resulting in $P_z$. Hence, a large SHG is possible as $d_{33}$ is coupled with $e_x$.

Similarly, in the nonlinear polarisation for the quasi-$TM$ mode where the $e_x$ component is negligible, the polarisation along $y$ and $z$ directions can be represented as follows;

$$P_{NL} = \begin{bmatrix} P_x \\ P_y \\ P_z \end{bmatrix} = \varepsilon_0 \begin{bmatrix} 0 & 0 & 0 & 0 & d_{31} & 0 \\ 0 & 0 & 0 & d_{31} & 0 & 0 \\ d_{31} & d_{31} & d_{33} & 0 & 0 & 0 \end{bmatrix} \begin{bmatrix} E_X^2 \\ E_Y^2 \\ 0 \\ 0 \\ 0 \\ 2E_xE_y \end{bmatrix} \qquad (3.9)$$

$$= \varepsilon_0 \begin{bmatrix} 0 \\ 0 \\ d_{31}E_X^2 + d_{31}E_Y^2 \end{bmatrix} = \varepsilon_0 \begin{bmatrix} 0 \\ 0 \\ d_{31}e_z^2 + d_{31}e_y^2 \end{bmatrix} \begin{matrix} \rightarrow \| z \\ \rightarrow \| y \end{matrix} \qquad (3.10)$$

where $E_X$ and $E_Y$ denote the electric field of $X$ and $Y$ respectively (i.e. frame of reference for poling) which are equivalent to the $e_y$ and $e_z$ electric field components along the $y$ and $z$ directions of the optical waveguide respectively. According to equation (3.10) nonlinear polarisation for $y$ and $z$ is zero. Therefore, generation of second harmonic $TM$ mode is not supported by the fundamental $TM$ mode in this orientation.

Equation (3.11) shows the nonlinear polarisation for the $TE$ mode in the $y$ direction.

$$P_{NL} = \begin{bmatrix} P_x \\ P_y \\ P_z \end{bmatrix} = \varepsilon_0 \begin{bmatrix} 0 & 0 & 0 & 0 & d_{31} & 0 \\ 0 & 0 & 0 & d_{31} & 0 & 0 \\ d_{31} & d_{31} & d_{33} & 0 & 0 & 0 \end{bmatrix} \begin{bmatrix} 0 \\ E_Y^2 \\ 0 \\ 0 \\ 0 \\ 0 \end{bmatrix} \qquad (3.11)$$

$$= \varepsilon_0 \begin{bmatrix} 0 \\ 0 \\ d_{31}E_Y^2 \end{bmatrix} = \varepsilon_0 \begin{bmatrix} 0 \\ 0 \\ d_{31}e_y^2 \end{bmatrix} \rightarrow \parallel y \qquad (3.12)$$

In equation (3.12) the second harmonic $TE$ mode is not supported due to the non-existence of nonlinear polarisation in the $y$ direction of the optical waveguide.

Analysis of nonlinear polarisation for the $TM$ mode when the poling direction $Z$ is parallel to $x$ can be represented in the following matrix form;

$$P_{NL} = \begin{bmatrix} P_x \\ P_y \\ P_z \end{bmatrix} = \varepsilon_0 \begin{bmatrix} 0 & 0 & 0 & 0 & d_{31} & 0 \\ 0 & 0 & 0 & d_{31} & 0 & 0 \\ d_{31} & d_{31} & d_{33} & 0 & 0 & 0 \end{bmatrix} \begin{bmatrix} E_X^2 \\ 0 \\ E_Z^2 \\ 0 \\ 2E_ZE_X \\ 0 \end{bmatrix} \qquad (3.13)$$

In equation (3.13) electric fields along $X$ and $Z$ poling directions exist for $TM$ mode.

$$= \varepsilon_0 \begin{bmatrix} 2d_{31}E_ZE_X \\ 0 \\ d_{31}E_X^2 + d_{33}E_Z^2 \end{bmatrix} = \varepsilon_0 \begin{bmatrix} 2d_{31}e_xe_z \\ 0 \\ d_{31}e_z^2 + d_{33}e_x^2 \end{bmatrix} \begin{matrix} \rightarrow \parallel z \\ \\ \rightarrow \parallel x \end{matrix} \qquad (3.14)$$

Equation (3.14) shows that the nonlinear polarisations for $x$ and $z$ are non-zero; therefore, the generation of second harmonic $TM$ mode is supported by the fundamental $TM$ mode in this orientation.

### 3.6.2   *Poling direction parallel to y*

In Figure 3.7 (a) the poling direction $Z$ is parallel to the $y$ direction of the optical waveguide. Figure 3.7 (b) shows the poling coordinates with respect to the Cartesian coordinates of the optical waveguides. A similar pattern to Section 3.6.1 can be seen when analysing nonlinear polarisation for $TE$ and $TM$ modes.
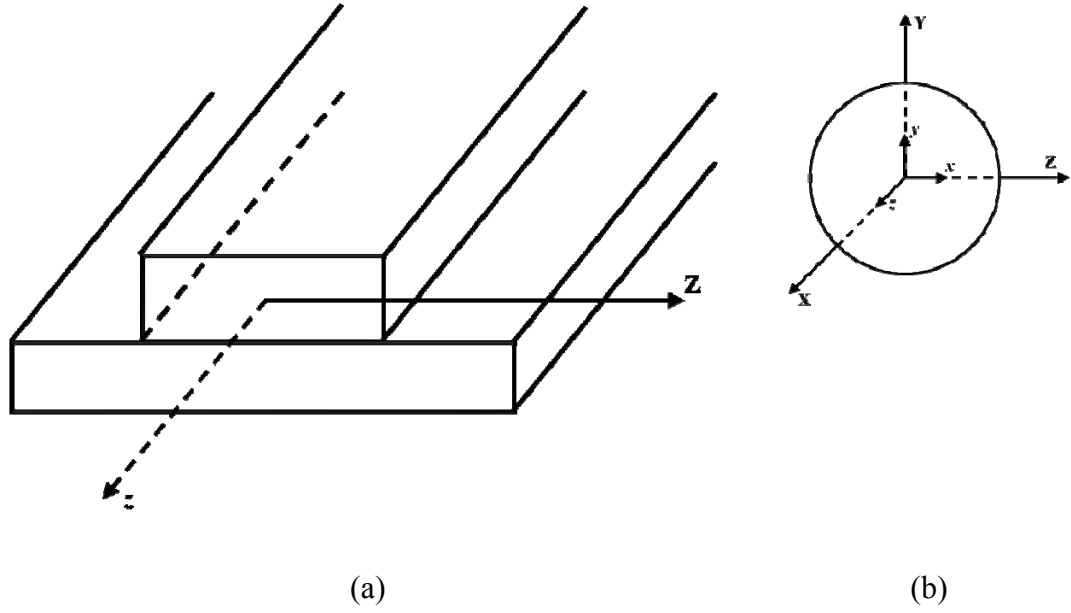
(a)                 (b)
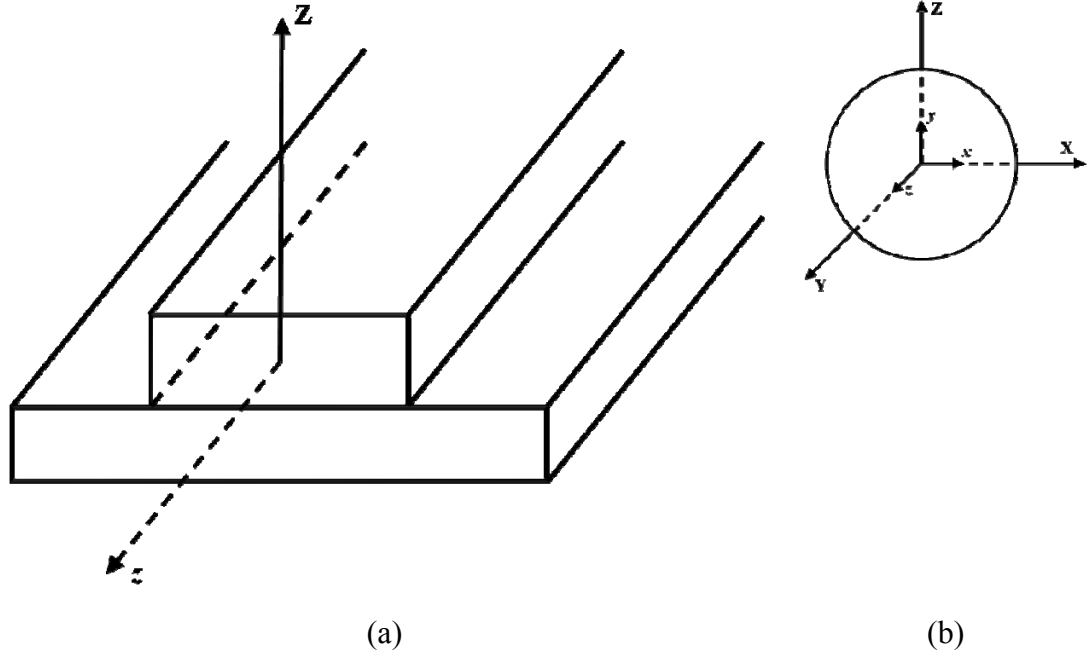
Figure 3.7 (a) Poling direction $Z$ parallel to the $y$ direction of the optical waveguide, (b) $x, y, z$ for optical waveguide coordinate axes and $X, Y, Z$ for poling directions.

$$P_{NL} = \begin{bmatrix} P_x \\ P_y \\ P_z \end{bmatrix} = \varepsilon_0 \begin{bmatrix} 0 & 0 & 0 & 0 & d_{31} & 0 \\ 0 & 0 & 0 & d_{31} & 0 & 0 \\ d_{31} & d_{31} & d_{33} & 0 & 0 & 0 \end{bmatrix} \begin{bmatrix} E_X^2 \\ 0 \\ 0 \\ 0 \\ 0 \\ 0 \end{bmatrix} \tag{3.15}$$

$$= \varepsilon_0 \begin{bmatrix} 0 \\ 0 \\ d_{31}E_X^2 \end{bmatrix} = \varepsilon_0 \begin{bmatrix} 0 \\ 0 \\ d_{31}e_x^2 \end{bmatrix} \xrightarrow{\rightarrow \parallel x} \tag{3.16}$$

In this case from equation (3.16) nonlinear polarisation in the $x$ direction is zero. Hence, generation of second harmonic $TE$ mode is not supported by the fundamental $TE$ mode in this orientation. (i.e. $Z$ is parallel to $y$).

The following equation can be written in the case of the $TM$ mode;

$$P_{NL} = \begin{bmatrix} P_x \\ P_y \\ P_z \end{bmatrix} = \varepsilon_0 \begin{bmatrix} 0 & 0 & 0 & 0 & d_{31} & 0 \\ 0 & 0 & 0 & d_{31} & 0 & 0 \\ d_{31} & d_{31} & d_{33} & 0 & 0 & 0 \end{bmatrix} \begin{bmatrix} 0 \\ E_Y^2 \\ E_Z^2 \\ 2E_Y E_Z \\ 0 \\ 0 \end{bmatrix} \tag{3.17}$$

$$= \varepsilon_0 \begin{bmatrix} 0 \\ 2d_{31}E_Y E_Z \\ d_{31}E_Y^2 + d_{33}E_Z^2 \end{bmatrix} = \varepsilon_0 \begin{bmatrix} 0 \\ 2d_{31}e_z e_y \\ d_{31}e_z^2 + d_{33}e_y^2 \end{bmatrix} \begin{matrix} \\ \rightarrow \parallel z \\ \rightarrow \parallel y \end{matrix} \tag{3.18}$$

In equation (3.18) generation of second harmonic $TM$ mode is supported by the fundamental $TM$ mode in this orientation due to $Z$ being parallel to $y$ and $Y$ being parallel to $z$.

If the $TE$ polarisation is parallel to the $y$ axis of the optical waveguide;

$$P_{NL} = \begin{bmatrix} P_x \\ P_y \\ P_z \end{bmatrix} = \varepsilon_0 \begin{bmatrix} 0 & 0 & 0 & 0 & d_{31} & 0 \\ 0 & 0 & 0 & d_{31} & 0 & 0 \\ d_{31} & d_{31} & d_{33} & 0 & 0 & 0 \end{bmatrix} \begin{bmatrix} 0 \\ 0 \\ E_Z^2 \\ 0 \\ 0 \\ 0 \end{bmatrix} \tag{3.19}$$

$$= \varepsilon_0 \begin{bmatrix} 0 \\ 0 \\ d_{33}E_Z^2 \end{bmatrix} = \varepsilon_0 \begin{bmatrix} 0 \\ 0 \\ d_{31}e_y^2 \end{bmatrix} \rightarrow \parallel y \tag{3.20}$$

Nonlinear polarisation for the $z$ direction of the optical waveguide is non-zero; therefore, generation of second harmonic $TE$ mode is supported by the fundamental $TE$ mode in this orientation.

Arrangement of the Cartesian coordinates of the optical waveguide and the poling coordinates for $TM$ mode can be represented in the following matrix form;

$$P_{NL} = \begin{bmatrix} P_x \\ P_y \\ P_z \end{bmatrix} = \varepsilon_0 \begin{bmatrix} 0 & 0 & 0 & 0 & d_{31} & 0 \\ 0 & 0 & 0 & d_{31} & 0 & 0 \\ d_{31} & d_{31} & d_{33} & 0 & 0 & 0 \end{bmatrix} \begin{bmatrix} E_X^2 \\ E_Y^2 \\ 0 \\ 0 \\ 0 \\ 2E_X E_Y \end{bmatrix} \tag{3.21}$$

$$= \varepsilon_0 \begin{bmatrix} 0 \\ 0 \\ d_{31}E_X^2 + d_{31}E_Y^2 \end{bmatrix} = \varepsilon_0 \begin{bmatrix} 0 \\ 0 \\ d_{31}e_x^2 + d_{31}e_z^2 \end{bmatrix} \begin{matrix} \rightarrow \parallel x \\ \rightarrow \parallel z \\ \\ \end{matrix} \tag{3.22}$$

### 3.6.3 *Poling direction parallel to z*

Figure 3.8 (a) shows an optical waveguide with poling direction $Z$ parallel to $z$. Figure 3.8 (b) shows the corresponding Cartesian coordinates for the waveguide and the poling. The matrix form of the $TE$ mode and the $TM$ mode are represented in equations (3.24) and (3.26) respectively.



(a)                                                                   (b)
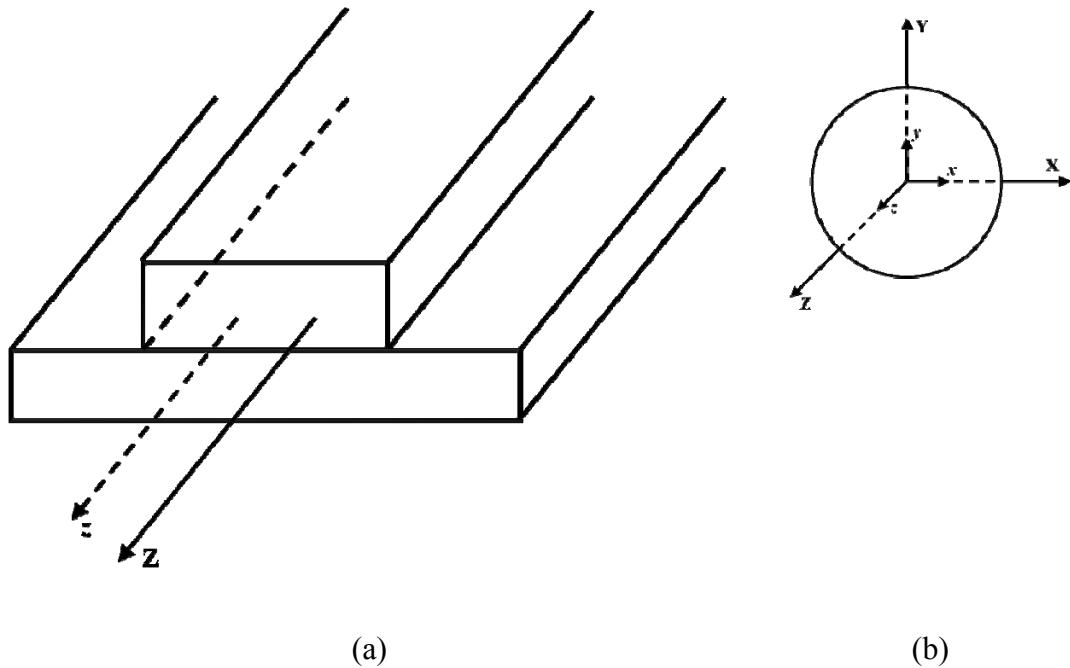
Figure 3.8 (a) Poling direction $Z$ parallel to the $z$ direction of the optical waveguide, (b) $x, y, z$ for optical waveguide coordinate axes and $X, Y, Z$ for poling directions.

When the $TE$ mode has its polarisation parallel to the $x$ axis of the waveguide, the following equation can be obtained;

$$P_{NL} = \begin{bmatrix} P_x \\ P_y \\ P_z \end{bmatrix} = \varepsilon_0 \begin{bmatrix} 0 & 0 & 0 & 0 & d_{31} & 0 \\ 0 & 0 & 0 & d_{31} & 0 & 0 \\ d_{31} & d_{31} & d_{33} & 0 & 0 & 0 \end{bmatrix} \begin{bmatrix} E_X^2 \\ 0 \\ 0 \\ 0 \\ 0 \\ 0 \end{bmatrix} \qquad (3.23)$$

$$= \varepsilon_0 \begin{bmatrix} 0 \\ 0 \\ d_{31}E_X^2 \end{bmatrix} = \varepsilon_0 \begin{bmatrix} 0 \\ 0 \\ d_{31}e_x^2 \end{bmatrix} \overset{\rightarrow \parallel x}{} \qquad (3.24)$$

Equation (3.24) implies that the generation of second harmonic $TE$ mode is not supported by the fundamental $TE$ mode in this orientation.

In a similar manner, when the $TE$ mode has its polarisation parallel to the $y$ axis of the waveguide;

$$P_{NL} = \begin{bmatrix} P_x \\ P_y \\ P_z \end{bmatrix} = \varepsilon_0 \begin{bmatrix} 0 & 0 & 0 & 0 & d_{31} & 0 \\ 0 & 0 & 0 & d_{31} & 0 & 0 \\ d_{31} & d_{31} & d_{33} & 0 & 0 & 0 \end{bmatrix} \begin{bmatrix} 0 \\ E_Y^2 \\ 0 \\ 0 \\ 0 \\ 0 \end{bmatrix} \tag{3.25}$$

$$= \varepsilon_0 \begin{bmatrix} 0 \\ 0 \\ d_{31}E_Y^2 \end{bmatrix} = \varepsilon_0 \begin{bmatrix} 0 \\ 0 \\ d_{31}e_y^2 \end{bmatrix} \rightarrow \parallel y \tag{3.26}$$

In equation (3.26) the poling direction is along the fibre; hence, the generation of second harmonic $TE$ mode is not supported by the fundamental $TE$ mode in this orientation.

Equations (3.28) and (3.30) represent the matrix form of the nonlinear polarisation in the $x$, $y$ and $z$ directions of the optical waveguide for the $TM$ mode.

$$P_{NL} = \begin{bmatrix} P_x \\ P_y \\ P_z \end{bmatrix} = \varepsilon_0 \begin{bmatrix} 0 & 0 & 0 & 0 & d_{31} & 0 \\ 0 & 0 & 0 & d_{31} & 0 & 0 \\ d_{31} & d_{31} & d_{33} & 0 & 0 & 0 \end{bmatrix} \begin{bmatrix} 0 \\ E_Y^2 \\ E_Z^2 \\ 2E_Y E_Z \\ 0 \\ 0 \end{bmatrix} \tag{3.27}$$

$$= \varepsilon_0 \begin{bmatrix} 0 \\ 2d_{31}E_Y E_Z \\ d_{31}E_Y^2 + d_{33}E_Z^2 \end{bmatrix} = \varepsilon_0 \begin{bmatrix} 0 \\ 2d_{31}e_y e_z \\ d_{31}e_y^2 + d_{33}e_z^2 \end{bmatrix} \begin{matrix} \\ \rightarrow \parallel y \\ \rightarrow \parallel z \end{matrix} \tag{3.28}$$

In this case the generation of second harmonic $TM$ mode is supported by the fundamental $TM$ mode in this orientation as shown in equation (3.28).

$$P_{NL} = \begin{bmatrix} P_x \\ P_y \\ P_z \end{bmatrix} = \varepsilon_0 \begin{bmatrix} 0 & 0 & 0 & 0 & d_{31} & 0 \\ 0 & 0 & 0 & d_{31} & 0 & 0 \\ d_{31} & d_{31} & d_{33} & 0 & 0 & 0 \end{bmatrix} \begin{bmatrix} E_X^2 \\ 0 \\ E_Z^2 \\ 0 \\ 2E_Z E_X \\ 0 \end{bmatrix} \tag{3.29}$$

$$= \varepsilon_0 \begin{bmatrix} 2d_{31}E_Z E_X \\ 0 \\ d_{31}E_X^2 + d_{33}E_Z^2 \end{bmatrix} = \varepsilon_0 \begin{bmatrix} 2d_{31}e_z e_x \\ 0 \\ d_{31}e_x^2 + d_{33}e_z^2 \end{bmatrix} \begin{matrix} \rightarrow \parallel x \\ \\ \rightarrow \parallel z \end{matrix} \qquad (3.30)$$

In summary, possible generation of SHG with respect to different combinations of poling directions and $TE/TM$ polarised excitations have been explored. This study facilitates choosing a poling direction that is both feasible for fabrication and is able to achieve a SHG as high as possible.

Sections 3.6.1, 3.6.2 and 3.6.3 can be summarised as shown in Table 3.1.

| Poling direction $Z \parallel$ to | Polarisation direction along the optical waveguide for $TE$ mode | Polarisation directions along the optical waveguide for $TM$ mode |
|---|---|---|
| $x$ | $x$ - supported<br>$y$ - not supported | $y \, \& \, z$ - not supported<br>$x \, \& \, z$ - supported |
| $y$ | $x$ - not supported<br>$y$ - supported | $y \, \& \, z$ - supported<br>$x \, \& \, z$ - not supported |
| $z$ | $x$ - not supported<br>$y$ - not supported | $y \, \& \, z$ - supported<br>$x \, \& \, z$ - supported |

Table 3.1 Waveguide geometry with respect to the poling directions.

## 3.7 SCALAR BEAM PROPAGATION METHOD FOR SHG

The scalar Beam Propagation Method (BPM) is used in this thesis to analyse the electromagnetic field propagation through optical waveguides. This is an efficient method in terms of computational resources. The scalar BPM is applied by splitting the field components into two. Therefore, this method facilitates the analysis of the Transverse Electric ($TE$) field and Transverse Magnetic ($TM$) field separately [144, 145]. It is assumed that the electromagnetic wave propagates near the propagation axis. Therefore, the paraxial approximation has been applied in the scalar BPM. The derivation of scalar BPM is presented in Appendix 4.

## 3.8 FULL VECTORIAL BEAM PROPAGATION METHOD FOR SHG

The full vectorial BPM approach is a basic technique for the precise analysis of optical waveguide devices where the nature of the field is hybrid. In full vectorial BPM it is assumed that the electromagnetic field propagates near the propagation axis of the optical waveguide. The derivation of the nonlinear term (i.e. source term) where the SHG is determined, of the coupled wave equation is discussed below.

### 3.8.1 *Derivation of full vectorial BPM*

From Maxwell's equations;

$$\nabla \times \boldsymbol{E} = -\mu_0 \frac{\partial \boldsymbol{H}}{\partial t} \tag{3.31}$$

$$\nabla \times \boldsymbol{H} = \frac{\partial \boldsymbol{D}}{\partial t} \tag{3.32}$$

Then the electric field and the magnetic field can be written as follows;

$$\boldsymbol{E}(x,y,t) = \frac{1}{2}\{e_\omega(y)\,e^{(j\omega t - j\beta z)} + e_{2\omega}(y)\,e^{(j2\omega t - j2\beta z)} + c.c\} \tag{3.33}$$

$$\boldsymbol{H}(x,y,t) = \frac{1}{2}\{h_\omega(y)\,e^{(j\omega t - j\beta z)} + h_{2\omega}(y)\,e^{(j2\omega t - j2\beta z)} + c.c\} \tag{3.34}$$

And the nonlinear electric displacement is;

$$\boldsymbol{D}(x, y, t) = \varepsilon_0\{[\varepsilon] + [d]\boldsymbol{E}(x, y, t)\}\boldsymbol{E}(x, y, t) \tag{3.35}$$

Here, $\omega$ is the angular frequency of the fundamental wave, $\beta$ is the propagation constant, $\mu_0$ is the vacuum permeability, $\varepsilon_0$ is the vacuum permittivity, $[\varepsilon]$ is the linear relative permittivity tensor (assumed diagonal), $[d]$ is the second order nonlinear susceptibility tensor, $e_\omega$ is the electric field component in the $x$ or $y$ direction for the fundamental frequency, $e_{2\omega}$ is the electric field component in the $x$ or $y$ direction for the SH frequency, $h_\omega$ is the magnetic field component in the $x$ or $y$ direction for the fundamental frequency, $h_{2\omega}$ is the magnetic field component in the $x$ or $y$ direction for the SH frequency and $c.c.$ denotes a complex conjugate. Note that $[\varepsilon]$ and $[d]$ depend on the frequency [146].

Substituting equation (3.33) into (3.31) yields,

*For Fundamental:*

$$\nabla \times \boldsymbol{E}_\omega = -j\omega\mu_0 \boldsymbol{H}_\omega \tag{3.36}$$

where $\boldsymbol{E}_\omega$ and $\boldsymbol{H}_\omega$ are the fundamental electric field and magnetic field respectively.

*For Second Harmonic:*

$$\nabla \times \boldsymbol{E}_{2\omega} = -j2\omega\mu_0 \boldsymbol{H}_{2\omega} \tag{3.37}$$

where $\boldsymbol{E}_{2\omega}$ and $\boldsymbol{H}_{2\omega}$ are the SH electric field and magnetic field respectively, where;

$$\boldsymbol{E}_\omega = e_\omega \, e^{(j\omega t - j\beta z)} \tag{3.38}$$

$$\boldsymbol{E}_{2\omega} = e_{2\omega} \, e^{(j2\omega t - j2\beta z)} \tag{3.39}$$

$$\boldsymbol{H}_\omega = h_\omega \, e^{(j\omega t - j\beta z)} \tag{3.40}$$

$$\boldsymbol{H}_{2\omega} = h_{2\omega} \, e^{(j2\omega t - j2\beta z)} \tag{3.41}$$

Substituting equations (3.34) and (3.35) into (3.32) yields;

$$\nabla \times \boldsymbol{H}_\omega = j\omega\varepsilon_0[\varepsilon_\omega]\boldsymbol{E}_\omega + j\omega\varepsilon_0[d_\omega]\boldsymbol{E}_{2\omega}\boldsymbol{E}_\omega^* \tag{3.42}$$

$$\nabla \times \boldsymbol{H}_{2\omega} = j2\omega\varepsilon_0[\varepsilon_{2\omega}]\boldsymbol{E}_{2\omega} + j\omega\varepsilon_0[d_{2\omega}]\boldsymbol{E}_\omega^2 \tag{3.43}$$

where an asterisk ('*') denotes a complex conjugate, $\varepsilon_\omega$ and $\varepsilon_{2\omega}$ are linear relative permittivity tensors for fundamental and SH frequencies respectively and $d_\omega$ and $d_{2\omega}$ are second order nonlinear susceptibility tensors for fundamental and SH frequencies respectively.

By substituting $\boldsymbol{H}_\omega$ and $\boldsymbol{H}_{2\omega}$ from equations (3.36) and (3.37) into (3.42) and (3.43) yields;

*For Fundamental:*

$$\nabla \times \nabla \times \boldsymbol{E}_\omega - k_0^2[\varepsilon_\omega]\boldsymbol{E}_\omega = k_0^2[d_\omega]\boldsymbol{E}_{2\omega}\boldsymbol{E}_\omega^* \tag{3.44}$$

*For Second Harmonic:*

$$\nabla \times \nabla \times \boldsymbol{E}_{2\omega} - 4k_0^2[\varepsilon_{2\omega}]\boldsymbol{E}_{2\omega} = 2k_0^2[d_{2\omega}]\boldsymbol{E}_\omega^2 \tag{3.45}$$

where $k_0$ is denotes the free space wavenumber.

Then equations (3.42) and (3.43) can be re-written as follows;

*For Fundamental:*

$$\boldsymbol{E}_\omega = \frac{[\varepsilon_\omega]^{-1}}{j\omega\varepsilon_0}(\nabla \times \boldsymbol{H}_\omega - j\omega\epsilon_0[d_\omega]\boldsymbol{E}_{2\omega}\boldsymbol{E}_\omega^*) \tag{3.46}$$

*For Second Harmonic:*

$$\boldsymbol{E}_{2\omega} = \frac{[\varepsilon_{2\omega}]^{-1}}{j2\omega\varepsilon_0}(\nabla \times \boldsymbol{H}_{2\omega} - j\omega\varepsilon_0[d_{2\omega}]\boldsymbol{E}_\omega^2) \tag{3.47}$$

Substituting equation (3.36) and (3.37) into (3.46) and (3.47) yields;

*For Fundamental:*

$$\nabla \times [\varepsilon_\omega]^{-1}\nabla \times \boldsymbol{H}_\omega - k_0^2\boldsymbol{H}_\omega = j\omega\varepsilon_0\nabla \times [\varepsilon_\omega]^{-1}[d_\omega]\boldsymbol{E}_{2\omega}\boldsymbol{E}_\omega^* \tag{3.48}$$

*For Second Harmonic:*

$$\nabla \times [\varepsilon_{2\omega}]^{-1}\nabla \times \boldsymbol{H}_{2\omega} - 4k_0^2\boldsymbol{H}_{2\omega} = j\omega\varepsilon_0\nabla \times [\varepsilon_{2\omega}]^{-1}[d_{2\omega}]\boldsymbol{E}_\omega^2 \tag{3.49}$$

It is necessary to consider the nonlinear part (i.e. R.H.S.) of equations (3.48) and (3.49) to find the nonlinear components in the $x$, $y$ and $z$ directions. Equations (3.60) (3.61) and (3.62) represent the nonlinear components in the $x$, $y$ and $z$ directions respectively.

By substituting $\boldsymbol{\psi}_{NL}(x, y, z)$ into the R.H.S. of equation (3.49) ;

$$\boldsymbol{\psi}_{NL}(x, y, z) = j\omega\varepsilon_0 \nabla \times [\varepsilon_{2\omega}]^{-1}[d_{2\omega}]\boldsymbol{E}_\omega^2 \tag{3.50}$$

By replacing $\omega\varepsilon_0$ (i.e. $\omega\varepsilon_0 = k_0 c\varepsilon_0 = k_0 \frac{1}{\sqrt{\varepsilon_0\mu_0}}\varepsilon_0 = k_0 \frac{\sqrt{\varepsilon_0}}{\sqrt{\mu_0}} = \frac{k_0}{Z_0}; \because Z_0 = \frac{\sqrt{\mu_0}}{\sqrt{\varepsilon_0}}$), equation (3.50) can be written as;

$$\boldsymbol{\psi}_{NL}(x, y, z) = j\frac{k_0}{Z_0} \nabla \times [\varepsilon_{2\omega}]^{-1}[d_{2\omega}]\boldsymbol{E}_\omega^2 \tag{3.51}$$

By substituting nonlinear polarisation equation ($P_{NL}$) into (3.51) ;

$$\boldsymbol{\psi}_{NL}(x, y, z) = j\frac{k_0}{Z_0} \nabla \times [\varepsilon_{2\omega}]^{-1} \left[\frac{P_{NL}}{\varepsilon_0}\right] \tag{3.52}$$

$$\boldsymbol{\psi}_{NL}(x, y, z) = j\frac{k_0}{Z_0\varepsilon_0} \nabla \times [\varepsilon_{2\omega}]^{-1}[P_{NL}] \tag{3.53}$$

$$\boldsymbol{\psi}_{NL}(x, y, z) = j\frac{k_0}{Z_0\varepsilon_0} \nabla \times [\varepsilon_{2\omega}]^{-1}[P_{NL}] \tag{3.54}$$

$$\boldsymbol{\psi}_{NL}(x, y, z) = j\frac{k_0}{Z_0\varepsilon_0} \nabla \times \begin{bmatrix} 1/\varepsilon_x & 0 & 0 \\ 0 & 1/\varepsilon_y & 0 \\ 0 & 0 & 1/\varepsilon_z \end{bmatrix} \begin{bmatrix} P_x \\ P_y \\ P_z \end{bmatrix} \tag{3.55}$$

$$\boldsymbol{\psi}_{NL}(x, y, z) = j\frac{k_0}{Z_0\varepsilon_0} \nabla \times \begin{bmatrix} P_x/\varepsilon_x \\ P_y/\varepsilon_y \\ P_z/\varepsilon_z \end{bmatrix} \tag{3.56}$$

$$\boldsymbol{\psi}_{NL}(x,y,z) = j\frac{k_0}{Z_0\varepsilon_0}\begin{vmatrix} i_x & i_y & i_z \\ \partial/\partial x & \partial/\partial y & \partial/\partial z \\ P_x/\varepsilon_x & P_y/\varepsilon_y & P_z/\varepsilon_z \end{vmatrix} \qquad (3.57)$$

Hence the nonlinear part of the coupled wave equation can be written as follows;

$$\boldsymbol{\psi}_{NL}(x,y,z) = j\omega\left\{i_x\left[\frac{\partial}{\partial y}\frac{P_z}{\varepsilon_z} - \frac{\partial}{\partial z}\frac{P_y}{\varepsilon_y}\right] - i_y\left[\frac{\partial}{\partial x}\frac{P_z}{\varepsilon_z} - \frac{\partial}{\partial z}\frac{P_x}{\varepsilon_x}\right] + i_z\left[\frac{\partial}{\partial x}\frac{P_y}{\varepsilon_y} - \frac{\partial}{\partial y}\frac{P_x}{\varepsilon_x}\right]\right\} \quad (3.58)$$

*For the x component*:

$$\psi_{NL}(x) = j\omega\left\{i_x\left[\frac{\partial}{\partial y}\frac{P_z}{\varepsilon_z} - \frac{\partial}{\partial z}\frac{P_y}{\varepsilon_y}\right]\right\} \qquad (3.59)$$

By substituting $\varepsilon_z = n_z^2$ , $\varepsilon_y = n_y^2$ and $\partial/\partial z = -2j\beta$  the following equation can be obtained;

$$\psi_{NL}(x) = \frac{k_0}{Z_0\varepsilon_0}\left\{i_x\left[j\frac{\partial}{\partial y}\frac{P_z}{n_z^2} - 2\beta\frac{P_y}{n_y^2}\right]\right\} \qquad (3.60)$$

Similarly the $y$ and $z$ components can be written as;

*For the y component:*

$$\psi_{NL}(y) = \frac{k_0}{Z_0\varepsilon_0}\left\{i_y\left[2\beta\frac{P_x}{n_x^2} - j\frac{\partial}{\partial x}\frac{P_z}{n_z^2}\right]\right\} \qquad (3.61)$$

*For the z component:*

$$\psi_{NL}(z) = \frac{k_0}{Z_0\varepsilon_0}\left\{i_z\left[\frac{\partial}{\partial x}\frac{P_y}{n_y^2} - \frac{\partial}{\partial y}\frac{P_x}{n_x^2}\right]\right\} \qquad (3.62)$$

In a similar way the R.H.S. ($j\omega\nabla \times [\varepsilon_{2\omega}]^{-1}[d_{2\omega}]\boldsymbol{E}_{2\omega}\boldsymbol{E}_\omega^*$) of equation (3.48) can be derived in order to find the nonlinear components of the fundamental frequency in the $x$, $y$ and $z$ directions.

From equation (3.48) $\boldsymbol{H}_\omega$ can be represented as follows;

$$\{\boldsymbol{H}_\omega\} = \begin{Bmatrix} H_{\omega x} \\ H_{\omega y} \\ H_{\omega z} \end{Bmatrix} = \begin{Bmatrix} \boldsymbol{\phi}_\omega \\ H_{\omega z} \end{Bmatrix} \qquad (3.63)$$

where $\boldsymbol{\phi}_\omega = \begin{Bmatrix} H_{\omega x} \\ H_{\omega y} \end{Bmatrix}$

Equations (3.48) and (3.49) are similar to equation (A2.53) in Appendix 4, the difference being the addition of the source term which represents the nonlinear part of the equation. Hence BPM can be applied using the split-step procedure as shown above.

Let;

$$\{H_\omega\} = \begin{Bmatrix} \boldsymbol{\phi}_\omega \\ H_{\omega z} \end{Bmatrix} \tag{3.64}$$

where $\boldsymbol{\phi}_\omega = \begin{Bmatrix} H_{\omega x} \\ H_{\omega y} \end{Bmatrix}$

and

$$\{H_{2\omega}\} = \begin{Bmatrix} \boldsymbol{\phi}_{2\omega} \\ H_{2\omega z} \end{Bmatrix} \tag{3.65}$$

where $\boldsymbol{\phi}_{2\omega} = \begin{Bmatrix} H_{2\omega x} \\ H_{2\omega y} \end{Bmatrix}$

Therefore, the propagation model of the fundamental field can be represented in a similar manner to equation (2.39) in Chapter 2 but with the R.H.S. nonlinear term added and it can be written as follows;

$$-2jn_0 k_0 [\widetilde{M}] \frac{d\{\boldsymbol{\phi}_\omega\}}{dz} + ([K] - n_0^2 k_0^2 [M])\{\boldsymbol{\phi}_\omega\} = \{\boldsymbol{\psi}_{NL}^\omega\} \tag{3.66}$$

where $[M]$ and $[K]$ are given in equation (2.36) and equation (2.37) respectively in Chapter 2.

For SHG propagation it is necessary to modify equation (2.39) in Chapter 2 to include $2\beta$, hence the following equation can be written;

$$-4jn_0 k_0 [\widetilde{M}] \frac{d\{\boldsymbol{\phi}_{2\omega}\}}{dz} + ([K] - 4n_0^2 k_0^2 [M])\{\boldsymbol{\phi}_{2\omega}\} = \{\boldsymbol{\psi}_{NL}^{2\omega}\} \tag{3.67}$$

Then the split-step procedure and CN scheme can be applied to equation (3.66) to derive the following;

$$[A]_k\{\boldsymbol{\phi}_\omega\}_{k+1} = [B]_k\{\boldsymbol{\phi}_\omega\}_k \tag{3.68}$$

where,

$$[A]_k = -2jn_0k_0[\widetilde{\boldsymbol{M}}]_k + \theta\Delta z([K]_k - n_0^2k_0^2[\boldsymbol{M}]_k) \tag{3.69}$$

$$[B]_k = -2jn_0k_0[\widetilde{\boldsymbol{M}}]_k + (\theta - 1)\Delta z([K]_k - n_0^2k_0^2[\boldsymbol{M}]_k) \tag{3.70}$$

Then the following equation can be derived for the fundamental frequency;

$$\left\{\boldsymbol{\phi}_\omega^{(2)}\right\}_{k+1} = \left\{\boldsymbol{\phi}_\omega^{(1)}\right\}_{k+1} + j\frac{\Delta z}{2\beta\varepsilon_r^{-1}}\{\boldsymbol{\psi}_{NL}^\omega\} \tag{3.71}$$

By applying equation (3.68) into equation (3.71) the following can be derived;

$$\left\{\boldsymbol{\phi}_\omega^{(2)}\right\}_{k+1} = \frac{[B]_k}{[A]_k}\left\{\boldsymbol{\phi}_\omega^{(1)}\right\}_{k+1} + j\frac{\Delta z}{2\beta\varepsilon_r^{-1}}\{\boldsymbol{\psi}_{NL}^\omega\} \tag{3.72}$$

Similarly the following equation can be derived for the SH frequency;

$$\left\{\boldsymbol{\phi}_{2\omega}^{(2)}\right\}_{k+1} = \frac{[B]_k}{[A]_k}\left\{\boldsymbol{\phi}_{2\omega}^{(1)}\right\}_{k+1} + j\frac{\Delta z}{4\beta\varepsilon_r^{-1}}\{\boldsymbol{\psi}_{NL}^{2\omega}\} \tag{3.73}$$

The equations (3.72) and (3.73) have been used in the numerical analysis of the SHG in optical waveguides in this thesis.

**3.9    SUMMARY**

In this chapter two key contributions have been presented, these being fundamental to the work described in subsequent chapters of the thesis and are as described below.

The matrix form of the second order nonlinear susceptibilities for materials such as $SiO_2$, $SF57$ and $ZnO$ have been presented at the start of the chapter. The optimisation of the SHG has then been introduced by using the polar axis with respect to the waveguide geometry, which is a key factor that determines the efficiency of the SHG: this represents the first key contribution in this chapter from the work of the author. Further, the coherence length of the optical waveguides has been discussed. Here, the Quasi Phase Matching (QPM) technique to eliminate the phase mismatch between the fundamental and SH waves has been considered. Moreover, the practical implementation of the QPM by applying higher order QPM and enabling the SHG in a non-centrosymmetric material, by reversing the second order nonlinear sign with different poling techniques, has been discussed.

Additionally in this chapter, the scalar formulation of the Beam Propagation technique to analyse the SHG wave propagation through an optical waveguide, with and without the use of pumping, has been discussed. Furthermore, the ***H***-field based full vectorial formulation has been implemented, for the first time, to study the SHG wave propagation through an optical waveguide where the modes are of a hybrid nature: this represents another key contribution of this chapter by the author.

# Chapter 4

# Photonic Crystal Fibres

This chapter presents Second Harmonic Generation (SHG) in different Photonic Crystal Fibre (PCF) structures, i.e. Hexagonal PCF in Section 4.4 and Equiangular Spiral PCF in Section 4.6. The numerical analyses using the Finite Element Method (FEM) and Beam Propagation Method (BPM) are employed in order to a) implement the Quasi Phase Matching technique (QPM) to prevent phase mismatching between the fundamental and second harmonic modes (Section 4.6.2) and b) analyse the effects of fabrication error in PCF (Section 4.6.3).

## 4.1 INTRODUCTION

Recently, considerable interest has been shown in guided wave Second Harmonic Generation (SHG) devices implementing compact short-wavelength coherent light sources which are useful across a range of applications such as optical data storage, xerography, spectroscopy, photolithography and telecommunication [147]. Practical experimentation of SHG is complicated and expensive due to technological challenges. Therefore, numerical methods are widely employed in the analysis and design optimisation of such nonlinear optical devices. The Beam Propagation Method (BPM) is a well known numerical method and has been very attractive due

to its ability to study a wide range of optical waveguides. In 1995, H. M. Masoudi and J. M. Arnold have developed a numerical method by using BPM to model three-dimensional optical waveguides to analyse the second order nonlinearity [148].

Numerical modelling of an optical waveguide also facilitates the analysis of phase mismatching in a precise manner. As discussed in Chapter 3, application of the QPM technique is used to eliminate phase mismatch where the phase difference between the two interacting waves is corrected at regular intervals by means of a structural periodicity applied into the nonlinear material in the fabrication process by using different poling techniques. In 1997, F. A. Katsriku *et al*. numerically analysed the SHG in *LiNbO₃* channel waveguides with the QPM scheme by using the Finite Element based Beam Propagation Method (FE-BPM) [149].

PCF is an ideal candidate for SHG due to its unique range of optical properties. For example, the effective area of PCFs can be tailored to be as large as nearly three times larger or as small as four times smaller than the mode size in conventional dispersion-shifted fibres and standard telecommunications fibres: the latter case is useful in enhancing nonlinear effects [150]. Other unique properties of PCFs are that they are endlessly single mode [151] and can be fabricated to exhibit remarkable dispersion characteristics such as broad-band flattened [150] and zero Group Velocity Dispersion (GVD) [152]. Further, PCFs can be used in many nonlinear applications such as supercontinuum generation [153], soliton generation and propagation [154], ultra-short pulse compression [155], soliton lasers [156], four-wave mixing [157] and Second Harmonic Generation [158].

## 4.2    STRUCTURE OF THE PHOTONIC CRYSTAL FIBRE

A typical modelling of the honeycomb configuration of a hexagonal PCF structure with circular air-holes is shown in Figure 4.1.
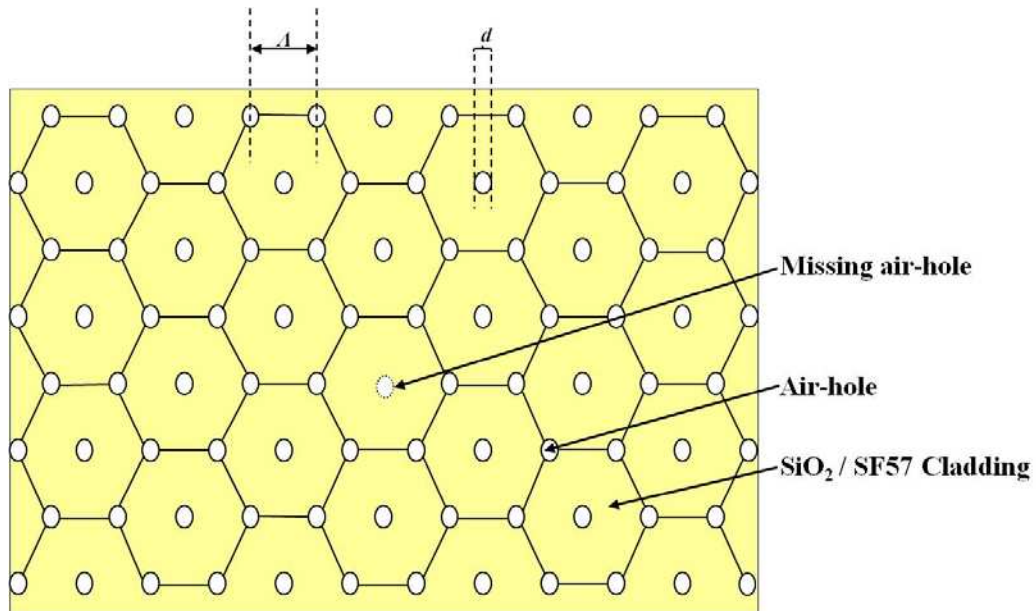


Figure 4.1 Schematic diagram of a PCF with hexagonal arrays of air-holes.

By eliminating the middle air-hole as shown in Figure 4.1, it is possible to guide the light as is done through the core of a typical optical fibre. Figure 4.1 shows a regular array of equal-sized air-holes. The air-hole diameter is taken as $d$ $\mu m$ while the pitch length, i.e. the distance between the centres of two adjacent holes, is taken as $\Lambda$ $\mu m$.

The pitch length details in the first ring of the PCF are shown in Figure 4.2 where a sample hexagon from the honeycomb configuration has been enlarged to illustrate the distance and angles between the air-holes.
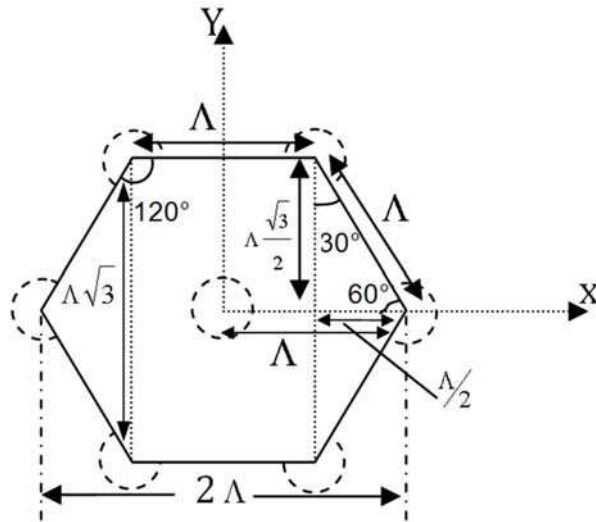
Figure 4.2 Schematic diagram of the distances between the air-holes from their centre in the first ring of hexagonal PCF.

It is possible to tailor the PCF structure as desired. For example, Figure 4.3 shows a hexagonal honeycomb configuration with expanded air-holes in the first ring of the PCF.
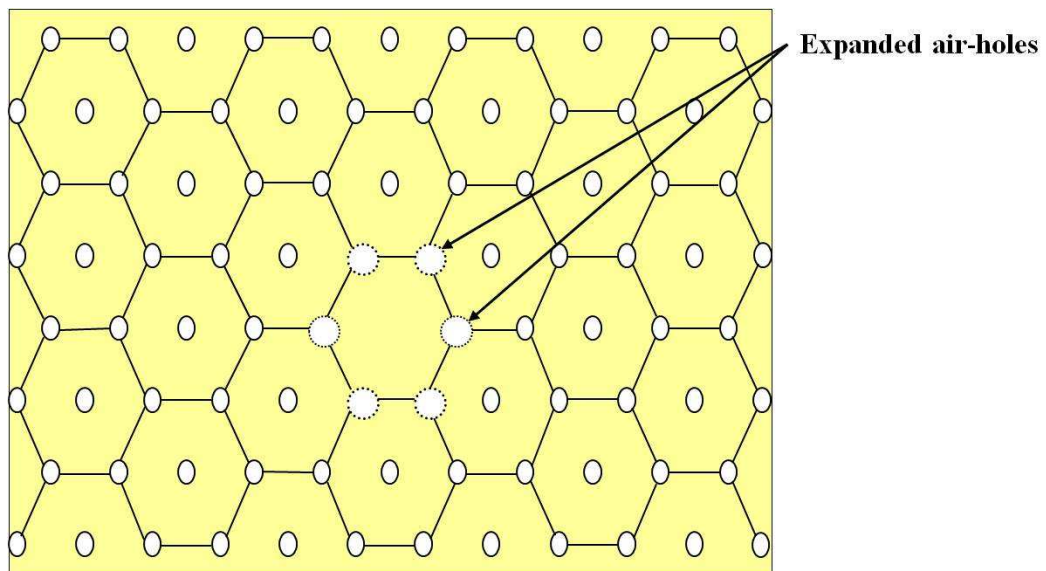


Figure 4.3 Schematic diagram of a hexagonal PCF with expanded air-holes in the first ring.

### 4.3 NUMERICAL MODELLING OF THE PHOTONIC CRYSTAL FIBRE

The quarter structure of a hexagonal PCF is shown in Figure 4.4. It is important to assign all the air-holes in a Cartesian coordinate system in order to model such a complicated structure numerically.
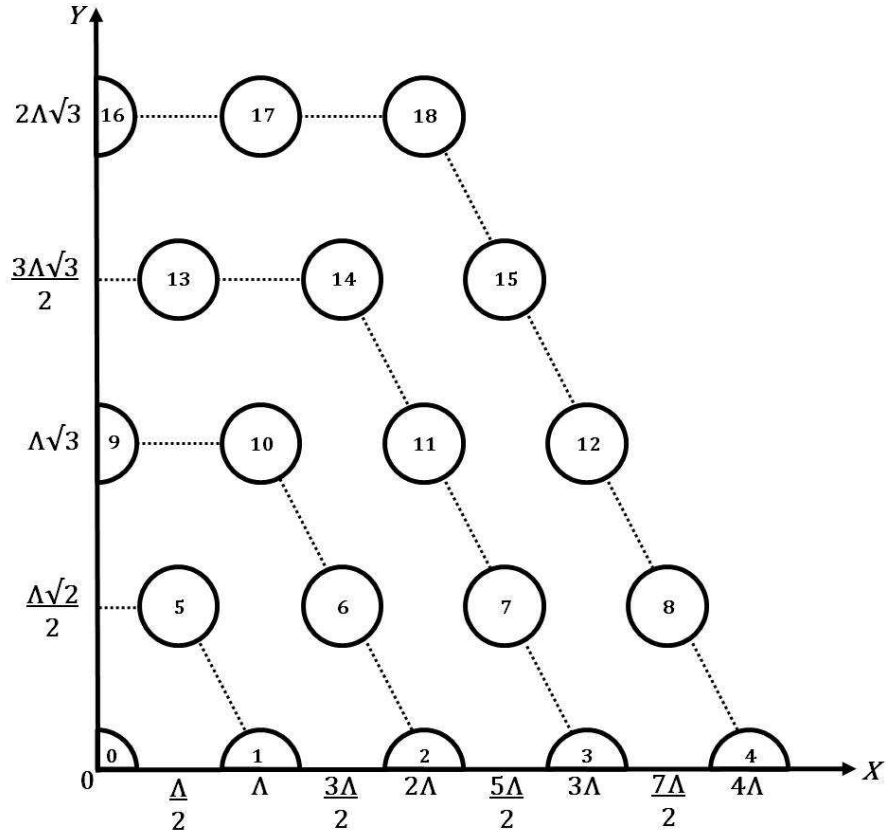


Figure 4.4 The quarter structure of the hexagonal PCF in Cartesian coordinates.

The following equations represent the values of the $X$ and $Y$ coordinates of the centres of the air-holes (from number 0 to 18): these relationships are used in the computer program to generate a hexagonal PCF structure.

$$X_0 = 0, Y_0 = 0, \qquad X_1 = \Lambda, Y_1 = 0, \qquad X_2 = 2\Lambda, Y_2 = 0, \qquad X_3 = 3\Lambda, Y_3 = 0,$$

$$X_4 = 4\Lambda, Y_4 = 0, \qquad X_5 = \frac{\Lambda}{2}, Y_5 = \frac{\Lambda\sqrt{2}}{2}, \qquad X_6 = \frac{3\Lambda}{2}, Y_6 = \frac{\Lambda\sqrt{2}}{2}, \qquad X_7 = \frac{5\Lambda}{2}, Y_7 = \frac{\Lambda\sqrt{2}}{2},$$

$$X_8 = \frac{7\Lambda}{2}, Y_8 = \frac{\Lambda\sqrt{2}}{2}, \quad X_9 = 0, Y_9 = \Lambda\sqrt{3}, \quad X_{10} = \Lambda, Y_{10} = \Lambda\sqrt{3}, \quad X_{11} = 2\Lambda, Y_{11} = \Lambda\sqrt{3},$$

$$X_{12} = 3\Lambda, Y_{12} = \Lambda\sqrt{3}, \qquad X_{13} = \frac{\Lambda}{2}, Y_{13} = \frac{3\Lambda\sqrt{3}}{2}, \qquad X_{14} = \frac{3\Lambda}{2}, Y_{14} = \frac{3\Lambda\sqrt{3}}{2},$$

$$X_{15} = \frac{5\Lambda}{2}, Y_{15} = \frac{3\Lambda\sqrt{3}}{2}, \qquad X_{16} = 0, Y_{16} = 2\Lambda\sqrt{3}, \qquad X_{17} = \Lambda, Y_{17} = 2\Lambda\sqrt{3},$$

$$X_{18} = 2\Lambda, Y_{18} = 2\Lambda\sqrt{3}.$$

The analysis and results presented in this thesis have been produced by implementing the *H*-field based finite element equations in the FORTRAN programming language. The version of the FORTRAN program is F77, and it is based on the UNIX platform.

Figure 4.5 represents the full structure hexagonal PCF in the Cartesian coordinate system, generated by the FORTRAN program. It is possible to analyse the behaviour of the electromagnetic field by assigning Cartesian coordinates to each node or each element of the finite element domain.
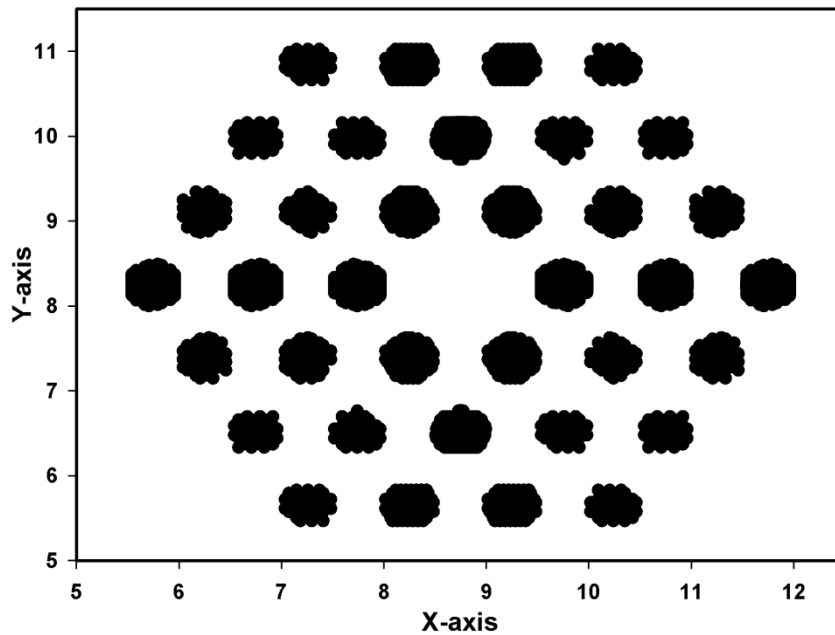


Figure 4.5 Hexagonal air-hole PCF structure represented on Cartesian coordinates, generated by the FORTRAN program.

## 4.4    SIMULATION RESULTS FOR HEXAGONAL PCF

This section first validates numerical simulations by comparing results of conventional optical fibres using the Finite Element based Beam Propagation Method (FE-BPM). Then the simulation results for hexagonal PCF are then presented which were obtained by using the scalar BPM.

### 4.4.1   *Validation of numerical simulations*

Initially, the accuracy of the FE-BPM is demonstrated by comparing with corresponding practical results. In 1997, V. Pruneri and P. G. Kazansky have reported the first demonstration of efficient Quasi Phase Matched (QPM) SHG to the blue of picosecond pulses in thermally poled fibres, and the experiment is carried out to investigate the second order nonlinearity and conversion efficiency of the periodically poled silica fibres [159]. The numerical model of the silica fibre has the exact dimensions as the fibre used in the experiment, i.e. a core diameter of $5.8 \, \mu m$, outer diameter of $150 \, \mu m$ and distance between plane surface (flat surface) and core region of $5.0 \, \mu m$. Furthermore, in the numerical simulation the fundamental wavelength has been used as $840 \, nm$ and the second harmonic wavelength has been used as $420 \, nm$ and both fundamental and second harmonic wavelengths are taken as Continuous Waves (CW). Figure 4.6 shows the QPM second harmonic output power against the propagation length.
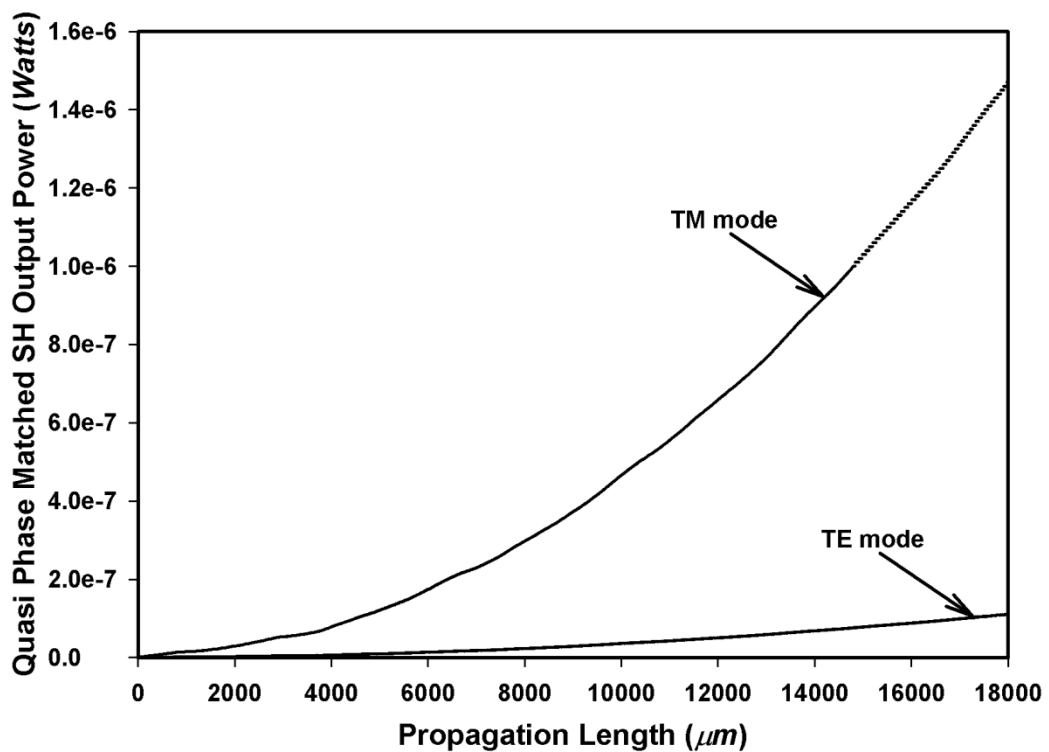


Figure 4.6 Variation of the QPM SH output power against the propagation length.

In Figure 4.6, the QPM SH output power for the *TM*-mode is considerably higher than that of the *TE*-mode. The *TM*-mode SH output power is high due to the more suitable crystal orientation of $SiO_2$. Furthermore, in this experiment the application

of thermal poling was considered perpendicular to the propagation axis (i.e. crystal axis). Therefore, as discussed in Chapter 3 a maximum SH output power can be obtained with the $TM$-mode. In Figure 4.6, the results are obtained by using the scalar BPM. In this case the fundamental power (i.e. pump power) is $150\,mW$. As can be observed in Figure 4.6, the SH output power for the $TM$-mode after propagation of $1.8\,cm$ is $\sim 1.47\,\mu W$, which is comparable with the corresponding experimental value of $\sim 1.1\,\mu W$ [159]. The main reason for the slightly higher SH output power in the numerical simulation is that, when applying QPM the coherence length can produce an error in practice.

### 4.4.2  Hexagonal PCF

Following the numerical validation test carried out in the previous section, a hexagonal PCF structure is considered here. The variation of the effective index of the $H_{11}^{x}$ mode with the pitch ($\Lambda$) at the fundamental wavelengths is shown in Figure 4.7. The effective index is defined as $n_{eff} = \beta/k_0$ where $\beta$ is the propagation constant and the wavenumber $k_0 = 2\pi/\lambda$, where $\lambda$ is the wavelength. The refractive indices of $SiO_2$ as used in Figure 4.7 and Figure 4.8 are taken as 1.4440234 [160] at the operating wavelength of $1.55\,\mu m$ (fundamental wavelength) and as 1.4537603 at the SH wavelength of $0.775\,\mu m$.
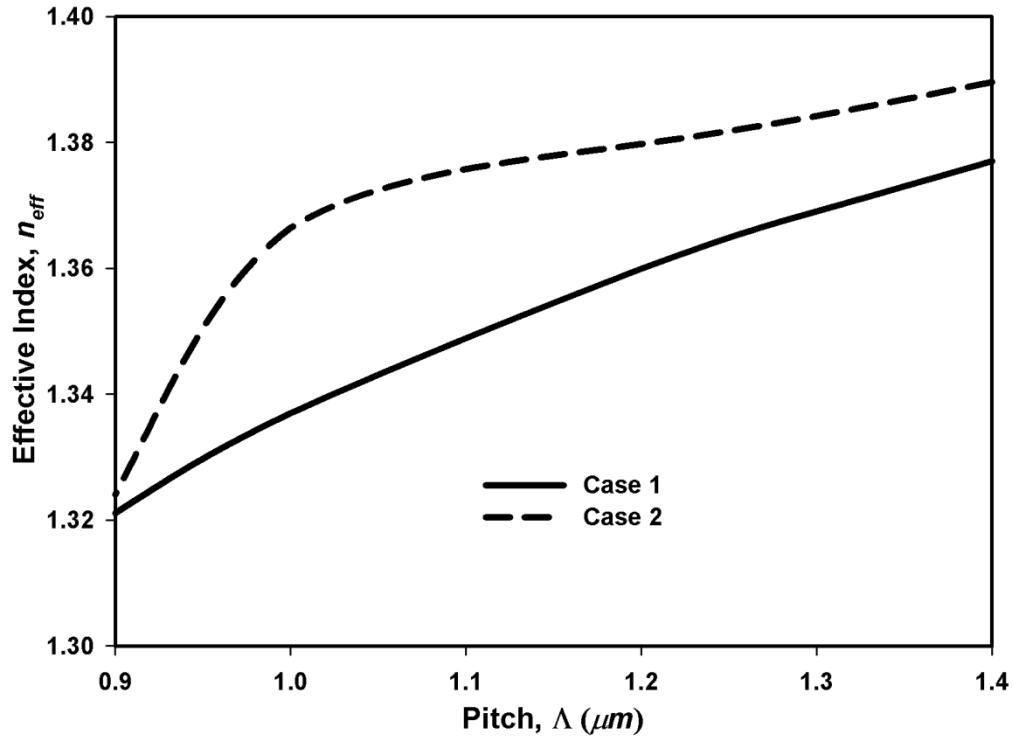
Figure 4.7 Variation of the effective index, $n_{eff}$ with the pitch, $\Lambda$.

In Figure 4.7, the dashed curve represents Case 1 where $d/\Lambda$ values of 0.5, 0.5 and 0.5 are set for the first, second and third rings of air-holes of the hexagonal PCF respectively. Similarly, the solid curve represents Case 2 where $d/\Lambda$ values of 0.5, 0.4 and 0.4 are set for the first, second and third rings of air-holes respectively. It is shown that as the pitch is reduced; the effective index is monotonically reduced. As the pitch is decreased the field which is confined inside the core becomes highly exposed to the air-holes, resulting in a decrease in the effective index. Furthermore, as the pitch is reduced, initially the effective indices of the first order mode of the fundamental frequency, $\omega$ ($H_{11}^x, \omega$), reduces slowly in both cases (i.e. Case 1 and Case 2), but these decrease rapidly as the modes approach their cut-off conditions. Moreover, it can be noted that as the pitch is increased, the effective index asymptotically approaches that of $SiO_2$, i.e. when the majority of the field is confined in the $SiO_2$ core. Further, at a given pitch value the effective index of Case 2 is higher than that of Case 1. This is due to the reduced $d/\Lambda$ values of the second (0.4) and third (0.4) rings of air-holes and the reduced air-filling fraction in the cladding area in Case 2 which results in a higher effective index value. Further, Case 2 reaches its cut-off condition faster than Case 1 due the less confined field as the index contrast (i.e. $\Delta n$) between core and cladding is smaller.

The spot-size ($\sigma$) is a significant modal property of a guided mode in optical waveguides. The rapid expansion of the spot-size in optical waveguides is used to analyse the cut-off condition. Figure 4.8 shows the variation of the spot-size with the pitch for Case 1 where the $d/\Lambda$ values of the first, second and third rings are constant at 0.5.
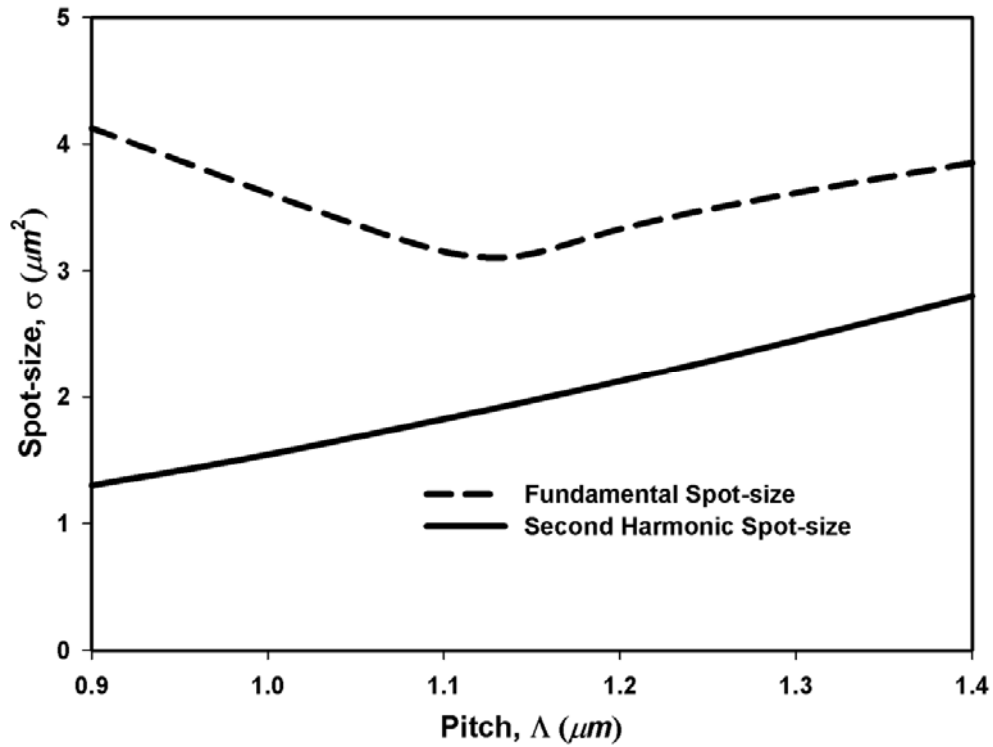


Figure 4.8 Variation of the spot-size ($\sigma$) with the pitch ($\Lambda$).

Here, the spot-size, $\sigma$ is defined as the area where the field intensity is greater than $1/e^2$ of the maximum intensity (i.e. taking the power intensity values as $1/e^2$). In Figure 4.8 it can be clearly seen that as the pitch is reduced the fundamental spot-size ($\sigma_\omega$), i.e. in first order mode of the fundamental frequency ($H_{11}^x, \omega$), shrinks. Further, at lower pitch values the core size reduces and the air-holes become closer to each other, resulting in an increase of the air-filling fraction in the cladding of the hexagonal PCF which prevents the mode spreading into the air-cladding. Therefore, the mode becomes more confined in the smaller core. However, the modal cut-off condition is approached as the pitch is reduced further and then the spot-size expands rapidly. For the second harmonic spot-size ($\sigma_{2\omega}$), i.e. in the first order mode of the second harmonic frequency ($H_{11}^x, 2\omega$) in contrast, the cut-off condition appears at a

much lower pitch value (not shown in Figure 4.8) compared to that of $H_{11}^x, \omega$ due to the stronger confinement of the second harmonic modes.

Variation of the coherence length (i.e. $L_c = \pi/\Delta\beta$ as discussed in Chapter 3) with the pitch is shown in Figure 4.9. In this case the $d/\Lambda$ values of the first, second and third rings are 0.5.
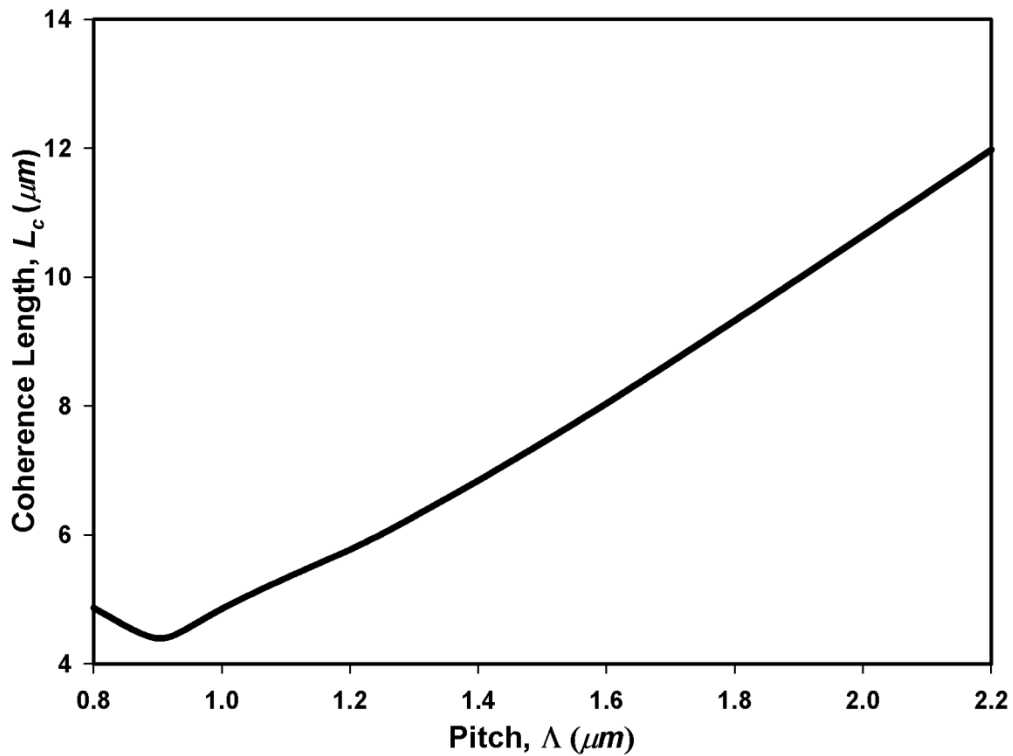


Figure 4.9 Variation of the coherence length, $L_c$ with the pitch, $\Lambda$.

It can be noted that as the pitch is increased the dimensions of the core are also increased. Hence, the $SiO_2$ region expands and $L_c$ asymptotically approaches the value for bulk $SiO_2$ ($\sim39.8\,\mu m$). Furthermore, the effective index ($n_{eff}$) increases due to the increased area of the solid core at the centre. Further, $\beta$ increases along with $n_{eff}$ as $n_{eff} = \beta/k_0$. Therefore, $\beta_\omega$ grows faster than $\beta_{2\omega}$ bringing $2\beta_\omega$ close to $\beta_{2\omega}$ (as $2\beta_\omega \approx \beta_{2\omega}$) which results in higher $L_c$. It can be observed in Figure 4.9 that higher pitch values lead to higher $L_c$ values. However, when the pitch increases the modes in the PCF become multi-mode reducing the power density due to the increased core size.

### 4.4.3 Hexagonal PCF with defect air-hole

By introducing the air hole at the centre it would be possible to lower the propagation constant of the mode. Because the field profile of SHG is smaller than the fundamental wavelength the effective index of the SHG wavelength should be affected more in this case. This could improve the coherence length. The results of SHG of defect-core PCF is discussed in this section. Figure 4.10 shows the numerical model of a hexagonal PCF with a defect air-hole at the centre of the $SiO_2$ core.
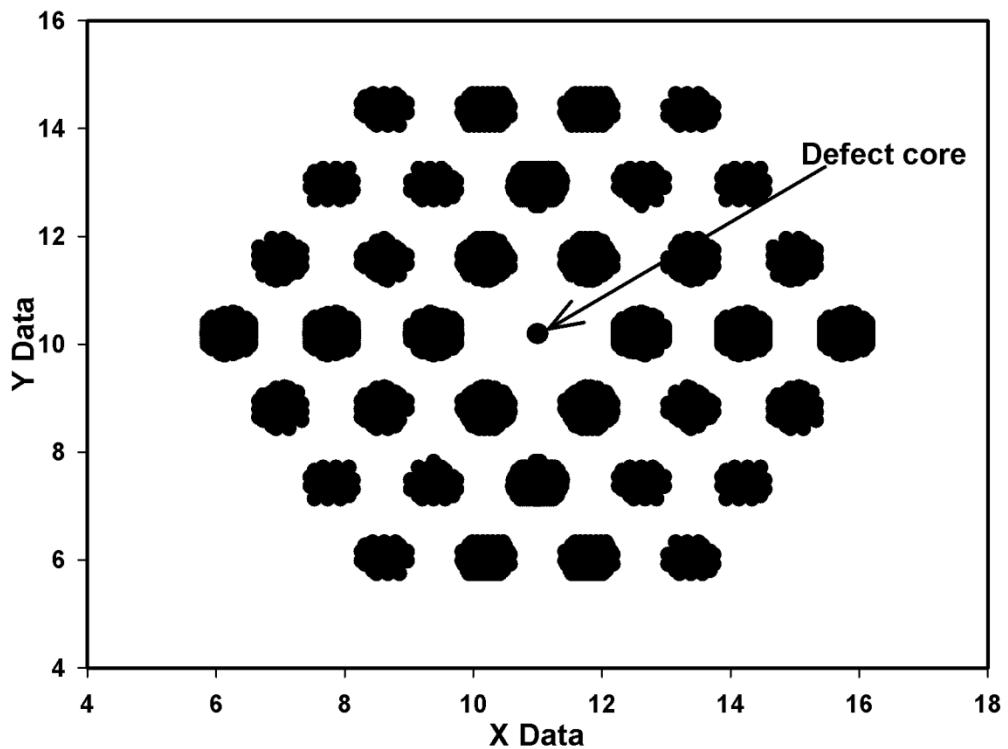


Figure 4.10 Hexagonal PCF structure with a defect air-hole.

Figure 4.11 and Figure 4.12 present the variation of the effective index and coherence length results, respectively, for a defect-core hexagonal PCF with the $d/\Lambda$ values of the first, second and third rings set to 0.5, while the operating wavelength is 1.55 $\mu m$. Figure 4.11 shows the $n_{eff}$ variation with the $\Lambda$ for different centre hole radii. The comparison for with and without centre hole are also discussed.
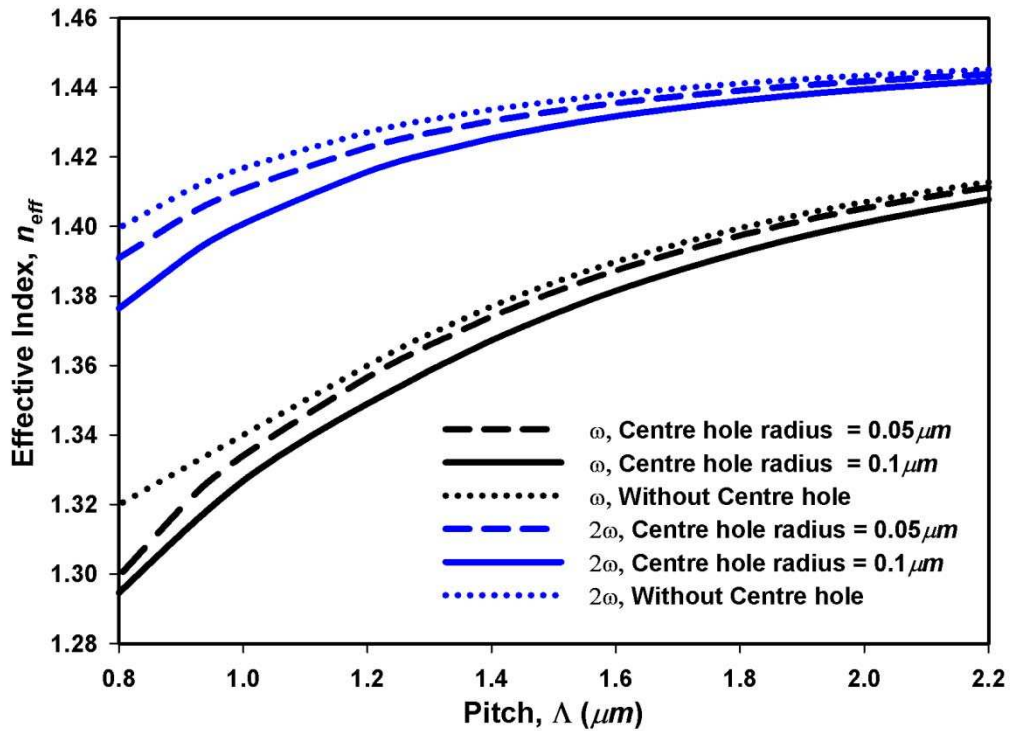
Figure 4.11 Variation of the effective index ($n_{eff}$) with the pitch ($\Lambda$).

The effective indices of the modes reduce with respect to the pitch as explained in Figure 4.7. It can be noted that the effective index at a particular pitch reduces when the radius of the defect air-hole increases. This is due to the fact that the peak intensity of the modal field profile overlaps with the defect air-hole. Further, for the fundamental frequency, $n_{eff}$ reaches the cut-off condition faster than in the case of the second harmonic frequency because of less confinement of the mode in the core. At a given pitch, when the radius of the defect-core increases for both fundamental and second harmonic frequencies, the mode tends to push into the air-cladding region decreasing $n_{eff}$. This is due to the lower refractive index at the core of the PCF.
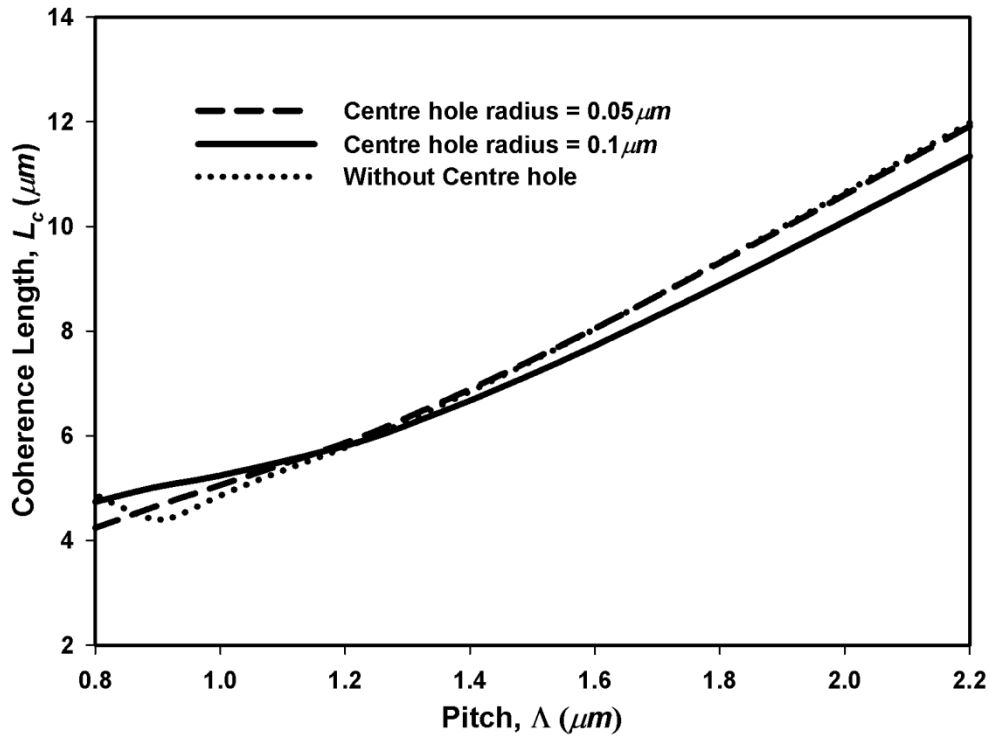
Figure 4.12 Variation of the coherence length, ($L_c$) with the pitch (Λ).

The coherence length variation with the pitch for different defect-core radii is shown in Figure 4.12. It can be observed that at a given pitch, when the defect-core radius is increased (i.e. from 0 to 0.1 $\mu m$) the $L_c$ goes down due to the increased $n_{eff}$ difference between fundamental and second harmonic modes (as shown in Figure 4.11). However, at lower pitch values it can be seen that $L_c$ becomes lightly higher for the defect core structure. Furthermore, higher defect core radii lead to lower overlap integral values, resulting in less power confinement in the hexagonal PCF core and reduced SH output power. This is due to the lower refractive index in the core region. Moreover, as the pitch reduces the solid curve (0.1 $\mu m$) reaches its cut-off condition faster than in the case of the dotted curve (i.e. without a defect-core) because, as the defect-core expands the mode is more exposed into the air-cladding and the $n_{eff}$ difference between fundamental and second harmonic becomes more significant.

### 4.4.4   *Hexagonal PCF with soft glass SF57*

In this section the hexagonal PCF with soft glass *SF*57 is presented in Figure 4.13 and Figure 4.14 at the operating wavelength of 1.064 $\mu m$ (i.e. fundamental wavelength) with the refractive index value of 1.81173. *SF*57 material has unique

properties which will be discussed in Section 4.5.1. Further, the results are obtained for three different cases where Case 1 has $d/\Lambda$ values of the first, second and third rings as 0.4, Case 2 has $d/\Lambda$ values of the first, second and third rings as 0.5 and Case 3 has $d/\Lambda$ values of the first, second and third rings as 0.9.
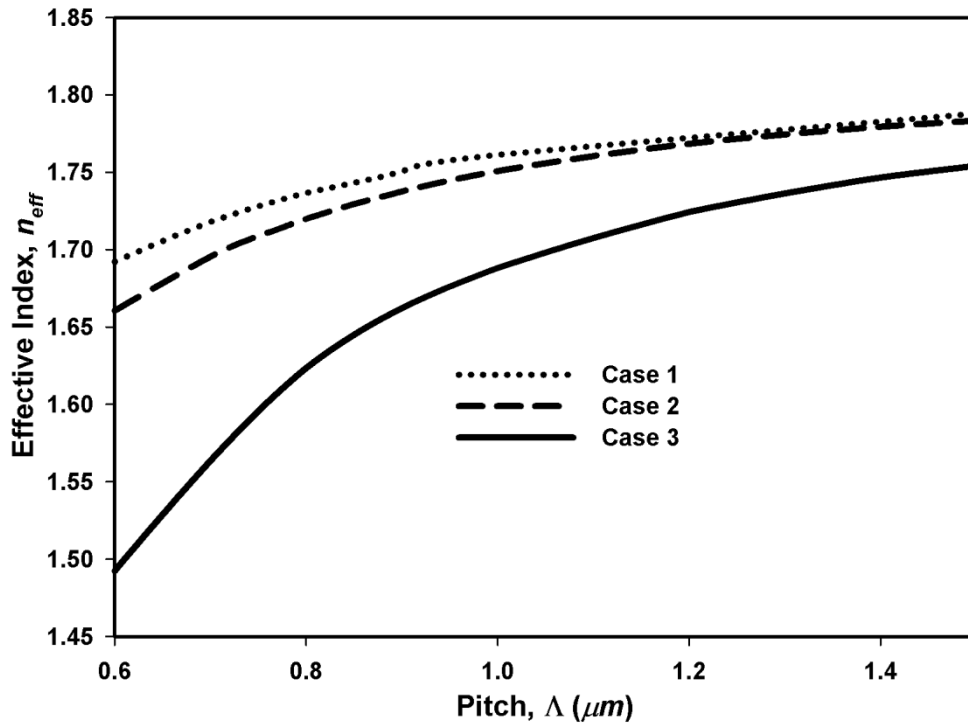


Figure 4.13 Variation of the effective index ($n_{eff}$) with the pitch ($\Lambda$).

Similar to the silica PCF case as discussed in Figure 4.7, when the pitch is reduced $n_{eff}$ also reduces. Furthermore, at a given pitch value as the $d/\Lambda$ value decreases, $n_{eff}$ is increased. It can be noted that as the pitch goes up, $n_{eff}$ asymptotically approaches the effective index of $SF57$ material due to the increased material region. Further, the refractive index for $SF57$ is higher than that of $SiO_2$. Hence, the mode confinement in $SF57$ PCF is higher than that of $SiO_2$ PCF.

Figure 4.14 shows the variation of the spot-size with the pitch for the three aforementioned cases.
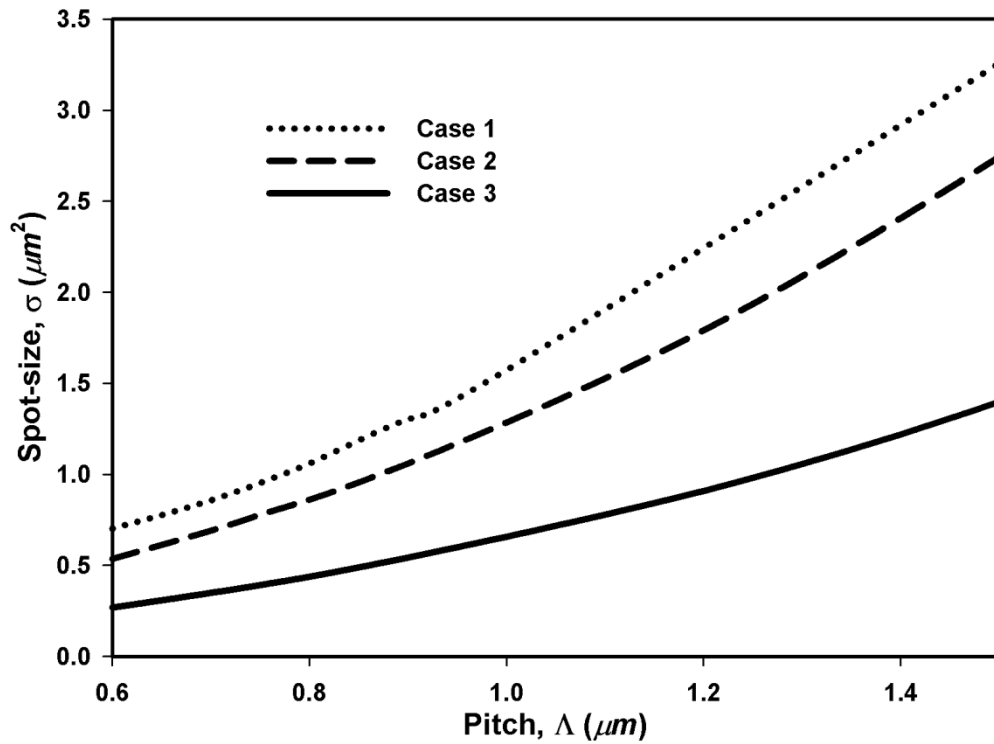
Figure 4.14 Variation of the spot-size ($\sigma$) with the pitch ($\Lambda$).

It can be observed that, when the pitch decreases the spot-size also decreases due to the reduction of core size of the hexagonal PCF. Further, at a given pitch value the spot-size shrinks as the $d/\Lambda$ value increases, which can be explained as follows. The higher the $d/\Lambda$, the higher size of the air-holes in the cladding region. Hence, the refractive index difference between core and the cladding becomes significant for the higher $d/\Lambda$ values, resulting in a tighter mode in the core region.

Different PCF structures can improve the power conversion efficiency by enhancing the overlap integral between the fundamental and second harmonic modes, which is a result of unique air-hole orientation of the PCF structure. Accordingly, a different PCF structure is presented in the next section.

## 4.5   EQUIANGULAR SPIRAL PCF

An appropriate design of the microstructure of air-holes allows significant flexibility in tailoring the modal and dispersion properties of a PCF, for example, in achieving small mode area (for high non-linearity), flat dispersion, lower bending loss and the ability to optimise performance over more than one parameter simultaneously. Recently, A. Agrawal *et al.* have numerically modelled a PCF with equiangular

spirals (or logarithmic spirals) called Equiangular Spiral Photonic Crystal Fibres (ES-PCF). ES-PCF provides several design parameters by which the modal properties as well as the dispersion can be controlled more easily [161]. The ES-PCF provides better confinement of the fundamental mode in the core area compared to conventional PCF. For a given material, ES-PCF achieves better overlap between the optical fields of the fundamental mode at the frequencies of interest (i.e. of the pump and second harmonic) than in conventional PCF. Hence an ES-PCF is an excellent choice for nonlinear applications such as SHG, Four Wave Mixing (FWM) and Supercontinuum Generation.

Section 4.5.1 details the choice of material used while Section 4.5.2 provides a description of the ES-PCF structure considered. Section 4.6 presents detailed results as follows: Section 4.6.1 discusses the effective indices, effective area and overlap integral of the fundamental and second harmonic modes; Section 4.6.2 contains results and discussion on the coherence length and quasi-phase matching; Section 4.6.3 discusses the error tolerance in the coherence length and Section 4.6.4 discusses the power comparison between ES-PCF and PCF for fundamental and second harmonic frequencies.

### 4.5.1 *Choice of Material for ES-PCF*

Traditionally, Silica has been the material of choice for the fabrication of PCF due to its superior optical and material properties. However, the inversion symmetry of the Silica glass implies that its second order nonlinear susceptibility ($\chi^{(2)}$) is zero. So far, various thermal poling techniques have been implemented to overcome this problem [162-165] which can bring the second order susceptibility of Silica glass to $d_{33} \sim 0.22\ pm/V$ [132]. Alternatively, commercially available lead Silicate glass (also called soft glass) of type $SF57$ (manufactured by Schott) can achieve a much higher second order susceptibility tensor value (of $d_{33} \sim 0.35\ pm/V$) when the electron-beam irradiation technique is applied (i.e. Note that electron-beam irradiation cannot be applied to pure Silica) [135, 166]. Therefore, $SF57$ which is the earliest available single mode non-Silica glass PCF is a promising candidate material for SHG. Further, $SF57$-based PCF has been reported to have the highest nonlinearity in optical fibres ($640\ W^{-1}km^{-1}$) [167]. Also, challenging structures such as nano-wires have been fabricated using $SF57$ glass [168]. This glass also

possesses a higher thermal expansion coefficient ($9.2 \times 10^{-6}\ K^{-1}$ [169]) compared to that of Silica ($\sim 5 \times 10^{-7}\ K^{-1}$ [170]) which may allow for higher flexibility in adjusting the coherence length of the fibre.

### 4.5.2   Numerical Modelling of ES-PCF

The structure of the Equiangular Spiral Photonics Crystal Fibre (ES-PCF) is shown in Figure 4.15. The air-hole arrangement of the ES-PCF structure mimics the "spira mirabilis" (Equiangular Spiral) which is seen in nature in nautilus shells and sunflower heads [161]. This ES pattern of the sunflower head produces the most efficient packing of seeds within the flower head without altering the angle or the shape of the curve and thus the air-holes in the ES-PCF are arranged in a similar pattern.
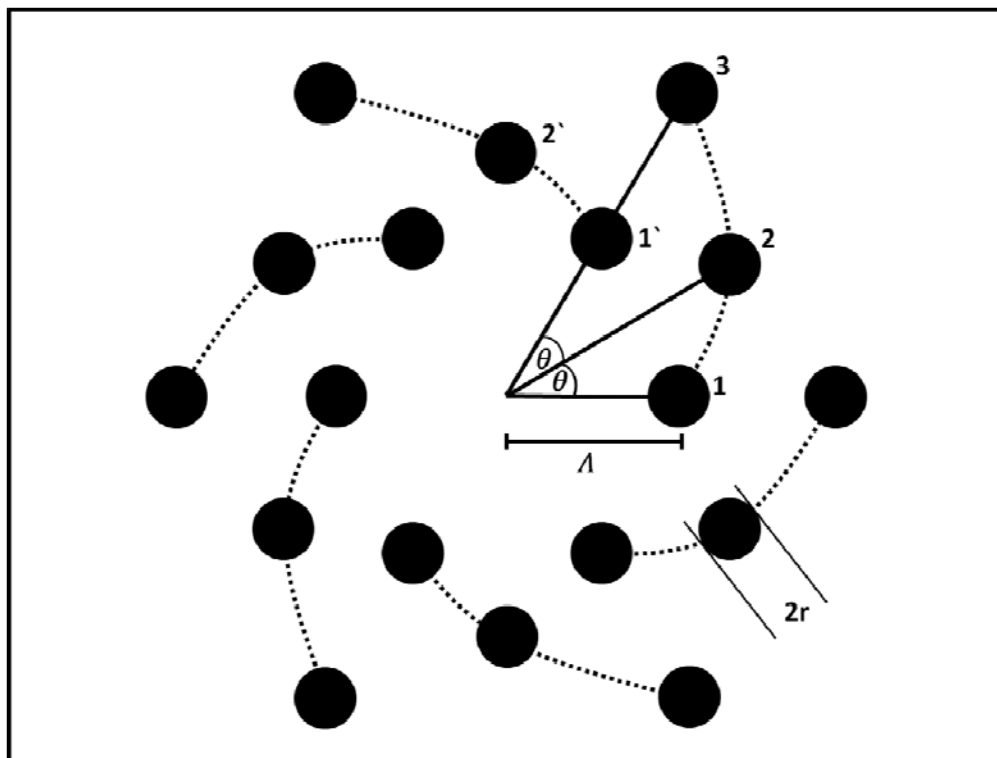


Figure 4.15 Structure of the Equiangular Spiral-Photonic Crystal Fibre.

In the ES-PCF, each arm of air-holes forms a single ES where the angle from the centre of the core to adjacent holes of a given arm or ES differs by $\theta$ (e.g. the angular increment from hole 1 to hole 2 is $\theta$ and hole 2 to hole 3 is also $\theta$ ). The diameter ($d$) of each air-hole is fixed at $2r$ where $r$ is the air-hole radius. It should be noted that

the equivalent holes of each arm can be considered to form a ring, e.g. the first holes of all the arms form the first ring and the second holes of all the arms form the second ring and so on. The radius ($\Lambda$) of the ES-PCF is defined as the distance between the centre of the core and the centre of an air-hole in the first ring. The radii drawn to the centre of air-holes on subsequent rings of the same ES, i.e. at intervals of $\theta$, form a geometric progression. The distance between the air-holes within a ring increases with the ring number (e.g. the distance between holes 2 and 2' is larger than the distance between holes 1 and 1').

The main advantage of the ES-PCF is the improved field confinement in comparison to that of conventional PCF. This is due to the hole-orientation of the ES-PCF, where the outer air-holes block the field escaping through the material (i.e. inter-hole region) of the previous ring.

## 4.6   SIMULATION RESULTS FOR ES-PCF

The results presented in this section show that the SH output power of $SF57$ ES-PCF is considerably higher than that of conventional PCF, e.g. $\sim 2.1W$ in ES-PCF as opposed to $\sim 1.6W$ in conventional PCF after the propagation of $250\mu m$ with a fundamental pump power of $1kW$ (continuous wave), operating fundamental wavelength of $1.064\ \mu m$, corresponding second harmonic wavelength of $0.532\ \mu m$, $d/\Lambda = 0.5$ and $\Lambda = 1.0\ \mu m$, while the ES-PCF design consisted of 6 arms, 4 rings and $\theta = 30^0$. The ES-PCF structure with air-holes arranged in a spiral lattice in the cladding is represented in the simulation by an irregular mesh of 28800 triangular elements. Further, the results in this section are obtained by using the scalar BPM.

### 4.6.1   *Modal Properties and SHG in the ES-PCF*

The variation of the effective index $n_{eff}$ with pitch ($\Lambda$) has been studied for the first order mode at the two frequencies $\omega$ and $2\omega$ which is shown in Figure 4.16. The dispersion properties of $SF57$ have been considered by using the refractive indices for $SF57$ and the Sellmeier coefficients of $SF57$ [169]. Here, $n_{eff} = \beta/k_0$ where $\beta$ is the propagation constant and $k_0$ is the wavenumber ($k_0 = 2\pi/\lambda$ where $\lambda$ denotes the

wavelength). The first order mode $H_{11}^x$ of the fundamental frequency $\omega$ is indicated by $H_{11}^x, \omega$.
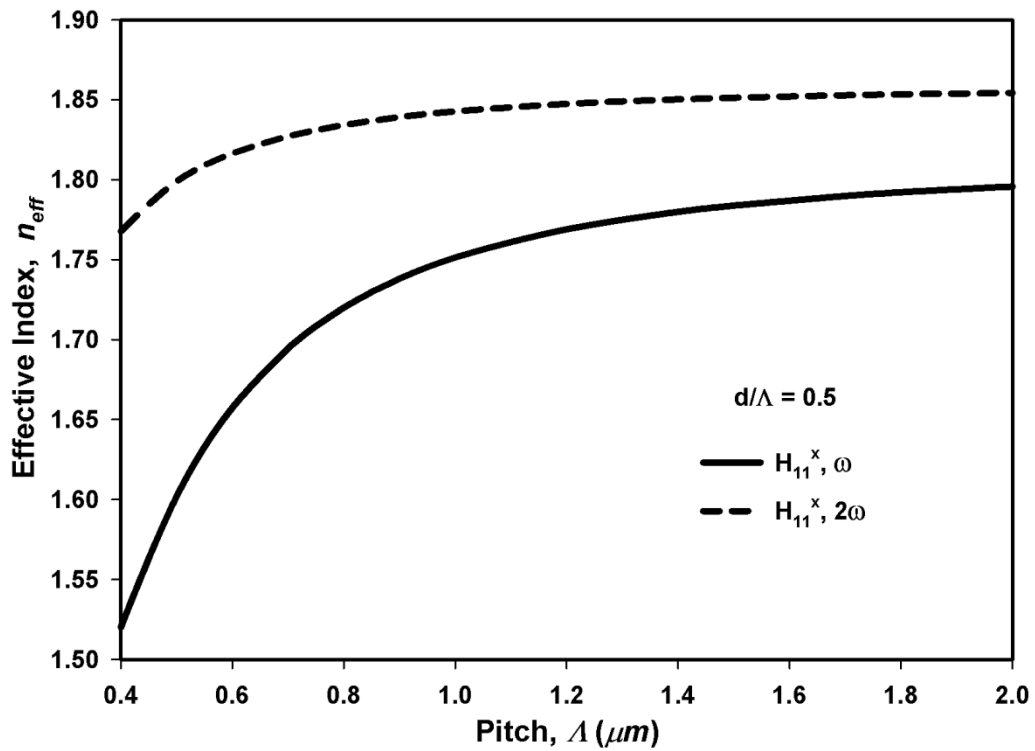


Figure 4.16 Variation of the effective index with the pitch for the first order mode at $\omega$ and $2\omega$.

As can be seen in Figure 4.16, a reduction of the pitch results in a reduction of $n_{eff}$ as the confined mode gets exposed to the first ring of air-holes. Initially the effective indices of the modes reduce slowly, but these decrease rapidly as the modes approach their cut-off conditions. Moreover the effective index of $H_{11}^x, 2\omega$ (i.e. $H_{11}^x$ mode of the second harmonic frequency) is shown to move towards the cut-off condition at a lower rate than of $H_{11}^x, \omega$. This is because the first order mode of the higher frequency (i.e. of second harmonic) is more confined in the centre than that of the lower frequency. Furthermore, as the pitch is increased, the mode becomes more confined to the core, resulting in $n_{eff}$ asymptotically approaching the refractive index of $SF57$ (i.e. $n_\omega = 1.81173$ and $n_{2\omega} = 1.85841$).

The mode size, or its effective area ($A_{eff}$), is an important modal parameter which can be used to evaluate the overlap integral of the pump and the second harmonic modes. The definition of $A_{eff}$ is given by [171];

$$A_{eff} = \frac{\left(\iint_s |E_t|^2 \, dxdy\right)^2}{\left(\iint_s |E_t|^4 \, dxdy\right)} \tag{4.1}$$

where $E_t$ represents the transverse electric field vectors and $S$ represents a cross-section of the fibre. Figure 4.17 shows the variation of the effective area with the pitch for the dominant and higher order modes at $\omega$ and $2\omega$.
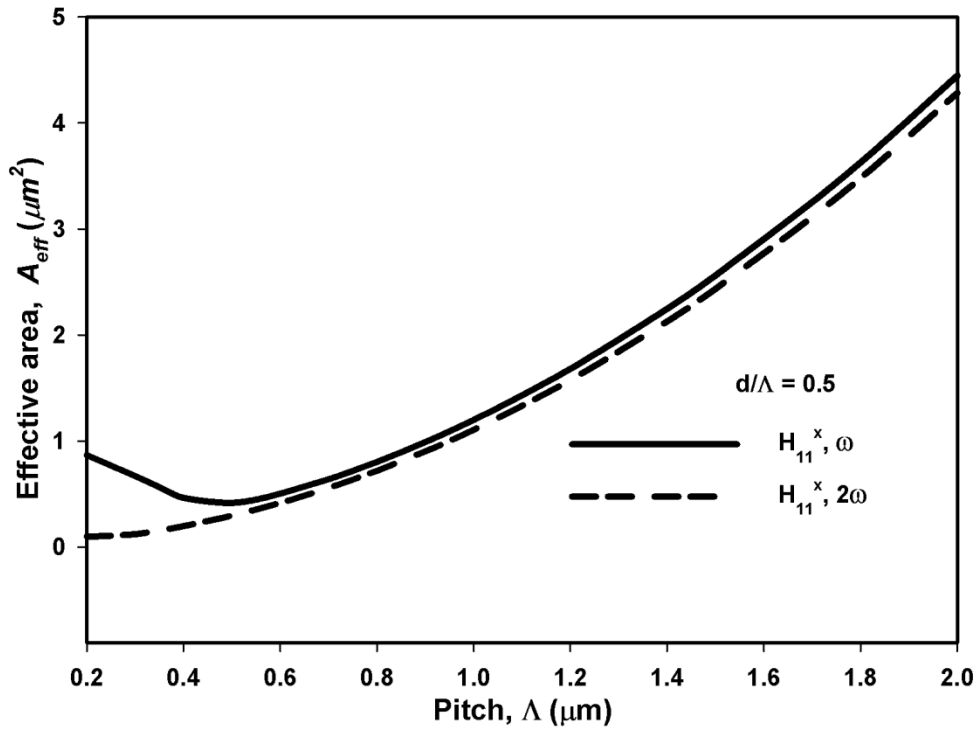


Figure 4.17 Variation of the effective area with the pitch for the first order mode at $\omega$ and $2\omega$.

For a given pitch the fundamental wavelength ($1.064 \, \mu m$) has higher $A_{eff}$ than that of the second harmonic wavelength ($0.532 \, \mu m$) which can be seen by comparing the $H_{11}^x, \omega$ curve with the respective second harmonic case $H_{11}^x, 2\omega$. For all the modes, it can be observed that $A_{eff}$ goes down as the pitch $\Lambda$ is reduced. However when the pitch falls below a certain value, $A_{eff}$ starts to increase slowly due to reaching the cut-off condition. The cut-off value of $\Lambda$ is $\sim 0.5 \, \mu m$ for the first order mode of the fundamental frequency. Further, due to the high confinement of the second harmonic mode (i.e. $H_{11}^x, 2\omega$), the effective area approach the cut-off region at lower pitch values (not shown here) compared to the fundamental mode (i.e. $H_{11}^x, \omega$). The

relationship between the effective area of fundamental and second harmonic modes is used as a guideline for design optimisation.

The overlap integral ($\Gamma$) between the interacting fundamental and second harmonic first order modes ($H_{11}^x$) directly relates to the efficiency of power transfer between these modes, i.e. a higher value of the overlap integral results in a higher conversion efficiency and vice versa [32]. The definition of the overlap integral is given by;

$$\Gamma = \frac{|\iint E_\omega^2 \cdot E_{2\omega} \cdot dx \cdot dy|}{(\iint E_\omega^2 \cdot dx \cdot dy) \cdot (\iint E_{2\omega}^2 \cdot dx \cdot dy)^{\frac{1}{2}}} \tag{4.2}$$

where $E_\omega$ and $E_{2\omega}$ are the electric field distribution of the fundamental and second harmonic waves respectively [172]. Figure 4.18 illustrates how the overlap integral of the first order modes $H_{11}^x$ for $\omega$ and $2\omega$ vary with the pitch ($\Lambda$) for three different $d/\Lambda$ values.
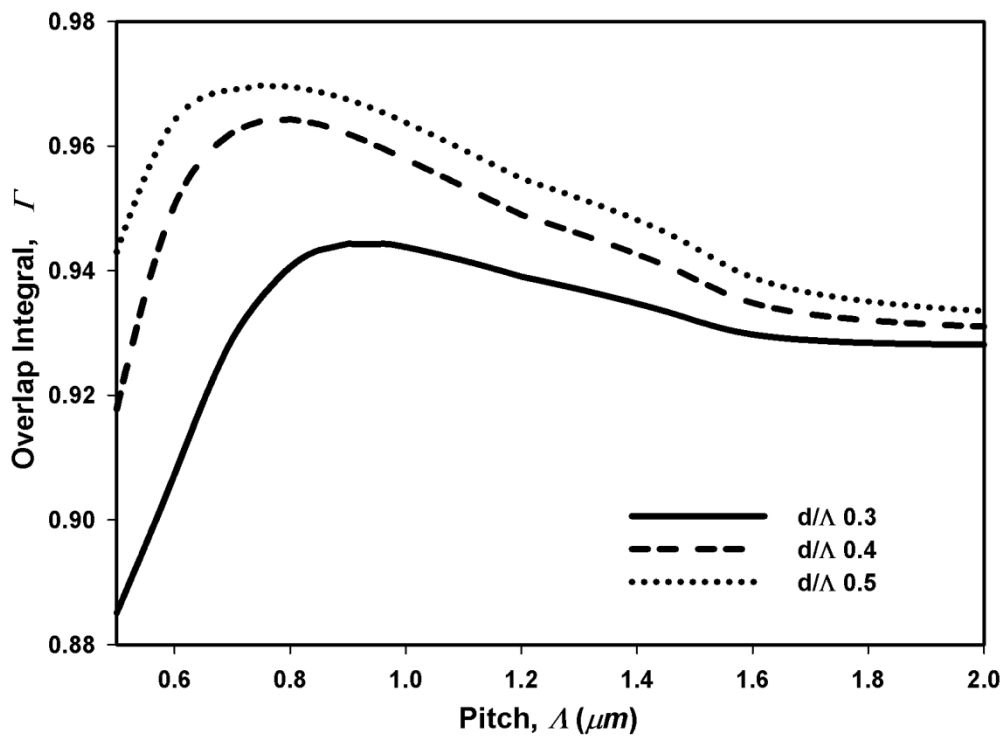


Figure 4.18 Variation of the overlap integral ($\Gamma$) with the pitch ($\Lambda$).

For a given pitch, the overlap integral increases as $d/\Lambda$ increases. This arises because, as $d$ increases, the equivalent index of the cladding decreases, increasing the index contrast between core and cladding, which in turn increases the confinement of the mode in the ES-PCF. Further, as the pitch decreases for a given

value of $d/\Lambda$ , the overlap integral increases reaching a maximum value (in the region $0.7\,\mu m\,\leq\,\Lambda\,\leq 1\,\mu m$) then starts to decrease: this can be explained as follows. Reducing the pitch makes $H_{11}^{x},\omega$ and $H_{11}^{x},2\omega$ more confined which reduces the mismatch of their effective areas leading to an increase in the overlap integral. However, at very small pitch values the fundamental field reaches its cut-off region faster than the second harmonic field. Therefore, even though the second harmonic field becomes more confined to the core, the mismatch between fundamental and second harmonic fields becomes significant and the overlap integral starts to reduce at very small $\Lambda$ values.

The overlap integral ($\Gamma$) and the Second Harmonic susceptibility tensor values ($d_{ij}$) are key parameters in determining the rate of power conversion. High SH power can be gained by $d_{ij}$ values which are material properties; indeed the $d_{ij}$ values of $SF57$ (i.e. $d_{33}\sim 0.35\,pm/V$) are high in comparison with that of Silica (i.e. $d_{33}\sim 0.22\,pm/V$). On the other hand, the overlap between the interacting modes depends on the fibre design. When the fundamental and second harmonic waves are not phase matched, the second harmonic power increases until the waves are out of phase and the SH power starts depleting.

Figure 4.19 shows the variation of the maximum output power ($P_{Lc}$) with the pitch ($\Lambda$), for different $d/\Lambda$ values, where $P_{Lc}$ is the power after the propagation of one coherence length ($L_c$). This value is obtained by FE-BPM which takes into account all factors including phase matching.
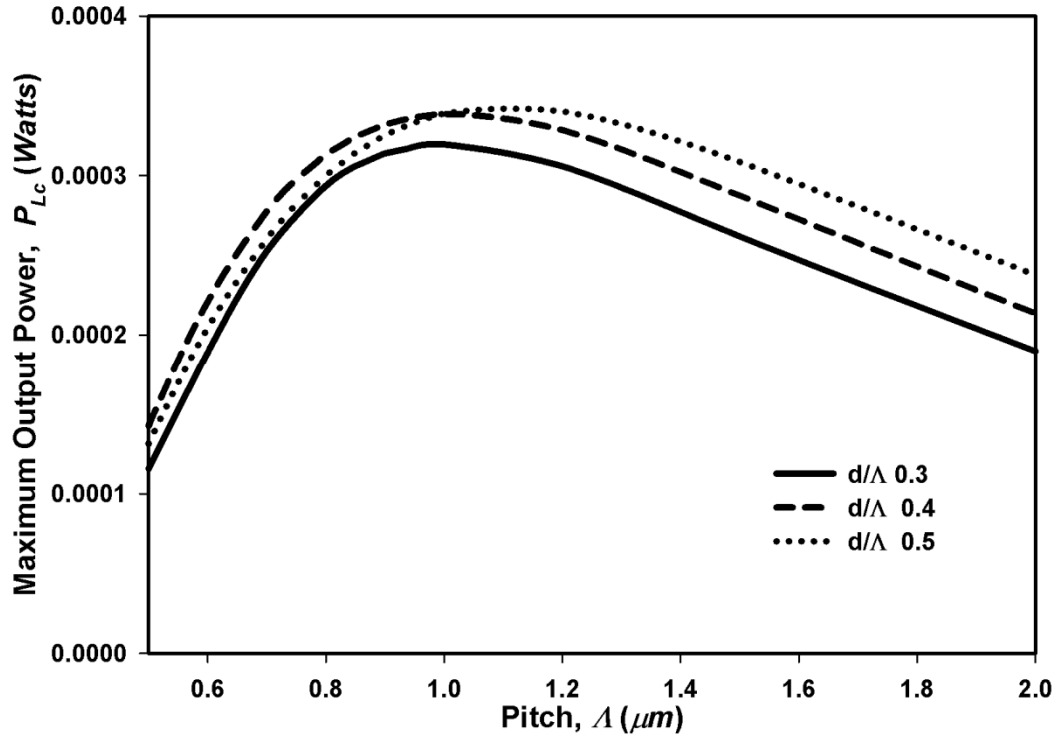
Figure 4.19 Variation of the maximum SH output power ($P_{Lc}$) with the pitch ($\Lambda$).

It can be observed that a higher $d/\Lambda$ value yields a higher value of $P_{Lc}$: this is because as $d/\Lambda$ increases, the fraction of air increases in the ES-PCF, and the power intensity is more confined in the core. Even though the decreasing of the pitch causes the power to be further confined into the core, once it reaches its threshold, the power spreads into the air region and dissipates, reducing $P_{Lc}$ and hence creating the peak values (in the region $0.9\,\mu m \leq \Lambda \leq 1.1\,\mu m$). Further, since the air filling fraction is higher for larger $d/\Lambda$ values (e.g. $d/\Lambda = 0.5$), the cut-off region is reached faster than in the case of lower $d/\Lambda$ values (e.g. $d/\Lambda = 0.3$).

### 4.6.2 Coherence Length and Quasi Phase Matching

The variation of $L_c$ with respect to the pitch is plotted in Figure 4.20.
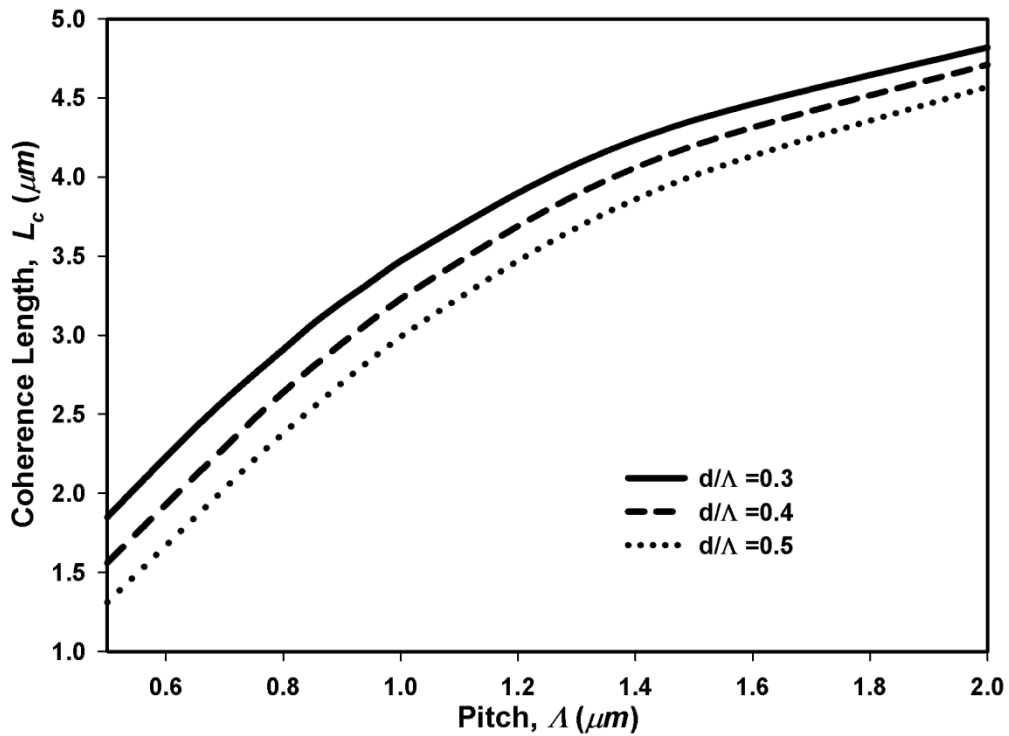


Figure 4.20 Variation of the coherence length ($L_c$) with the pitch ($\Lambda$).

As $d/\Lambda$ decreases for a given pitch ($\Lambda$), the effective index ($n_{eff}$) increases due to the increased area of the solid $SF57$ bridges between the air-holes: this results in an increase of $L_c$. Moreover, as the pitch is increased, the $SF57$ area is further increased and $L_c$ asymptotically approaches the value for bulk $SF57$ ($\sim 5.69\,\mu m$). As the effective index increases, the propagation constant ($\beta$) also increases. As seen in Figure 4.16, for higher $\Lambda$ values, $\beta_\omega$ increases faster than $\beta_{2\omega}$ bringing $2\beta_\omega$ close to $\beta_{2\omega}$ (i.e. $2\beta_\omega \approx \beta_{2\omega}$) which results in a higher value of $L_c$. Further, the ideal condition occurs when $n^\omega = n^{2\omega}$ (where $n^\omega$ and $n^{2\omega}$ are the fundamental and second harmonic refractive indices respectively) which cannot be realised in practice due to the chromatic dispersion of the material.

The most rapid growth of the second harmonic output power can be achieved by changing the sign of $\chi^{(2)}$ for every $L_c$ (which is known as first order QPM) as shown in Figure 4.21 (for $d/\Lambda = 0.5$ and $\Lambda = 1.0\,\mu m$).
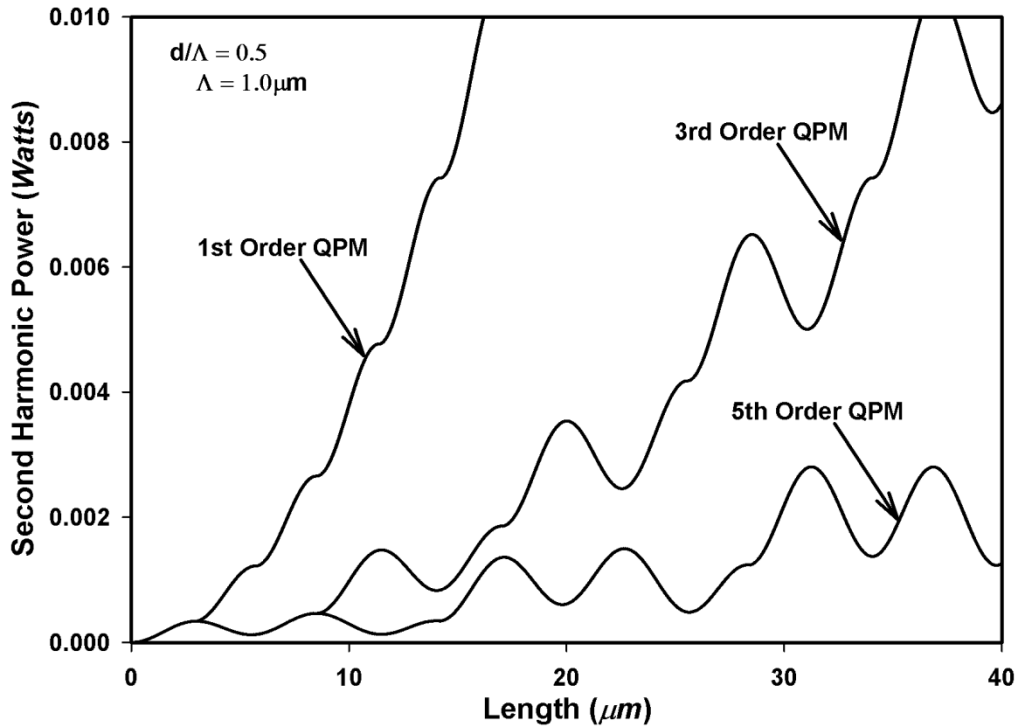
Figure 4.21 Generated Second Harmonic power with first, third and fifth order Quasi Phase Matching.

The QPM for the first, third and fifth order modulations are shown in Figure 4.21 where $L_c \approx 2.9\ \mu m$, $d/\Lambda = 0.5$ and $\Lambda = 1.0\ \mu m$. Note that even though higher order QPMs need a longer propagation distance to reach a given level of SH output power, higher order QPMs make the fabrication process easier especially in the case of short coherence lengths.

### 4.6.3   Error Tolerance in Quasi Phase Matching

During the fabrication process, an error denoted by $\Delta L_c$ can occur, which is defined as the difference between the desired coherence length and the actual coherence length achieved after the fabrication. Assuming that the fundamental frequency propagates through $N$ periodically poled regions, and the second harmonic output power builds up along the length of the ES-PCF, the accumulated error in length after propagating a distance $NL_c$ is given by $N\Delta L_c$. After a distance of propagation during which the accumulated length error becomes equal to the coherence length, the phase mismatch is equal to $\pi$ and the power starts to reduce [173]. This behaviour can be observed in Figure 4.22 and Figure 4.23 for the first order and the fifth order QPM respectively.
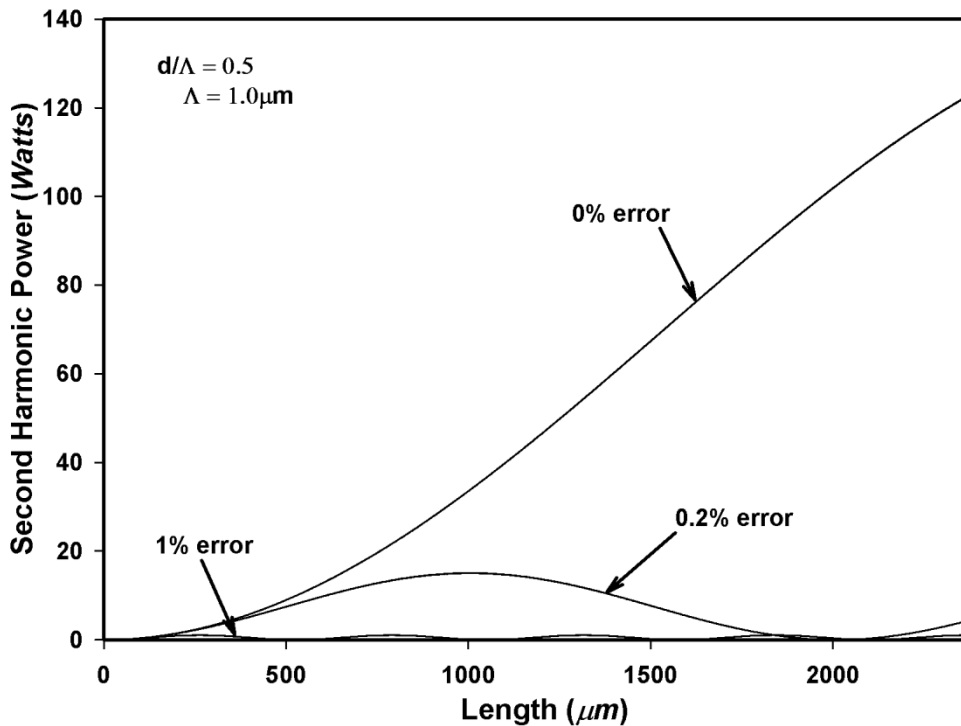
Figure 4.22 Effect of fabrication tolerance on Second Harmonic output power with first order Quasi Phase Matching.
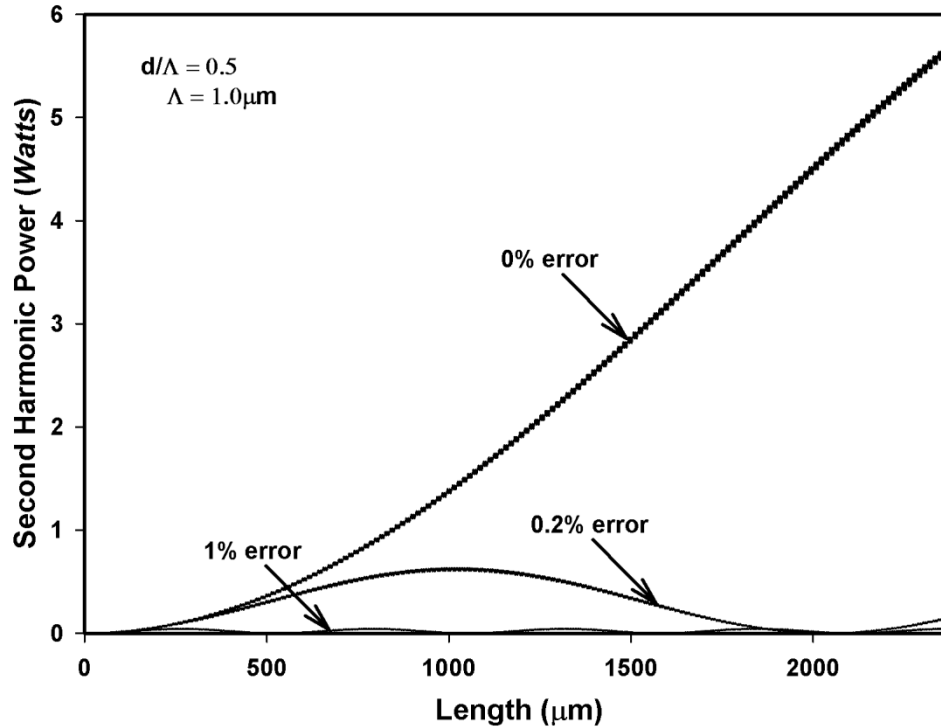
Figure 4.23 Effect of fabrication tolerance on Second Harmonic output power with fifth order Quasi Phase Matching.

It can be seen that with the first order QPM, the maximum SH output power for the 0% error case (i.e. no fabrication error) reaches a value of $\sim120W$ (and $\sim5.6W$ with fifth order QPM) over a distance of $\sim2350\,\mu m$ while a 0.2% error reduces the maximum power to $\sim15W$ (and $\sim0.7W$ with fifth order QPM) for the same distance. Therefore, once a reasonable coherence length is achieved by using poling techniques, it is important to fine-tune $L_c$ by employing techniques such as temperature tuning of the period [174] or strained period of a long period grating [175] in order to minimise the error.

### 4.6.4   *Second Harmonic Power Comparison*

Figure 4.24 (a) and Figure 4.24(b) show the second harmonic mode profile for silica hexagonal PCF after propagating 100 steps and 25000 steps respectively. As can be seen in Figure 4.24 (a), after 100 steps the SH mode magnitude is low (magnitude of $8 \times 10^{-4} A/m^{-1}$ and the SH output power of $\sim4.6 \times 10^{-5}\,W$); however, after propagation of 25000 steps (magnitude of $0.09\,A/m^{-1}$ and the SH output power of $\sim0.65\,W$) the mode magnitude becomes high due to the power transfer from the

fundamental field. Hence, the fundamental mode becomes depleted: this is not shown as the pump depletion is not significant.
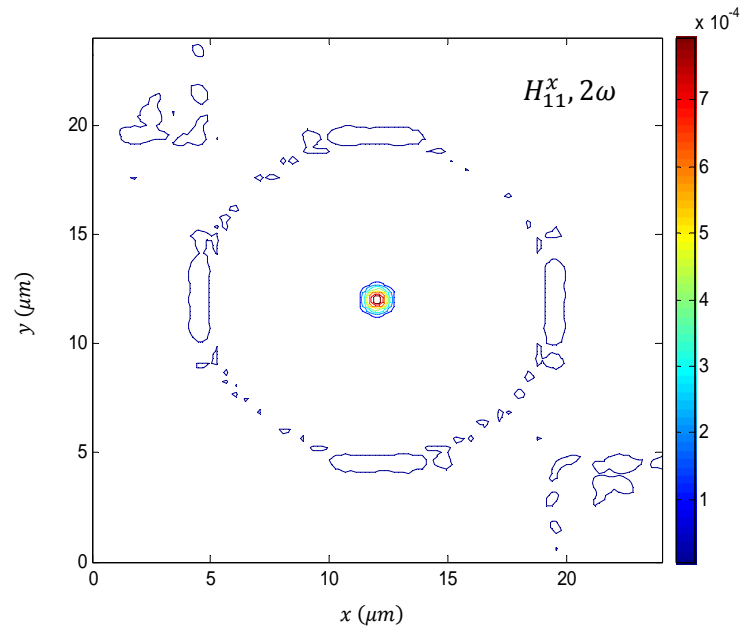


(a)
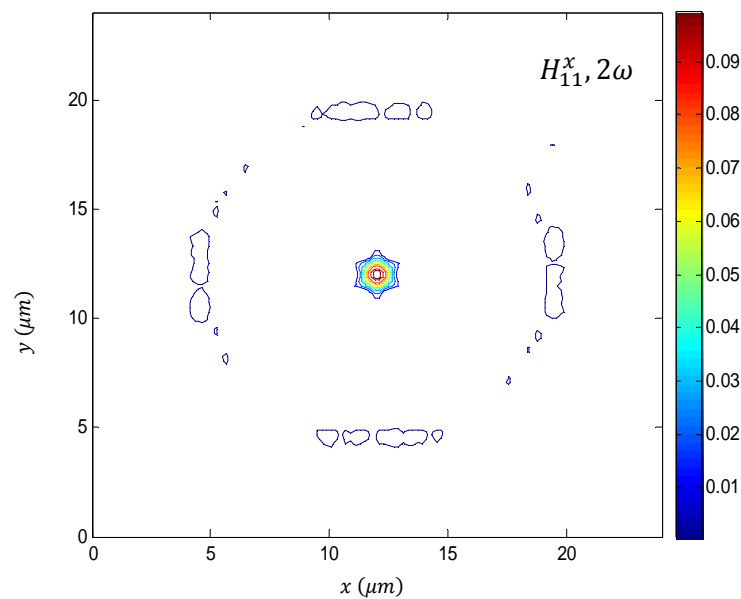


(b)

Figure 4.24 Second Harmonic mode profile for silica hexagonal PCF after (a) 100 steps, (b) 25000 steps.

Figure 4.25 shows the mode profiles for the second harmonic frequency in *SF*57 ES-PCF. The mode profiles behave in a similar manner to the case of silica hexagonal PCF for the same reasons explained above. However, the mode magnitudes in both

cases, i.e. fundamental (not shown here for the same reasons as above) and second harmonic, are significantly higher (magnitude of $0.14\,A/m^{-1}$ and the SH output power of $\sim 3.5\,W$) in $SF57$ ES-PCF after propagation of 25000 steps due to its unique structure and material.



(a)



(b)
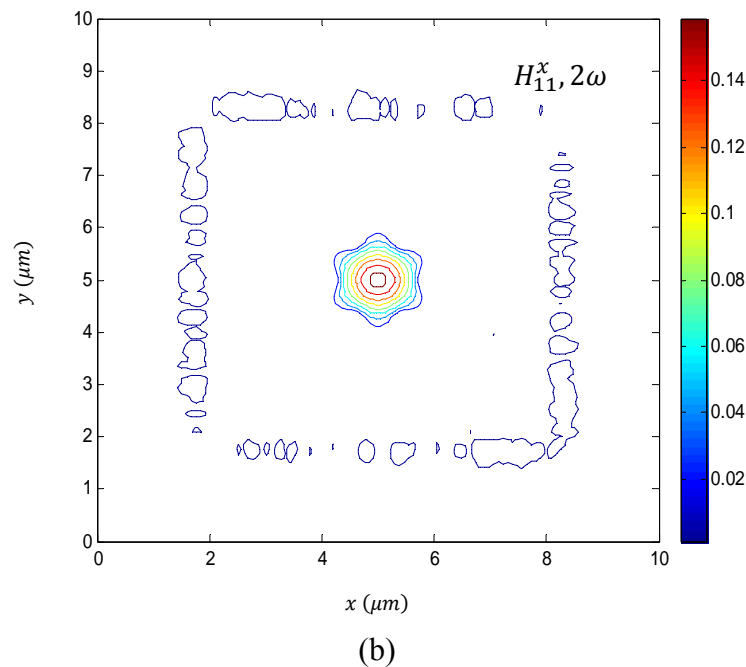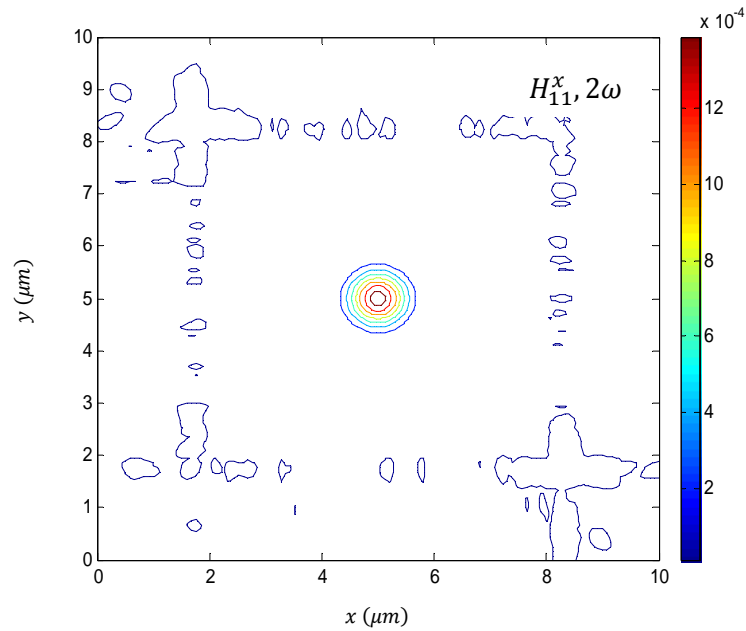
Figure 4.25 Second Harmonic mode profile for SF57 ES-PCF (a) after 100 steps, (b) 25000 steps.

Figure 4.26 shows the first order QPM SH output power for ES-PCF (*SF*57) and PCF (Silica and *SF*57) with varied numbers of air-holes. In all the cases $d/\Lambda = 0.5$ and $\Lambda = 1.0\ \mu m$.
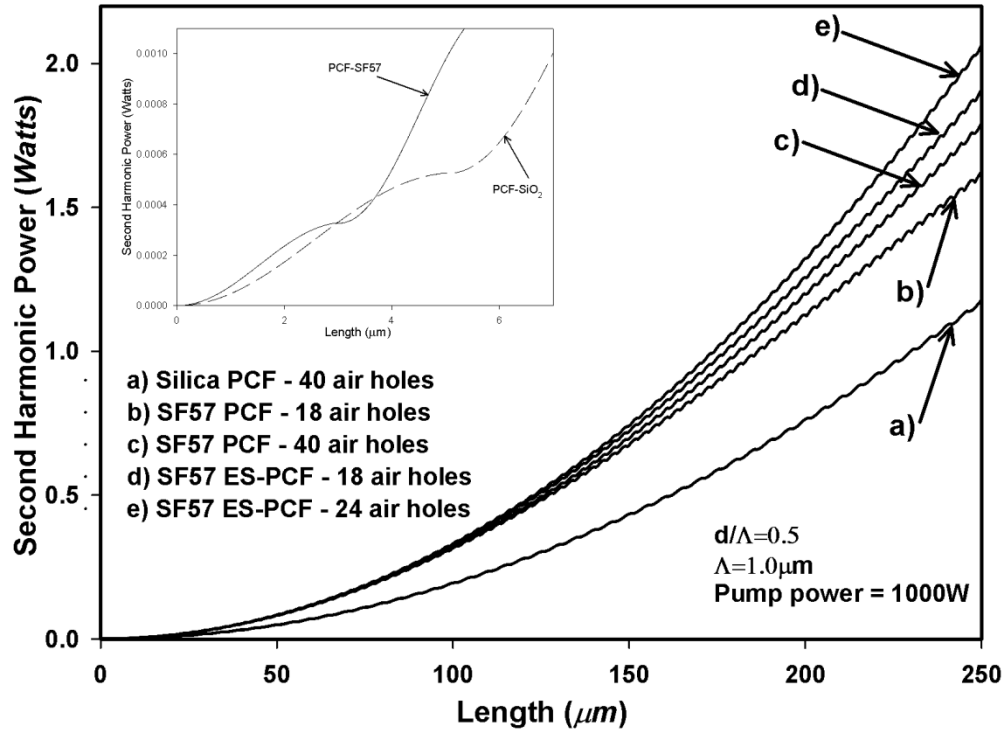


Figure 4.26 Comparison of QPM SH output power against length for different PCF structures and different materials. Inset graph: enlarged version of curves a) and c) for the propagation of a single coherence length.

It is clear that as the number of air-holes is increased, the SH power improves for both conventional PCF and ES-PCF. The SH power can be further improved by employing the ES-PCF structure (instead of conventional PCF) and the *SF*57 material (instead of Silica). Considering curves a) and c), i.e. conventional PCF with Silica and *SF*57 respectively, both with 40 air-holes it can be seen clearly that the SH output power of curve c) is much higher, which is due to the high $d_{33}$ value of the *SF*57 material. The superiority of the ES-PCF structure is clearly illustrated by curve d), i.e. ES-PCF with 18 air-holes, which has a considerably higher output power ($\sim 1.9W$) than that of curve b) ($\sim 1.6W$), i.e. PCF with the same number of air-holes (and same material); and still higher compared with that of curve c) ($\sim 1.8W$), i.e. PCF with almost twice the number of air-holes (i.e. 40). Moreover, curve e) shows

that the SH output power ($\sim 2.1W$) can be further improved by increasing the number of air-holes (i.e. 24 air-holes) in the ES-PCF. This improvement is already seen at a propagation length of $250\,\mu m$ and will be much more significant with further propagation. The difference between the two structures is a result of the superior confinement of the mode in the core region in ES-PCF which results in a better overlap integral compared to that of the conventional PCF structure.

The inset graph shows an enlarged version of curves a) and c) for the propagation over a single coherence length. The value of $L_c$ of Silica is higher than that of $SF57$ which is due to the lower material refractive index difference between the fundamental and the SH waves (i.e. for $SF57$ $\Delta n = 0.0467$, for Silica $\Delta n = 0.0097$). The inset graph shows clearly that the SH output power is higher in Silica after the propagation of a distance equal to one $L_c$. Nevertheless, as mentioned above, observations made at further propagation lengths show that $SF57$ leads to a higher level of power compared to Silica while the ES-PCF structure helps further increase the power.

## 4.7   SUMMARY

This chapter provides one of the key contributions by the author which represents a novel aspect of this thesis in the numerical analysis of the ES-PCF design in *SF*57 soft glass. Here, for the first time, the approach has included the analysis of SH output power, modal properties and error tolerance. The main aspects of the work and achievements are summarised below.

Numerical simulations have first been validated by comparison of the outputs with corresponding real experiments on conventional optical fibre. Further numerically simulated results show that a significantly higher level of SH output power can be achieved by employing the ES-PCF design in *SF*57 soft glass rather than conventional Silica PCF. For example, a power increase of 31% was numerically demonstrated from conventional PCF ($\sim 1.6W$) to ES-PCF ($\sim 2.1W$) for a propagation length of $250\ \mu m$. The higher output power is a result of the higher overlap integral arising from the better modal properties in ES-PCF. The Quasi Phase Matching technique has also been applied in order to achieve maximum SH output power. It has been shown that potential fabrication tolerances can lead to errors in the coherence length, which could result in a substantial reduction in the generated QPM SH power. However, it may be possible to minimize the fabrication errors by temperature or strain tuning. Moreover, the ability of the ES-PCF structure to effectively control more than one parameter simultaneously: this is a significant advantage over conventional PCF and this has been demonstrated by the work carried out by the author in this thesis.

# Chapter 5

# Zinc Oxide Waveguides

This chapter presents the numerical analysis of Zinc Oxide Waveguides by employing the full vectorial Beam Propagation Method (BPM). Section 5.1 gives a brief introduction while Section 5.2 provides a description of the *ZnO* waveguide structure considered and Section 5.3 presents detailed results of the investigation carried out including the validation of the simulation results. Finally, Section 5.4 summarises the study.

## 5.1 INTRODUCTION

Adaptation of nanotechnology is currently becoming popular in a variety of engineering applications. Among various nanoscale devices, nanowires are widely utilised in nanophotonics. In such optical devices, SHG continues to play a vital role in a wide range of applications such as cell imaging in biology [176]. This is due to the fact that in smaller core size of waveguides the power density can be high for a given input power and SHG directly depends on power density, i.e. reduced effective area ($A_{eff}$) results in enhanced SHG efficiency. Currently there is a growing interest in nonlinear materials which can be fabricated in nanoscale. *ZnO* is one such

material: although $\chi^{(2)}$ may be lower than that of $LiNbO_3$, its overall efficiency is expected to be higher. However for $ZnO$ structures with dimensions lower than the wavelength, the index contrast becomes high which causes the fields to be of hybrid nature. Therefore, a full-vectorial approach is needed for the numerical analysis of SHG. This chapter employs a full vectorial FE-BPM analysis of SHG in $ZnO$ waveguides.

### 5.1.1 Choice of Material

Materials with non-inversion symmetry such as $LiNbO_3$, $KNbO_3$, $BaTiO_3$ and $ZnO$ are commonly used to fabricate optical waveguides due to their higher second order nonlinear optical response (i.e. second-order nonlinear susceptibility $\chi^{(2)}$). Among the various materials available, Lithium Niobate ($LiNbO_3$) exibits excellent properties of second order nonlinearity with the use of periodical poling methods [177], which can be utilised in many second order NLO devices [149]. However, it is challenging to achieve high second order nonlinearity in nanoscale $LiNbO_3$ waveguide structures due to lack of flexibility and the high costs required for their practical implementaions, such as is needed in modern crystal growth technology. Hence there is a growing demand for alternative NLO (Nonlinear Optical) materials in which the waveguide cross-section can be reduced to enhance effective nonlinearity.

Zinc Oxide ($ZnO$), a II-VI semiconductor, has many excellent optical and photomechanical properties compared to those of other nonlinear materials such as $LiNbO_3$ and $ZnO$ has the capability to be deposited on different types of substrates [178]. Alternatively, $ZnO$ can also be grown on various substrates such as silica [179], silicon [180], $GaAs$ [181], quartz [182], diamond [183], Diamond-Like-Carbon (DLC) [184, 185], $LiTaO_3$ [186] and $LiNbO_3$ [187]. Therefore, due to their positive characteristics in terms of their fabrication potential and ability to be readily integrated, $ZnO$ nanomaterials are promising candidates for integrated optics devices such as solar cells, lasers and transparent transistors and $ZnO$-based blue light emitting diodes (LEDs) etc. [188]. Furthermore, second order susceptibilies in $ZnO$ can be enhanced by decreasing the thin film thickness, regardless of the technology being used. Further, by varying the growth time in $ZnO$ nanorods, it is possible to vary the aspect ratio and the second order suceptibilies [126]. Moreover, exploiting

SHG in various forms of $ZnO$ is becoming popular for a wide range of applications, espcially in biophotonics where it is used to understand better some of the biological molecules used [189]. Studying induced luminescence is another aspect of the use of SHG in $ZnO$ [190] and recently, $ZnO$ has been employed as hybrid optical material for fabricating integrated active optical devices operating in the visible, near-infrared, mid-infrared and $TH_z$ frequency regions, taking full advantage of the highly transparent nature of $ZnO$ [191].

## 5.2    ZINC OXIDE WAVEGUIDE DESIGN

$ZnO$ thin films exhibit significant second-order nonlinear susceptibility $\chi^{(2)}$ (i.e. in the region of $10 \, pm/V$) across different crystallinities and thicknesses [125]. Another advantage of using $ZnO$ films is that the well-defined crystal polarity can be identified in advance in order to understand the origin of the NLO response in the thin film [192]. $ZnO$ thin films have been employed for many practical applications e.g. nanocrystalline $ZnO$ thin film for gas sensor applications [193] and in producing $ZnO$ thin film transistors (TFTs) [194] for next-generation displays. $ZnO$ waveguides can also be used to fabricate low power CMOS (Complementary Metal–Oxide–Semiconductor) compatible $ZnO$ nanocomb-based gas sensors.  In this chapter, a $ZnO$ nanostructure has been considered and it is assumed that the $ZnO$ nanowires have been grown on a silica/silicon substrate with the crystal axis perpendicular to the silica/silicon substrate.
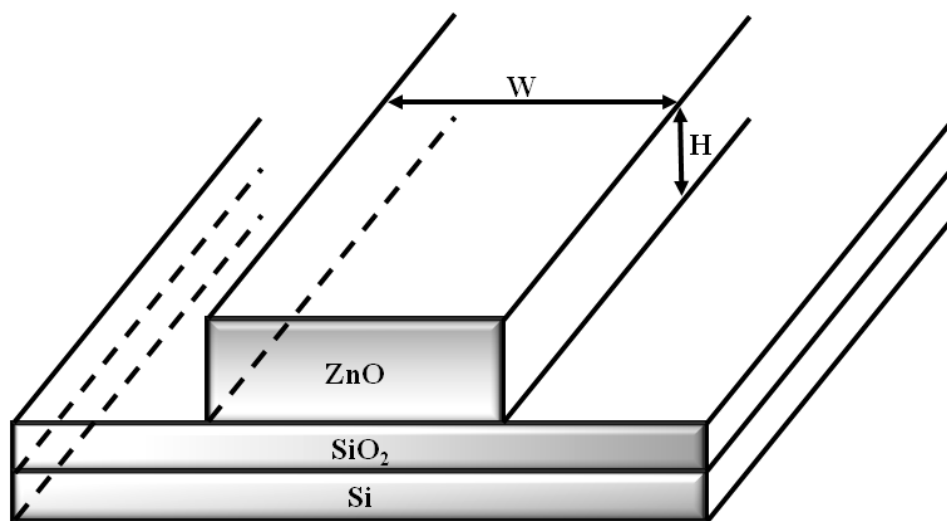


Figure 5.1 **$ZnO$** planar waveguide with silica buffer layer on a silicon substrate.

Figure 5.1 shows the structure of the $ZnO$ planar waveguide with a silica buffer layer on a silicon substrate. In Figure 5.1, $H$ and $W$ denote the height and the width of the planar waveguide, respectively. In practice, rectangular-shaped $ZnO$ crystals have been used in the form of fabricated thin films, achieved by using different growing techniques, which have shown promising SHG performance. An initial investigation was carried out to optimise $ZnO$ waveguides with different aspect ratios. The refractive indices of $ZnO$ and $SiO_2$ are taken as 1.95494 [195] and 1.54292 [196], respectively, at the fundamental wavelength $\lambda_\omega = 1.064\ \mu m$. The refractive indices of the $ZnO$ and $SiO_2$ for the second harmonic wavelength $\lambda_{2\omega} = 0.532\ \mu m$ were given by 2.04651 [195] and 1.55609 [196], respectively. The $ZnO$ waveguide with the $SiO_2$ / $Si$ substrate and air-cladding was represented by an irregular mesh of 9800 triangular elements in this numerical simulation. In this analysis, the fundamental pump power is taken as $1W$ and the $H_{mn}^x$ (quasi-$TM$) and $H_{mn}^y$ (quasi-$TE$) mode notations are used.

### 5.3    SIMULATION RESULTS

Numerical simulation results are presented in Section 5.3.1 for the periodically poled silica fibre which was discussed in Chapter 4 in order to validate the numerical results. Section 5.3.2 presents the simulation results for $ZnO$ waveguides.

### *5.3.1    Validation of numerical simulations*

In Chapter 4, numerical results have been validated by comparing with experimental results for the periodically poled silica fibres [159]. The scalar BPM has been used to analyse the SHG in Chapter 4 whereas the full vectorial BPM has been implemented in order to obtain a numerical analysis for $ZnO$ waveguides in this chapter. The derivation of the full vectorial BPM and the application of full vectorial BPM for the analysis of SHG have been discussed in detail in Chapter 2 and Chapter 3 respectively. In this section, results of the analysis of SHG in periodically poled silica fibre have been used to test the full vectorial approach for SHG. Therefore, a structure with a small index contrast, for which both vector and scalar approaches are reasonable and acceptable has been considered.
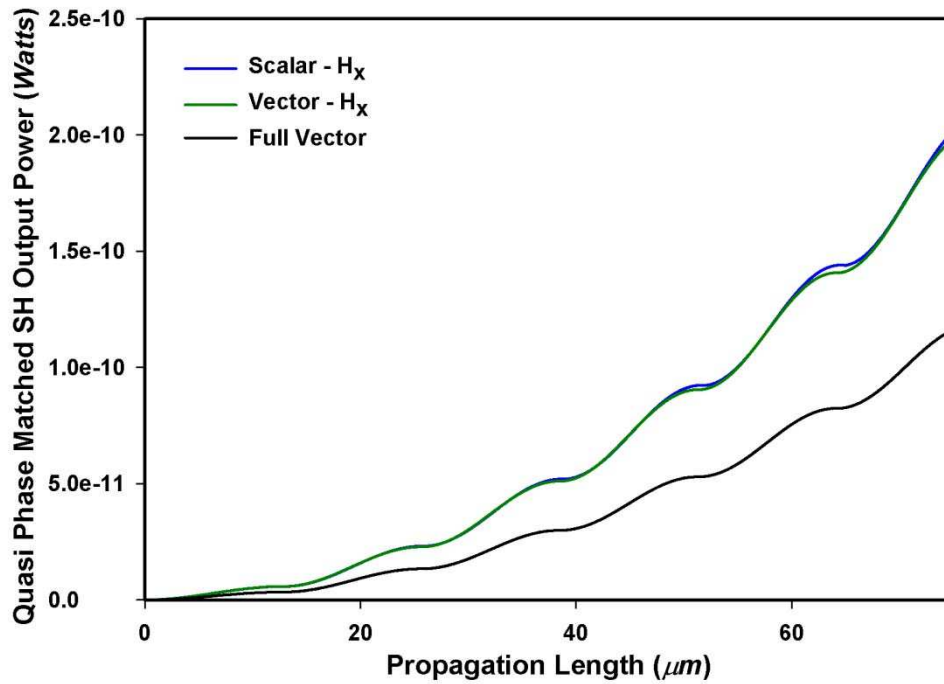
Figure 5.2 Comparison of the QPM SH output power of the scalar $H_x$, vector $H_x$ and full vectorial fields against the propagation length.

Figure 5.2 shows the comparison of QPM second harmonic output power for the scalar- $H_x$ field (*TM*- mode), vector- $H_x$ field (i.e. only the *TM*- mode of the full vectorial BPM is used) and full vectorial fields up to a propagation length of 75 *μm*. The blue and green curves show the SH output power of $\sim 2 \times 10^{-10}\,W$ after propagation of 75 *μm* and the black curve shows $\sim 1.1 \times 10^{-10}\,W$. Further, all three curves have the same coherence length of $\sim 13\,\mu m$. It can be observed in Figure 5.2 that the SH output power of the full vectorial field is lower than that of scalar- $H_x$ and vector- $H_x$ fields. The reason for this behaviour is that in full vectorial BPM, all the $H_x$, $H_y$ and $H_z$ components are considered whereas the others consider only the $H_x$ field component. The crystal orientation in these cases (i.e. in the blue and green curves) supports mainly a higher $H_x$ field for SHG. This has been further discussed under choosing the optimised crystal orientation and poling direction in Chapter 3. On the other hand, in the black curve the magnitudes of the other two field components ($H_y$ and $H_z$) become very low and contribution to the overall SH power becomes lower than in the other two curves. Moreover, the second harmonic output power of the scalar- $H_x$ field component can be represented as follows;

$$P_{SHG\,(scalar)} = \left(\frac{Z_0\beta}{k_0 n_{2\omega}^2}\right)\frac{1}{2}H_{x(2\omega)}^2 \tag{5.1}$$

where $Z_0$ is the free space impedance ($\approx 377\Omega$), $\beta$ is the propagation constant, $k_0$ is the wavenumber and $n$ is the refractive index of the material.

In the case of full vectorial the power is equally distributed into $H_x$ and $H_y$ components and it can be expressed as follows;

$$P_{SHG(full\,vector)} = \left(\frac{Z_0\beta}{k_0 n_{2\omega}^2}\right)\frac{1}{2}H_{x(2\omega)}^2 + \left(\frac{Z_0\beta}{k_0 n_{2\omega}^2}\right)\frac{1}{2}H_{y(2\omega)}^2 \tag{5.2}$$

$$P_{SHG(full\,vector)} = \left(\frac{Z_0\beta}{k_0 n_{2\omega}^2}\right)\frac{1}{2}\left(H_{x(2\omega)}^2 + H_{y(2\omega)}^2\right) \tag{5.3}$$

Equation (5.3) shows the full vectorial SHG power due to the both $H_x$ and $H_y$ components of the propagating SH field. However, the $H_y$ component of SH is not generated.

When the fundamental mode is launched, the $H_{x(\omega)}$ and $H_{y(\omega)}$ components propagate with equal intensities. The relationship between the scalar- $H_x$ and the full vectorial field components for the fundamental frequency can be expressed as follows;

$$\frac{1}{2}H_{x\,(\omega-scalar)}^2 = H_{x\,(\omega-full\,vectorial)}^2 \tag{5.4}$$

$$H_{x\,(\omega-full\,vectorial)} \approx \frac{H_{x(\omega-scalar)}}{\sqrt{2}} \tag{5.5}$$

As can be seen in equation (5.5) the $H_{x\,(\omega-full\,vectorial)}$ is lower than $H_{x(\omega-scalar)}$ for a given values of launched power. Therefore, the two conditions from equations (5.3) and (5.5) suggest a full vectorial mode produces a lower SHG power as shown in Figure 5.2.

Figure 5.3 shows the QPM second harmonic output power in full and quarter structure for periodically poled silica fibres. The results shown in Figure 5.3 were obtained by using scalar BPM and full vector BPM. It can also be noted that the

scalar and vector BPM results are similar, because the pure *TM* mode has been launched (i.e. using only the $H_x$ field component).
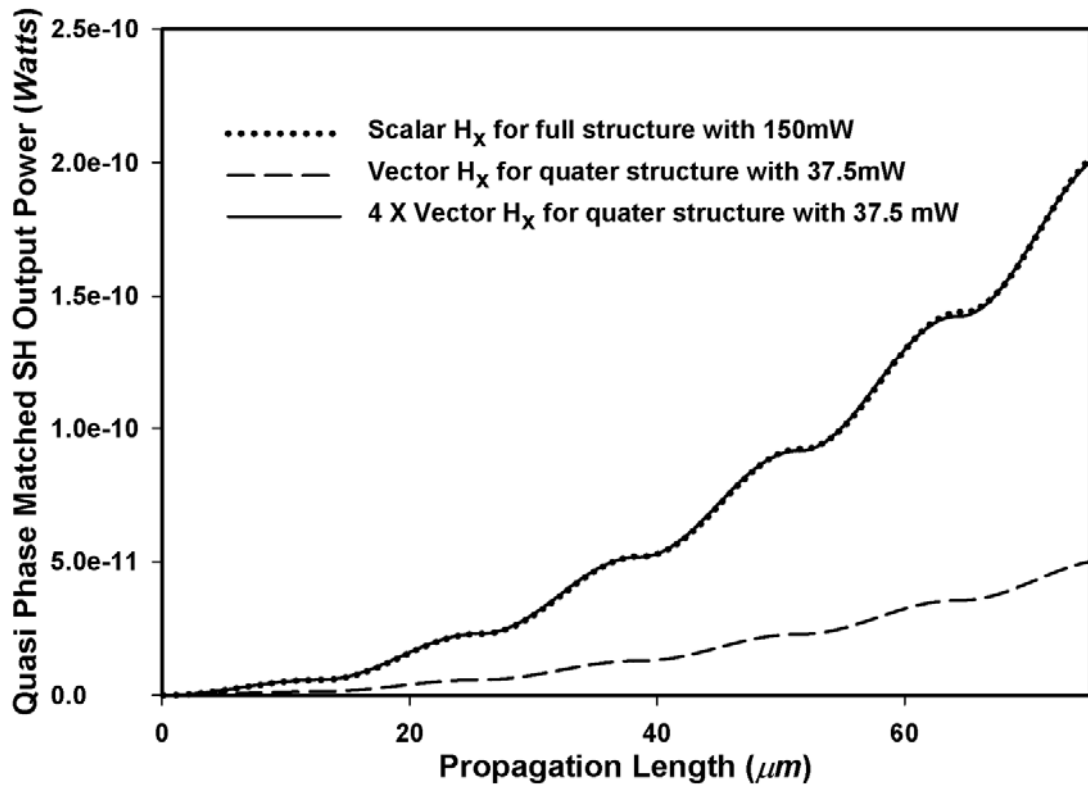


Figure 5.3 Comparison of the QPM SH output power of the scalar full structure and vector quarter structure fields with different pump powers against the propagation length.

Furthermore, it can be observed in Figure 5.3 that the scalar- $H_x$ second harmonic output power is $\sim 2 \times 10^{-10}\ W$ in the full structure with the input power of $150\ mW$ (dotted curve) while the vector-$H_x$ second harmonic output power is $\sim 5 \times 10^{-11}\ W$ in the quarter structure with the input power of $37.5\ mW$ (dashed curve) which is four times lower. Further the solid curve represents the vector-$H_x$ second harmonic output power for quarter structure similar to the dashed curve. However in this case (i.e. solid curve) the power values are multiplied by four in order to compare with the SH output power of the full structure.

The relationship between the pump power and the QPM second harmonic output power is shown in Figure 5.4.
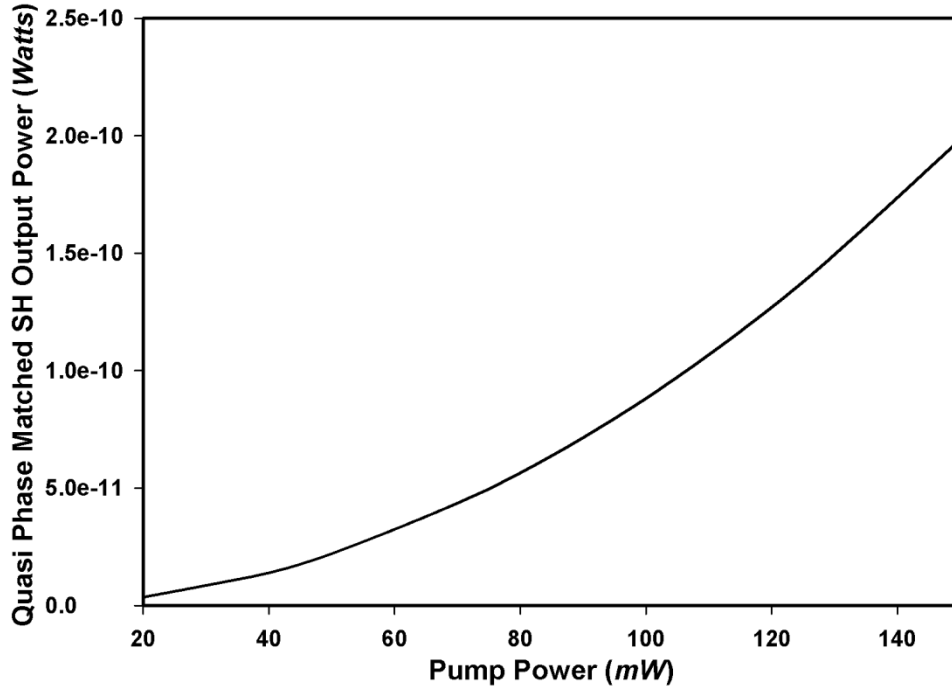


Figure 5.4 Variation of the QPM SH output power with different pump power levels.

The relationship between the SH electric field, magnetic field and the pump power ($P_\omega$) can be represented as follows;

$$E_{2\omega} \propto P_\omega \tag{5.6}$$

$$H_{2\omega} \propto P_\omega \tag{5.7}$$

Then the nonlinear relationship in Figure 5.4 can be expressed as follows;

For the electric field;

$$E_{2\omega} \propto E_\omega^2 \tag{5.8}$$

where $E_\omega$ and $E_{2\omega}$ denote the electric fields for the fundamental and second harmonic frequencies respectively.

For the magnetic field;

$$H_{2\omega} \propto H_{\omega}^2 \qquad (5.9)$$

where $H_{\omega}$ denotes the magnetic field for the fundamental frequency and $H_{2\omega}$ denotes the magnetic field for the second harmonic frequency;

Squaring both sides of equation (5.8) yields the following relationship;

$$[E_{2\omega}]^2 \propto [E_{\omega}^2]^2 \qquad (5.10)$$

Then the relationship between the fundamental and second harmonic power can be expressed as follows;

$$P_{2\omega} \propto [P_{\omega}]^2 \qquad (5.11)$$

The behaviour of equation (5.11) is represented in Figure 5.4. Furthermore, the linear relationship between the maximum $H_{2\omega}$ value (i.e. in this case $H_x$) and the pump power is shown in Figure 5.5 and the relationship is given in equation (5.7)
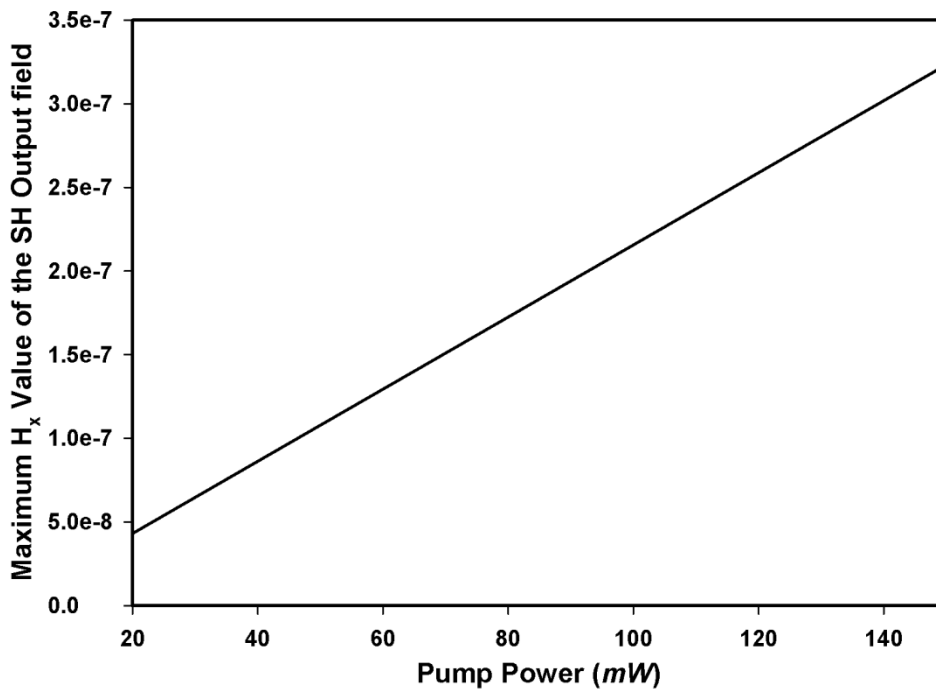


Figure 5.5 Variation of the maximum $H_x$ value of the SH output field with different pump power levels.

Figure 5.6 shows the full structure field profiles for the fundamental and second harmonic frequencies after the propagation of $75\,\mu m$. These field profiles are obtained based on Figure 5.2, where the evolution of SHG is shown.
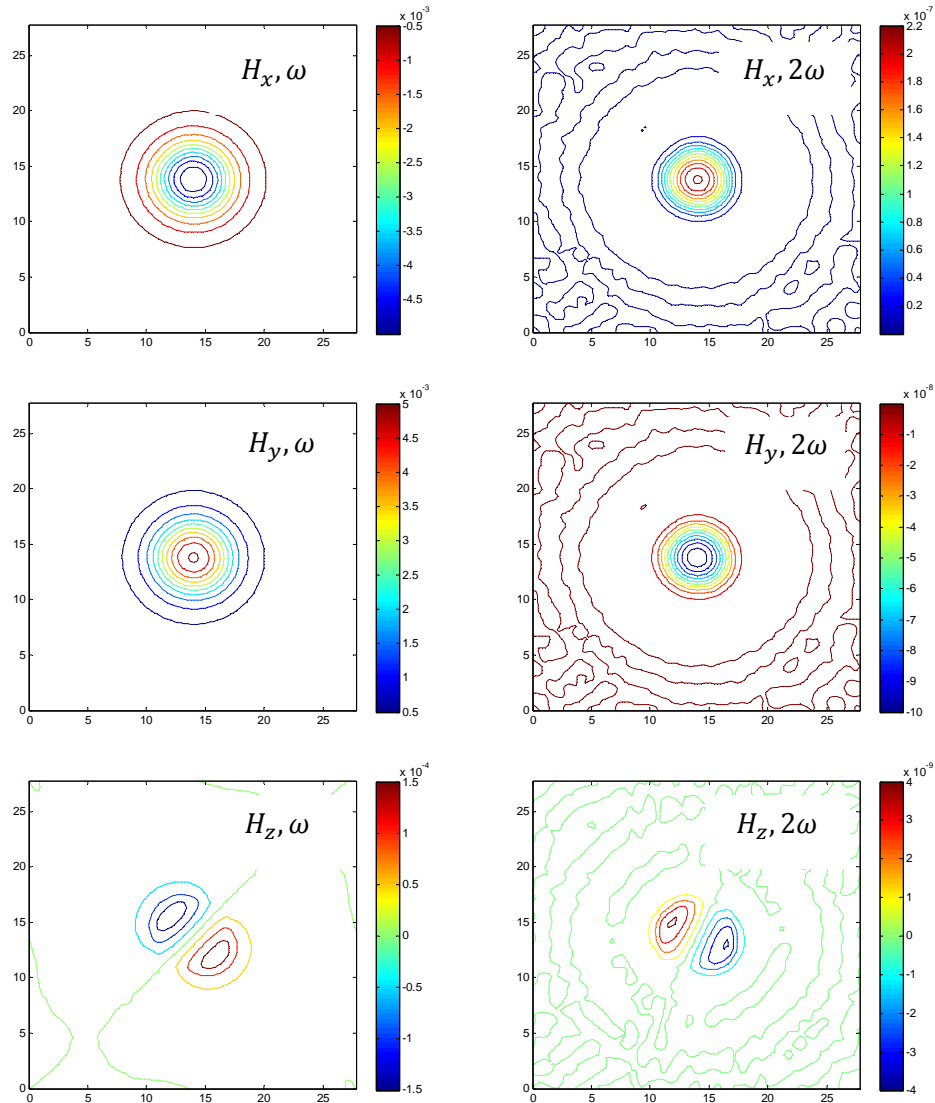


Figure 5.6 Fundamental and SH field profiles after propagation of $75\,\mu m$ for full structure optical fibre.

It can be observed in Figure 5.6 that the field profiles of $H_x,\omega$ and $H_y,\omega$ have similar magnitudes in both cases: this is due to the mode degeneration in a circular core. Further, the field profiles of $H_x,\omega$ and $H_y,\omega$ are in the Gaussian shape and the field profile of $H_z,\omega$ appears as two lobes of opposite polarity. Moreover, the crystal orientation and the poling direction have been chosen in order to optimise the *TM*-mode. Therefore, the $H_x,2\omega$ field profile has a higher magnitude than that of $H_y,2\omega$.

Figure 5.7 shows the quarter structure field profiles for the fundamental and second harmonic frequencies after the propagation of 75 $\mu m$. These field profiles are obtained based on Figure 5.3.
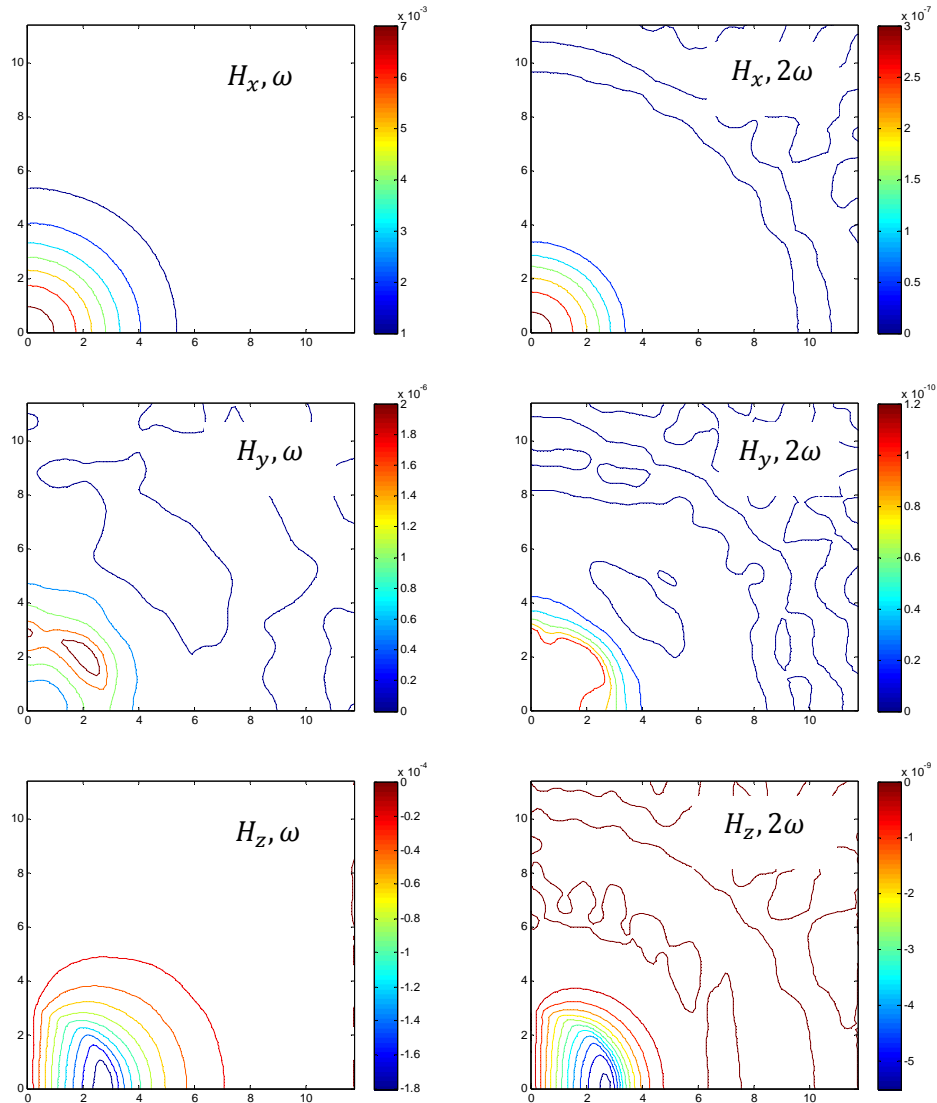


Figure 5.7 Fundamental and SH field profiles after propagation of 75 $\mu m$ for quarter structure optical fibre.

As shown in Figure 5.7 the field profiles ($H_x, \omega$ and $H_y, \omega$) behave in a similar manner to that of the full vectorial case, albeit with a quarter structure. However, the magnitude of the $H_x, \omega$ field profile is higher than that of $H_y, \omega$: this is caused by all the power being used to excite the *TM*-mode while *TE*-mode is prohibited by imposing the boundary conditions. Further, similar behaviour can be observed in the case of $H_x, 2\omega$ and $H_y, 2\omega$ field profiles as discussed in relation to Figure 5.6 (i.e.

magnitude of the $H_x, 2\omega$ is higher than that of $H_y, 2\omega$ due to the chosen crystal orientation and poling direction which mostly support the $TM$-mode).
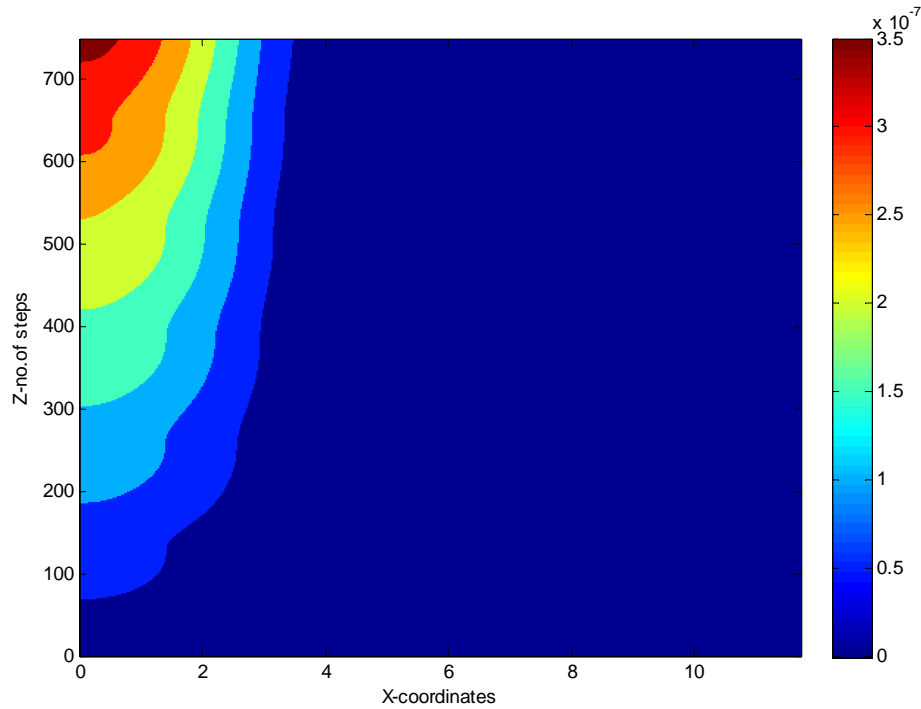


Figure 5.8 SH field profile on the Z-axis after propagation of 75 $\mu m$ for quarter structure optical fibre.

Figure 5.8 shows the propagation of the second harmonic vector- $H_x$ field profile on the Z-axis for the propagation length of 75 $\mu m$. In this case the field profile is obtained from Figure 5.7 (i.e. using $H_x, 2\omega$). It can be observed that initially the magnitude of the field is zero and then gradually increases along the Z-axis (i.e. propagation axis): this is due to the power transfer from the fundamental field to the second harmonic field. Further, similar behaviour can be noticed for $H_y, 2\omega$ and $H_z, 2\omega$.

### 5.3.2   *Analysis of Zinc Oxide waveguides*

The variation of the effective index ($n_{eff}$) with height has been studied for the first order mode at two frequencies, $\omega$ and $2\omega$, each with different widths, $W$ (i.e. $1\,\mu m$ and $2\,\mu m$), and the results of this are shown in Figure 5.9. The first order mode $H_{11}^x$ of the fundamental frequency, $\omega$, is indicated by $H_{11}^x, \omega$.
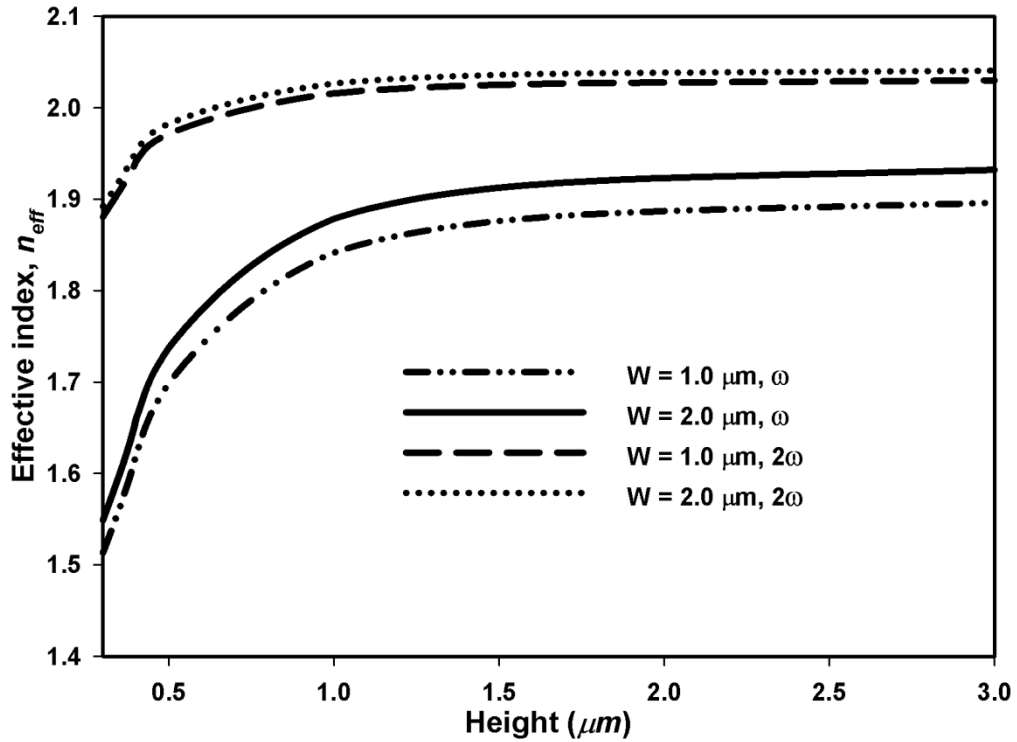


Figure 5.9 Variation of the effective index of the propagating modes with the height at the fundamental and second harmonic frequencies for width values of $1\mu m$ and $2\mu m$.

As can be seen in Figure 5.9, a reduction of the height results in a reduction of $n_{eff}$ as the confined mode becomes exposed to the air cladding of the *ZnO* waveguide. Initially the effective indices of the modes reduce slowly, but these decrease rapidly as the modes approach their cut-off conditions (i.e. height values of $0.3\,\mu m -$ $0.7\,\mu m$). Moreover, the effective index of $H_{11}^x, 2\omega$ (i.e. $H_{11}^x$ of the second harmonic frequency) is shown to move towards the cut-off condition at a slower rate than does the $H_{11}^x, \omega$ mode. This is because the first order mode of the higher frequency (i.e. of second harmonic) is more confined in the centre of the *ZnO* core, in comparison with that of the lower frequency. Further, as the height is increased, the mode becomes more confined to the core, resulting in the value of $n_{eff}$ asymptotically approaching the refractive index of *ZnO* (i.e. $n_\omega = 1.95494$ and $n_{2\omega} = 2.04651$). For very small

dimensions the difference between the effective indices of the fundamental and SH wavelength is high indicating a deviation from the phase matching in the cut-off region.
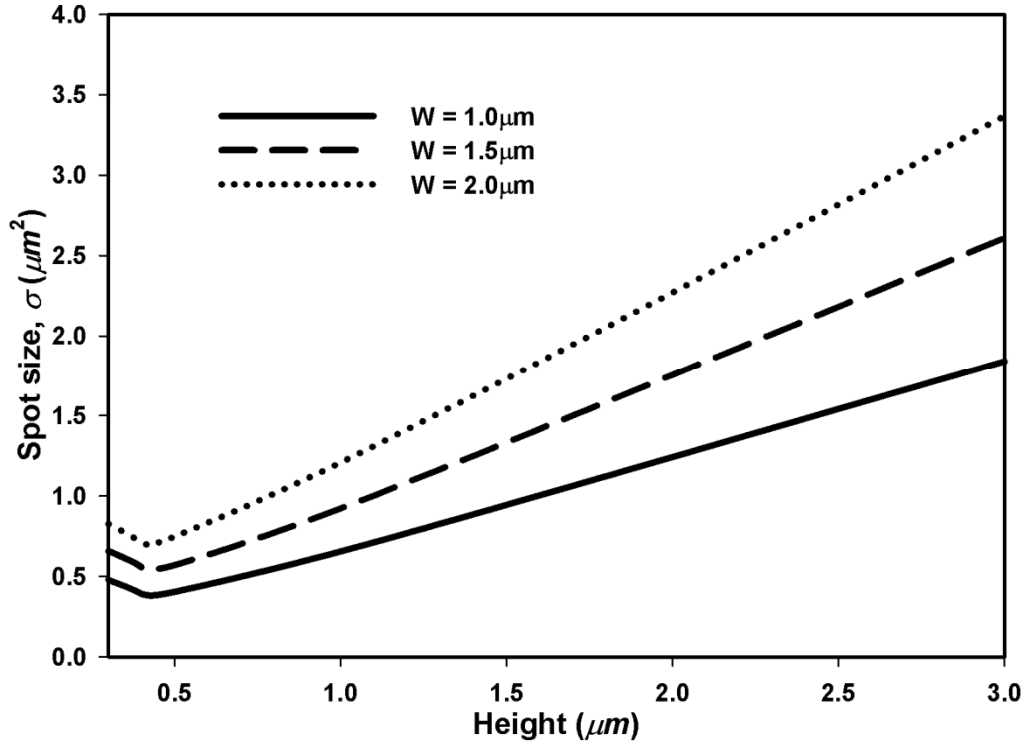


Figure 5.10 Variation of the spot-size of the $H_{11}^x$ mode of the fundamental frequency with the height for different width values.

The spot-size ($\sigma$) is an important modal parameter which can be used to understand better the power confinement and the resulting power density of the pump and the second harmonic modes. The spot-size, in this work, has been defined as the area where the Poynting vector is more than $1/e^2$ of its maximum value for a given mode (or area where field is greater than $1/e$ of its maximum field value). Figure 5.10 shows the variation of the spot-size with height for the dominant first order modes $H_{11}^x$ at the fundamental frequency, $\omega$, indicated by $H_{11}^x, \omega$ for different widths. For a given height, $\sigma$ reduces when the width decreases from $2\,\mu m$ to $1\,\mu m$. For all the width values, it can be observed that $\sigma$ reduces as the height is reduced until the cut-off condition is reached. However, when the dimensions of the waveguide reduces, $\sigma$ also reduces due to the high confinement of the $H_{11}^x, \omega$, and as shown in Figure 5.10, a further reduction of the dimensions results in spreading the field into the air-cladding due to reaching the cut-off condition when the $H = 0.4\,\mu m$. Therefore, the

fundamental mode reaches its cut-off condition when $W = 1\,\mu m$ more rapidly than when $W = 2\,\mu m$. The relationship between $\sigma$ and the dimensions of the *ZnO* waveguide is used as a guideline for design optimization.

It can be seen that lower height values give smaller spot-sizes leading to a high SHG generation. However it should be noted that when $H < 0.5\,\mu m$ the second harmonic generation will deteriorate as the fundamental mode loses it high power density. Next, it is necessary to consider the spot-size of the SH wavelength. This is because the modal area of both fundamental and SH modes should match spatially to achieve efficient power transfer between modes. Hence the overlap integral has been analysed as follows.
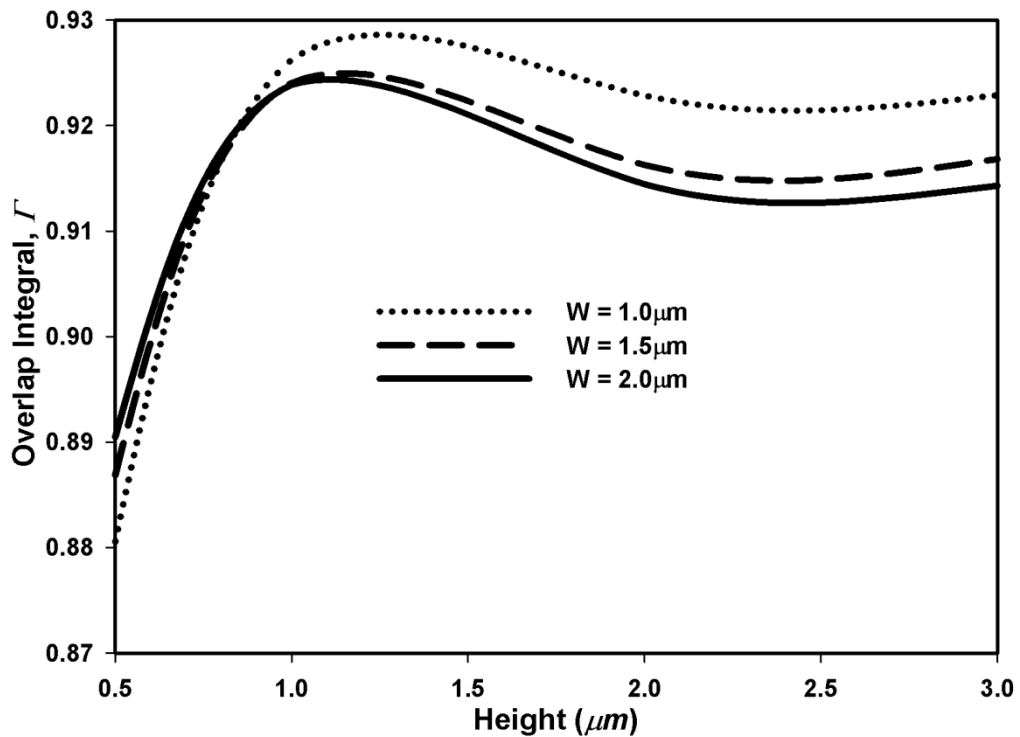


Figure 5.11 Variation of the overlap integral of the $H_{11}^{x}$ mode (between the fundamental and the second harmonic frequencies) against the height for different width values.

The overlap integral ($\Gamma$) between the interacting fundamental and second harmonic first order dominant modes $H_{11}^{x}$ relates directly to the efficiency of power transfer between these modes (equation (4.2) ), i.e. a higher value of the overlap integral results in higher conversion efficiency and vice versa.

Figure 5.11 illustrates how the overlap integral of the first order modes $H_{11}^x$ for the $\omega$ and $2\omega$ varies with the height over a range of width values. For small width values, both the $H_{11}^x, \omega$ and the $H_{11}^x, 2\omega$ modes are well confined and the overlap integral is high, particularly when height is also large. However, as has been mentioned, for a smaller waveguide width, its cut-off is reached more rapidly as the height is reduced; hence the overlap integral reduces in this operating range. It can be observed that, as the height decreases for a given value of width, the overlap integral initially increases, reaching a maximum value (in the region $1\,\mu m \leq H \leq 1.3\,\mu m$) and then starts to decrease. This can be explained as follows: by reducing the height, this makes $H_{11}^x, \omega$ and $H_{11}^x, 2\omega$ more confined which reduces the mismatch of their spot-sizes, leading to an increase in the overlap integral. However, as illustrated in Figure 5.10, when the height is very small the fundamental mode reaches its cut-off region more rapidly than the second harmonic mode, as shown in Figure 5.9 and Figure 5.10. Therefore, even though the second harmonic field becomes more confined to the core of the waveguide, the overall mismatch between fundamental and second harmonic fields becomes significant and the overlap integral starts to reduce at very small values of the waveguide heights.

In the above analysis the spot-sizes of the fundamental frequency were used to identify a highly confined mode. Furthermore, the optimized dimensions of the *ZnO* waveguide required to achieve the highest SHG has been identified using the overlap integral. To complete the analysis, the propagation length should be considered. This is because; even though SH power generated is directly proportional to the propagation length, this length is limited by a value called coherence length which is explained as follows.
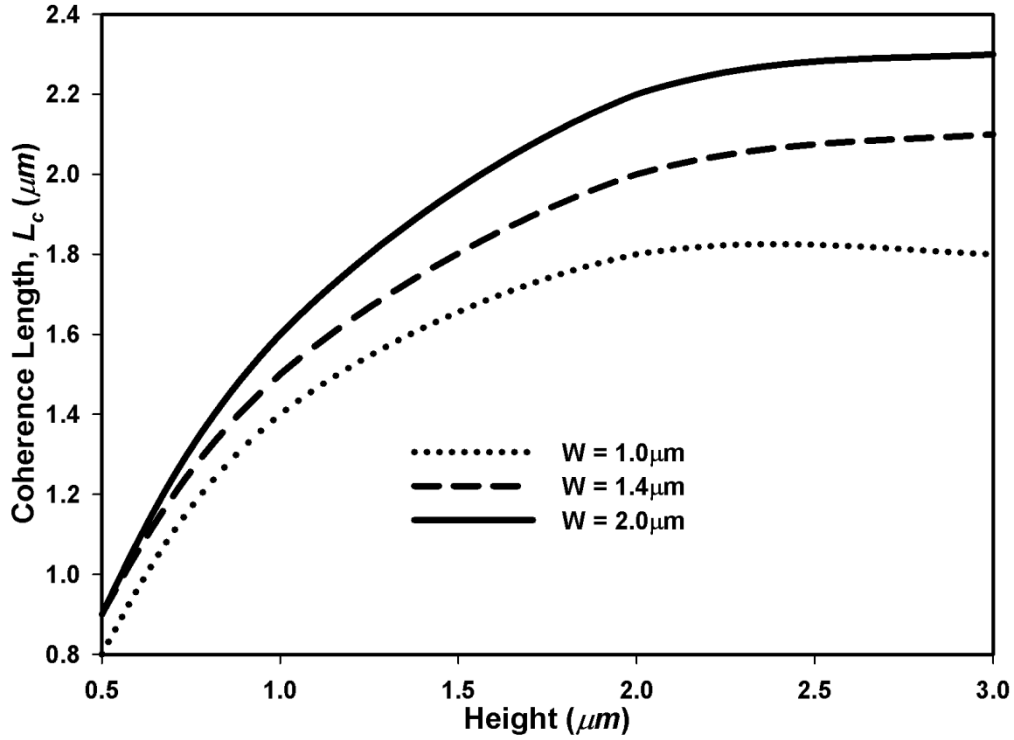
Figure 5.12 Variation of the coherence length for the quasi-*TM* modes against the height with different width values.

Due to material and waveguide dispersions the effective indices ($n_{eff}$) of the fundamental and SH modes are not identical. Therefore, the fundamental and second harmonic waves accumulate a $\pi$ radian phase shift over a distance known as the coherence length ($L_c$). Here $L_c = \pi/\Delta\beta$ and $\Delta\beta = \beta_{2\omega} - 2\beta_\omega$, where $\beta_\omega$ and $\beta_{2\omega}$ are the propagation constants of the fundamental and second harmonic waves, respectively. The variation of $L_c$ with the height and width is shown in Figure 5.12. Furthermore, a larger $L_c$ value would allow for a longer interaction between the fundamental and SH waves for higher SHG. As waveguide height decreases for a given width, the effective index decreases due to the decreased area of the *ZnO* core enabling the confined mode to be more exposed to the air cladding. Therefore, the propagation constant ($\beta$) decreases with $n_{eff}$, as shown in Figure 5.9. However, when the height increases, $\beta_\omega$ increases faster than $\beta_{2\omega}$ bringing $2\beta_\omega$ close to $\beta_{2\omega}$ (i.e. $2\beta_\omega \approx \beta_{2\omega}$) which results in a higher value of $L_c$. The ideal condition is possible if $n_{eff}^\omega = n_{eff}^{2\omega}$ (where $n_{eff}^\omega$ and $n_{eff}^{2\omega}$ are the effective indices of the fundamental and second harmonic); however, this cannot be realised for this particular material due to the chromatic dispersion of the *ZnO*. Moreover, as the height is increased, the *ZnO* core area is further increased and $L_c$ asymptotically approaches the value for bulk

*ZnO* material (~2.9 $\mu m$). However, if the core area is increased, the power density of the fundamental wave will become smaller and as a result the power transfer rate will be reduced. The trade-off between overlap integral and coherence length can be seen in Figure 5.13.
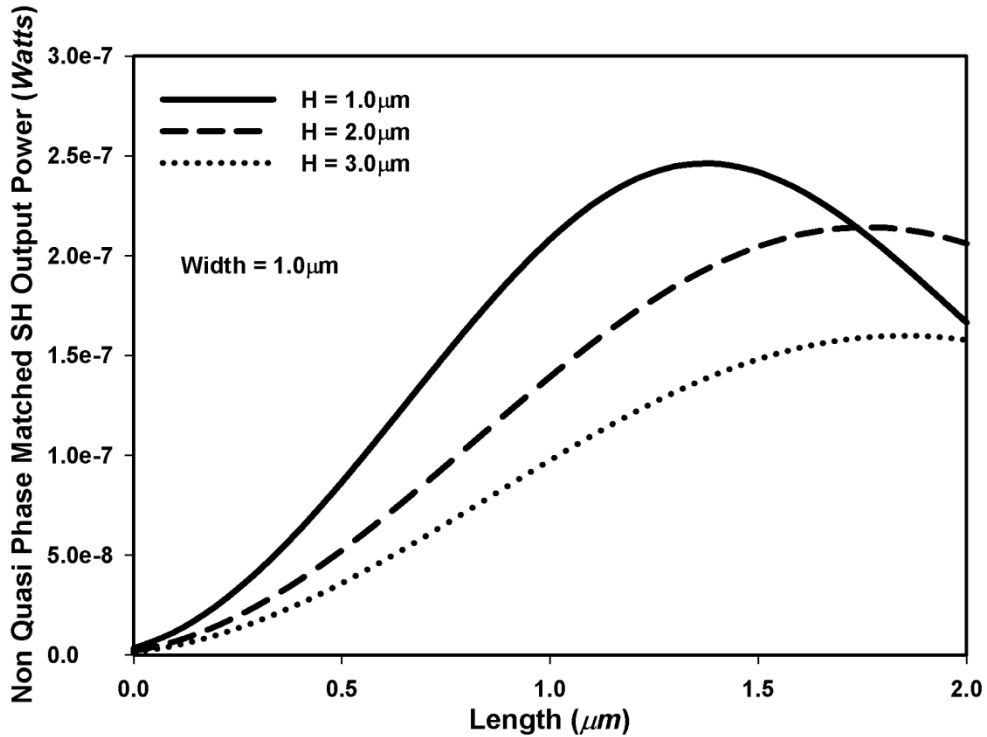


Figure 5.13 Variation of the non-QPM SH output power with the propagation length for different height values.

Figure 5.13 shows the non Quasi Phase Matched (non-QPM) second harmonic output power for different *ZnO* waveguide heights as a function of the propagation length. In all three cases, the *ZnO* waveguide width is fixed at 1 $\mu m$. It can be observed that the conversion rate of the non-QPM SH output power increases as the height decreases, over the range from 3 $\mu m$ to 1 $\mu m$. This arises because of the $H_{11}^x$ mode, which becomes more confined to the core and also increases the overlap integral, resulting in high field intensities leading to high power conversion rates. For the quasi-*TM* mode, the $H_{11}^x$ field component is dominant. Reducing the height of the waveguide can be use to tailor *TM* mode operation. It has been observed that when the height is further reduced (i.e. below 1 $\mu m$) the mode spreads in to the air cladding.
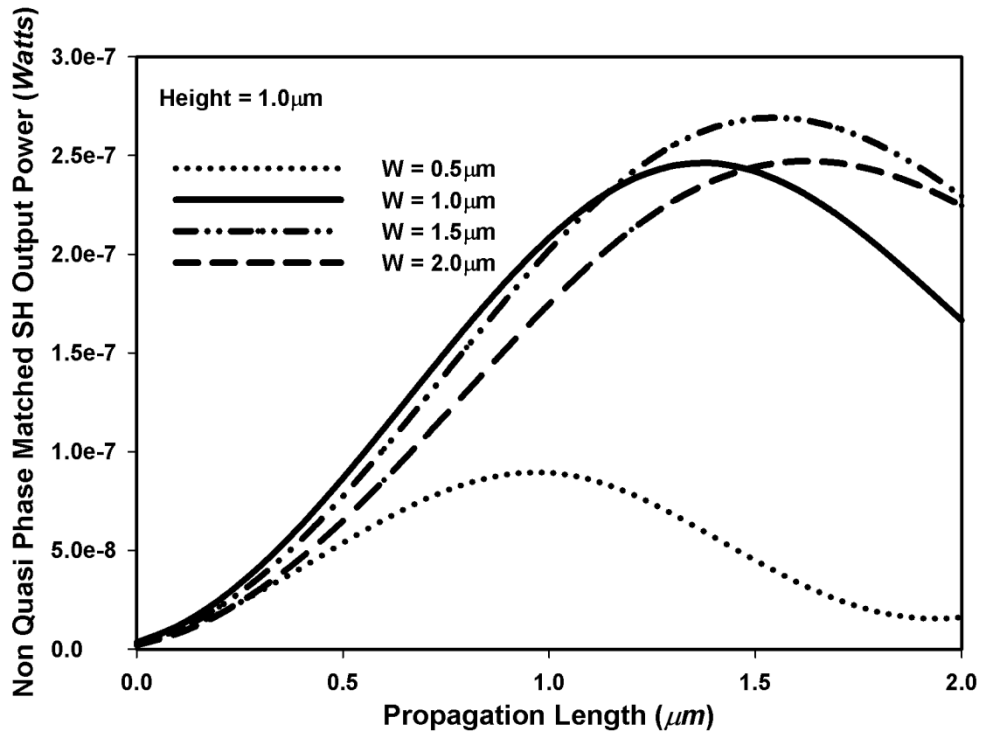
Figure 5.14 Variation of the non quasi phase matched SH output power against the propagation length for different width values.

In addition to the height, the width of the waveguide has also been considered for the optimisation. Accordingly, Figure 5.14 shows the non-QPM second harmonic output power along the axial direction for different widths of the *ZnO* waveguide; in this case the height is $1\,\mu m$. The SH output power increases along the axial direction in Figure 5.14, reaches its maximum after a distance equal to the first coherence length and reduces due to the phase mismatch. As the width decreases from $2\,\mu m$ to $1\,\mu m$, the rate of change increases due to the higher overlap integral. A further reduction in the width (i.e. from $1\,\mu m$ to $0.5\,\mu m$) causes the $H_{11}^x, \omega$ mode to start to spread into the air cladding while the $H_{11}^x, 2\omega$ mode becomes more confined to the waveguide core, resulting in a decreased overlap integral. Therefore, the rate of change reduces for $W = 0.5\,\mu m$ compared to its width $1\,\mu m$. It can be observed that the initial rate of change of the $W = 1\,\mu m$ curve was greater due to the maximum overlap integral, as shown in Figure 5.11. Furthermore, the coherence length increases as the width increases from $0.5\,\mu m$ to $2\,\mu m$. In the case of $W = 1\,\mu m$, the predicted rate of generation of SH output power is higher, but the coherence length is smaller than that of $W = 1.5\,\mu m$. Hence, it can be observed that the maximum conversion efficiency can be achieved when the $W = 1.5\,\mu m$.
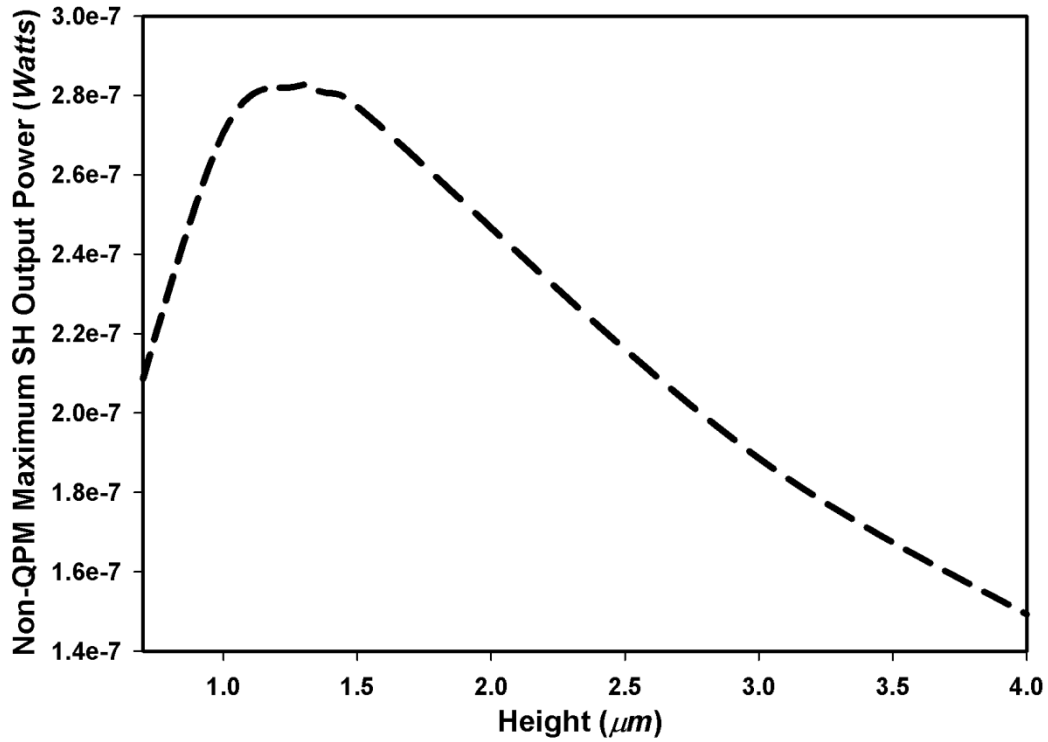
Figure 5.15 Variation of the non QPM maximum SH output power against the height.

As mentioned in Section 5.1.1, *ZnO* can be fabricated with different dimensions in order to achieve an optimised structure to produce maximum second harmonic output power. First, for each height value of the *ZnO* waveguide, the width value is optimised at which the non-quasi phase matched second harmonic output power is maximum (the range of width was between $(1.3\,\mu m - 1.6\,\mu m)$: these maximum power values achieved after a propagation length equal to $L_c$ are shown in Figure 5.15. As explained in Figure 5.13 and Figure 5.14, when the dimension of the *ZnO* waveguide reduces, the SH output power generated increases due to the better mode confinement and improved overlap integral (unless the waveguide approaches mode cut-off). In Figure 5.15, the maximum SH output power is obtained at a height of $1.3\,\mu m$ with the corresponding width value of $1.5\,\mu m$. It was observed that the dimensions of the maximum point as shown in Figure 5.15 strongly support the $H_{11}^x$ mode for both the fundamental and the second harmonic frequencies.

In the analysis above, it should be noted that the high SHG power achieved is limited by the respective coherence lengths. This limitation can be removed by a technique called quasi phase matching, where the sign of the nonlinear susceptibility $(\chi^2)$ of

the core material is inverted periodically at every $L_c$ as explained in relation to Figure 5.16.
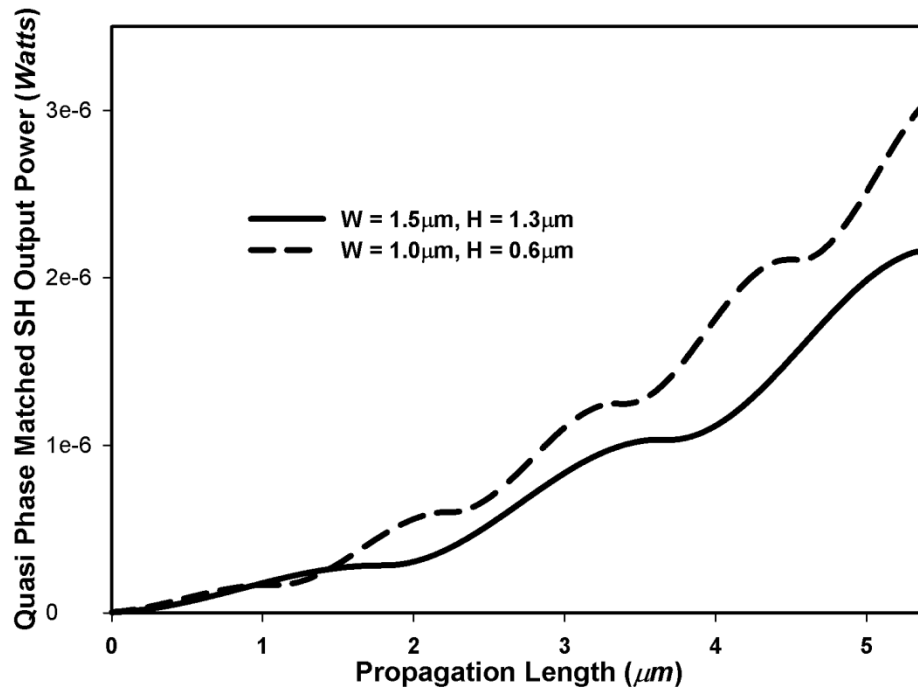


Figure 5.16 Variation of the QPM SH output power against the propagation length with different width and height combinations.

The direction of power exchange between the fundamental and second harmonic waves depends on their relative phase difference and this changes sign at a distance equal to the coherence length. Furthermore, noting the change of sign of the nonlinear susceptibility ($\chi^{(2)}$) at every $L_c$, the phase of the polarisation wave will be shifted by $\pi$, effectively re-phasing the interaction and leading to a monotonic power flow into the second harmonic wave [136]. In Figure 5.16 the solid curve shows the first order Quasi Phase Matched (QPM) SH output power for a width of 1.5 $\mu m$ and height of 1.3 $\mu m$, i.e. optimised dimensions as per Figure 5.13 and Figure 5.14, against the length. In this case (i.e. solid curve) the $L_c$ is ~1.9$\mu m$. The fabrication of the QPM for every sub-micrometer scale $L_c$ (~1.9$\mu m$) can be achieved in practice by using different techniques such as the lithography technique [197]. Figure 5.16 also shows the first order QPM SH output power for a core width of 1.0 $\mu m$ and height of 0.6$\mu m$. In this case, the normalised conversion efficiency of $\eta_{norm} = 1.0 \times 10^{-7} W^{-1} \mu m^{-2}$. This value was higher than the reported value of $\eta_{norm} = 0.15 \times$

$10^{-7} W^{-1} \mu m^{-2}$ for a periodically poled $LiNbO_3$ waveguide device [198]. Although power conversion within a single $L_c$ section was lower for $H = 0.6\,\mu m$ and $W = 1.0\,\mu m$, compared to that for $H = 1.3\,\mu m$ and $W = 1.5\,\mu m$, its overall rate of energy transfer was higher. Therefore, when QPM was implemented, the overall SHG for the first case (i.e. $H = 0.6\,\mu m$ and $W = 1.0\,\mu m$) was higher as shown here.



(a) $H = 1.3\,\mu m$ and $W = 1.5\,\mu m$      (b) $H = 0.6\,\mu m$ and $W = 1.0\,\mu m$
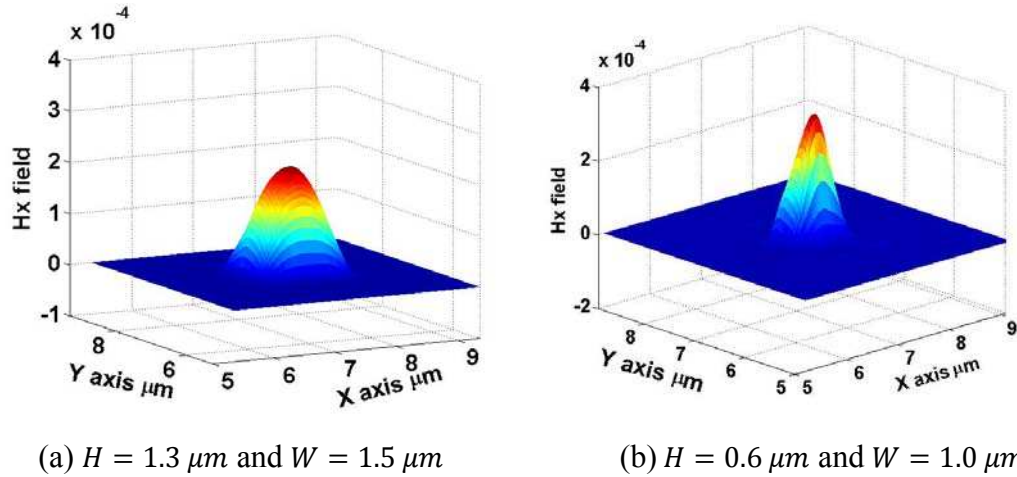
Figure 5.17 The 3-D mode profiles of the QPM SH output mode after propagation of a distance of $5.5\,\mu m$.

Figure 5.17 (a) and (b) show the QPM SH output 3-D field profiles of the two curves in Figure 5.16, after the propagation of $5.5\,\mu m$. The field magnitude value in Figure 5.17 (a) is 50% higher than that of Figure 5.17 (b). Further, in Figure 5.17 (a) the spot-size is higher ($1.14\,\mu m^2$) than that of Figure 5.17 (b) ($0.35\,\mu m^2$) due to the higher dimensions of the $ZnO$ optical waveguide and this difference can be clearly seen.

## 5.4 SUMMARY

This chapter presents another key contribution and novel aspect of the work of this thesis carried out by the author in the application of the rigorous full-vectorial FE-based BPM formulation to the analysis of SHG in optical waveguides with hybrid modes. The major aspects and achievements of the work are summarised below.

In this chapter, a rigorous full-vectorial FE based BPM formulation has been applied to determine the mode spectrum of different *ZnO* optical waveguide structures. This numerical method has been applied to analyse the modal solutions and to allow calculation of the SHG in *ZnO* waveguides where inherently hybrid modes exist. It can be noted that by changing the height and width values of the *ZnO* waveguide, it is possible to achieve an improved SH output power. The higher output power is a result of the higher overlap integral due to the optimised modal properties in the waveguide structure. The key finding of the work of the author presented in this chapter is that the SHG efficiency in *ZnO* can be higher than in the more widely used $LiNbO_3$, due to the stronger confinement and the modal overlap integral. The QPM technique has been applied in order to obtain higher SH output power and to eliminate the phase mismatch between the fundamental and SH waves. Moreover, the practical implementation of the fabrication techniques of the *ZnO* waveguides and the application of QPM in the waveguide have also been addressed.

# Conclusions and Future Directions

The work presented in this thesis has addressed primarily the generation of SHG in several optical waveguides of emerging importance and interest, such as hexagonal Photonic Crystal Fibres (PCF), Equiangular Spiral PCF (ES-PCF) and *ZnO* waveguides. The prime objective of this thesis, which was to demonstrate enhanced SHG in optical waveguides by employing different materials ($SiO_2$, $SF57$ and $ZnO$) and optimised waveguide structures, has been successfully achieved by applying the rigorous numerical analysis methods introduced at the beginning of the thesis. Section 6.1 presents the conclusions from each chapter and a summary of how the contributions made in this work relate the aims and objectives set out in Chapter 1 drawn while Section 6.2 provides suggestions for potential future research building on the work done and results achieved.

## 6.1 CONCLUSIONS AND CONTRIBUTIONS

At the outset of this work, in Chapter 1, a number of specific aims and objectives were set and the major contributions to knowledge in the field from the work of the author can be summarised below (*with contributions in each chapter summarised in italics*):

(i)    To produce a methodology for the analysis of second harmonic generation in different types of optical waveguides with different materials by implementing the Finite Element based Beam propagation Method (FE-BPM) based on the rigorous full vectorial $H$-field formulation: *this formulation was developed in Chapter 3*.

(ii)   To investigate Second Harmonic Generation (SHG) in nonlinear materials such as $SiO_2$, $SF57$ and $ZnO$ and their poling orientations; also to optimise second harmonic output power with the use of the Quasi Phase Matching (QPM) technique and adjusting the poling direction: *the details of the results obtained from this work were presented in Chapter 3*.

(iii)  To employ the scalar Beam Propagation Method (BPM) in order to analyse SHG guided wave propagation in optimised conventional PCF and Equiangular Spiral PCFs; further, to investigate error tolerances of the coherence length and the fabrication errors in the QPM technique: *this work and its results were reported in Chapter 4*.

(iv)   To employ the full vectorial Beam Propagation Method (BPM) in order to analyse SHG guided wave propagation in optimised $ZnO$ optical waveguides: *this work and its results were reported in Chapter 5*.

(v) To report findings to the community through papers published in the international journals and conferences: *The key contributions from the author were disseminated to the research community via recognised channels (given in the list of Author Publications on page 173)*.

The contributions are discussed in detail below.

The Finite Element based Beam Propagation Method (FE-BPM), which is one of the most widely used numerical methods used in the analysis of optical waveguides, has been employed in this work in order to analyse the propagation of SHG in optical waveguides, while the vectorial Finite Element Method (FEM) has been used to analyse the modal solutions of the optical waveguides. Further, for the stationary analysis of the modal fields, the finite element formulation with the use of vector-$H$ field, which consists of the penalty function to eliminate spurious solutions has been employed. Moreover, it was necessary to consider special boundary conditions at the

dielectric interfaces of the optical waveguides. Therefore, the *H* field has been utilised in this work due to its natural ability to be continuous across the dielectric interfaces of the optical waveguides. The scalar BPM has also been utilised to analyse the SHG propagation in hexagonal PCF and ES-PCF and the full vectorial BPM has been employed to analyse the SHG propagation in *ZnO* waveguides with the use of the Quasi Phase Matching (QPM) technique in order to optimise the SHG.

Chapter 2 of this thesis has built the theoretical formulation needed for the use of FEM and BPM as a numerical analysis and modelling technique for various optical waveguides. Traditionally the scalar field approximation can be implemented by splitting the field components into two subcomponents, i.e. *TE* mode *TM* modes. However, the application of the scalar field approximation has not been sufficient for the optical waveguides with reduced dimensions and a high index contrast between the core and cladding. Therefore, the full vector-*H* field formulation has been employed where the modes of such optical waveguides are largely hybrid in nature, i.e. consist of six components of electric and magnetic fields. Following that a full vectorial FE-BPM has been developed by the author (Chapter 3) with the assumption of the slowly varying envelope function and the application of the finite element approach by applying the Crank-Nicolson scheme.

A novel optimisation of the SHG optical waveguide structures with respect to polar axis in nonlinear materials was undertaken by the author and this work was presented in Chapter 3. Further, an extended study was done to identify the axis of propagation in the waveguide with respect to the poling direction and for different orientation of crystal axes to achieve a higher SH conversion efficiency, while choosing the waveguide structure with the fabrication constraints has also been considered. The QPM technique has been used to eliminate phase mismatches between the fundamental and SH frequencies; the application of the higher order QPMs were also studied.

Chapter 4 enabled a presentation of the results on SHG in PCFs by using the scalar BPM (based on the numerical formulation from Chapter 3). This chapter included the analysis by the author of two types of PCF structures, i.e. hexagonal PCF and ES-PCF. In the analysis of SHG in a conventional silica fibre, the numerical results were first validated by comparing with corresponding practical results. The SHG in

hexagonal PCF with a defect air-hole was compared with the hexagonal PCF without a defect hole and it was proved that introducing a defect hole does not improve the overlap integral and results in low SH output power. In this case silica has been used as a material. Further, modal solutions in hexagonal PCF with *SF*57 have also been studied. The recently introduced ES-PCF structure was studied by using *SF*57, and shown to have significant improvement in producing SH output power compared to that of hexagonal silica PCF. Further, the advantages of the *SF*57 material when fabricating such a complicated structure by using extrusion methods have been identified. In the work demonstrated, the power was increased by 31% in ES-PCF with *SF*57 material after propagation of 250 $\mu m$ in comparison with hexagonal silica PCF. The hexagonal PCF was employed in order to assess the impact of choice of material using silica and *SF*57 on SHG, where hexagonal *SF*57 PCF showed a good improvement in the SH output power over the others. QPM was applied in all cases to eliminate the phase mismatch between fundamental and SH frequencies. The error tolerance in QPM including higher order QPMs were also analysed which are very useful factors when it comes to practical implementation of optical waveguide devices.

The investigation of SHG in *ZnO* planar waveguides by using the full vectorial BPM was presented in Chapter 5 (based on the numerical formulation from Chapter 3). In this chapter *ZnO* planar waveguides were analysed for different width and height values. In this study the SH output power was observed while varying the dimensions of the *ZnO* planar waveguide. Initially the numerical results were validated by comparing with the scalar BPM results presented in Chapter 4 with the same conventional silica fibre. Further validation has been done by comparing the SH output power with full and quarter structures. The nonlinear relationship between the pump power and QPM SH output power and the linear relationship between the maximum $H_x$ and the pump power were also discussed in order to further analyse the full vectorial BPM results. Moreover, results were obtained for modal solutions of the *ZnO* planar waveguides by using full vectorial FEM for different aspect ratios of the *ZnO* planar waveguides. It was also found that the maximum SH output power was obtained at a height of 1.3 $\mu m$ with the corresponding width value of 1.5 $\mu m$ of the *ZnO* planar waveguide after the propagation of a 5.5 $\mu m$. Possible fabrication techniques to achieve QPM for every sub-micron scale of coherence length values

were also discussed. Subsequently, it was shown that the normalised conversion efficiency of $ZnO$ planar waveguide (i.e. $\eta_{norm} = 1.0 \times 10^{-7} W^{-1} \mu m^{-2}$) was considerably higher than the reported value for a periodically poled $LiNbO_3$ waveguide device (i.e. $\eta_{norm} = 0.15 \times 10^{-7} W^{-1} \mu m^{-2}$).

Thus the work of this thesis has enabled a major contribution to knowledge by the author which was disseminated to the international community through published papers and conference presentations.

## 6.2 FUTURE DIRECTIONS

This research work has focused predominantly on the numerical analysis of SHG in optical waveguides based on the successful development of the full vectorial BPM and identified various design choices that would greatly enhance the SHG in optical waveguides. The application of QPM in nonlinear crystals with alternating second order nonlinear susceptibility and the use of correct poling direction was also identified. This provides the basis for valuable future work which could be carried out in order to further optimise and refine the optical waveguide parameters for an efficient SHG. Some important future directions are identified below.

The SHG approach relies mainly on optical waveguide characteristics, nonlinear material as well as phase matching techniques. Therefore, it appears sensible to consider alternative materials for optical waveguides such as highly nonlinear thermally poled chalcogenide glasses ($Ga_5 Ge_{20} Sb_{10} S_{65}$) [199] to overcome the main limitations such as second order nonlinear susceptibility and coherence length. Furthermore, $ZnO$ planar waveguides can be numerically modelled in the nano region and analysed with various substrates and claddings such as silica, silicon, $GaAs$, quartz and $LiNbO_3$ in order to model optical devices such as solar cells, thin film transistors and biophotonics, especially when analysing SHG in nano scale optical waveguides where the modes exists in hybrid nature for which the full vectorial BPM becomes an ideal candidate.

Moreover, the full vectorial method developed in this research work can also be extended to model and analyse the SHG in PCFs with a seeding SH power. In this work, initial SH power is zero and it slowly builds up along the propagation length. Therefore, application of seeding SH power can be a useful factor to prevent the excessive use of pump powers. The seeding SH power has been applied to reduce the

complexity of master oscillator power amplifiers with single stage ytterbium doped PCF amplifiers by using continuous wave fibre lasers [200]. Hence, the seeding SH power is a potential candidate in optoelectronics for continuous wave fibre lasers and can be analysed with the use of full vectorial BPM.

Another important consideration is the parametric nonlinearities arising from third order nonlinear polarisation i.e. $P_{NL} = \varepsilon_0 \chi^{(3)} E^3$. Third order nonlinearity is similar to second order processes which involves three waves together although the third order processes four waves together. Four-wave mixing is a nonlinear effect arising from third order optical nonlinearity which can also be numerically analysed by using the full vectorial BPM. The main difference is that third order nonlinearity can exist in materials without non-inversion symmetry whereas second order nonlinearity does not exist in materials without non-inversion symmetry. Furthermore, four-wave mixing can be utilised in a wide range of applications such as real-time holographic imaging [201], phase conjunction [202] and real-time image processing [203].

Overall, the above future directions provide considerable scope for future research which would greatly advance the field of photonics.

# Appendix 1

The evaluation of the element matrix $[A]_e$ from equation (2.60);

$$[A]_e = \varepsilon^{-1} \int_\Delta [Q]^*[Q] d\Omega$$

$$= \varepsilon^{-1} \int_\Delta \begin{bmatrix} -\beta^2 [N]^T[N] + \dfrac{\partial[N]^T}{\partial y}\dfrac{\partial[N]}{\partial y} & -\dfrac{\partial[N]^T}{\partial y}\dfrac{\partial[N]}{\partial x} & j\beta[N]^T\dfrac{\partial[N]}{\partial x} \\[2mm] -\dfrac{\partial[N]^T}{\partial x}\dfrac{\partial[N]}{\partial y} & -\beta^2[N]^T[N] + \dfrac{\partial[N]^T}{\partial x}\dfrac{\partial[N]}{\partial x} & j\beta[N]^T\dfrac{\partial[N]}{\partial y} \\[2mm] j\beta\dfrac{\partial[N]^T}{\partial x}[N] & j\beta\dfrac{\partial[N]^T}{\partial y}[N] & \dfrac{\partial[N]^T}{\partial y}\dfrac{\partial[N]}{\partial y} + \dfrac{\partial[N]^T}{\partial x}\dfrac{\partial[N]}{\partial x} \end{bmatrix} d\Omega \qquad (A1.1)$$

The evaluation of the element matrix $[B]_e$ from equation (2.61);

$$[B]_e = \mu \int_\Delta [\boldsymbol{N}]^T[\boldsymbol{N}] \, d\Omega = \mu \int_\Delta \begin{bmatrix} [N]^T[N] & [0]^T[0] & [0]^T[0] \\ [0]^T[0] & [N]^T[N] & [0]^T[0] \\ [0]^T[0] & [0]^T[0] & [N]^T[N] \end{bmatrix} d\Omega \qquad (A1.2)$$

The evaluation of the integrations of the shape functions in equation (A1.1) and (A1.2) for a triangular element;

$$\int_\Delta N_1^i N_2^j N_3^k d\Omega = \frac{i! \, j! \, k! \, 2!}{(i + j + k + 2)!} A_e \qquad (A1.3)$$

where $A_e$ is the area of the triangular element.

Therefore the following integrals can be obtained;

$$\int_\Delta N_1^2 d\Omega = \int_\Delta N_2^2 d\Omega = \int_\Delta N_3^2 d\Omega = \frac{A_e}{6} \qquad (A1.4)$$

$$\int_\Delta N_1 N_2 d\Omega = \int_\Delta N_2 N_3 d\Omega = \int_\Delta N_1 N_3 d\Omega = \frac{A_e}{12} \qquad (A1.5)$$

$$\int\limits_{\Delta} d\Omega = A_e \tag{A1.6}$$

From equation (A1.1) some of the elements of the $9 \times 9$ $[A]_e$ matrix can be written as;

$$[A]_{e(1,1)} = \frac{1}{\varepsilon} \int\limits_{\Delta} -\beta^2 N_1^2 + \left(\frac{\partial N_1}{\partial y}\right)^2 d\Omega = \frac{1}{\varepsilon}\left[\frac{-\beta^2 A_e}{6} + c_1^2 A_e\right] \tag{A1.7}$$

$$[A]_{e(1,2)} = \frac{1}{\varepsilon} \int\limits_{\Delta} -\beta^2 N_1 N_2 \frac{\partial N_1}{\partial y}\frac{\partial N_2}{\partial y} d\Omega = \frac{1}{\varepsilon}\left[\frac{-\beta^2 A_e}{12} + c_1 c_2 A_e\right] \tag{A1.8}$$

$$[A]_{e(1,4)} = \frac{1}{\varepsilon} \int\limits_{\Delta} -\frac{\partial N_1}{\partial y}\frac{\partial N_1}{\partial x} d\Omega = -\frac{1}{\varepsilon} c_1 b_1 A_e \tag{A1.9}$$

From equation (A1.2) some of the elements of the $9 \times 9$ $[B]_e$ matrix can be written as;

$$[B]_{e(1,1)} = \mu \int\limits_{\Delta} N_1^2 d\Omega = \mu \frac{A_e}{6} \tag{A1.10}$$

$$[B]_{e(1,2)} = \mu \int\limits_{\Delta} N_1 N_2 d\Omega = \mu \frac{A_e}{12} \tag{A1.11}$$

$$[B]_{e(1,4)} = 0 \tag{A1.12}$$

# Appendix 2

From equation (2.36), the matrices $[M_{xx}]$ and $[M_{yy}]$ can be represented as;

$$[M_{xx}] = [M_{yy}] = \varepsilon_r^{-1} \begin{bmatrix} \int_e N_1^2 \, ds & \int_e N_1 N_2 \, ds & \int_e N_1 N_3 \, ds \\ \int_e N_2 N_1 \, ds & \int_e N_2^2 \, ds & \int_e N_2 N_3 \, ds \\ \int_e N_3 N_1 \, ds & \int_e N_3 N_2 \, ds & \int_e N_3^2 \, ds \end{bmatrix} \qquad (A2.1)$$

From equation (2.37), the matrices $[K_{xx}]$ and $[K_{yy}]$ can be represented as;

$$[K_{xx}] = [K_{tt}] = [K_{xx}]_{\Gamma_e} \qquad (A2.2)$$

$$[K_{yy}] = [K_{tt}] = [K_{yy}]_{\Gamma_e} \qquad (A2.3)$$

where,

$$[\boldsymbol{K}_{tt}] = k_0^2 \begin{bmatrix} \int\limits_e N_1^2 ds & \int\limits_e N_1 N_2 ds & \int\limits_e N_1 N_3 ds \\[2em] \int\limits_e N_2 N_1 ds & \int\limits_e N_2^2 ds & \int\limits_e N_2 N_3 ds \\[2em] \int\limits_e N_3 N_1 ds & \int\limits_e N_3 N_2 ds & \int\limits_e N_3^2 ds \end{bmatrix}$$

$$- \varepsilon_r^{-1} \alpha_y^2 \begin{bmatrix} \int\limits_e N_{1y}^2 ds & \int\limits_e N_{1y} N_{2y} ds & \int\limits_e N_{1y} N_{3y} ds \\[2em] \int\limits_e N_{2y} N_{1y} ds & \int\limits_e N_{2y}^2 ds & \int\limits_e N_{2y} N_{3y} ds \\[2em] \int\limits_e N_{3y} N_{1y} ds & \int\limits_e N_{3y} N_{2y} ds & \int\limits_e N_{3y}^2 ds \end{bmatrix} \qquad \text{(A2.4)}$$

$$- \varepsilon_r^{-1} \alpha_x^2 \begin{bmatrix} \int\limits_e N_{1x}^2 ds & \int\limits_e N_{1x} N_{2x} ds & \int\limits_e N_{1x} N_{3x} ds \\[2em] \int\limits_e N_{2x} N_{1x} ds & \int\limits_e N_{2x}^2 ds & \int\limits_e N_{2x} N_{3x} ds \\[2em] \int\limits_e N_{3x} N_{1x} ds & \int\limits_e N_{3x} N_{2x} ds & \int\limits_e N_{3x}^2 ds \end{bmatrix}$$

where $N_{ix}$ and $N_{iy}$, ($i = 1,2,3$) denotes the $x$ and $y$ derivatives of the shape function $N_i$, respectively.

From equation (A2.2) and (A2.3) the matrices $[\boldsymbol{K}_{xx}]_{\Gamma_e}$ and $[\boldsymbol{K}_{yy}]_{\Gamma_e}$ can be written as;

$$[\boldsymbol{K}_{xx}]_{\Gamma_e} = \varepsilon_r^{-1} \alpha_x^2 \begin{bmatrix} \oint\limits_{\Gamma_e} N_1 N_{1x} n_x d\Gamma_e & \oint\limits_{\Gamma_e} N_1 N_{2x} n_x d\Gamma_e & \oint\limits_{\Gamma_e} N_1 N_{3x} n_x d\Gamma_e \\[2em] \oint\limits_{\Gamma_e} N_2 N_{1x} n_x d\Gamma_e & \oint\limits_{\Gamma_e} N_2 N_{2x} n_x d\Gamma_e & \oint\limits_{\Gamma_e} N_2 N_{3x} n_x d\Gamma_e \\[2em] \oint\limits_{\Gamma_e} N_3 N_{1x} n_x d\Gamma_e & \oint\limits_{\Gamma_e} N_3 N_{2x} n_x d\Gamma_e & \oint\limits_{\Gamma_e} N_3 N_{3x} n_x d\Gamma_e \end{bmatrix} \qquad \text{(A2.5)}$$

$$\left[\boldsymbol{K}_{yy}\right]_{\Gamma_e} = \varepsilon_r^{-1}\alpha_y^2 \begin{bmatrix} \oint\limits_{\Gamma_e} N_1 N_{1y} n_y d\Gamma_e & \oint\limits_{\Gamma_e} N_1 N_{2y} n_y d\Gamma_e & \oint\limits_{\Gamma_e} N_1 N_{3y} n_y d\Gamma_e \\ \oint\limits_{\Gamma_e} N_2 N_{1y} n_y d\Gamma_e & \oint\limits_{\Gamma_e} N_2 N_{2y} n_y d\Gamma_e & \oint\limits_{\Gamma_e} N_2 N_{3y} n_y d\Gamma_e \\ \oint\limits_{\Gamma_e} N_3 N_{1y} n_y d\Gamma_e & \oint\limits_{\Gamma_e} N_3 N_{2y} n_y d\Gamma_e & \oint\limits_{\Gamma_e} N_3 N_{3y} n_y d\Gamma_e \end{bmatrix} \quad (A2.6)$$

The matrices $\left[\boldsymbol{K}_{xy}\right]$ and $\left[\boldsymbol{K}_{yx}\right]$ in equation (2.37) can be written as;

$$\left[\boldsymbol{K}_{xy}\right] = [\boldsymbol{K}_1] - [\boldsymbol{K}_2] + \left[\boldsymbol{K}_{xy}\right]_{\Gamma_e} \quad (A2.7)$$

$$\left[\boldsymbol{K}_{yx}\right] = [\boldsymbol{K}_2] - [\boldsymbol{K}_1] + \left[\boldsymbol{K}_{yx}\right]_{\Gamma_e} \quad (A2.8)$$

where,

$$[\boldsymbol{K}_1] = \varepsilon_r^{-1}\alpha_x\alpha_y \begin{bmatrix} \int\limits_e N_{1y} N_{1x} ds & \int\limits_e N_{1y} N_{2x} ds & \int\limits_e N_{1y} N_{3x} ds \\ \int\limits_e N_{2y} N_{1x} ds & \int\limits_e N_{2y} N_{2x} ds & \int\limits_e N_{2y} N_{3x} ds \\ \int\limits_e N_{3y} N_{1x} ds & \int\limits_e N_{3y} N_{2x} ds & \int\limits_e N_{3y} N_{3x} ds \end{bmatrix} \quad (A2.9)$$

$$[\boldsymbol{K}_2] = \varepsilon_r^{-1}\alpha_x\alpha_y \begin{bmatrix} \int\limits_e N_{1x} N_{1y} ds & \int\limits_e N_{1x} N_{2y} ds & \int\limits_e N_{1x} N_{3y} ds \\ \int\limits_e N_{2x} N_{1y} ds & \int\limits_e N_{2x} N_{2y} ds & \int\limits_e N_{2x} N_{3y} ds \\ \int\limits_e N_{3x} N_{1y} ds & \int\limits_e N_{3x} N_{2y} ds & \int\limits_e N_{3x} N_{3y} ds \end{bmatrix} \quad (A2.10)$$

$$\left[\boldsymbol{K}_{xy}\right]_{\Gamma_e} = \varepsilon_r^{-1}\alpha_x\alpha_y \begin{bmatrix} \oint_{\Gamma_e} N_1 N_{1y} n_x d\Gamma_e & \oint_{\Gamma_e} N_1 N_{2y} n_x d\Gamma_e & \oint_{\Gamma_e} N_1 N_{3y} n_x d\Gamma_e \\ \oint_{\Gamma_e} N_2 N_{1y} n_x d\Gamma_e & \oint_{\Gamma_e} N_2 N_{2y} n_x d\Gamma_e & \oint_{\Gamma_e} N_2 N_{3y} n_x d\Gamma_e \\ \oint_{\Gamma_e} N_3 N_{1y} n_x d\Gamma_e & \oint_{\Gamma_e} N_3 N_{2y} n_x d\Gamma_e & \oint_{\Gamma_e} N_3 N_{3y} n_x d\Gamma_e \end{bmatrix} \quad (A2.11)$$

$$\left[\boldsymbol{K}_{yx}\right]_{\Gamma_e} = \varepsilon_r^{-1}\alpha_x\alpha_y \begin{bmatrix} \oint_{\Gamma_e} N_1 N_{1x} n_y d\Gamma_e & \oint_{\Gamma_e} N_1 N_{2x} n_y d\Gamma_e & \oint_{\Gamma_e} N_1 N_{3x} n_y d\Gamma_e \\ \oint_{\Gamma_e} N_2 N_{1x} n_y d\Gamma_e & \oint_{\Gamma_e} N_2 N_{2x} n_y d\Gamma_e & \oint_{\Gamma_e} N_2 N_{3x} n_y d\Gamma_e \\ \oint_{\Gamma_e} N_3 N_{1x} n_y d\Gamma_e & \oint_{\Gamma_e} N_3 N_{2x} n_y d\Gamma_e & \oint_{\Gamma_e} N_3 N_{3x} n_y d\Gamma_e \end{bmatrix} \quad (A2.12)$$

The shape function integrals in $[\boldsymbol{M}]_e$ and $[\boldsymbol{K}]_e$ matrices can be derived by using the following formulae;

$$\int_e N_1^i N_2^j N_3^k ds = \frac{i!\,j!\,k!\,2!}{(i+j+k+2)!} A_e \quad (A2.13)$$

$$\int_{\Gamma_e} N_1^i N_2^j d\Gamma_e = \frac{i!\,j!}{(i+j+1)!} l_{12} \quad (A2.14)$$

where $A_e$ is the element area related to the nodal coordinates of the triangular element, $\Gamma_e$ and $l_{12}$ are the part and length of the element boundary connecting the nodes 1 and 2, respectively.

### *Shape Function*

The shape function can be defined in terms of complete polynomials which are normalised over each element. These are also known as interpolation functions. The shape function can be applied for a typical triangular element such that it uniquely defines the field within the element under consideration. This section will present the derivation of the interpolation polynomials for the basic two dimensional elements in terms of the global coordinates that are defined for the entire domain. Figure A2.1 shows a two dimensional first order triangular element where $a$, $b$ and $c$ are the three nodal points of the element and $(x_1, y_1)$, $(x_2, y_2)$ and $(x_3, y_3)$ are their coordinates respectively.
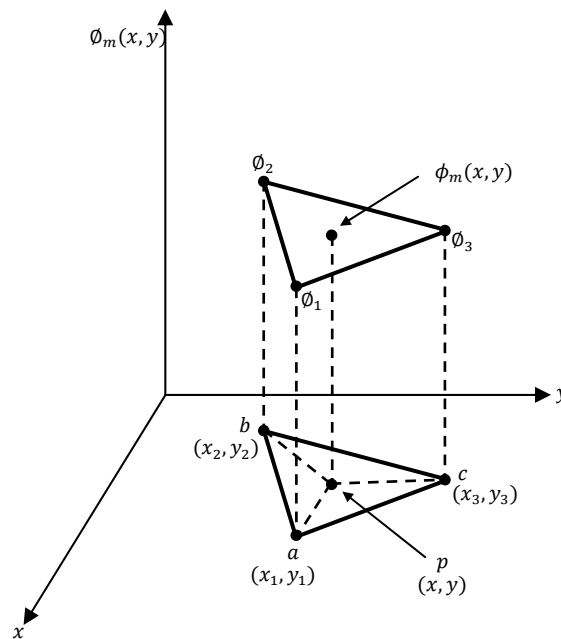


Figure A2.1 Diagram of a typical two dimensional first order triangular element.

Inside the triangular element, the field $\phi$ is interpolated continuously. $N_i(x, y)$ is defined as the shape function and $\phi_m(x, y)$ is defined as the field inside each element. For $i = 1, 2, 3$;

$$\phi_m(x, y) = \sum_{i=1}^{3} N_i(x, y) \cdot \phi_i \qquad (A2.15)$$

where $\phi_i$ are the nodal field values. Equation (A2.15) can be written in the following matrix form;

$$\phi_m(x,y) = [N_1 \quad N_2 \quad N_2] \begin{Bmatrix} \phi_1 \\ \phi_2 \\ \phi_3 \end{Bmatrix} \tag{A2.16}$$

Therefore;

$$\phi_m(x,y) = [N]\{\phi_m\} \tag{A2.17}$$

where $[N]$ is the matrix form of the shape function and $\{\phi_m\}$ is the vector corresponding to the element nodal field values at the three nodes of the triangular element.

Linear approximation of the field inside an element is considered in order to obtain the shape function, $N_i(x,y), i = 1,2,3$;

$$\phi_m(x,y) = \alpha_1 + \alpha_2 x + \alpha_3 y \tag{A2.18}$$

where $\alpha_1, \alpha_2$ and $\alpha_3$ are constants.

Equation (A2.18) can be rewritten to satisfy the following condition;

$$\phi_m(x_i, y_i) = \phi_i \tag{A2.19}$$

Therefore, the three nodal field values $\phi_i$ can be expressed as;

$$\phi_1 \equiv \phi_m(x_1, y_1) = \alpha_1 + \alpha_2 x_1 + \alpha_3 y_1 \tag{A2.20}$$

$$\phi_2 \equiv \phi_m(x_2, y_2) = \alpha_1 + \alpha_2 x_2 + \alpha_3 y_2 \tag{A2.21}$$

$$\phi_3 \equiv \phi_m(x_3, y_3) = \alpha_1 + \alpha_2 x_3 + \alpha_3 y_3 \tag{A2.22}$$

Further, this can be written in the matrix form as;

$$\begin{Bmatrix} \phi_1 \\ \phi_2 \\ \phi_3 \end{Bmatrix} = \begin{bmatrix} 1 & x_1 & y_1 \\ 1 & x_2 & y_2 \\ 1 & x_3 & y_3 \end{bmatrix} \begin{Bmatrix} \alpha_1 \\ \alpha_2 \\ \alpha_3 \end{Bmatrix} \tag{A2.23}$$

From equation (A2.23), the constants $\alpha_1$, $\alpha_2$ and $\alpha_3$ can be determined in terms of $\phi_i, \ i = 1,2,3$:

$$\alpha_1 = \frac{1}{2A_e}[\phi_1(x_2y_3 - x_3y_2) + \phi_2(x_3y_1 - x_1y_3) + \phi_3(x_1y_2 - x_2y_1)] \quad \text{(A2.24)}$$

$$\alpha_2 = \frac{1}{2A_e}[\phi_1(y_2 - y_3) + \phi_2(y_3 - y_1) + \phi_3(y_2 - y_1)] \quad \text{(A2.25)}$$

$$\alpha_3 = \frac{1}{2A_e}[\phi_1(x_3 - x_2) + \phi_2(x_1 - x_3) + \phi_3(x_2 - x_1)] \quad \text{(A2.26)}$$

where $A_e$ denotes the area of the triangular element which is given by;

$$A_e = \frac{1}{2}\begin{vmatrix} 1 & x_1 & y_1 \\ 1 & x_2 & y_2 \\ 1 & x_3 & y_3 \end{vmatrix} = \frac{1}{2}[(x_2y_3 - x_3y_2) + (x_3y_1 - x_1y_3) + (x_1y_2 - x_2y_1)] \quad \text{(A2.27)}$$

Substituting equation (A2.24), (A2.25) and (A2.26) into equation (A2.18) yields the following;

$$\phi_m(x, y) = N_1(x, y) \cdot \phi_1 + N_2(x, y) \cdot \phi_2 + N_3(x, y) \cdot \phi_3 \quad \text{(A2.28)}$$

Hence,

$$\phi_m(x, y) = [N]\{\phi_m\}$$

Equation (A2.28) is similar to the equation (A2.17) and $N_i(x, y), i = 1, 2, 3$; therefore, the shape function can be written as;

$$[N]^T = \begin{bmatrix} N_1 \\ N_2 \\ N_3 \end{bmatrix} = \frac{1}{2A_e}\begin{bmatrix} x_2y_3 - x_3y_2 & y_2 - y_3 & x_3 - x_2 \\ x_3y_1 - x_1y_3 & y_3 - y_1 & x_1 - x_3 \\ x_1y_2 - x_2y_1 & y_1 - y_2 & x_2 - x_1 \end{bmatrix}\begin{bmatrix} 1 \\ x \\ y \end{bmatrix} \quad \text{(A2.29)}$$

where $T$ denotes the transpose of the matrix $[N]$. The shape function can be represented in a similar matrix form, i.e.;

$$[N]^T = \begin{bmatrix} N_1 \\ N_2 \\ N_3 \end{bmatrix} = \begin{bmatrix} a_1 + b_1x + c_1y \\ a_2 + b_2x + c_2y \\ a_3 + b_3x + c_3y \end{bmatrix} \quad \text{(A2.30)}$$

where $a_i, b_i, c_i$ $(i = 1, 2, 3)$ are the coefficients of the shape function which can be determined as follows;

$$a_1 = \frac{x_2y_3 - x_3y_2}{2A_e} \quad \text{(A2.31)}$$

$$b_1 = \frac{y_2 - y_3}{2A_e} \quad \text{(A2.32)}$$

$$c_1 = \frac{x_3 - x_2}{2A_e} \qquad (A2.33)$$

$a_2, b_2, c_2$ and $a_3, b_3, c_3$ can be determined in a cyclic pattern.

As shown in Figure A2.1, a typical point $p$ can be assigned inside the triangular element. Therefore, the shape function $N_i$ can be expressed in terms of the areas of the triangles.

$$N_1 = \frac{area\ of\ the\ sub\ triangle\ (p, b, c)}{area\ of\ the\ full\ triangle\ (a, b, c)} \qquad (A2.34)$$

$N_2$ and $N_3$ can be expressed similarly. Therefore, $N_i$ has the following property.

$$\sum_{i=1}^{3} N_i = 1 \qquad (A2.35)$$

According to the equation (A2.35), the value of the shape function $N_1$ at $a(x_1, y_1)$ is one, and for $b(x_2, y_2)$ and $c(x_3, y_3)$ the value of the shape function $N_1$ is zero. This is known as the unique first-degree interpolation function for $a(x_1, y_1)$. Similarly the shape functions $N_2$ and $N_3$ give a value of one at $b(x_1, y_1)$ and $c(x_1, y_1)$ respectively and zero at other nodes.

### *Assembly of Element and Global Matrices*

The FEM can be expressed as a standard eigenvalue problem as given in equation (2.21). The matrices [*A*] and [*B*] are known as the global matrices and consist of triangular element matrices of the discretized cross-section of the waveguide. In this section the generation of element matrices and assembly of global matrices are shown for the vector *H*-field formulation. Within each triangular element the unknown *H*-field components $H_x$, $H_y$ and $H_z$ can be written as;

$$H_x(x, y) = [N_1 \quad N_2 \quad N_3] \begin{Bmatrix} H_{x1} \\ H_{x2} \\ H_{x3} \end{Bmatrix} \qquad (A2.36)$$

$$H_y(x, y) = [N_1 \quad N_2 \quad N_3] \begin{Bmatrix} H_{y1} \\ H_{y2} \\ H_{y3} \end{Bmatrix} \qquad (A2.37)$$

$$H_z(x, y) = [N_1 \quad N_2 \quad N_3] \begin{Bmatrix} H_{z1} \\ H_{z2} \\ H_{z3} \end{Bmatrix} \tag{A2.38}$$

where, $H_{xi}$, $H_{yi}$ and $H_{zi}$; $i = 1, 2, 3$, denotes $x$, $y$ and $z$ components of nodal magnetic fields of each triangular element. From equation (A2.36), (A2.37) and (A2.38) the magnetic field vector $[\boldsymbol{H}]_e$ can be written as;

$$[\boldsymbol{H}]_e = \begin{bmatrix} H_x(x, y) \\ H_y(x, y) \\ H_z(x, y) \end{bmatrix} = \begin{bmatrix} N_1 & N_2 & N_3 & 0 & 0 & 0 & 0 & 0 & 0 \\ 0 & 0 & 0 & N_1 & N_2 & N_3 & 0 & 0 & 0 \\ 0 & 0 & 0 & 0 & 0 & 0 & N_1 & N_2 & N_3 \end{bmatrix} \begin{Bmatrix} H_{x1} \\ H_{x2} \\ H_{x3} \\ H_{y1} \\ H_{y2} \\ H_{y3} \\ H_{z1} \\ H_{z2} \\ H_{z3} \end{Bmatrix} \tag{A2.39}$$

Equation (A2.39) can also be expressed as in the following form;

$$[\boldsymbol{H}]_e = [N]\{H\}_e \tag{A2.40}$$

where $[N]$ is the shape function matrix and $\{H\}_e$ is the column vector representing the three components of the nodal field values in the triangular element.

From equation (A2.40) the curl of magnetic field vector $(\nabla \times \boldsymbol{H})_e$ can be applied in order to define each element and can be written as;

$$(\nabla \times \boldsymbol{H})_e = \nabla \times [N]\{H\}_e = \begin{bmatrix} 0 & -\partial/\partial z & \partial/\partial y \\ \partial/\partial z & 0 & -\partial/\partial x \\ -\partial/\partial y & \partial/\partial x & 0 \end{bmatrix} [N]\{H\}_e = [Q]\{H\}_e \tag{A2.41}$$

where the matrix $[Q]$ can be written as;

$$\begin{aligned} [Q] &= \begin{bmatrix} [0] & -\partial[N]/\partial z & \partial[N]/\partial y \\ \partial[N]/\partial z & [0] & -\partial[N]/\partial x \\ -\partial[N]/\partial y & \partial[N]/\partial x & [0] \end{bmatrix} \\ &= \begin{bmatrix} [0] & j\beta[N] & \partial[N]/\partial y \\ -j\beta[N] & [0] & -\partial[N]/\partial x \\ -\partial[N]/\partial y & \partial[N]/\partial x & [0] \end{bmatrix} \end{aligned} \tag{A2.42}$$

where, $[0] = [0 \quad 0 \quad 0]$, $[N] = [N_1 \quad N_2 \quad N_3]$, $\partial[N]/\partial x = [b_1 \quad b_2 \quad b_3]$ and $\partial[N]/\partial y = [c_1 \quad c_2 \quad c_3]$ and the $\partial[N]/\partial x$ and $\partial[N]/\partial y$ are the differentiated form of equations (A2.32) and (A2.33).

The vector $\mathbf{H}$-field formulation can be expressed for an element by substituting equation (A2.40) and (A2.41) into equation (2.24), and can be obtained as follows;

$$J_e = \int_\Delta \{\mathbf{H}\}_e^T [Q]^* \frac{1}{\hat{\varepsilon}} [Q] \{\mathbf{H}\}_e d\Omega - \omega^2 \int_\Delta \{\mathbf{H}\}_e^T [N]^T \hat{\mu} [N] \{\mathbf{H}\}_e d\Omega \qquad (A2.43)$$

where $T$ and $*$ denote the transpose of a matrix and the complex conjugate respectively, and the integration is carried out over the waveguide cross-section $\Omega$. In isotropic materials, the permittivity ($\varepsilon$) is a scalar value whereas for tensor permittivity, the $\varepsilon$ can be represented in terms of the $3 \times 3$ inverse matrix format.

The relationship between total function, $J$ and the summation of the $n$ number of individual elements over the waveguide cross-section, $J_e$ can be written as;

$$J = \sum_{e=1}^{n} J_e \qquad (A2.44)$$

By differentiating equation (A2.44) with respect to field nodal values and equating it to zero, the relationship can be obtained;

$$\frac{\partial J}{\partial \{H\}_e} = 0 \qquad\qquad e = 1, 2, \ldots \ldots, n \qquad (A2.45)$$

Therefore the following eigenvalue equation can be obtained;

$$[\mathbf{A}]\{\mathbf{H}\} - \omega^2 [\mathbf{B}]\{\mathbf{H}\} = 0 \qquad (A2.46)$$

where,

$$[\mathbf{A}] = \sum_{e=1}^{n} [A]_e = \sum_{e=1}^{n} \int_\Omega \frac{1}{\varepsilon} [Q]^* [Q] d\Omega \qquad (A2.47)$$

$$[\boldsymbol{B}] = \sum_{e=1}^{n} [B]_e = \sum_{e=1}^{n} \int_{\Omega} \mu \, [\boldsymbol{N}]^T [\boldsymbol{N}] d\Omega \qquad \text{(A2.48)}$$

where $[\boldsymbol{A}]$ and $[\boldsymbol{B}]$ are the global matrices, where as $[A]_e$ and $[B]_e$ denote the element matrices. The $\{\boldsymbol{H}\}$ column matrix consists of all the $\boldsymbol{H}$-field nodal values of the waveguide cross-section.

### *Guided Wave Formulation*

The following guided wave formulation can be derived in order to analyse the electromagnetic wave propagation of an optical waveguide using BPM.

By substituting equation (2.7) into (2.10) and equation (2.6) into (2.11), the following Maxwell's curl equations can be derived [118];

$$\nabla \times \boldsymbol{E} = -j\omega\mu_0 \boldsymbol{H} \qquad \text{(A2.49)}$$

$$\nabla \times \boldsymbol{H} = j\omega\varepsilon_0\varepsilon_r \boldsymbol{E} \qquad \text{(A2.50)}$$

where

$$\nabla = \hat{\boldsymbol{x}}\alpha_x \frac{\partial}{\partial x} + \hat{\boldsymbol{y}}\alpha_y \frac{\partial}{\partial y} + \hat{\boldsymbol{z}}\alpha_z \frac{\partial}{\partial z} \qquad \text{(A2.51)}$$

and substituting equation (A2.50) into equation (A2.49) gives;

$$\nabla \times \frac{\nabla \times \boldsymbol{H}}{j\omega\varepsilon_0\varepsilon_r} = -j\omega\mu_0 \boldsymbol{H} \qquad \text{(A2.52)}$$

Hence;

$$\nabla \times [\varepsilon_r^{-1} \nabla \times \boldsymbol{H}] = (j\omega\varepsilon_0)(-j\omega\mu_0)\boldsymbol{H} = k_0^2 \boldsymbol{H} \qquad \text{(A2.53)}$$

Equation (A2.53) which is the full vectorial magnetic field equation, consists of three magnetic field components. However, by using the zero divergence condition, equation (A2.53) can be reduced to two transverse components and by assuming $n^2 (i.e.\ 1/n^2 = \varepsilon_r^{-1})$ varies slowly along the $z$ direction (i.e. direction of propagation); then $\frac{\partial}{\partial z}(\varepsilon_r^{-1}) \approx 0$; and the coupled wave equation for the $H_x$ component can be derived as;

$$\frac{\partial}{\partial z}\left(\varepsilon_r^{-1}\frac{\partial H_x}{\partial z}\right) + \alpha_y\frac{\partial}{\partial y}\left(\varepsilon_r^{-1}\alpha_y\frac{\partial H_x}{\partial y}\right) + \varepsilon_r^{-1}\alpha_x\frac{\partial}{\partial x}\left(\alpha_x\frac{\partial H_x}{\partial x}\right) + k_0^2 H_x$$

$$+ \varepsilon_r^{-1}\alpha_x\frac{\partial}{\partial x}\left(\alpha_y\frac{\partial H_y}{\partial y}\right) - \alpha_y\frac{\partial}{\partial y}\left(\varepsilon_r^{-1}\alpha_x\frac{\partial H_y}{\partial x}\right) = 0$$

(A2.54)

Similarly the coupled wave equation for the $H_y$ component can be derived as;

$$\frac{\partial}{\partial z}\left(\varepsilon_r^{-1}\frac{\partial H_y}{\partial z}\right) + \alpha_x\frac{\partial}{\partial x}\left(\varepsilon_r^{-1}\alpha_x\frac{\partial H_y}{\partial x}\right) + \varepsilon_r^{-1}\alpha_y\frac{\partial}{\partial y}\left(\alpha_y\frac{\partial H_y}{\partial y}\right) + k_0^2 H_y$$

$$+ \varepsilon_r^{-1}\alpha_y\frac{\partial}{\partial y}\left(\alpha_x\frac{\partial H_x}{\partial x}\right) - \alpha_x\frac{\partial}{\partial x}\left(\varepsilon_r^{-1}\alpha_y\frac{\partial H_x}{\partial y}\right) = 0$$

(A2.55)

In equation (A2.54) and (A2.55) the parameter $\alpha_z$ is set to unity (i.e. $\alpha_z = 1$).

Assume the light wave propagates along the z direction in the one-way wave equation. The fields can be separated as a slowly varying field ($\boldsymbol{\phi}_t$) and a fast oscillating term ($e^{-jn_0 k_0 z}$): the relationship can be written as;

$$\boldsymbol{H}_t = \boldsymbol{\phi}_t e^{-jn_0 k_0 z}$$

(A2.56)

where

$$\boldsymbol{H}_{t(x,y,z)} = \hat{x}H_{x(x,y,z)} + \hat{y}H_{y(x,y,z)}$$

$$\boldsymbol{\phi}_t = \hat{x}\phi_{x(x,y,z)} + \hat{y}\phi_{y(x,y,z)}$$

where $t = x$ or $y$, $\boldsymbol{\phi}_t$ are the slowly varying envelopes of the $H_x$ and $H_y$ components respectively and $n_0$ is a reference index of refraction which should be chosen such that the envelope varies slowly in the propagation direction z. Therefore, $n_0$ should be chosen very close to the effective index of the guided mode of the optical waveguide. Further, in monomode optical waveguides, $n_0$ is equal to the effective index of the fundamental mode, whereas in multimode optical waveguides $n_0$ approximates the average of the guide and substrate refractive indices [204]. The following relationship can be identified by taking the differentiation of the equation (A2.56) along the z direction;

$$\frac{\partial \boldsymbol{H}_t}{\partial z} = \left(\frac{\partial \boldsymbol{\phi}_t}{\partial z} - jn_0 k_0 \boldsymbol{\phi}_t\right)e^{-jn_0 k_0 z}$$

(A2.57)

Let $\frac{\partial}{\partial z}\left(\varepsilon_r^{-1}\frac{\partial H_t}{\partial z}\right) \approx \varepsilon_r^{-1}\frac{\partial^2 H_t}{\partial z^2}$ and $\frac{\partial \varepsilon_r^{-1}}{\partial z} \approx 0$, then;

$$\frac{\partial^2 \boldsymbol{H_t}}{\partial z^2} = \left( \frac{\partial^2 \boldsymbol{\phi_t}}{\partial z^2} - 2jn_0 k_0 \frac{\partial \boldsymbol{\phi_t}}{\partial z} - n_0^2 k_0^2 \boldsymbol{\phi_t} \right) e^{-jn_0 k_0 z} \tag{A2.58}$$

By substituting equation (A2.58) into equation (A2.54) and equation (A2.55);

$$\varepsilon_r^{-1} \frac{\partial^2 \phi_x}{\partial z^2} - 2jn_0 k_0 \varepsilon_r^{-1} \frac{\partial \phi_x}{\partial z} + \alpha_y \frac{\partial}{\partial y} \left( \varepsilon_r^{-1} \alpha_y \frac{\partial \phi_x}{\partial y} \right) + \alpha_x \varepsilon_r^{-1} \frac{\partial}{\partial x} \left( \alpha_x \frac{\partial \phi_x}{\partial x} \right)$$

$$+ k_0^2 (1 - \varepsilon_r^{-1} n_0^2) \phi_x + \alpha_x \varepsilon_r^{-1} \frac{\partial}{\partial x} \left( \alpha_y \frac{\partial \phi_y}{\partial y} \right) - \alpha_y \frac{\partial}{\partial y} \left( \varepsilon_r^{-1} \alpha_x \frac{\partial \phi_y}{\partial x} \right) \tag{A2.59}$$

$$= 0$$

$$\varepsilon_r^{-1} \frac{\partial^2 \phi_y}{\partial z^2} - 2jn_0 k_0 \varepsilon_r^{-1} \frac{\partial \phi_y}{\partial z} + \alpha_x \frac{\partial}{\partial x} \left( \varepsilon_r^{-1} \alpha_x \frac{\partial \phi_y}{\partial x} \right) + \alpha_y \varepsilon_r^{-1} \frac{\partial}{\partial y} \left( \alpha_y \frac{\partial \phi_y}{\partial y} \right)$$

$$+ k_0^2 (1 - \varepsilon_r^{-1} n_0^2) \phi_y + \alpha_y \varepsilon_r^{-1} \frac{\partial}{\partial y} \left( \alpha_x \frac{\partial \phi_x}{\partial x} \right) - \alpha_x \frac{\partial}{\partial x} \left( \varepsilon_r^{-1} \alpha_y \frac{\partial \phi_x}{\partial y} \right) \tag{A2.60}$$

$$= 0$$

Therefore, applying standard Galerkin's procedure into equations (A2.59) and (A2.60) gives;

$$\int_e \varepsilon_r^{-1} \frac{\partial^2 \phi_x}{\partial z^2} N_i ds - \int_e 2jn_0 k_0 \varepsilon_r^{-1} \frac{\partial \phi_x}{\partial z} N_i ds + \int_e \alpha_y^2 \frac{\partial}{\partial y} \left( \varepsilon_r^{-1} \frac{\partial \phi_x}{\partial y} \right) N_i ds$$

$$+ \int_e \alpha_x^2 \varepsilon_r^{-1} \frac{\partial^2 \phi_x}{\partial x^2} N_i ds + \int_e k_0^2 (1 - \varepsilon_r^{-1} n_0^2) \phi_x N_i ds \tag{A2.61}$$

$$+ \int_e \alpha_x \alpha_y \varepsilon_r^{-1} \frac{\partial^2 \phi_y}{\partial x \partial y} N_i ds - \int_e \alpha_x \alpha_y \frac{\partial}{\partial y} \left( \varepsilon_r^{-1} \frac{\partial \phi_y}{\partial x} \right) N_i ds = 0$$

$$\int_e \varepsilon_r^{-1} \frac{\partial^2 \phi_y}{\partial z^2} N_i ds - \int_e 2jn_0 k_0 \varepsilon_r^{-1} \frac{\partial \phi_y}{\partial z} N_i ds + \int_e \alpha_x^2 \frac{\partial}{\partial x}\left(\varepsilon_r^{-1} \frac{\partial \phi_y}{\partial x}\right) N_i ds$$

$$+ \int_e \alpha_y^2 \varepsilon_r^{-1} \frac{\partial^2 \phi_y}{\partial y^2} N_i ds + \int_e k_0^2 (1 - \varepsilon_r^{-1} n_0^2) \phi_y N_i ds \qquad \text{(A2.62)}$$

$$+ \int_e \alpha_x \alpha_y \varepsilon_r^{-1} \frac{\partial^2 \phi_x}{\partial x \partial y} N_i ds - \int_e \alpha_x \alpha_y \frac{\partial}{\partial x}\left(\varepsilon_r^{-1} \frac{\partial \phi_x}{\partial y}\right) N_i ds = 0$$

where $N_i$ $(i = 1, 2, 3)$ is the shape function over the first order triangular element, $e$, while $\int_e (.) ds$ denotes the integration over each element. It is also be assumed in equation (A2.61) and (A2.62) that the refractive index ($n$) and the PML parameters ($\alpha_x$ and $\alpha_y$) are constant within each triangular element. In step index waveguides, the discontinuity of the refractive index and the associated interface boundary conditions will not be considered. Therefore, Green's theorem has been applied to equations (A2.61) and (A2.62) in order to find the line integral around each triangular element in the problem domain. Hence, Green's theorem can be used to satisfy interface boundary conditions such as;

    i.    Continuity of $E_z$, $E_z \propto \varepsilon_r^{-1}\left(\frac{\partial \phi_y}{\partial x} - \frac{\partial \phi_x}{\partial y}\right)$

    ii.    Discontinuity of $\varepsilon_r^{-1}\frac{\partial \phi_x}{\partial x}$ and $\varepsilon_r^{-1}\frac{\partial \phi_y}{\partial y}$

By applying Green's theorem for integration by parts into equations (A2.61) and (A2.62) and considering the interface boundary conditions given above;

$$\int_e \varepsilon_r^{-1} \frac{\partial^2 \phi_x}{\partial z^2} N_i ds - 2jn_0 k_0 \int_e \varepsilon_r^{-1} \frac{\partial \phi_x}{\partial z} N_i ds - \int_e \alpha_y^2 \varepsilon_r^{-1} \frac{\partial \phi_x}{\partial y} \frac{\partial N_i}{\partial y} ds$$

$$- \int_e \alpha_x^2 \varepsilon_r^{-1} \frac{\partial \phi_x}{\partial x} \frac{\partial N_i}{\partial x} ds + \oint_{\Gamma_e} \alpha_x^2 \varepsilon_r^{-1} \frac{\partial \phi_x}{\partial x} N_i n_x d\Gamma_e$$

$$\qquad \text{(A2.63)}$$

$$+ \int_e k_0^2 (1 - \varepsilon_r^{-1} n_0^2) \phi_x N_i ds - \int_e \alpha_x \alpha_y \varepsilon_r^{-1} \frac{\partial \phi_y}{\partial y} \frac{\partial N_i}{\partial x} ds$$

$$+ \oint_{\Gamma_e} \alpha_x \alpha_y \varepsilon_r^{-1} \frac{\partial \phi_y}{\partial y} N_i n_x d\Gamma_e + \int_e \alpha_x \alpha_y \varepsilon_r^{-1} \frac{\partial \phi_y}{\partial x} \frac{\partial N_i}{\partial y} ds = 0$$

$$\int_e \varepsilon_r^{-1} \frac{\partial^2 \phi_y}{\partial z^2} N_i ds - 2jn_0 k_0 \int_e \varepsilon_r^{-1} \frac{\partial \phi_y}{\partial z} N_i ds - \int_e \alpha_x^2 \varepsilon_r^{-1} \frac{\partial \phi_y}{\partial x} \frac{\partial N_i}{\partial x} ds$$

$$- \int_e \alpha_y^2 \varepsilon_r^{-1} \frac{\partial \phi_y}{\partial y} \frac{\partial N_i}{\partial y} ds + \oint_{\Gamma_e} \alpha_y^2 \varepsilon_r^{-1} \frac{\partial \phi_y}{\partial y} N_i n_y d\Gamma_e$$

$$+ \int_e k_0^2 (1 - \varepsilon_r^{-1} n_0^2) \phi_y N_i ds - \int_e \alpha_x \alpha_y \varepsilon_r^{-1} \frac{\partial \phi_x}{\partial y} \frac{\partial N_i}{\partial x} ds$$

$$+ \oint_{\Gamma_e} \alpha_x \alpha_y \varepsilon_r^{-1} \frac{\partial \phi_x}{\partial x} N_i n_y d\Gamma_e + \int_e \alpha_x \alpha_y \varepsilon_r^{-1} \frac{\partial \phi_x}{\partial x} \frac{\partial N_i}{\partial y} ds = 0$$

$$(A2.64)$$

where $n_x$ and $n_y$ denote the direction cosines between the normal element boundary ($\Gamma_e$) and $x$ and $y$ directions, respectively, and $\oint_{\Gamma_e} (.) d\Gamma_e$ denotes the line integral around the triangular element boundary ($\Gamma_e$). The line integral has been implemented in equation (A2.63) and equation (A2.64) in order to consider the interface boundary conditions which is also responsible for the coupling and polarisation dependence.

# Appendix 3

The Poynting vector for power calculation in the electromagnetic field;

$$S = \int_\Delta (E^* \times H)\, d\Omega \tag{A3.1}$$

The cross product from equation (A3.1) can be written as;

$$E^* \times H = \begin{vmatrix} \bar{a}_x & \bar{a}_y & \bar{a}_z \\ E_x^* & E_y^* & E_z^* \\ H_x & H_y & H_z \end{vmatrix}$$
$$= \bar{a}_x\left(E_y^* H_z - E_z^* H_y\right) - \bar{a}_y\left(E_x^* H_z - E_z^* H_x\right) + \bar{a}_z\left(E_x^* H_y - E_y^* H_x\right) \tag{A3.2}$$

Consider the Poynting Vector along the propagation direction of the waveguide (*z*-direction);

$$S_z = \int_\Delta \left(E_x^* H_y - E_y^* H_x\right) d\Omega \tag{A3.3}$$

The final expression can be reduced to one variable by establishing a relationship between the *E* and the *H* components. From Maxwell's equations;

$$\nabla \times H^* = j\omega\varepsilon E^* = \begin{vmatrix} \bar{x} & \bar{y} & \bar{z} \\ \partial_x & \partial_y & \partial_z \\ H_x^* & H_y^* & H_z^* \end{vmatrix} \tag{A3.4}$$

Then the following can be obtained;

$$j\omega\varepsilon\left(E_x^* \bar{x} + E_y^* \bar{y} + E_z^* \bar{z}\right) = \left(\frac{\partial H_z^*}{\partial y} - \frac{\partial H_y^*}{\partial z}\right)\bar{x} + \left(\frac{\partial H_z^*}{\partial x} - \frac{\partial H_x^*}{\partial z}\right)\bar{y} + \left(\frac{\partial H_y^*}{\partial x} - \frac{\partial H_x^*}{\partial y}\right)\bar{z} \tag{A3.5}$$

By equating terms with corresponding coefficients;

$$j\omega\varepsilon\bar{x}E_x^* = \left(\frac{\partial H_z^*}{\partial y} - \frac{\partial H_y^*}{\partial z}\right)\bar{x} \tag{A3.6}$$

$$j\omega\varepsilon\bar{y}E_y^* = \left(\frac{\partial H_z^*}{\partial x} - \frac{\partial H_x^*}{\partial z}\right)\bar{y} \tag{A3.7}$$

Replacing $\partial/\partial z$ components with $-j\beta$;

$$j\omega\varepsilon E_x^* = \frac{\partial H_x^*}{\partial y} + j\beta H_y^* \Rightarrow E_x^* = -\frac{1}{j\omega\varepsilon}\frac{\partial H_z^*}{\partial y} + \frac{\beta}{\omega\varepsilon}H_y^* \tag{A3.8}$$

$$j\omega\varepsilon E_y^* = \frac{\partial H_z^*}{\partial x} + j\beta H_x^* \Rightarrow E_y^* = \frac{1}{j\omega\varepsilon}\frac{\partial H_z^*}{\partial x} - \frac{\beta}{\omega\varepsilon}H_x^* \tag{A3.9}$$

Substituting equation (A3.8) and equation (A3.9) into equation (A3.3);

$$S_z = \int_\Delta \frac{1}{\omega\varepsilon}\left(\beta H_y^* - j\frac{\partial H_z^*}{\partial y}\right)H_y - \frac{1}{\omega\varepsilon}\left(-\beta H_x^* + \frac{\partial H_z^*}{\partial x}\right)H_x d\Omega \tag{A3.10}$$

Hence;

$$S_z = \int_\Delta \left[\frac{1}{\omega\varepsilon}\left(\beta H_y^* H_y + \beta H_x^* H_x\right) - \frac{1}{\omega\varepsilon}\left(j\frac{\partial H_z^*}{\partial x}H_x + j\frac{\partial H_z^*}{\partial y}\right)H_y\right]d\Omega \tag{A3.11}$$

The eigenvalue solutions are complex for media with a complex propagation constant $\beta = \beta' + j\beta''$ and a complex dielectric permittivity $\varepsilon = \varepsilon' + j\varepsilon''$. Therefore, the resultant complex fields can be represented as; $H_x = H_x' + jH_x''$, $H_y = H_y' + jH_y''$ and $H_z = H_z' + jH_z''$ and similarly the conjugate fields can be represented as; $H_x^* = H_x' - jH_x''$, $H_y^* = H_y' - jH_y''$ and $H_z^* = H_z' - jH_z''$.

Application of the shape functions to analyse the power in each triangular element;

$$\boldsymbol{H} = [N]\{\boldsymbol{H}\}_e \; and \; \boldsymbol{H}^* = \{\boldsymbol{H}\}_e^T[N]^T \tag{A3.12}$$

Using equation (A3.12), equation (A3.11) can be expressed as;

$$S_z = \int_\Delta \left[\frac{\beta}{\omega\varepsilon}\left(\{H_y\}_e^T[N]^T[N]\{H_y\}_e + [N]^T\{H_x\}_e^T[N]\{H_x\}_e\right)\right.$$
$$\left. - \frac{j}{\omega\varepsilon}\left(\{H_z\}_e^T\frac{\partial[N]^T}{\partial x}[N]\{H_x\}_e + \{H_z\}_e^T\frac{\partial[N]^T}{\partial y}[N]\{H_y\}\right)\right]d\Omega \tag{A3.13}$$

where shape function derivative $\frac{\partial [N]^T}{\partial x}[N]$ can be represented as;

$$\frac{\partial [N]^T}{\partial x}[N] = \begin{bmatrix} \frac{\partial N_1}{\partial x}N_1 & \frac{\partial N_1}{\partial x}N_2 & \frac{\partial N_1}{\partial x}N_3 \\ \frac{\partial N_2}{\partial x}N_1 & \frac{\partial N_2}{\partial x}N_2 & \frac{\partial N_2}{\partial x}N_3 \\ \frac{\partial N_3}{\partial x}N_1 & \frac{\partial N_3}{\partial x}N_2 & \frac{\partial N_3}{\partial x}N_3 \end{bmatrix} \qquad (A3.14)$$

by applying shape function approximation in equation (A2.30) into equation (A3.14);

$$\frac{\partial [N]^T}{\partial x}[N] = \begin{bmatrix} b_1 N_1 & b_1 N_2 & b_1 N_3 \\ b_2 N_1 & b_2 N_2 & b_2 N_3 \\ b_3 N_1 & b_3 N_2 & b_3 N_3 \end{bmatrix} \qquad (A3.15)$$

similarly shape function derivative $\frac{\partial [N]^T}{\partial y}[N]$ can be represented as;

$$\frac{\partial [N]^T}{\partial y}[N] = \begin{bmatrix} \frac{\partial N_1}{\partial y}N_1 & \frac{\partial N_1}{\partial y}N_2 & \frac{\partial N_1}{\partial y}N_3 \\ \frac{\partial N_2}{\partial y}N_1 & \frac{\partial N_2}{\partial y}N_2 & \frac{\partial N_2}{\partial y}N_3 \\ \frac{\partial N_3}{\partial y}N_1 & \frac{\partial N_3}{\partial y}N_2 & \frac{\partial N_3}{\partial y}N_3 \end{bmatrix} \qquad (A3.16)$$

$$\frac{\partial [N]^T}{\partial y}[N] = \begin{bmatrix} c_1 N_1 & c_1 N_2 & c_1 N_3 \\ c_2 N_1 & c_2 N_2 & c_2 N_3 \\ c_3 N_1 & c_3 N_2 & c_3 N_3 \end{bmatrix} \qquad (A3.17)$$

where $b_1$, $b_2$, $b_3$, $c_1$, $c_2$ and $c_3$ coefficients can be defined as;

$$\frac{\partial N_1}{\partial x} = b_1; \quad \frac{\partial N_2}{\partial x} = b_2; \quad \frac{\partial N_3}{\partial x} = b_3$$

$$\frac{\partial N_1}{\partial y} = c_1; \quad \frac{\partial N_2}{\partial y} = c_2; \quad \frac{\partial N_3}{\partial y} = c_3$$

Therefore, the power calculation for propagation direction *z* can be written as;

$$
\begin{aligned}
S_z = \frac{\beta}{\omega\varepsilon} &\left( \{H_y\}_e^T \begin{bmatrix} \frac{A_e}{6} & \frac{A_e}{12} & \frac{A_e}{12} \\ \frac{A_e}{12} & \frac{A_e}{6} & \frac{A_e}{12} \\ \frac{A_e}{12} & \frac{A_e}{12} & \frac{A_e}{6} \end{bmatrix} \{H_y\}_e + \{H_x\}_e^T \begin{bmatrix} \frac{A_e}{6} & \frac{A_e}{12} & \frac{A_e}{12} \\ \frac{A_e}{12} & \frac{A_e}{6} & \frac{A_e}{12} \\ \frac{A_e}{12} & \frac{A_e}{12} & \frac{A_e}{6} \end{bmatrix} \{H_x\}_e \right) \\
&- \frac{j}{\omega\varepsilon} \left( \{H_z\}_e^T \frac{A_e}{3} \begin{bmatrix} b_1 & b_1 & b_1 \\ b_2 & b_2 & b_2 \\ b_3 & b_3 & b_3 \end{bmatrix} \{H_x\}_e \right. \\
&\left. + \{H_z\}_e^T \frac{A_e}{3} \begin{bmatrix} c_1 & c_1 & c_1 \\ c_2 & c_2 & c_2 \\ c_3 & c_3 & c_3 \end{bmatrix} \{H_y\}_e \right)
\end{aligned}
$$

(A3.18)

# Appendix 4

Considering two fields propagating at two different frequencies in the material, the total optical field ($\phi$) can be written as;

$$\phi(x, y, z, t) = \tfrac{1}{2}\{\phi_\omega(x, y)\, e^{[j(\omega t - \beta z)]} + \phi_{2\omega}(x, y, z)\, e^{[j(2\omega t - 2\beta z)]} + c.c.\} \qquad \text{(A4.1)}$$

where $\phi_\omega$ is the input field of the fundamental field, $\phi_{2\omega}$ is the slowly varying amplitude of the SH field, $\omega$ is the angular frequency and $\beta$ is the propagation constant of the fundamental wave.

From equation (A4.1) and making the assumption that the fundamental field $\phi_\omega$ is independent of the direction of propagation ($z$), with;

$$\phi_\omega = \begin{cases} E_x \; for \; E^x \; modes \\ H_x \; for \; E^y \; modes \end{cases} \qquad \text{(A4.2)}$$

where $E^x$ mode is approximated by $TE^y$, $E_y \equiv 0$, leading function is $E_x$

where $E^y$ mode is approximated by $TM^y$, $H_y \equiv 0$, leading function is $H_x$.

***Second Harmonic Generation without pump depletion***

For the stationary analysis of the fundamental field;

$$p_{x\omega} \frac{\partial^2 \phi_\omega}{\partial x^2} + p_{y\omega} \frac{\partial^2 \phi_\omega}{\partial y^2} - p_{z\omega}\beta^2 \phi_\omega + q_\omega k_0^2 \phi_\omega = 0 \qquad \text{(A4.3)}$$

For the propagation model of the second harmonic field;

$$-j4\beta p_{z2\omega} \frac{\partial \phi_{2\omega}}{\partial z} + p_{x2\omega} \frac{\partial^2 \phi_{2\omega}}{\partial x^2} + p_{y2\omega} \frac{\partial^2 \phi_{2\omega}}{\partial y^2} - 4p_{z2\omega}\beta^2 \phi_{2\omega} + 4q_{2\omega} k_0^2 \phi_{2\omega}$$
$$= \psi_{NL} \qquad \text{(A4.4)}$$

where subscript $\omega$ and $2\omega$ are for the fundamental and SH waves respectively and the coefficients $p_{xj}, p_{yj}, p_{zj}, q_j$ and the nonlinear source field $\psi_{NL}$ can be expressed as follows;

*TE mode:*

$$\phi_j = E_{xj}, \qquad p_{xj} = n_{xj}^2/n_{yj}^2, \qquad p_{yj} = 1, \qquad q_j = n_{xj}^2$$

$$\psi_{NL} = -\frac{2k_0^2}{\varepsilon_0}(i_x.P_{NL}) \tag{A4.5}$$

*TM mode:*

$$\phi_j = H_{xj}, \quad p_{xj} = 1/n_{yj}^2, \quad p_{yj} = 1/n_{zj}^2, \quad p_{zj} = 1/n_{yj}^2, \quad q_j = 1$$

$$\psi_{NL} = \frac{k_0}{\varepsilon_0 Z_0}\left[\frac{2\beta(i_y.P_{NL})}{n_{y2\omega}^2} - j\frac{1}{n_{z2\omega}^2}\frac{\partial(i_z.P_{NL})}{\partial y}\right] \tag{A4.6}$$

where $Z_0$ denotes the free space impedance ($\approx 377\Omega$) and $j$ represents either $\omega$ or $2\omega$.

Note that $n_{xj} = n_{yj} = n_{zj}$ for isotropic materials while $n_{xj} \neq n_{yj} \neq n_{zj}$ for anisotropic materials. Further, $\partial/\partial x = 0$ for planar optical waveguides where $i_x, i_y$ and $i_z$ are the unit vectors in the $x, y$ and $z$ directions respectively, and the second-order nonlinear polarisation $P_{NL}$ is given by;

$$P_{NL} = \begin{bmatrix} P_x \\ P_y \\ P_z \end{bmatrix} = \varepsilon_0 \begin{bmatrix} d_{11} & d_{12} & d_{13} & d_{14} & d_{15} & d_{16} \\ d_{21} & d_{22} & d_{23} & d_{24} & d_{25} & d_{26} \\ d_{31} & d_{32} & d_{33} & d_{34} & d_{35} & d_{36} \end{bmatrix} \begin{bmatrix} E_{x\omega}^2 \\ E_{y\omega}^2 \\ E_{z\omega}^2 \\ 2E_{y\omega}E_{z\omega} \\ 2E_{z\omega}E_{x\omega} \\ 2E_{x\omega}E_{y\omega} \end{bmatrix} \tag{A4.7}$$

Note that $P_{NL}^{\omega} = 2dE_{\omega}^*E_{2\omega}$ and $P_{NL}^{2\omega} = 2dE_{\omega}^2$, where $P_{NL}^{\omega}$ and $P_{NL}^{2\omega}$ are fundamental and SH nonlinear polarisation respectively. An asterisk ('*') is used to denote a complex conjugate; i.e. the relationship between $d_{ij}$ and $\chi_{ij}^{(2)}$ is $d_{ij} = \frac{1}{2}\chi_{ij}^{(2)}$ with;

$$E_{\omega} = \begin{bmatrix} E_{x\omega} \\ E_{y\omega} \\ E_{z\omega} \end{bmatrix} = \frac{1}{2}\begin{bmatrix} E_{x\omega}(x,y)e^{[j(\omega t - \beta z)]} + c.c \\ E_{y\omega}(x,y)e^{[j(\omega t - \beta z)]} + c.c \\ E_{z\omega}(x,y)e^{[j(\omega t - \beta z)]} + c.c \end{bmatrix} \tag{A4.8}$$

$E_{2\omega}$ can be written similarly.

In equation (A4.4), the Slowly Varying Envelope Approximation (SVEA) $|\partial^2 \phi_{2\omega}/\partial z^2| \ll |4\beta p_{z2\omega} \partial \phi_{2\omega}/\partial z|$ has been applied, and the pump depletion has also been neglected. Therefore, negligible depletion of the fundamental beam at $\omega$ is valid only for cases where the conversion efficiency is very low, i.e. $\eta_{SHG} \ll 1$. Furthermore, at low conversion efficiencies the amplitude of the fundamental electric field $E_\omega$ remains essentially constant over the interaction length (as $E_{2\omega} \ll E_\omega$).

The amplitudes of the fundamental electric fields, $E_{x\omega}$, $E_{y\omega}$ and $E_{z\omega}$ are approximated as;

*TE mode:*

$$E_{x\omega} = \phi_\omega \tag{A4.9}$$

$$E_{y\omega} = 0 \tag{A4.10}$$

$$E_{z\omega} = 0 \tag{A4.11}$$

*TM mode:*

$$E_{x\omega} = 0 \tag{A4.12}$$

$$E_{y\omega} = -\frac{Z_0 \beta}{n_{y\omega}^2 k_0} \phi_\omega \tag{A4.13}$$

$$E_{z\omega} = j\frac{Z_0}{n_{z\omega}^2 k_0} \frac{\partial \phi_\omega}{\partial y} \tag{A4.14}$$

Applying the Finite Element Method (FEM) to equations (A4.3) and (A4.4) yields;

*For fundamental:*

$$[K_\omega]\{\phi_\omega\} - \beta^2 [M_\omega]\{\phi_\omega\} = \{0\} \tag{A4.15}$$

*For second harmonic:*

$$-j4\beta[M_{2\omega}]\frac{d\{\phi_{2\omega}\}}{dz} + ([K_{2\omega}] - 4\beta^2[M_{2\omega}]\{\phi_{2\omega}\}) = \{\psi_{NL}\} \qquad \text{(A4.16)}$$

Equation (A4.15) is a standard eigenvalue problem whose eigenvalue and eigenvector corresponds to $\beta^2$ and $\{\phi_{\omega}\}$ respectively [see Appendix 2].

In equation (A4.15) and (A4.16); $[K_{\omega}]$, $[K_{2\omega}]$, $[M_{\omega}]$ and $[M_{2\omega}]$ can be expressed as follows;

$$[K_{\omega}] = \sum_{e} \iint_{e} \left[ q_{\omega}k_0^2\{N\}\{N\}^T - p_{x\omega}\{N_x\}\{N_x\}^T - p_{y\omega}\{N_y\}\{N_y\}^T \right] dx\,dy \qquad \text{(A4.17)}$$

$$[M_{\omega}] = \sum_{e} \iint_{e} [p_{z\omega}\{N\}\{N\}^T]\,dx\,dy \qquad \text{(A4.18)}$$

$$[K_{2\omega}] = \sum_{e} \iint_{e} \left[ 4q_{2\omega}k_0^2\{N\}\{N\}^T - p_{x2\omega}\{N_x\}\{N_x\}^T - p_{y2\omega}\{N_y\}\{N_y\}^T \right] dx\,dy \qquad \text{(A4.19)}$$

$$[M_{2\omega}] = \sum_{e} \iint_{e} [p_{z2\omega}\{N\}\{N\}^T]\,dx\,dy \qquad \text{(A4.20)}$$

In aiming to solve (A4.16), it is difficult to analyse the interaction of linear and nonlinear mechanisms; therefore the split-step procedure which consists of a propagation effect and a nonlinear effect can be applied. The split-step procedure can be written as follows [109];

By considering the Left Hand Side (L.H.S.) of the equation (A4.16) for the propagation effect;

$$-j4\beta[M_{2\omega}]\frac{d\left\{\phi_{2\omega}^{(1)}\right\}}{dz} + \left([K_{2\omega}] - 4\beta^2[M_{2\omega}]\left\{\phi_{2\omega}^{(1)}\right\}\right) = \{0\} \qquad \text{(A4.21)}$$

Then considering the split-step procedure the Right Hand Side (R.H.S.) of the equation (A4.16) can be represented as;

$$\left\{\phi_{2\omega}^{(2)}\right\} = \left\{\phi_{2\omega}^{(1)}\right\} + \int j \frac{1}{4\beta p_{z2}}\{\psi_{NL}\}dz \tag{A4.22}$$

where superscript 1 and 2 in equation (A4.21) and (A4.22) denote the field for step 1 and 2 respectively.

The following matrix equation can be obtained by applying the Finite Difference Method (FDM) to equation (A4.21) for a short interval $\Delta z \le z < (k+1)\Delta z$, (where $k = 0, 1, 2, ...$) along the propagation direction $z$.

$$-j4\beta[M_{2\omega}]\left(\left\{\phi_{2\omega}^{(1)}\right\}_{k+1} - \left\{\phi_{2\omega}^{(1)}\right\}_{k}\right)/\Delta z$$
$$+ ([K_{2\omega}] - 4\beta^2[M_{2\omega}])\left[\theta\left\{\phi_{2\omega}^{(1)}\right\}_{k+1} + (1-\theta)\left\{\phi_{2\omega}^{(1)}\right\}_{k}\right] = \{0\} \tag{A4.23}$$

Then equation (A4.23) can be reduced as follows;

$$[L(\theta)]\left\{\phi_{2\omega}^{(1)}\right\}_{k+1} = [L(\theta-1)]\left\{\phi_{2\omega}^{(1)}\right\} \tag{A4.24}$$

where;

$$[L(\theta)] = -j4\beta[M_{2\omega}] + \theta\Delta z([K_{2\omega}] - 4\beta^2[M_{2\omega}]) \tag{A4.25}$$

where artificial parameter $\theta = 0.5$ (i.e. Crank Nicolson (CN) scheme which was discussed in Chapter 2).

The difference version of equation (A4.22) can be represented as;

$$\left\{\phi_{2\omega}^{(2)}\right\}_{k+1} = \left\{\phi_{2\omega}^{(1)}\right\}_{k+1} + j\frac{\Delta z}{4\beta p_{z2}}\{\psi_{NL}\} \tag{A4.26}$$

Substituting equation (A4.24) into equation (A4.26), the following equation can be obtained;

$$\{\phi_{2\omega}\}_{k+1} = [L(\theta)]^{-1}[L(\theta-1)]\{\phi_{2\omega}\}_{k} + j\frac{\Delta z}{4\beta p_{z2}}\{\psi_{NL}\} \tag{A4.27}$$

where $\{\phi_{2\omega}\}_k \equiv \left\{\phi_{2\omega}^{(1)}\right\}_k$ and $\{\phi_{2\omega}\}_{k+1} \equiv \left\{\phi_{2\omega}^{(2)}\right\}_{k+1}$ are the initial and final SH fields within the interval $k\Delta z \le z < (k+1)\Delta z$ respectively.

***Second Harmonic Generation with pump depletion***

In some cases the power conversion from fundamental to SH can be considerably high and the second harmonic becomes significant; therefore it is necessary to consider the pump depletion (i.e. more power transferred from fundamental to the SH). The total field of two different waves propagating at two different frequencies $\omega$ and $2\omega$, can be written as the coupled wave equation (A4.28). Further, the fundamental field $\phi_\omega$ is now dependant of $z$.

In consideration of pump depletion the nonlinear part (i.e. R.H.S. or source term) of the fundamental wave equation exists. Therefore, the fundamental wave equation with the nonlinear term $\psi_{NL}^\omega$ can be represented as;

$$-j2\beta p_{z\omega}\frac{\partial \phi_\omega}{\partial z} + p_{x\omega}\frac{\partial^2 \phi_\omega}{\partial x^2} + p_{y\omega}\frac{\partial^2 \phi_\omega}{\partial y^2} - p_{z\omega}\beta^2 \phi_\omega + q_\omega k_0^2 \phi_\omega = \psi_{NL}^\omega \qquad \text{(A4.28)}$$

Application of FEM yields;

$$-j2\beta[M_{2\omega}]\frac{d\{\phi_\omega\}}{dz} + ([K_\omega] - \beta^2[M_\omega]\{\phi_\omega\}) = \{\psi_{NL}^\omega\} \qquad \text{(A4.29)}$$

where,

$$[K_\omega] = \sum_e \iint_e \left[ q_\omega k_0^2 \{N\}\{N\}^T - p_{x\omega}\{N_x\}\{N_x\}^T - p_{y\omega}\{N_y\}\{N_y\}^T \right] dx\,dy \qquad \text{(A4.30)}$$

$$[M_\omega] = \sum_e \iint_e \left[ p_{z\omega}\{N\}\{N\}^T \right] dx\,dy \qquad \text{(A4.31)}$$

The nonlinear part of the equation for *TE* and *TM* modes can be written as follows;

*TE mode:*

$$\psi_{NL}^\omega = -\frac{2k_0^2}{\varepsilon_0}(i_x . P_{NL}^\omega)$$

$$\text{(A4.32)}$$

*TM mode:*

$$\psi_{NL}^{\omega} = \frac{k_0}{\varepsilon_0 Z_0} \left[ \frac{2\beta \left( i_y . P_{NL}^{\omega} \right)}{n_{y\omega}^2} - j \frac{1}{n_{z\omega}^2} \frac{\partial \left( i_z . P_{NL}^{\omega} \right)}{\partial y} \right] \tag{A4.33}$$

The SH wave equation with pump depletion can be derived in a similar manner (without pump depletion). Then the split-step procedure and CN scheme can be applied to both the fundamental and SH wave equations.

# Author Publications

- **I. N. M. Wijeratne,** N. Kejalakshmy, B. M. A. Rahman and K. T. V. Grattan, "Rigorous Full-Vectorial Beam Propagation Analysis of Second-Harmonic Generation in Zinc Oxide Waveguides", IEEE Photonics Journal, vol. 5, no. 2, April 2013.

- **I. N. M. Wijeratne,** N. Kejalakshmy, A. Agrawal, B. M. A. Rahman and K. T. V. Grattan, "Numerical analysis of second harmonic generation in soft glass equiangular spiral photonic crystal fibers", IEEE Photonics Journal, vol. 4, no. 2, April 2012.

- B. M. A. Rahman, A. K. M. S. Kabir, K. Namassivayane, **I. N. M. Wijeratne**, M. Rajarajan and K.T.V. Grattan, "Modal solution of photonic crystal fibres by using full-vectorial finite element method", 3$^{rd}$ International conference on computers and devices for communications (CODEC-06), Calcutta, India, pg 533-536, December 18$^{th}$ – 20$^{th}$, 2006.

- A. K. M. S. Kabir, B. M. A. Rahman, K. Namassivayam, **I. N. M. Wijeratne**, M. Rajarajan and K.T.V. Grattan, "Characterization of photonic crystal fibers by using a full-vectorial finite element method", Proceedings of SPIE, Vol. 6369, Photonic crystals and photonic crystal fibers for sensing applications II, 2006.

- B. M. A. Rahman, A. K. M. S. Kabir, M. Vaghjiani, **I. N. M. Wijeratne**, G. S. Sahota, M. Rajarajan, K. T. V. Grattan, "Modal solutions of photonic crystal fibers by using a full-vectorial finite element method", Proceedings of SPIE, Vol. 6128, Photonic Crystal Materials and Devices IV, 2006.

- B. M. A. Rahman, A. K. M. S. Kabir, G. S. Sahota, M. Vaghjiani, **I. N. M. Wijeratne**, N. Somasiri, S. Alam, S. Obayya, M. Rajarajan and K. T. V. Grattan, "Modal solutions and birefringence studies of PCFs", IEEE seminar on Photonics Crystal Fibres, City University, London, United Kingdom, September 22$^{nd}$, 2005.

# Bibliography

[1]     J. C. Palais, *Fiber optic communications*, 2nd ed.: Prentice-Hall International, 1988.

[2]     R. J. Forbes, *Studies in Ancient Technology*, 2nd Revised ed. vol. 5. S.l.: E. J. Brill, 1966.

[3]     J. Hecht, *City of light: the story of fiber optics*, Rev. and expanded ed. Oxford; New York: Oxford University Press, 2004.

[4]     M. Biagioli, *Galileo's instruments of credit: telescopes, images, secrecy*. Chicago, Ill; London: University of Chicago Press, 2006.

[5]     R. Tricker, *Optoelectronics and fiber optic technology*. Oxford: Newnes, 2002.

[6]     R. N. Wilson, *Reflecting telescope optics*, 2nd ed. Berlin; London: Springer, 2004.

[7]     J. A. M. Bleeker, J. Geiss, and M. Huber, *The century of space science volume II*. Dordrecht; London: Kluwer Academic, 2001.

[8]     A. A. Huurdeman, *The worldwide history of telecommunications*. New York; Chichester: Wiley, 2003.

[9]     T. Teshirogi and T. Yoneyama, *Modern millimeter-wave technologies*. Tokyo: Ohmsha; Oxford: IOS Press, 2001.

[10]    S. Hong, *Wireless: from Marconi's black-box to the audion*. Cambridge, Mass; London: MIT Press, 2001.

[11]    J. M. Senior, *Optical fiber communications: principles and practice*, 2nd ed.: Prentice-Hall, 1992.

[12]    Y. Suematsu, K. B. Iga, and W. A. Gambling, *Introduction to optical fiber communications*. New York; Chichester: Wiley, 1982.

[13]    K. C. Kao and G. A. Hockham, "Dielectric-fibre surface waveguides for optical frequencies," *Electrical Engineers, Proceedings of the Institution of,* vol. 113, pp. 1151-1158, Jul 1966.

[14]    G. J. Ogilvie, R. J. Esdaile, and G. P. Kidd, "Transmission loss of tetrachloroethylene-filled liquid-core-fibre light guide," *Electronics Letters,* vol. 8, pp. 533-534, Nov 1972.

[15]    W. A. Gambling, D. N. Payne, and H. Matsumura, "Gigahertz bandwidths in multimode, liquid-core, optical fibre waveguide," *Optics Communications,* vol. 6, pp. 317-322, Dec 1972.

[16]    D. N. Payne and W. A. Gambling, "Zero material dispersion in optical fibres," *Electronics Letters,* vol. 11, pp. 176-178, 1975.

[17]    T. Katsuyama and H. Matsumura, *Infrared optical fibers*: IOP, 1989.

[18]    H. H. Hansen, *Textbook of lung cancer*, 2nd ed. London: Informa Healthcare, 2008.

[19]    T. L. Koch and U. Koren, "Semiconductor photonic integrated circuits," *IEEE Journal of Quantum Electronics,* vol. 27, pp. 641-653, Mar 1991.

[20]    L. A. Coldren, S. W. Corzine, and M. Mashanovitch, *Diode lasers and photonic integrated circuits*, 2nd ed. Hoboken, N.J.: Wiley, 2012.

[21]    M. Tsuchiya and T. Hoshida, "Nonlinear photodetection scheme and its system applications to fiber-optic millimeter-wave wireless down-links," *IEEE Transactions on Microwave Theory and Techniques,* vol. 47, pp. 1342-1350, 1999.

[22] D. B. Payne and R. P. Davey, "The future of fibre access systems?," *BT Technology Journal,* vol. 20, pp. 104-114, Oct 2002.

[23] P. Newman, G. Minshall, T. Lyon, and L. Huston, "IP switching and gigabit routers," *IEEE Communications Magazine,* vol. 35, pp. 64-69, 1997.

[24] TFOT. (2013, 02 Jan). *Optical storage - The future of things*. Available: http://thefutureofthings.com/articles/56/mempile-terabyte-on-a-cd.html

[25] Panasonic. (2013, 02 Jan). *Blu-Ray Disk*. Available: http://panasonic.net/blu-ray/technology/story01/

[26] A. K. Dutta, "Prospects of highly efficient AlGaInP based surface emitting type ring-LED for 50 and 156 Mb/s POF data link systems," *Journal of Lightwave Technology,* vol. 16, pp. 106-113, 1998.

[27] C. K. N. Patel, "Continuous-wave laser action on vibrational rotational transitions of $CO_2$," *Physical Review,* vol. 136, pp. A1187-A1193, 1964.

[28] J. E. Geusic, H. M. Marcos, and L. G. Van Uitert, "Laser oscillations in Nd-doped Yttrium Aluminum, Yttrium Gallium and Gadolinium Garnets," *Applied Physics Letters,* vol. 4, pp. 182-184, 1964.

[29] F. Schwarz, N. Pütz, T. Georg, and E. Reich, "Effect of an Er:YAG laser on periodontally involved root surfaces: an in vivo and in vitro SEM comparison," *Lasers in Surgery and Medicine,* vol. 29, pp. 328-335, 2001.

[30] H. X. Zhu, X. F. Zhou, F. Y. Su, Y. Q. Tian, S. Ashili, M. R. Holl, and D. R. Meldrum, "Micro-patterning and characterization of PHEMA-co-PAM-based optical chemical sensors for lab-on-a-chip applications," *Sensors and Actuators B-Chemical,* vol. 173, pp. 817-823, Oct 2012.

[31] D. J. Wagner and RPI. (2012, 30 Dec). *Total internal reflection*. Available: http://www.rpi.edu/dept/phys/Dept2/APPhys1/optics/optics/node15.html

[32] G. P. Agrawal, *Nonlinear fiber optics*, 4th ed. Amsterdam; London: Elsevier/Academic Press, 2007.

[33] J. Kerr, "XL. A new relation between electricity and light: Dielectrified media birefringent," *Philosophical Magazine Series 4,* vol. 50, pp. 337-348, Nov 1875.

[34] R. Baumgartner and R. Byer, "Optical parametric amplification," *IEEE Journal of Quantum Electronics,* vol. 15, pp. 432-444, 1979.

[35] R. L. Byer and A. Piskarskas, "Optical parametric oscillation and amplification," *Journal of the Optical Society America B,* vol. 10, pp. 1656-1656, 1993.

[36] M. Bass, P. A. Franken, A. E. Hill, C. W. Peters, and G. Weinreich, "Optical mixing," *Physical Review Letters,* vol. 8, pp. 18-18, 1962.

[37] A. Savage and R. C. Miller, "Measurements of second harmonic generation of the ruby laser line in piezoelectric crystals," *Applied Optics,* vol. 1, pp. 661-664, 1962.

[38] F. Shimizu, "Frequency broadening in liquids by a short light pulse," *Physical Review Letters,* vol. 19, pp. 1097-1100, 1967.

[39] R. L. Carman, R. Y. Chiao, and P. L. Kelley, "Observation of degenerate stimulated four-photon Interaction and four-wave parametric amplification," *Physical Review Letters,* vol. 17, pp. 1281-1283, 1966.

[40] M. N. Islam, L. F. Mollenauer, R. H. Stolen, J. R. Simpson, and H. T. Shang, "Cross-phase modulation in optical fibers," *Optics Letters,* vol. 12, pp. 625-627, 1987.

[41]     P. D. Maker, R. W. Terhune, M. Nisenoff, and C. M. Savage, "Effects of dispersion and focusing on the production of optical harmonics," *Physical Review Letters,* vol. 8, pp. 21-22, 1962.

[42]     R. Eckardt and J. Reintjes, "Phase matching limitations of high efficiency second harmonic generation," *IEEE Journal of Quantum Electronics,* vol. 20, pp. 1178-1187, 1984.

[43]     T. Y. Fan, C. E. Huang, B. Q. Hu, R. C. Eckardt, Y. X. Fan, R. L. Byer, and R. S. Feigelson, "Second harmonic generation and accurate index of refraction measurements in flux-grown $KTiOPO_4$," *Applied Optics,* vol. 26, pp. 2390-2394, 1987.

[44]     P. F. Bordui, R. G. Norwood, D. H. Jundt, and M. M. Fejer, "Preparation and characterization of off-congruent lithium-niobate crystals," *Journal of Applied Physics,* vol. 71, pp. 875-879, Jan 1992.

[45]     P. K. Tien, R. Ulrich, and R. J. Martin, "Optical second harmonic generation in form of coherent Čerenkov radiation from a thin-film waveguide," *Applied Physics Letters,* vol. 17, pp. 447-450, 1970.

[46]     J. A. Armstrong, N. Bloembergen, J. Ducuing, and P. S. Pershan, "Interactions between light waves in a nonlinear dielectric," *Physical Review,* vol. 127, pp. 1918-1939, 1962.

[47]     Q. Li and J. Y. Wang, "A Modified ray-optic method for arbitrary dielectric waveguides," *IEEE Journal of Quantum Electronics,* vol. 28, pp. 2721-2727, Dec 1992.

[48]     R. Srivastava, C. K. Kao, and R. V. Ramaswamy, "WKB analysis of planar surface waveguides with truncated index profiles," *Journal of Lightwave Technology,* vol. 5, pp. 1605-1609, Nov 1987.

[49]     K. S. Chiang, "Review of numerical and approximate methods for the modal analysis of general optical dielectric waveguides," *Optical and Quantum Electronics,* vol. 26, pp. S113-S134, Mar 1994.

[50]     R. Knox and P. Toulios, "Integrated circuits for the millimeter through optical frequency range," in *Proceedings of the Symposium Submillimeter Waves*, 1970, pp. 497-515.

[51]     E. A. J. Marcatili, "Dielectric rectangular waveguide and directional coupler for integrated optics," *The Bell System Technical Journal,* vol. 48, pp. 2071-2102, 1969.

[52]     C. L. Chen, *Foundations for guided-wave optics*. Hoboken, N.J.: Wiley; Chichester: John Wiley, 2007.

[53]     K. Okamoto, *Fundamentals of optical waveguides*, 2nd ed. Burlington, Mass; London: Academic Press, 2006.

[54]     K. S. Chiang, K. M. Lo, and K. S. Kwok, "Effective-index method with built-in perturbation correction for integrated optical waveguides," *Journal of Lightwave Technology,* vol. 14, pp. 223-228, Feb 1996.

[55]     K. S. Chiang, "Analysis of optical fibers by the effective-index method," *Applied Optics,* vol. 25, pp. 348-354, Feb 1986.

[56]     K. Vandevelde, H. Thienpont, and R. Vangeen, "Extending the effective index method for arbitrarily shaped inhomogeneous optical waveguides," *Journal of Lightwave Technology,* vol. 6, pp. 1153-1159, Jun 1988.

[57]     K. S. Chiang, "Dual effective-index method for the analysis of rectangular dielectric waveguides," *Applied Optics,* vol. 25, pp. 2169-2174, Jul 1986.

[58]   J. J. G. M. Vandertol and N. H. G. Baken, "Correction to effective index method for rectangular dielectric waveguides," *Electronics Letters,* vol. 24, pp. 207-208, Feb 1988.

[59]   J. B. Davies, "Review of methods for numerical solution of hollow-waveguide problem," *Proceedings of the Institution of Electrical Engineers-London,* vol. 119, pp. 33-37, 1972.

[60]   S. M. Saad, "Review of numerical methods for the analysis of arbitrarily shaped microwave and optical dielectric waveguides," *IEEE Transactions on Microwave Theory and Techniques,* vol. 33, pp. 894-899, 1985.

[61]   F. L. Ng, "Tabulation of methods for numerical solution of hollow waveguide problem," *IEEE Transactions on Microwave Theory and Techniques,* vol. TT-22, pp. 322-329, 1974.

[62]   S. Kagami and I. Fukai, "Application of boundary element method to electromagnetic field problems," *IEEE Transactions on Microwave Theory and Techniques,* vol. 32, pp. 455-461, 1984.

[63]   M. Koshiba and M. Suzuki, "Boundary-element analysis of dielectric slab waveguide discontinuities," *Applied Optics,* vol. 25, pp. 828-829, Mar 1986.

[64]   K. Hirayama and M. Koshiba, "Analysis of discontinuities in an open dielectric slab waveguide by combination of finite and boundary elements," *IEEE Transactions on Microwave Theory and Techniques,* vol. 37, pp. 761-768, Apr 1989.

[65]   J. E. Goell, "A circular-harmonic computer analysis of rectangular dielectric waveguides," *Bell System Technical Journal,* vol. 48, pp. 2133-2160, 1969.

[66]   A. L. Cullen, O. Ozkan, and L. A. Jackson, "Point-matching technique for rectangular cross section dielectric rod," *Electronics Letters,* vol. 7, p. 497, 1971.

[67]   S. T. Peng and A. A. Oliner, "Guidance and leakage properties of a class of open dielectric waveguides: Part I- Mathematical Formulations," *IEEE Transactions on Microwave Theory and Techniques,* vol. MTT-29, pp. 843-855, 1981.

[68]   N. Dagli and C. G. Fonstad, "Microwave equivalent circuit representation of rectangular dielectric waveguides," *Applied Physics Letters,* vol. 49, pp. 308-310, Aug 1986.

[69]   P. C. Kendall, P. W. A. McIlroy, and M. S. Stern, "Spectral index method for rib waveguide analysis," *Electronics Letters,* vol. 25, pp. 107-108, Jan 1989.

[70]   M. S. Stern, P. C. Kendall, and P. W. A. McIlroy, "Analysis of the spectral index method for vector modes of rib waveguides," *IEE Proceedings-Journal of Optoelectronics,* vol. 137, pp. 21-26, Feb 1990.

[71]   J. R. P. Pola, W. Biehlig, and F. Lederer, "A generalization of the spectral index method toward multiple rib waveguides," *Journal of Lightwave Technology,* vol. 14, pp. 454-461, Mar 1996.

[72]   W. C. Ng and M. S. Stern, "Analysis of multiple-rib waveguide structures by the discrete spectral-index method," *IEE Proceedings-Optoelectronics,* vol. 145, pp. 365-371, Dec 1998.

[73]   N. Ida, *Engineering electromagnetics*, 2nd ed. New York; London: Springer, 2004.

[74]   M. D. Feit and J. A. Fleck, "Computation of mode properties in optical fiber waveguides by a propagating beam method," *Applied Optics,* vol. 19, pp. 1154-1164, 1980.

[75] Y. Tsuji and M. Koshiba, "A Finite element beam propagation method for strongly guiding and longitudinally varying optical waveguides," *Journal of Lightwave Technology,* vol. 14, pp. 217-222, Feb 1996.

[76] B. M. A. Rahman and J. B. Davies, "Finite element analysis of optical and microwave waveguide problems," *IEEE Transactions on Microwave Theory and Techniques,* vol. MTT-32, pp. 20-28, 1984.

[77] B. M. A. Rahman and J. B. Davies, "Penalty-function improvement of waveguide solution by finite elements," *IEEE Transactions on Microwave Theory and Techniques,* vol. MTT-32, pp. 922-928, 1984.

[78] B. M. A. Rahman and J. B. Davies, "Finite element solution of integrated optical waveguides," *Journal of Lightwave Technology,* vol. 2, pp. 682-688, 1984.

[79] R. Courant, "Variational methods for the solution of problems of equilibrium and vibrations," *Bulletin of the American Mathematical Society,* vol. 49, pp. 1-23, 1943.

[80] M. J. Turner, R. W. Clough, H. C. Martin, and L. P. Topp, "Stiffness and deflection analysis of complex structures," *Journal of the Aeronautical Sciences,* vol. 23, Sep 1956.

[81] J. Greenstadt, "On the reduction of continuous problems to discrete form," *IBM Journal of Research and Development,* vol. 3, pp. 355-363, 1959.

[82] R. W. Clough, "The finite element method in plane stress analysis," *Proceedings of 2nd ASCE Conference on Electronic Computation, Pittsburgh, PA,* pp. 8-9, Sep 1960.

[83] M. Koshiba, K. Hayata, and M. Suzuki, "Approximate scalar finite element analysis of anisotropic optical waveguides," *Electronics Letters,* vol. 18, pp. 411-413, 1982.

[84] K. Morishita and N. Kumagai, "Unified approach to derivation of variational expression for electromagnetic fields," *IEEE Transactions on Microwave Theory and Techniques,* vol. MTT-25, pp. 34-40, 1977.

[85] M. Koshiba, K. Hayata, and M. Suzuki, "Finite element formulation in terms of the electric field vector for electromagnetic waveguide problems," *IEEE Transactions on Microwave Theory and Techniques,* vol. 33, pp. 900-905, 1985.

[86] N. Mabaya, P. E. Lagasse, and P. Vandenbulcke, "Finite element analysis of optical waveguides," *IEEE Transactions on Microwave Theory and Techniques,* vol. 29, pp. 600-605, 1981.

[87] J. A. M. Svedin, "A numerically efficient finite element formulation for the general waveguide problem without spurious modes," *IEEE Transactions on Microwave Theory and Techniques,* vol. 37, pp. 1708-1715, Nov 1989.

[88] W. J. English, "Vector variational solutions of inhomogeneously loaded cylindrical waveguide structures," *IEEE Transactions on Microwave Theory and Techniques,* vol. MTT-19, pp. 9-18, 1971.

[89] Z. J. Csendes and P. P. Silvester, "Numerical solution of dielectric loaded waveguides: I - finite element analysis," *IEEE Transactions on Microwave Theory and Techniques,* vol. MTT-18, pp. 1124-1131, 1970.

[90] S. Ahmed and P. Daly, "Finite element methods for inhomogeneous waveguides," *Proceedings of the Institution of Electrical Engineers-London,* vol. 116, pp. 1661-1664, 1969.

[91]  M. Ikeuchi, H. Sawami, and H. Niki, "Analysis of open type dielectric waveguides by the finite element iterative method," *IEEE Transactions on Microwave Theory and Techniques,* vol. 29, pp. 234-239, 1981.

[92]  R. B. Wu and C. H. Chen, "A variational analysis of dielectric waveguides by the conformal mapping technique," *IEEE Transactions on Microwave Theory and Techniques,* vol. 33, pp. 681-685, 1985.

[93]  T. Angkaew, M. Matsuhara, and N. Kumagai, "Finite element analysis of waveguide modes - a novel approach that eliminates spurious modes," *IEEE Transactions on Microwave Theory and Techniques,* vol. MTT-35, pp. 117-123, Feb 1987.

[94]  M. Ohtaka, M. Matsuhara, and N. Kumagai, "Analysis of guided modes in slab-coupled waveguides using a variational method," *IEEE Journal of Quantum Electronics,* vol. QE-12, pp. 378-382, 1976.

[95]  A. D. Berk, "Variational principles for electromagnetic resonators and waveguides," *IRE Transactions on, Antennas and Propagation,* vol. 04, pp. 104-111, 1956.

[96]  J. Katz, "Novel solution of 2-D waveguides using the finite element method," *Applied Optics,* vol. 21, pp. 2747-2750, 1982.

[97]  M. Koshiba, K. Hayata, and M. Suzuki, "Vector **E**-field finite element analysis of dielectric optical waveguides," *Applied Optics,* vol. 25, pp. 10-11, Jan 1986.

[98]  M. Koshiba, K. Hayata, and M. Suzuki, "Improved finite element formulation in terms of the magnetic field vector for dielectric waveguides," *IEEE Transactions on Microwave Theory and Techniques,* vol. MTT-33, pp. 227-233, 1985.

[99]  O. C. Zienkiewicz, *The finite element method*, 3rd, expanded and rev ed. London: McGraw-Hill (UK), 1977.

[100]  P. P. Silvester and R. L. Ferrari, *Finite elements for electrical engineers*, 2nd ed.: Cambridge University Press, 1990.

[101]  J. N. Reddy, *An introduction to the finite element method*. New York; London: McGraw-Hill, 1984.

[102]  A. Konrad, "Vector variational formulation of electromagnetic fields in anisotropic media," *IEEE Transactions on Microwave Theory and Techniques,* vol. MTT-24, pp. 553-559, 1976.

[103]  J. B. Davies, F. A. Fernandez, and G. Y. Philippou, "Finite element analysis of all modes in cavities with circular symmetry," *IEEE Transactions on Microwave Theory and Techniques,* vol. MTT-30, pp. 1975-1980, 1982.

[104]  K. Hayata, M. Koshiba, M. Eguchi, and M. Suzuki, "Novel finite element formulation without any spurious solutions for dielectric waveguides," *Electronics Letters,* vol. 22, pp. 295-296, Mar 1986.

[105]  M. D. Feit and J. A. Fleck, "Light propagation in graded-index optical fibers," *Applied Optics,* vol. 17, pp. 3990-3998, 1978.

[106]  S. T. Hendow and S. A. Shakir, "Recursive numerical solution for nonlinear wave propagation in fibers and cylindrically symmetrical systems," *Applied Optics,* vol. 25, pp. 1759-1764, Jun 1986.

[107]  D. Yevick and B. Hermansson, "Efficient beam propagation techniques," *IEEE Journal of Quantum Electronics,* vol. 26, pp. 109-112, Jan 1990.

[108]  P. C. Lee, D. Schulz, and E. Voges, "3-Dimensional finite difference beam propagation algorithms for photonic devices," *Journal of Lightwave Technology,* vol. 10, pp. 1832-1838, Dec 1992.

[109] K. Hayata, A. Misawa, and M. Koshiba, "Split-step finite element method applied to nonlinear integrated optics," *Journal of the Optical Society of America B-Optical Physics,* vol. 7, pp. 1772-1784, Sep 1990.

[110] R. Clauberg and P. Vonallmen, "Vectorial beam-propagation method for integrated optics," *Electronics Letters,* vol. 27, pp. 654-655, Apr 1991.

[111] P. L. Liu, S. L. Yang, and D. M. Yuan, "The semivectorial beam propagation method," *IEEE Journal of Quantum Electronics,* vol. 29, pp. 1205-1211, Apr 1993.

[112] S. V. Polstyanko, R. Dyczij-Edlinger, and J. F. Lee, "Full vectorial analysis of a nonlinear slab waveguide based on the nonlinear hybrid vector finite element method," *Optics Letters,* vol. 21, pp. 98-100, Jan 1996.

[113] S. S. A. Obayya, B. M. A. Rahman, and H. A. El-Mikati, "Full-vectorial finite-element beam propagation method for nonlinear directional coupler devices," *IEEE Journal of Quantum Electronics,* vol. 36, pp. 556-562, May 2000.

[114] S. S. A. Obayya, B. M. A. Rahman, and H. A. El-Mikati, "New full-vectorial numerically efficient propagation algorithm based on the finite element method," *Journal of Lightwave Technology,* vol. 18, pp. 409-415, Mar 2000.

[115] S. S. A. Obayya, B. M. A. Rahman, and H. A. El-Mikati, "Vector beam propagation analysis of polarization conversion in periodically loaded waveguides," *IEEE Photonics Technology Letters,* vol. 12, pp. 1346-1348, Oct 2000.

[116] J. P. Berenger, "A perfectly matched layer for the absorption of electromagnetic-waves," *Journal of Computational Physics,* vol. 114, pp. 185-200, Oct 1994.

[117] M. Koshiba, Y. Tsuji, and M. Hikari, "Finite element beam propagation method with perfectly matched layer boundary conditions," *IEEE Transactions on Magnetics,* vol. 35, pp. 1482-1485, May 1999.

[118] S. S. A. Obayya, *Computational Photonics*. Oxford: Wiley, 2011.

[119] P. A. Franken, A. E. Hill, C. W. Peters, and G. Weinreich, "Generation of optical harmonics," *Physical Review Letters,* vol. 7, pp. 118-119, 1961.

[120] P. A. Franken and J. F. Ward, "Optical harmonics and nonlinear phenomena," *Reviews of Modern Physics,* vol. 35, pp. 23-39, 1963.

[121] Y. Fujii, B. S. Kawasaki, K. O. Hill, and D. C. Johnson, "Sum frequency light generation in optical fibers," *Optics Letters,* vol. 5, pp. 48-50, 1980.

[122] Y. Sasaki and Y. Ohmori, "Phase matched sum-frequency light generation in optical fibers," *Applied Physics Letters,* vol. 39, pp. 466-468, 1981.

[123] Y. Ohmori and Y. Sasaki, "Two-wave sum-frequency light generation in optical fibers," *IEEE Journal of Quantum Electronics,* vol. 18, pp. 758-762, 1982.

[124] U. Österberg and W. Margulis, "Dye laser pumped by Nd:YAG laser pulses frequency doubled in a glass optical fiber," *Optics Letters,* vol. 11, pp. 516-518, 1986.

[125] H. Cao, J. Y. Wu, H. C. Ong, J. Y. Dai, and R. P. H. Chang, "Second harmonic generation in laser ablated zinc oxide thin films," *Applied Physics Letters,* vol. 73, pp. 572-574, Aug 1998.

[126] S. W. Chan, R. Barille, J. M. Nunzi, K. H. Tam, Y. H. Leung, W. K. Chan, and A. B. Djurisic, "Second harmonic generation in zinc oxide nanorods," *Applied Physics B-Lasers and Optics,* vol. 84, pp. 351-355, Jul 2006.

[127] R. Prasanth, L. K. Van Vugt, D. A. M. Vanmaekelbergh, and H. C. Gerritsen, "Resonance enhancement of optical second harmonic generation in a ZnO nanowire," *Applied Physics Letters,* vol. 88, May 2006.

[128] A. Yariv, *Quantum electronics*, 3rd ed.: Wiley, 1989.

[129] P. N. Butcher and D. Cotter, *The elements of nonlinear optics*: Cambridge University Press, 1990.

[130] R. W. Boyd, *Nonlinear optics*, 3rd ed. London: Academic, 2008.

[131] R. A. Myers, N. Mukherjee, and S. R. J. Brueck, "Large second order nonlinearity in poled fused silica," *Optics Letters,* vol. 16, pp. 1732-1734, 1991.

[132] H. Takebe, P. G. Kazansky, P. S. J. Russell, and K. Morinaga, "Effect of poling conditions on second harmonic generation in fused silica," *Optics Letters,* vol. 21, pp. 468-470, Apr 1996.

[133] P. Petropoulos, H. Ebendorff-Heidepriem, V. Finazzi, R. C. Moore, K. Frampton, D. J. Richardson, and T. M. Monro, "Highly nonlinear and anomalously dispersive lead silicate glass holey fibers," *Optics Express,* vol. 11, pp. 3568-3573, Dec 2003.

[134] V. Diez-Blanco, J. Siegel, and J. Solis, "Waveguide structures written in SF57 glass with fs-laser pulses above the critical self-focusing threshold," *Applied Surface Science,* vol. 252, pp. 4523-4526, Apr 2006.

[135] P. G. Kazansky, A. Kamal, and P. S. J. Russell, "High second order nonlinearities induced in lead silicate glass by electron beam irradiation," *Optics Letters,* vol. 18, pp. 693-695, May 1993.

[136] D. S. Hum and M. M. Fejer, "Quasi phase matching," *Comptes Rendus Physique,* vol. 8, pp. 180-198, Mar 2007.

[137] R. C. Miller, "Optical harmonic generation in single Crystal $BaTiO_3$," *Physical Review,* vol. 134, pp. A1313-A1319, 1964.

[138] Y. H. Xue, N. B. Min, J. S. Zhu, and D. Feng, "The second harmonic generation in $LiNbO_3$ crystals with periodic laminar ferroelectric domains," *Chinese Physics,* vol. 4, pp. 554-564, 1984.

[139] A. Feisst and P. Koidl, "Current induced periodic ferroelectric domain-structures in $LiNbO_3$ applied for efficient nonlinear optical frequency mixing," *Applied Physics Letters,* vol. 47, pp. 1125-1127, 1985.

[140] E. J. Lim, M. M. Fejer, and R. L. Byer, "Second harmonic generation of green light in periodically poled planar lithium niobate waveguide," *Electronics Letters,* vol. 25, pp. 174-175, Feb 1989.

[141] C. J. Van der Poel, J. D. Bierlein, J. B. Brown, and S. Colak, "Efficient type-I blue second harmonic generation in periodically segmented $KTiOPO_4$ waveguides," *Applied Physics Letters,* vol. 57, pp. 2074-2076, Nov 1990.

[142] S. Matsumoto, E. J. Lim, H. M. Hertz, and M. M. Fejer, "Quasiphase-matched second harmonic generation of blue light in electrically periodically poled lithium tantalate waveguides," *Electronics Letters,* vol. 27, pp. 2040-2042, Oct 1991.

[143] P. G. Kazansky and P. S. J. Russell, "Thermally poled glass: frozen-in electric field or oriented dipoles," *Optics Communications,* vol. 110, pp. 611-614, 1994.

[144] K. Saitoh and M. Koshiba, "Approximate scalar finite-element beam-propagation method with perfectly matched layers for anisotropic optical waveguides," *Journal of Lightwave Technology,* vol. 19, pp. 786-792, May 2001.

[145] Y. Tsuji, M. Koshiba, and T. Shiraishi, "Finite element beam propagation method for three-dimensional optical waveguide structures," *Journal of Lightwave Technology,* vol. 15, pp. 1728-1734, Sep 1997.

[146] K. Hayata, T. Sugawara, and M. Koshiba, "Modal analysis of the second harmonic electromagnetic field generated by the cherenkov effect in optical waveguides," *IEEE Journal of Quantum Electronics,* vol. 26, pp. 123-134, Jan 1990.

[147] D. Fluck, T. Pliska, P. Gunter, S. Bauer, L. Beckers, and C. Buchal, "Blue-light second harmonic generation in ion-implanted $KNbO_3$ channel waveguides of new design," *Applied Physics Letters,* vol. 69, pp. 4133-4135, Dec 1996.

[148] H. M. Masoudi and J. M. Arnold, "Modeling 2nd-order nonlinear effects in optical waveguides using a parallel processing beam propagation method," *IEEE Journal of Quantum Electronics,* vol. 31, pp. 2107-2113, Dec 1995.

[149] F. A. Katsriku, B. M. A. Rahman, and K. T. V. Grattan, "Numerical modeling of second harmonic generation in optical waveguides using the finite element method," *IEEE Journal of Quantum Electronics,* vol. 33, pp. 1727-1733, Oct 1997.

[150] T. M. Monro, D. J. Richardson, N. G. R. Broderick, and P. J. Bennett, "Holey optical fibers: An efficient modal model," *Journal of Lightwave Technology,* vol. 17, pp. 1093-1102, Jun 1999.

[151] T. A. Birks, J. C. Knight, and P. S. J. Russell, "Endlessly single-mode photonic crystal fiber," *Optics Letters,* vol. 22, pp. 961-963, Jul 1997.

[152] J. C. Knight, J. Arriaga, T. A. Birks, A. Ortigosa-Blanch, W. J. Wadsworth, and P. S. Russell, "Anomalous dispersion in photonic crystal fiber," *IEEE Photonics Technology Letters,* vol. 12, pp. 807-809, Jul 2000.

[153] J. M. Dudley, G. Genty, and S. Coen, "Supercontinuum generation in photonic crystal fiber," *Reviews of Modern Physics,* vol. 78, pp. 1135-1184, Oct-Dec 2006.

[154] K. Sakamaki, M. Nakao, M. Naganuma, and M. Izutsu, "Soliton induced supercontinuum generation in photonic crystal fiber," *IEEE Journal of Selected Topics in Quantum Electronics,* vol. 10, pp. 876-884, Sep-Oct 2004.

[155] G. McConnell and E. Riis, "Ultra-short pulse compression using photonic crystal fibre," *Applied Physics B-Lasers and Optics,* vol. 78, pp. 557-563, Mar 2004.

[156] M. A. Arbore, M. M. Fejer, M. E. Fermann, A. Hariharan, A. Galvanauskas, and D. Harter, "Frequency doubling of femtosecond erbium-fiber soliton lasers in periodically poled lithium niobate," *Optics Letters,* vol. 22, pp. 13-15, Jan 1997.

[157] J. K. Ranka, R. S. Windeler, and A. J. Stentz, "Optical properties of high-delta air-silica microstructure optical fibers," *Optics Letters,* vol. 25, pp. 796-798, Jun 2000.

[158] I. N. M. Wijeratne, N. Kejalakshmy, A. Agrawal, B. M. A. Rahman, and K. T. V. Grattan, "Numerical analysis of second harmonic generation in soft glass equiangular spiral photonic crystal fibers," *IEEE Photonics Journal,* vol. 4, pp. 357-368, Apr 2012.

[159] V. Pruneri and P. G. Kazansky, "Frequency doubling of picosecond pulses in periodically poled D-shape silica fibre," *Electronics Letters,* vol. 33, pp. 318-319, Feb 1997.

[160]  I. H. Malitson, "Interspecimen comparison of the refractive index of fused silica," *Journal of the Optical Society of America,* vol. 55, pp. 1205-1208, 1965.

[161]  A. Agrawal, N. Kejalakshmy, B. M. A. Rahman, and K. T. V. Grattan, "Soft glass equiangular spiral photonic crystal fiber for supercontinuum generation," *IEEE Photonics Technology Letters,* vol. 21, pp. 1722-1724, Nov 2009.

[162]  R. A. Myers, N. Mukherjee, and S. R. J. Brueck, "Large 2nd-order nonlinearity in poled fused silica," *Optics Letters,* vol. 16, pp. 1732-1734, Nov 1991.

[163]  D. Faccio, A. Busacca, W. Belardi, V. Pruneri, P. G. Kazansky, T. M. Monro, D. J. Richardson, B. Grappe, M. Cooper, and C. N. Pannell, "Demonstration of thermal poling in holey fibres," *Electronics Letters,* vol. 37, pp. 107-108, Jan 2001.

[164]  V. Pruneri, G. Bonfrate, P. G. Kazansky, C. Simonneau, P. Vidakovic, and J. A. Levenson, "Efficient frequency doubling of 1.5 mm femtosecond laser pulses in quasi-phase-matched optical fibers," *Applied Physics Letters,* vol. 72, pp. 1007-1009, Mar 1998.

[165]  V. Pruneri and P. G. Kazansky, "Electric-field thermally poled optical fibers for quasi phase matched second harmonic generation," *IEEE Photonics Technology Letters,* vol. 9, pp. 185-187, Feb 1997.

[166]  M. X. Qiu, F. Pi, and G. Orriols, "The role of lead component in second harmonic generation in lead silica by electron beam irradiation," *Applied Physics Letters,* vol. 73, pp. 3040-3042, Nov 1998.

[167]  M. Feng, A. K. Mairaj, D. W. Hewak, and T. M. Monro, "Nonsilica glasses for holey fibers," *Journal of Lightwave Technology,* vol. 23, pp. 2046-2054, Jun 2005.

[168]  N. A. Wolchover, F. Luan, A. K. George, J. C. Knight, and F. G. Omenetto, "High nonlinearity glass photonic crystal nanowires," *Optics Express,* vol. 15, pp. 829-833, Feb 2007.

[169]  S. Glass. Soft glass SF57 data sheet - lead containing glass type [Online]. Available: http://www.us.schott.com/advanced_optics/us/abbe_datasheets/schott_datash eet_sf57.pdf?highlighted_text=sf57

[170]  D. Wong, "Thermal stability of intrinsic stress birefringence in optical fibers," *Journal of Lightwave Technology,* vol. 8, pp. 1757-1761, Nov 1990.

[171]  T. Martynkien, J. Olszewski, M. Szpulak, G. Golojuch, W. Urbanczyk, T. Nasilowski, F. Berghmans, and H. Thienpont, "Experimental investigations of bending loss oscillations in large mode area photonic crystal fibers," *Optics Express,* vol. 15, pp. 13547-13556, Oct 2007.

[172]  C. Flueraru and C. P. Grover, "Overlap integral analysis for second harmonic generation within inverted waveguide using mode dispersion phase match," *IEEE Photonics Technology Letters,* vol. 15, pp. 697-699, May 2003.

[173]  F. A. Katsriku, B. M. A. Rahman, and K. T. V. Grattan, "Finite element analysis of second-harmonic generation in AlGaAs waveguides," *IEEE Journal of Quantum Electronics,* vol. 36, pp. 282-289, Mar 2000.

[174]  C. Martelli, J. Canning, N. Groothoff, and K. Lyytikainen, "Strain and temperature characterization of photonic crystal fiber Bragg gratings," *Optics Letters,* vol. 30, pp. 1785-1787, Jul 2005.

[175] V. Bhatia and A. M. Vengsarkar, "Optical fiber long-period grating sensors," *Optics Letters,* vol. 21, pp. 692-694, May 1996.

[176] D. Staedler, T. Magouroux, R. Hadji, C. Joulaud, J. Extermann, S. Schwungi, S. Passemard, C. Kasparian, G. Clarke, M. Gerrmann, R. Le Dantec, Y. Mugnier, D. Rytz, D. Ciepielewski, C. Galez, S. Gerber-Lemaire, L. Juillerat-Jeanneret, L. Bonacina, and J. P. Wolf, "Harmonic nanocrystals for biolabeling: A survey of optical properties and biocompatibility," *ACS Nano,* vol. 6, pp. 2542-2549, Mar 2012.

[177] M. M. Fejer, "Nonlinear optical frequency conversion," *Physics Today,* vol. 47, pp. 25-32, May 1994.

[178] V. Kapustianyk, B. Turko, A. Kostruba, Z. Sofiani, B. Derkowska, S. Dabos-Seignon, B. Barwinski, Y. Eliyashevskyi, and B. Sahraoui, "Influence of size effect and sputtering conditions on the crystallinity and optical properties of ZnO thin films," *Optics Communications,* vol. 269, pp. 346-350, Jan 2007.

[179] N. Ylilammi, J. Ella, M. Partanen, and J. Kaitila, "Thin film bulk acoustic wave filter," *IEEE Transactions on Ultrasonics Ferroelectrics and Frequency Control,* vol. 49, pp. 535-539, Apr 2002.

[180] P. Wu, N. W. Emanetoglu, X. Tong, and Y. Lu, "Temperature compensation of SAW in ZnO/SiO$_2$/Si structure," *IEEE Ultrasonics Symposium Proceedings,* vol. 1 and 2, pp. 211-214, 2001.

[181] V. Y. Zhang, J. E. Lefebvre, and T. Gryba, "SAW characteristics in a layered ZnO/GaAs structure for design of integrated SAW filters," *IEEE Ultrasonics Symposium Proceedings,* vol. 1 and 2, pp. 261-264, 2001.

[182] K. K. Zadeh, A. Trinchi, W. Wlodarski, and A. Holland, "A novel love-mode device based on a ZnO/ST-cut quartz crystal structure for sensing applications," *Sensors and Actuators A-Physical,* vol. 100, pp. 135-143, Sep 2002.

[183] S. H. Seo, W. C. Shin, and J. S. Park, "A novel method of fabricating ZnO/diamond/Si multilayers for surface acoustic wave (SAW) device applications," *Thin Solid Films,* vol. 416, pp. 190-196, Sep 2002.

[184] M. H. Lee, S. M. Chang, C. K. Park, J. B. Lee, and J. S. Park, "Characterization of ZnO/DLC/Si saw devices using FCVA-produced DLC films," *IEEE International Frequency Control Symposium & PDA Exhibition Proceedings,* pp. 70-73, 2002.

[185] I. T. Tang, Y. C. Wang, W. C. Hwang, C. C. Hwang, N. C. Wu, M. P. Houng, and Y. H. Wang, "Investigation of piezoelectric ZnO film deposited on diamond like carbon coated onto Si substrate under different sputtering conditions," *Journal of Crystal Growth,* vol. 252, pp. 190-198, May 2003.

[186] F. Herrmann, M. Weihnacht, and S. Buttgenbach, "Properties of sensors based on shear-horizontal surface acoustic waves in LiTaO$_3$/SiO$_2$ and quartz/SiO$_2$ structures," *IEEE Transactions on Ultrasonics Ferroelectrics and Frequency Control,* vol. 48, pp. 268-273, Jan 2001.

[187] K. Nakamura, H. Kitazume, and Y. Kawamura, "Optical TE-TM mode conversion using SH-SAW in ZnO/Y-X LiNbO$_3$," *IEEE Ultrasonics Symposium Proceedings,* vol. 1 and 2, pp. 637-641, 1999.

[188] J. D. Ye, S. L. Gu, S. M. Zhu, S. M. Liu, Y. D. Zheng, R. Zhang, Y. Shi, Q. Chen, H. Q. Yu, and Y. D. Ye, "Raman study of lattice dynamic behaviors in phosphorus-doped ZnO films," *Applied Physics Letters,* vol. 88, Mar 2006.

[189] B. E. Urban, P. B. Neogi, S. J. Butler, Y. Fujita, and A. Neogi, "Second harmonic imaging of plants tissues and cell implosion using two-photon

process in ZnO nanoparticles," *Journal of Biophotonics,* vol. 5, pp. 283-291, Mar 2012.

[190]   D. C. Dai, S. J. Xu, S. L. Shi, M. H. Xie, and C. M. Che, "Observation of both second harmonic and multiphoton absorption induced luminescence in ZnO," *IEEE Photonics Technology Letters,* vol. 18, pp. 1533-1535, Jul-Aug 2006.

[191]   S. Ono, H. Murakami, A. Quema, G. Diwa, N. Sarukura, R. Nagasaka, Y. Ichikawa, H. Ogino, E. Ohshima, A. Yoshikawa, and T. Fukuda, "Generation of terahertz radiation using zinc oxide as photoconductive material excited by ultraviolet pulses," *Applied Physics Letters,* vol. 87, Dec 2005.

[192]   J. S. Park, Y. Yamazaki, Y. Takahashi, S. K. Hong, J. H. Chang, T. Fujiwara, and T. Yao, "Origin of second order nonlinear optical response of polarity controlled ZnO films," *Applied Physics Letters,* vol. 94, Jun 2009.

[193]   F. A. Mahmoud and G. Kiriakidis, "Nanocrystalline ZnO thin film for gas sensor application," *Journal of Ovonic Research,* vol. 5, pp. 15-20, Jan-Feb 2009.

[194]   Y. Kawamura, N. Hattori, N. Miyatake, M. Horita, and Y. Uraoka, "ZnO thin films fabricated by plasma assisted atomic layer deposition," *Japanese Journal of Applied Physics,* vol. 50, Apr 2011.

[195]   M. Bass, E. W. Van Stryland, D. R. Williams, and W. L. Wolfe, *Handbook of optics*, 2nd / Michael Bass, editor in chief / Eric W. Van Stryland, associate editor, David R. Williams, associate editor, William L. Wolfe, associate editor. ed. New York ; London: McGraw-Hill, 1995.

[196]   M. Bass and V. N. Mahajan, *Handbook of optics*, 3rd / Michael Bass, editor-in-chief. ed. New York: McGraw-Hill, 2010.

[197]   A. P. Vasudev, J. A. Schuller, and M. L. Brongersma, "Nanophotonic light trapping with patterned transparent conductive oxides," *Optics Express,* vol. 20, pp. A385-A394, May 2012.

[198]   K. R. Parameswaran, R. K. Route, J. R. Kurz, R. V. Roussev, M. M. Fejer, and M. Fujimura, "Highly efficient second harmonic generation in buried waveguides formed by annealed and reverse proton exchange in periodically poled lithium niobate," *Optics Letters,* vol. 27, pp. 179-181, Feb 2002.

[199]   M. Guignard, V. Nazabal, J. Troles, F. Smektala, H. Zeghlache, Y. Quiquempois, A. Kudlinski, and G. Martinelli, "Second harmonic generation of thermally poled chalcogenide glass," *Optics Express,* vol. 13, pp. 789-795, Feb 2005.

[200]   V. Novak, R. Petkovsek, B. Podobnik, and J. Mozina, "CW fiber laser for second harmonic generation," *Strojniski Vestnik-Journal of Mechanical Engineering,* vol. 57, pp. 789-798, Nov 2011.

[201]   H. J. Gerritsen, "Nonlinear effects in image formation," *Applied Physics Letters,* vol. 10, pp. 239-241, 1967.

[202]   A. Yariv, "Phase conjugate optics and real-time holography," *Journal of the Optical Society of America,* vol. 69, pp. 1475-1475, 1979.

[203]   D. M. Pepper, J. AuYeung, D. Fekete, and A. Yariv, "Spatial convolution and correlation of optical fields via degenerate four-wave mixing," *Optics Letters,* vol. 3, pp. 7-9, 1978.

[204]   S. S. A. Obayya, "Vector finite element based beam propagation analysis of optical guided wave devices," *A thesis for PhD Degree,* 1999.